جامعة سيدي محمد بن عبد الله بفاس
UNIVERSITÉ SIDI MOHAMED BEN ABDELLAH DE FES

كلية العلوم ظهر المهراز فاس
FACULTE DES SCIENCES DHAR EL MAHRAZ FES

N° d'ordre : 50/2024

Centre des Etudes Doctorales : *Sciences et Techniques et Sciences Médicales.*

Formation Doctorale : *Sciences et Technologies de l'Information et de Communication.*

Discipline : *Physique*

Spécialité : *Génie électrique*

Laboratoire d'Ingénierie, Modélisation et Analyse des Systèmes

THÈSE DE DOCTORAT

Développement et Implémentation des Commandes Avancées pour une Génératrice Asynchrone à Double Alimentation dans un Système Éolien à l'aide de l'Intelligence Artificielle et un Système Embarqué

Présentée par :

YESSEF Mourad

Soutenue le 05/10/2024 devant le jury :

Nom et Prénom	Grade	Etablissement	Qualité
Pr EL BEKKALI Chakib	PES	Faculté des Sciences Dhar El Mahraz, USMBA, Fès	Président
Pr BENABOUD Aziza	PES	Ecole Royale Navale, Casablanca	Rapporteur & examinateur
Pr EL GHZAOUI Mohammed	PES	Faculté des Sciences Dhar El Mahraz, USMBA, Fès	Rapporteur & examinateur
Pr BOUZI Mostafa	PES	Faculté des Sciences et Techniques, Settat	Rapporteur & examinateur
Pr TAOUSSI Mohammed	MCH	Ecole Supérieure de Technologie, USMBA, Fès	Examinateur
Pr EL ALAMI Rachid	MCH	Faculté des Sciences Dhar El Mahraz, USMBA, Fès	Examinateur
Pr BOSSOUFI Badre	PES	Faculté des Sciences Dhar El Mahraz, USMBA, Fès	Directeur de thèse
Pr LAGRIOUI Ahmed	MCH	Ecole Nationale Supérieure des Arts et Métiers, Meknès	Co-Directeur de thèse

Année universitaire 2023-2024

N° d'ordre : 50/2024

Centre des Etudes Doctorales : *Sciences et Techniques et Sciences Médicales.*

Formation Doctorale : *Sciences et Technologies de l'Information et de Communication.*

Discipline : *Physique*

Spécialité : *Génie électrique*

Laboratoire d'Ingénierie, Modélisation et Analyse des Systèmes

THÈSE DE DOCTORAT

Development and Implementation of Advanced Control Techniques for a Doubly-Fed Induction Generator-Based Wind Energy System Using Artificial intelligence and an Embedded System

Présentée par :

YESSEF Mourad

Soutenue le 05/10/2024 devant le jury :

Nom et Prénom	Grade	Etablissement	Qualité
Pr EL BEKKALI Chakib	PES	Faculté des Sciences Dhar El Mahraz, USMBA, Fès	Président
Pr BENABOUD Aziza	PES	Ecole Royale Navale, Casablanca	Rapporteur & examinateur
Pr EL GHZAOUI Mohammed	PES	Faculté des Sciences Dhar El Mahraz, USMBA, Fès	Rapporteur & examinateur
Pr BOUZI Mostafa	PES	Faculté des Sciences et Techniques, Settat	Rapporteur & examinateur
Pr TAOUSSI Mohammed	MCH	Ecole Supérieure de Technologie, USMBA, Fès	Examinateur
Pr EL ALAMI Rachid	MCH	Faculté des Sciences Dhar El Mahraz, USMBA, Fès	Examinateur
Pr BOSSOUFI Badre	PES	Faculté des Sciences Dhar El Mahraz, USMBA, Fès	Directeur de thèse
Pr LAGRIOUI Ahmed	MCH	Ecole Nationale Supérieure des Arts et Métiers, Meknès	Co-Directeur de thèse

﴿بِسْمِ اللَّهِ الرَّحْمَٰنِ الرَّحِيمِ﴾

﴿وَمِنْ آيَاتِهِ أَن يُرْسِلَ الرِّيَاحَ مُبَشِّرَاتٍ وَلِيُذِيقَكُم مِّن رَّحْمَتِهِ وَلِتَجْرِيَ الْفُلْكُ بِأَمْرِهِ وَلِتَبْتَغُوا مِن فَضْلِهِ وَلَعَلَّكُمْ تَشْكُرُونَ﴾

(الروم - 46)

﴿In the name of Allah, the Most Gracious, the Most Merciful﴾

"And one of His signs is that He sends the winds, ushering in good news ˹of rain˺ so that He may give you a taste of His mercy, and that ships may sail by His command, and that you may seek His bounty, and perhaps you will be grateful."

(Surah Ar-Rum, 46)

In memory of my uncle YESSEF Larbi,

To my beloved parents for their enduring love,

motivation and support,

To my brothers and sisters,

To all my family,

To my friends,

and to all those who have supported me.

I dedicate this thesis.

Acknowledgement

First and foremost, I would like to express my deep gratitude to ALLAH for His countless blessings.

I warmly thank my thesis supervisors, Prof. Bossoufi Badre and Prof. Lagrioui Ahmed, for their support, encouragement, and inspiration. Without their insightful and constant guidance, this research project would not have come to fruition.

I would like to take this opportunity to express my deepest gratitude to Professor EL BEKKALI Chakib for kindly agreeing to serve as the president of the reading committee for my thesis.

I am also grateful to Prof. Mohammed Taoussi for his valuable advice throughout my research career.

I would also like to extend my sincere thanks to the rest of the reading committee members: Prof. Aziza Benaboud, Prof Mohammed El Ghzaoui, Prof. Mostafa Bouzi, and Prof. Rachid El Alami for their helpful comments and valuable suggestions.

I would like to express my deep gratitude to Dr. Habib Benbouhenni for his invaluable support, advice and encouragement throughout this research. His insightful comments and expertise have greatly contributed to the success of this work.

My thanks also go to Prof. Aziz Derouich, who gave me the opportunity to work on electrical machines in his laboratory at the Higher School of Technology of Fes.

I would like to express my profound gratitude to the jury members for agreeing to evaluate my work.

I am extremely grateful to the academic staff of the Faculty of Sciences Dhar El Mahraz of Fez for sharing their knowledge with me. I also wish to thank the administrative staff for their valuable help in simplifying the procedures.

Additionally, I thank all my friends for their moral and technical support, as well as their sympathy and friendship.

Finally, I am infinitely grateful to my parents and my relatives for their sacrifices, prayers, and the joyful moments they provided, especially during the difficult periods of this thesis.

List of publications

Articles

1. **Yessef, M**.; Bossoufi, B.; Taoussi, M.; Motahhir, S.; Lagrioui, A.; Chojaa, H.; Lee, S.; Kang, B.-G.; Abouhawwash, M. Improving the Maximum Power Extraction from Wind Turbines Using a Second-Generation CRONE Controller. *Energies* **2022**, *15*, 3644. https://doi.org/10.3390/en15103644.

2. **Yessef M**, Bossoufi B, Taoussi M, Lagrioui A, Chojaa H. Overview of control strategies for wind turbines: ANNC, FLC, SMC, BSC, and PI controllers. *Wind Engineering*. 2022;46(6):1820-1837. doi:10.1177/0309524X221109512.

3. **Yessef M**, Bossoufi B, Taoussi M, Lagrioui A. Enhancement of the direct power control by using backstepping approach for a doubly fed induction generator. Wind Engineering. 2022;46(5):1511-1525. doi:10.1177/0309524X221085670.

4. **M. Yessef** et al., "Experimental Validation of Feedback PI Controllers for Multi-Rotor Wind Energy Conversion Systems," in IEEE Access, vol. 12, pp. 7071-7088, 2024, doi: 10.1109/ACCESS.2024.3351355.

5. **M. Yessef** et al., "Real-Time Validation of Intelligent Super-Twisting Sliding Mode Control for Variable-Speed DFIG Using dSPACE 1104 Board," in IEEE Access, vol. 12, pp. 31892-31915, 2024, doi: 10.1109/ACCESS.2024.3367828**.**

6. **Yessef, M**., Taoussi, M., Benbouhenni, H., Lagrioui, A., Colak, I., Ameziane, H., Majout, B., & Bossoufi, B. (2024). Two different controllers-based DPC of the doubly-fed induction generator with real-time implementation on dSPACE 1104 controller board. *Measurement and Control*. https://doi.org/10.1177/00202940241236288.

7. H. Benbouhenni, **M. Yessef**, N. Bizon, B. Bossoufi and T. A. H. Alghamdi, "Experimental Assessment of a Dual Super-Twisting Control Technique of Variable-Speed Multi-Rotor Wind Turbine Systems," in *IEEE Access*, vol. 12, pp. 103744-103763, 2024, doi: 10.1109/ACCESS.2024.3434534.

8. Habib Benbouhenni, **Mourad Yessef**, Nicu Bizon, Sara Kadi, Badre Bossoufi, Ayman Alhejji, Hardware-in-the-loop simulation to validate the fractional-order neuro-fuzzy power control of variable-speed dual-rotor wind turbine systems, Energy Reports, Volume 11, 2024, Pages 4904-4923, ISSN 2352-4847, https://doi.org/10.1016/j.egyr.2024.04.049.

9. Benbouhenni, H., **Yessef, M**., Colak, I. *et al.* Dynamic performance of rotor-side nonlinear control technique for doubly-fed multi-rotor wind energy based on improved super-twisting algorithms under variable wind speed. *Sci Rep* 14, 5664 (2024). https://doi.org/10.1038/s41598-024-55271-7.

10. Habib Benbouhenni, Nicu Bizon, Ilhami Colak, Mohamed I. Mosaad, **Mourad Yessef**, Direct active and reactive powers control of double-powered asynchronous generators in multi-rotor wind power systems using modified synergetic control, Energy Reports, Volume 10, 2023, Pages 4286-4301, ISSN 2352-4847, https://doi.org/10.1016/j.egyr.2023.10.085.

11. Chojaa, H.; Derouich, A.; Taoussi, M.; Chehaidia, S.E.; Zamzoum, O.; Mosaad, M.I.; Alhejji, A.; **Yessef, M.** Nonlinear Control Strategies for Enhancing the Performance of DFIG-Based WECS under a Real Wind Profile. *Energies* **2022**, *15*, 6650. https://doi.org/10.3390/en15186650

Communications

1. **Yessef M**, Bossoufi B, Taoussi M, et al. (2021) Improved hybrid control strategy of the doubly-fed induction generator under a real wind profile. In: Motahhir S, Ossoufi B(eds) *Digital Technologies and Applications. ICDTA 2021. Lecture Notes in Networks and Systems*, vol. 211. Cham: Springer, pp.1279–1290.

2. **Yessef M**, Bossoufi B, Taoussi M, et al. (2022c) Evaluation of adaptive backstepping control applied to DFIG wind system used on the real wind profile of the Dakhla-Morocco City. In: Bennani S, Lakhrissi Y, Khaissidi G, et al. (eds) *WITS 2020. Lecture Notes in Electrical Engineering*, vol. 745. Singapore: Springer, pp.661–671.

3. **Yessef, M**., Bossoufi, B., Taoussi, M., Benbouhenni, H., Lagrioui, A., Chojaa, H. (2023). Intelligent Direct Power Control Based on the Neural Super-Twisting Sliding Mode Controller of a DFIG. In: Motahhir, S., Bossoufi, B. (eds) Digital Technologies and Applications. ICDTA 2023. Lecture Notes in Networks and Systems, vol 669. Springer, Cham. https://doi.org/10.1007/978-3-031-29860-8_73.

4. **Yessef, M**. *et al*. (2022). Robust Control of a Wind Conversion System Based on a Doubly Fed Induction Generator: A Comparison Between Adaptive Backstepping and Integral Sliding Mode Controllers. In: Motahhir, S., Bossoufi, B. (eds) Digital Technologies and Applications. ICDTA 2022. Lecture Notes in Networks and Systems, vol 454. Springer, Cham. https://doi.org/10.1007/978-3-031-01942-5_72.

5. O. E. Fadli, **M. Yessef** and A. Lagrioui, "Optimal Wind Farm Site Selection Using MCDM Approaches: A Combination of the VIMM Weighting Method and TOPSIS Ranking Algorithm," 2024 16th International Conference on Electronics, Computers and Artificial Intelligence (ECAI), Iasi, Romania, 2024, pp. 1-4, doi: 10.1109/ECAI61503.2024.10607467.

6. A. Yahya, **M. Yessef**, E. G. Bennouna, A. Lagrioui and N. Boutammachte, "Parabolic Trough Plant Performance In Morocco For Techno-economic Evaluation: A Case Study Of Noor 1," 2024 16th International Conference on Electronics, Computers and Artificial Intelligence (ECAI), Iasi, Romania, 2024, pp. 1-4, doi: 10.1109/ECAI61503.2024.10607532.

7. Chojaa, H., Derouich, A., Chehaidia, S.E., Taoussi, M., Zamzoum, O., Mosaad, M.I., Benbouhenni, H., **Yessef, M**., 2022. Advanced Control Techniques for Doubly-Fed Induction Generators Based Wind Energy Conversion Systems, in: 2022 Global Energy Conference (GEC). Presented at the 2022 Global Energy Conference (GEC), IEEE, Batman, Turkey, pp. 282–287. https://doi.org/10.1109/GEC55014.2022.9987088.

8. Chojaa, H., Derouich, A., Bourkhime, Y., Chetouani, E., Meghni, B., Chehaidia, S.E., **Yessef, M.**, 2022. Comparative Study of MPPT Controllers for a Wind Energy Conversion System, in: Saidi, R., El Bhiri, B., Maleh, Y., Mosallam, A., Essaaidi, M. (Eds.), Advanced Technologies for Humanity, Lecture Notes on Data Engineering and Communications Technologies. Springer International Publishing, Cham, pp. 300–310. https://doi.org/10.1007/978-3-030-94188-8_28.

9. Chojaa, H., Derouich, A., Taoussi, M., Zamzoum, O., **Yessef, M.** (2021). Optimization of DFIG Wind Turbine Power Quality Through Adaptive Fuzzy Control. In: Motahhir, S., Bossoufi, B. (eds) Digital Technologies and Applications. ICDTA 2021. Lecture Notes in Networks and Systems, vol 211. Springer, Cham. https://doi.org/10.1007/978-3-030-73882-2_113.

10. El Alami, H., Bossoufi, B., El Mahfoud, M., Btissam, M., **Yessef, M.**, Bekkour, E.-H., Salime, H., 2022. Improved Performance of Wind Turbines Based on Doubly Fed Generator Using the IFOC-SVM Control, in: Motahhir, S., Bossoufi, B. (Eds.), Digital Technologies and Applications, Lecture Notes in Networks and Systems. Springer International Publishing, Cham, pp. 812–822. https://doi.org/10.1007/978-3-031-02447-4_83.

11. Majout, B., Bossoufi, B., Karim, M., Ouanjli, N.E., Saady, I., Laggoun, Z.E.Z., Mahfoud, M.E., **Yessef, M.**, 2022. Model Reference Adaptive System Based DPC-SVM Control for Permanent Magnet Synchronous Generator, in: Motahhir, S., Bossoufi, B. (Eds.), Digital Technologies and Applications, Lecture Notes in Networks and Systems. Springer International Publishing, Cham, pp. 535–544. https://doi.org/10.1007/978-3-031-01942-5_53

12. El Mahfoud, M., Bossoufi, B., El Ouanjli, N., Mahfoud, S., **Yessef, M.**, Taoussi, M. (2021). Speed Sensorless Direct Torque Control of Doubly Fed Induction Motor Using Model Reference Adaptive System. In: Motahhir, S., Bossoufi, B. (eds) Digital Technologies and Applications. ICDTA 2021. Lecture Notes in Networks and Systems, vol 211. Springer, Cham. https://doi.org/10.1007/978-3-030-73882-2_165

Abstract

The aim of this thesis is to develop advanced and intelligent control techniques for wind energy conversion systems (WECS) based on a doubly-fed induction generator (DFIG) with variable speed, using fuzzy logic and artificial neural networks. The main objective is to optimize aerodynamic efficiency and maximize energy extraction by dynamically responding to wind speed fluctuations. Additionally, this research aims to improve the quality of the electrical power produced while ensuring the robustness and performance of the wind turbine against variations in system parameters and voltage dips.

We begin our research with the simulation and control of a 1.5 kW wind turbine using classical direct power control (C-DPC) based on hysteresis comparators and a commutation table. C-DPC relies on the direct control of active and reactive powers of the DFIG by selecting an optimal voltage vector to be applied to the rotor side converter (RSC) of the generator. However, this approach presents major drawbacks, such as significant oscillations in powers and currents, variable commutation frequency, risk of converter saturation, increased thermal losses, and complexity of the commutation table.

To address these issues, modified direct power control strategies have been developed. These include replacing the commutation table with pulse-width modulation (PWM) and substituting hysteresis comparators with controllers based on sliding mode control, super-twisting algorithm, as well as artificial intelligence techniques such as fuzzy logic and artificial neural networks. Thus, the controllers Fuzzy Super-Twisting Sliding Mode Control-based DPC (FSTSMC-DPC-PWM) and Neural Super-Twisting Sliding Mode Control-based DPC (NSTSMC-DPC-PWM) achieve the lowest levels of power and harmonic oscillations in stator currents, while ensuring excellent accuracy, effective tracking, and high robustness against variations in the generator's internal parameters. These improvements are reflected in reduced fluctuations in active and reactive power, decreased harmonic distortion rates of stator currents, as well as a reduction in steady-state error (SSE) and overshoot.

The intelligent techniques developed in this thesis have been rigorously tested through Processor-in-the-Loop (PIL) simulations using a dSPACE 1104 embedded system.

Keywords: Artificial Neural Networks, dSPACE 1104 Embedded Controller, DPC, DFIG, Fuzzy Logic, MPPT, SMC, Super-Twisting Algorithm, THD, PIL test, WECS.

Résumé

Le but de cette thèse est de développer des techniques de commande avancées et intelligentes pour les systèmes de conversion d'énergie éolienne (SCEE) basés sur une génératrice asynchrone à double alimentation (GADA) à vitesse variable, en utilisant la logique floue et les réseaux de neurones artificiels. L'objectif principal est d'optimiser l'efficacité aérodynamique et de maximiser l'extraction d'énergie en réagissant de manière dynamique aux fluctuations de la vitesse du vent. De plus, cette recherche vise à améliorer la qualité de l'énergie électrique produite tout en garantissant la robustesse et les performances de l'éolienne face aux variations des paramètres du système et aux creux de tension.

Nous commençons notre recherche par la simulation et le contrôle d'une éolienne de 1,5 kW en utilisant une commande directe de puissance (CDP) basée sur des comparateurs à hystérésis et une table de commutation. La CDP repose sur le contrôle direct des puissances actives et réactives de la GADA en sélectionnant un vecteur de tension optimal à appliquer au convertisseur côté rotor (CCR) de la génératrice. Cependant, cette approche présente des inconvénients majeurs, tels que de fortes oscillations au niveau des puissances et des courants, une fréquence de commutation variable, un risque de saturation des convertisseurs, une augmentation des pertes thermiques, et la complexité de la table de commutation.

Pour remédier à ces problèmes, des stratégies modifiées de commande directe de puissance ont été développées. Celles-ci incluent le remplacement de la table de commutation par la technique de modulation à largeur d'impulsion (MLI) et la substitution des comparateurs à hystérésis par des contrôleurs basés sur le contrôle par modes glissants, l'algorithme de super-torsion, ainsi que des techniques d'intelligence artificielle, telles que la logique floue et les réseaux de neurones artificiels. Ainsi, les contrôleurs (Fuzzy Super-Twisting Sliding Mode Control-based DPC) FSTSMC-DPC et (Neural Super-Twisting Sliding Mode Control-based DPC-PWM) NSTSMC-DPC-PWM permettent d'obtenir les niveaux les plus faibles d'oscillations de puissance et d'harmoniques dans les courants statoriques, tout en assurant une excellente précision, un suivi performant et une grande robustesse face aux variations des paramètres internes de la génératrice. Ces améliorations se traduisent par une réduction des ondulations des puissances actives et réactives, une diminution du taux de distorsion harmonique des courants statoriques, ainsi qu'une réduction de l'erreur de régime permanent (Steady-State Error, SSE) et du dépassement. Les techniques développées dans cette thèse ont été rigoureusement testées via des simulations Processor-in-the-Loop (PIL) en utilisant un système embarqué basé sur la carte dSPACE 1104.

Mots-clés : Algorithme de Super-Twisting, Carte embarquée dSPACE 1104, Contrôle direct de puissance, Contrôle par mode glissant, GADA, PIL test, Intelligence artificielle, Logique floue, MPPT, Réseaux de neurones artificiels, Système éolien, (Distorsion Harmonique Totale) THD.

Table of Contents

Acknowledgement ..... **iii**

List of publications.....**iv**

Abstract ..... **vii**

Résumé .....**viii**

Table of Contents .....**x**

List of Figures .....**xiv**

List of Tables .....**xviii**

Nomenclature .....**xx**

Abbreviations .....**xxiii**

General introduction.....**1**

Chapter 1: State of the art of wind energy conversion system…….....**5**

1.1. Introduction.....6

1.2. Definition of wind energy.....6

1.3. Types of wind turbine.....7

1.3.1 Vertical axis wind turbine……..……7

1.3.1.1 Savionis rotor.....8

1.3.1.1 Darrieus rotor.....8

1.3.2 Horizental axis wind turbines 9

1.4. Components of horizontal axis wind turbine.....10

1.4.1 The rotor……..……11

1.4.2 The nacelle ……..……12

1.4.3 The tower……..……..……13

1.5. Kinetic wind energy – Conversion to electrical energy and Betz Law……. 13

1.6. Aeodynamic power control…….14

1.7. Configurations of wind energy conversion system……..……...17

1.7.1 Fixed-speed wind turbine…….……18

1.7.2 Varaiable-speed wind turbines based on an asynchronous generator……..……18

1.7.3 Varaiable-speed wind turbines based on a doubly fed induction generator..…….....19

1.7.4 Varaiable-speed wind turbines based on a permanent magnet synchronous generator…….…...19

1.7.5 Comparison between the two types of configurations……..……....20

1.8. Principles and operating mode of the DFIM……...21

1.8.1 Operating principle…….……...21

1.8.2 Operation in sub-synchronous motor mode……..22
1.8.3 Operation in super-synchronous motor mode…….....22
1.8.4 Operation in sub-synchronous generator mode……..……...23
1.8.5 Operation in super-synchronous motor mode…….……..23
1.9. Configurations of converters related to the DFIG……...24
1.9.1 Krame structure: diode bridge and thyristor bridge……..24
1.9.2 Structure of diode bridge and transistor bridge…….25
1.9.3 Scherbius structure: Cycloconverters…….……...25
1.9.4 Scherbius structure with PWM converters…….……...26
1.10. Methods to improve wind turbines using DFIG…….....27
1.11. Thesis pbjectives…….……...28
1.12. Summary…….……...29
Chapter 2: Modeling of a DFIG-based wind energy conversion system…….……..…….30
2.1. Introduction.....31
2.2. Modeling of wind turbine.....31
2.2.1 Aerodynamic model.....31
2.2.2 Modeling of the mechanical components.....32
2.2.2.1 Gearbox model.....32
2.2.2.2 Dynamic shaft model.....33
2.3. DFIG modeling.....33
2.3.1 Three-phase modeling of DFIG.....33
2.3.1.1 Electrical equations in the (abc) reference frame.....34
2.3.1.2 Magnetic equations.....35
2.3.2 Two-phase modeling of DFIG.....36
2.3.2.1 Model of the DFIG in the αβ reference frame.....36
2.3.2.2 Model of the DFIG in the Park reference frame.....38
2.4. Combining DFIG with powers converters.....41
2.4.1 Rotor side converter (RSC).....42
2.4.2 DC bus modeling.....46
2.4.3 Grid side converter (GSC).....46
2.4.4 Modeling of the filter.....47
2.4.5 modeling of the grid.....48
2.4.6 Pulse width modelation (PWM) control.....48

2.4. Summary 51
Chapter 3: Direct Power Control (DPC) of Doubly-Fed Induction Generator…….....52
3.1. Introduction 53
3.2. Maximum power extraction technique 54
3.2.1 MPPT control with speed feedback 54
3.2.2 Matlab/Simulink simulations results 56
3.3. Direct power control 58
3.3.1 A review of various direct power control 58
3.3.2 Principle of classical Direct Power Control C-DPC 60
3.3.3 Classical DPC of DFIG 62
3.3.3.1 Estimation of active and reactive power 62
3.3.3.2 Choice of hysteresis comparators 64
3.3.3.2 Formulation of switching table 65
3.3.4 Simulations results 68
3.3.4.1 Simulations results under step wind profile of C-DPC strategy 68
3.3.4.2 Simulations results under variable wind profile of C-DPC strategy 71
3.4. the design of second-Order Sliding Mode Control (STSMC) 74
3.4.1 Application of the STSMC control 76
3.5. Simulations results 79
3.5.1 First test (step wind profile) 79
3.5.2 Second test (variable wind profile) 82
3.5. Summary 85
Chapter 4: Fuzzy Super-Twisting Sliding Control-Based Direct Power Control of Doubly Fed Induction Generators……...86
4.1. Introduction 87
4.2. Proposed FSTSMC controller 88
4.3. Simulations results 93
4.3.1 Step wind profile test 93
4.3.2 Test under variable wind profile of FSTSMC-DPC-PWM 97
4.4. Summary 100
Chapter 5: Intelligent Super-Twisting Sliding Mode Control for the DFIG using the Artificial Neural Network ……....101
5.1. Introduction 102
5.2. Designed NSTSMC-DPC-PWM control technique 104

5.3. Simulations results of NSTSMC-DPC-PWM control applied to DFIG 111
5.3.1 Simulations test under Step wind speed 111
5.3.2. Simulations results under wind profile test 115
5.3.3. Comparison in term of THD between developed control strategies in this thesis 117
5.3.3. Comparison in term of THD between NSTSMC-DPC-PWM and other researchers recent works 118
5.4. Robustness test 119
5.4. Processor-In-the-Loop test 122
5.4.1 PIL test with dSPACE 1104 123
5.5. Summary 131
General conclusion and perspectives 133
References 135
Appendix A 145

List of figures

Figure 1.1: Converting wind's kinetic energy into electrical energy……...……...….6
Figure 1.2: Type of wind turbines…….……...…7
Figure 1.3: (a) The Savonius type wind turbine. (b) The principle of the Savonius roto…..……..8
Figure 1.4: (a) The Savonius type wind turbine. (b) The principle of the Savonius roto……..…..9
Figure 1.5: Horizontal axis turbine……..9
Figure 1.6: Types of horizontal axis wind turbines…….....…...…10
Figure 1.7: Components of a horizontal axis wind turbine…….....11
Figure 1.8: Streamtube around a wind turbine……..13
Figure 1.9: P_m/P_{mt} as function of V_2/V_1……..……...14
Figure 1.10: Power characteristic as function of wind speed……..……..15
Figure 1.11: SCIG based wind enrgy conversion system……..18
Figure 1.12: WRIG based wind enrgy conversion system……...…….18
Figure 1.13: DFIG based wind enrgy conversion system……..19
Figure 1.14: PMSG based wind enrgy conversion system……..……..20
Figure 1.15: Operation in sub-synchronous motor mode…….……...……..22
Figure 1.16: Operation in super-synchronous motor mode…….……..23
Figure 1.17: Operation in sub-synchronous generator mode……..……..….23
Figure 1.18: Operation in super-synchronous generator mode……...……..….24
Figure 1.19: Kramer structure……..……...……..….25
Figure 1.20: DFIG powered by a diode and a PWM-based inverter……..…25
Figure 2.1: Functional diagram of a wind turbine based on a doubly fed induction generator connected to the grid……..31
Figure 2.2: Block diagram of a wind turbine……..…33
Figure 2.3: The three-phase stator and rotor winding of the DFIG……..…….34
Figure 2.4: Equivalent electrical circuit of the DFIG…….... ……...…….34
Figure 2.5: Equivalent circuit pf the DFIG in the αβ reference frame…….…….37
Figure 2.6: The two-phase model of the DFIG…….….39
Figure 2.7: Equivalent electrical circuit of the DFIG in the dq reference frame…...…….. ….41
Figure 2.8: Components of the DFIG power system…...……..…….. ….41
Figure 2.9: Rotor side converter (RSC)…...…….…….…….....43

Figure 2.10: Model of the DC bus…..…….. ……...46
Figure 2.11: Grid side converter (RSC)……..…47
Figure 2.12: Model of the phase (a) filter…….48
Figure 2.13: Principle of PWM control…….49
Figure 2.14: Example of signal generation using PWM……50
Figure 3.1: MPPT control with speed feedback……...……...…55
Figure 3.2: Speed controller used for MPPT…….55
Figure 3.3: MPPT simulations results…….……...….57
Figure 3.4: Configuration of the classical DPC (C-DPC) of the DFIG……..…62
Figure 3.5: The decomposition of the rotor flux vector in the αβ reference……..…64
Figure 3.6: Hysteresis comparators…… ……..……....64
Figure 3.7: Simulations results of C-DPC with step wind profile……..…..…..…..69
Figure 3.8: Simulations results of C-DPC with variable wind profile……..…...…..72
Figure 3.10: STSMC-DPC-PWM technique od DFIG-WT…….….77
Figure 3.11: STSMC controller of Ps and Qs powers …….…….79
Figure 3.12: Simulations results of C-DPC and STSMC-DPC-PWM (test 1)……..84
Figure 3.13: Simulations results of C-DPC and STSMC-DPC-PWM (test2)…….....…..84
Figure 4.1: Designed FSTSMC technique ……...…….89
Figure 4.2: MFs for inputs……...…….……..…...89
Figure 4.3: Structure of FL technique.……...……..…..90
Figure 4.4: FSTSMC-DPC-PWM technique for a DFIG……...…91
Figure 4.5: Active and reactive powers FSTSMC-DPC-PWM controllers.……..93
Figure 4.6: Simulations results of FSTSMC-DPC-PWM under step wind profile……...95
Figure 4.7: Simulations results of FSTSMC-DPC-PWM under variable wind profile…….....99
Figure 5.1: Design of research steps…….…...104
Figure 5.2: Diagram of the ANN controller training steps…….....…...106
Figure 5.3: Block diagram of the internal structure of the RSC control……...…...107
Figure 5.4: The STSMC – Ps and Qs techniques…….…....108
Figure 5.5: The NSTSMC command……...…….…...109
Figure 5.6: The ANN strategies……...…….…...110
Figure 5.7: Layer 1……...…….……...110
Figure 5.8: Layer 2……...…….…...110
Figure 5.9: The NSTSMC command……...…….…...110
Figure 5.10: Simulations results of NSTSMC-DPC-PWM under step wind profile……...113

Figure 5.11: Simulations results of NSTSMC-DPC-PWM under variable wind profile…..…...116
Figure 5.12: Simulations results of the robustness test under step wind profile……..…...120
Figure 5.13: Simulations results of the robustness test under variabvle wind profile…….…....121
Figure 5.14: dSPCAE DS 1104 R&D controller board…….……..126
Figure 5.15. PIL test setups of innovative proposed control strategies……...126
Figure 5.16: Results of PIL test under step wind profile…….128
Figure 5.17: Results of PIL test under variable wind profile…….…..130

List of tables

Table 1.1: Classification of wind turbines…….10

Table 1.2: Comparison between the operation modes……...21

Table 2.1: The components of the rotor voltage in the reference frame……....44

Table 2.2: The components of the rotor voltage in the αβ reference frame…….…..45

Table 3.1: Selection table of optimal vectors (active and reactive powers) ……...…...66

Table 3.2: Monitoring of reactive power variation……66

Table 3.3: Sector update table……67

Table 3.4: Generalized table of voltage vectors for DPF control…….……...……..67

Table 3.5 : Response time, overshoot, and energy ripples in the first test (step wind profile)…..70

Table 3.6 : Response time, overshoot, and energy ripples in the first test (step wind profile)…..73

Table 3.7: Improvement ratios and SSE, Response time, overshoot, and enrgy ripples in the first test (step wind profile) ……...…….. ……81

Table 3.8: Improvement ratios and SSE, Response time, overshoot, and enrgy ripples in the first test (step wind profile) ……...…….. ……84

Table 4.1: Fuzzy rules……89

Table 4.2: Improvement ratios and SSE, response time, energy ripples, overshoot in the first test…….…….96

Table 4.3: Improvement rates and SSE, response time, energy ripples, overshoot in the second test…….…….99

Table 5.1: Characteristics of the neural algorithms……..111

Table 5.2: Improvement ratios and SSE, response time, energy ripples, overshoot in the first test…….……...113

Table 5.3: Improvement ratios and SSE, response time, energy ripples, overshoot in the first test…….……...116

Table 5.4: Comparison of THD values……118

Table 5.5: Comparison in terms of THD values with other works values……...…118

Nomenclature

Symbol	Definition
Cp	Power Coefficient
Df	Damping Factor
Kp	Proportional Gain
Ki	Integral Gain
Kpwm	PWM Gain
LCL	Inductor-Capacitor-Inductor
ε	Error
Δε	Change in Error
η1	Gain for Qs Control
η2	Gain for Ps Control
r1	Control Parameter for Qs
r2	Control Parameter for Ps
Te	Electromagnetic Torque
Ps	Active Power
Qs	Reactive Power
Ias	Stator Current
SSE	Steady-State Error
TSR	Tip Speed Ratio
ωr	Rotor Angular Speed
λ1	Super-Twisting Control Parameter 1
λ2	Super-Twisting Control Parameter 2
Vqr*	Quadrature Rotor Voltage Reference
Vdr*	Direct Rotor Voltage Reference
Iqr*	Quadrature Rotor Current
Idr*	Direct Rotor Current
Ψrα	Rotor Flux Component α
Ψrβ	Rotor Flux Component β
Ψr	Rotor Flux

Vs	Stator Voltage
Lm	Magnetizing Inductance
σ	Leakage Factor
Ls	Stator Inductance
Lr	Rotor Inductance
ωr	Rotor Angular Speed
εrea	Reactive Power Error
εact	Active Power Error
ρ	Air Density
R	Radius of the Turbine
v	Wind Speed
Ωt	Rotational Speed of the Turbine
Vr	Rotor Voltage
Rr	Rotor Resistance
irα	Rotor Current Component α
irβ	Rotor Current Component β
Vr	Voltage Reference
ωr	Rotor Angular Speed
BM	Upper Bound of B
Bm	Lower Bound of B
AM	Upper Bound of A
A	System State
u	Input Function
y	Output Function
x	State Variable
εr	Error in reactive power
εp	Error in active power
Ψrβ	Rotor Flux Component β
Ψrα	Rotor Flux Component α
Ps*	Reference Active Power

Qs*	Reference Reactive Power
E	Wind Energy
P	Power
Ps	Active Power
Q	Reactive Power
ωm	Mechanical Angular Speed
θ	Rotor Position
Vds	Stator Voltage in d-axis
Vqs	Stator Voltage in q-axis
Ids	Stator Current in d-axis
Iqs	Stator Current in q-axis
ϕds	Stator Flux in d-axis
ϕqs	Stator Flux in q-axis
p	Number of Pole Pairs
J	Moment of Inertia
B	Friction Coefficient
Tm	Mechanical Torque
Ve	Back EMF Voltage

Abbreviations

Symbol	Definition
DFIG	Doubly Fed Induction Generator
DPC	Direct Power Control
WECS	Wind Energy Conversion System
DPC-STC	Direct Power Control based on Super-Twisting Control
MSTC	Modified Super-Twisting Control
GSC	Grid Side Converter
RSC	Rotor Side Converter
PWM	Pulse Width Modulation
THD	Total Harmonic Distortion
PIL	Processor-In-The-Loop
PWM	Pulse Width Modulation
ANN	Artificial Neural Network
BC	Backstepping Control
FL	Fuzzy logic
CPC	Continuous Power Control
FSTSMC-DPC	Fuzzy Super-Twisting Sliding Mode Control-based Direct Power Control
NSTSMC-DPC	Neural Super-Twisting Sliding Mode Control-based Direct power Control
SSE	Steady-State Error
PI	Proportional-Integral
PSO	Particle Swarm Optimization
PWM	Pulse Width Modulation
SMC	Sliding Mode Control
STA	Super-Twisting Algorithm
SVPWM	Space Vector Pulse Width Modulation
THD	Total Harmonic Distortion
WS	Wind Speed

General introduction

The intense industrialization of recent decades and the proliferation of electrical domestic devices (heating, air conditioning, washing, medical, computing, etc.) have led to substantial global demands for electrical energy [1]. However, before consuming it, it must be produced, generally in high-power production units, transported, and then distributed to each consumer. Today, more than 675 million people lack access to electricity due to fragile economies, costly and heavy infrastructure, difficult-to-reach areas, and dispersed habitats [2].

In response to the depletion of polluting fossil fuels (oil, gas, and coal) and the environmental issues caused by greenhouse gas emissions during the exploitation of these resources, other alternative energy sources have been and must continue to be developed. Among them, nuclear fission energy can be mentioned as it does not directly emit carbon dioxide (mainly CO2) [3]. However, the management of waste from this mode of production is very costly, and their radioactivity remains high for many years. Another alternative is to harness renewable energies, which offer the possibility of producing clean electricity and reduce dependence on resources, provided we accept their natural and sometimes unpredictable fluctuations.

Today, the production of electrical energy through wind systems is becoming competitive in terms of production costs and is contributing to the reduction of greenhouse gas emissions [4].

Wind energy systems represent the fastest-growing technology. Among these wind technologies, many different types of systems have been designed and developed, building on a long history of experience in this field that spans several centuries. Today, the most well-known and widely used form of wind technology is the wind turbine, a machine that harnesses energy from the wind to generate electrical current. The process of converting wind energy into electrical energy involves various electrotechnical components. To maximize the efficiency of this energy conversion, numerous solutions have been explored, both in terms of the generator used and the power electronics involved [5].

The wind turbine is the most commonly used technology for harnessing wind energy. Its power output can range from a few watts to several megawatts. The most widely used type is the three-blade horizontal-axis wind turbine [6].

Currently, the variable-speed wind turbine system based on the doubly-fed induction generator (DFIG) is the most widely used in onshore wind farms. Its main advantage, among others, is that its three-phase static converters are sized for only a portion of the generator’s nominal power. This offers significant economic benefits compared to other electromechanical conversion solutions (such as synchronous machines with permanent magnets). Indeed, the DFIG allows operation within a speed range of ±30% around the synchronous speed, thereby

ensuring a reduced sizing of the static converters as they are connected between the rotor winding of the DFIG and the electrical load [5].

The efficiency of conventional horizontal-axis three-blade wind turbines is around 0.4. This characteristic is constrained by the Betz limit, which reaches a maximum of 0.59. However, this limit is not insurmountable. Recent studies have been conducted to design more efficient wind turbines that offer improved power characteristics [5, 6, 7, 8].

In this context, the primary objective of this research is to enhance the electrical power output by employing a new control strategy for wind energy conversion systems. This involves a wind turbine coupled with a doubly-fed induction generator (DFIG) and includes an AC/DC converter, a DC bus, and an inverter, focusing on improving the direct power control of the rotor-side converter (RSC) using artificial intelligence techniques.

Direct Power Control (DPC) is a control strategy used to regulate active and reactive power in wind energy conversion systems, particularly with Doubly Fed Induction Generators (DFIGs). This method is valued for its conceptual simplicity and its ability to directly control active and reactive power by quickly adjusting output voltages. However, DPC has several drawbacks for DFIGs. Firstly, it relies on the use of hysteresis comparators and switching tables, which can lead to power ripples and high levels of harmonic distortion in the stator currents. Secondly, chattering, or unwanted oscillations, is a significant issue that can degrade system performance and reliability. Additionally, DPC can be less effective in handling variations in DFIG parameters, thus reducing its robustness in response to changing operating conditions [8, 9].

Sliding Mode Control (SMC) for nonlinear systems has been extensively studied and developed since its introduction [10,11]. It falls under a broader category known as variable structure control. The goal of this method is to drive the system to and maintain it on a surface known as the sliding surface, using a discontinuous control action. This sliding surface ensures that the system's behavior aligns with the desired dynamics after a finite time. The controlled system's operation is termed sliding mode, and its dynamics can be made insensitive to parametric variations, modeling errors, and certain external disturbances. Sliding Mode Control laws are relatively simple to design and exhibit robustness against specific classes of disturbances [12, 13]. However, there are some issues, such as the chattering phenomenon, which arises due to the discontinuous nature of Sliding Mode Control (SMC). whose principle is to reject discontinuities in the upper derivatives of the system input. The effect of chattering is thus reduced, while preserving robustness properties and even improving convergence accuracy [14, 15].

The drawbacks of Direct Power Control (DPC) and Sliding Mode Control (SMC) strategies can indeed be detrimental to machines, leading to significant heating of the windings or exciting high-frequency dynamics that are not modeled. They can also negatively impact the static converter, particularly affecting the switching frequency of static switches. Depending on the frequency of this

phenomenon, it can cause damage to power electronics during switching. Various methods exist to mitigate this issue. One approach is to replace the sign function with a continuous approximation near the sliding surface (such as a saturation function or sigmoid function) [14]. Another method involves using higher-order sliding modes [15, 16, 17], which helps eliminate discontinuities in the higher-order derivatives of the system's input. This reduces chattering effects while preserving robustness and even improving convergence accuracy.

The research conducted during the preparation of this thesis focused on improving the direct power control and sliding mode controller of the rotor-side converter (RSC) using artificial intelligence techniques.

The first chapter of this thesis is dedicated primarily to general concepts about wind energy and the various types of wind turbines. It will then explain the components and operating zones of horizontal-axis wind turbines. Depending on the operating zone, different aerodynamic power control strategies will be presented. Subsequently, the four types of Wind Energy Conversion Systems (WECS) will be discussed, with particular emphasis on power system type which involves WECS based on a Doubly Fed Induction Generator (DFIG), its operating modes, and the topologies of DFIG-converter associations [18].

The second chapter focuses on the modeling of a Wind Energy Conversion System (WECS) based on a Doubly Fed Induction Generator (DFIG). This chapter first presents the modeling of the wind turbine. Next, the model of the DFIG is established in several reference frames. This modeling will be useful for the following chapters. Finally, the power converters and their associated elements are modeled [19].

In the third chapter we design the direct power control (DPC) and the Super-twisting direct power pulse width modulation control (STC-DPC-PWM) for variable-speed doubly-fed induction generator-based wind turbines. The simulation results showed that Direct Power Control (DPC) delivers good performance in terms of tracking and robustness against parametric variations. However, it has a major drawback: the use of hysteresis controllers, which generate significant torque and flux ripples as well as current distortion. The STSMC-DPC technique has slightly reduced the oscillations and the Total Harmonic Distortion (THD) [20].

In Chapter 4, we propose an enhancement of the Super-Twisting Sliding Mode Direct Power Control (STSMC-DPC) discussed in Chapter 4 by incorporating fuzzy logic. To achieve this, we will explain the fundamental concepts of fuzzy logic and the basic principles of fuzzy logic control before applying them to STSMC-DPC. To verify the proposed control strategy,

simulation results will be presented, and the NSTSMC-DPC will also be implemented on the dSPACE 1104 board.

In the chapter 5, we propose an improvement to the control strategy discussed in Chapter 3 by using artificial neural networks. The fundamental concepts of neural networks are introduced, along with an overview of control methods utilizing this technique. The proposed idea involves replacing the sign function of the super-twisting algorithm with a neural network block. This technique has demonstrated its superiority over other methods in terms of reducing oscillations, steady-state error (SSE), overshoot, and total harmonic distortion (THD). It has also shown good performance in terms of robustness. This control strategy has also been test under Processor in the Loop test with the dSPACE 1104 controller board.

The general conclusion provides a comprehensive summary of the completed work in this thesis and offers several ideas and considerations for future research endeavors.

Chapter 1: State of the Art of Wind Energy Conversion Systems.

1.1. Introduction

The process of capturing kinetic energy from the wind and transforming it into various useful forms of energy has been practiced for thousands of years. Over 2,000 years ago, people began utilizing wind power. The Egyptians were among the earliest to use wind to sail on the Nile River. By 200 B.C., simple windmills in China were being used to pump water, while vertical-axis windmills were grinding grain in Persia (now Iran) and the Middle East. In Europe, windmills made their appearance in the 12th century, and in America, they were used between 1850 and 1900. By 1900, Denmark had about 2,500 windmills generating around 30 MW of power for mechanical tasks like pumping water and milling grain [21].

In the 20th century, the most significant impact of wind energy was the growing reliance on electricity. However, wind turbines only started gaining significant popularity as an alternative to oil-based energy during the 1970s oil crisis. Today, the primary motivation for the expansion and adoption of wind energy is the fight against global warming. The current focus on wind energy arises from the need to create sustainable, clean energy systems that can be depended upon over the long term [22].

1.2. Definition of wind energy

A wind turbine, sometimes referred to as a windmill, is a complex system that converts part of the wind's kinetic energy into mechanical energy on a drive shaft, which is then transformed into electrical energy through an electric generator [23], [24].

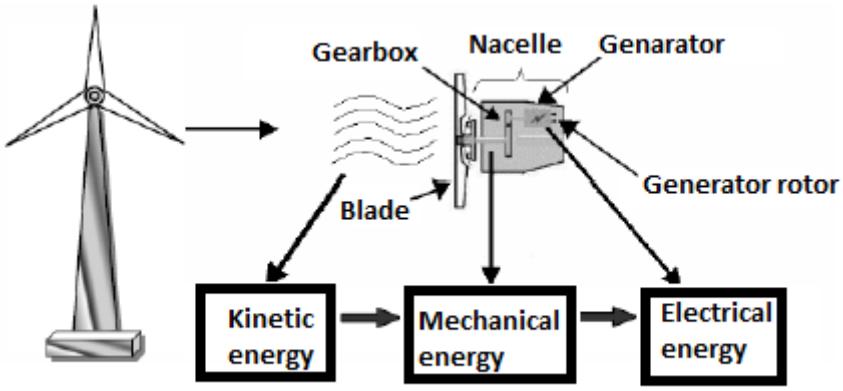
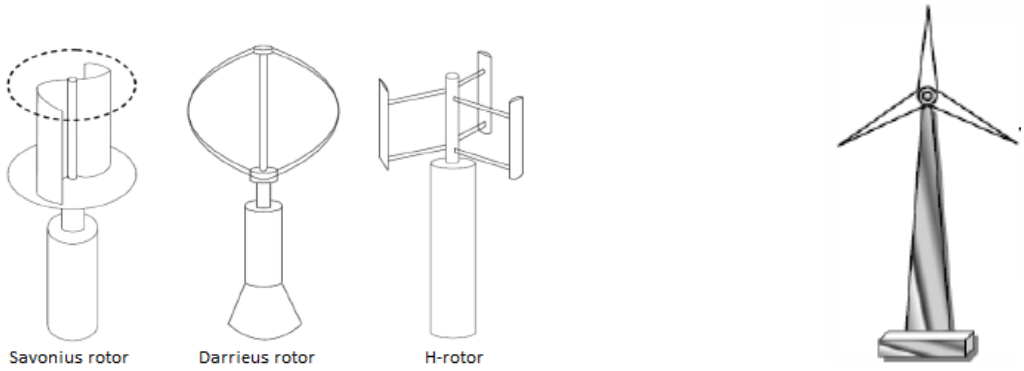


Figure 1.1 - Converting wind's kinetic energy into electrical energy

Figure 1.1 depicts the process of converting wind energy into electrical power. This conversion process integrates multiple areas of physics, including aerodynamics, mechanics, electrical engineering, power electronics, automation, and computing [25].

1.3. Types of wind turbines

Wind turbines are divided into two main categories: vertical axis wind turbines (VAWT) and horizontal axis wind turbines (HAWT). Nowadays, HAWTs are the most commercially available as they allow for capturing more wind energy compared to VAWTs [8].



a) Vertical axis wind turbines b) Horizontal axis wind turbine (HAWT)

Figure 1.2 - Types of wind turbines.

1.3.1. Vertical axis wind turbines

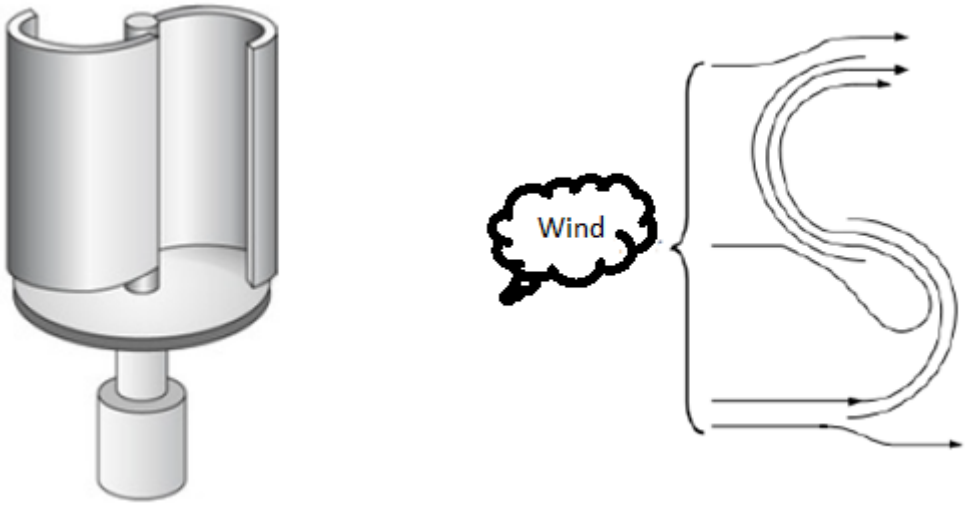
Vertical axis wind turbines were the earliest type of wind turbines developed, with evidence of their construction found in ruins dating back to 200 BC on the Persian-Afghan borders [9, 10]. Although several prototypes have been created, they have not been commercialized.

The design of vertical axis wind turbines is straightforward. They can automatically start at low wind speeds because they naturally align with the wind direction without requiring a directional system, unlike horizontal axis wind turbines. One advantage of these turbines is that they are easy to access, as they are installed close to the ground. This proximity helps to lower maintenance costs since most of the electrical and mechanical components are located at or near ground level [11]. However, this also presents a significant drawback, as such installations tend to be less efficient [12], given that wind is generally stronger and more consistent at higher altitudes. Additionally, they require a large amount of space [26].

Vertical axis wind turbines are typically categorized into two types: the Savonius rotor and the Darrieus rotor [27].

1.3.1.1. Savonius rotor

This type, shown in Figure 1.2, was invented by the Finnish architect Sigurd Johannes Savonius in 1925 and was patented in 1929 [27].



(a) (b)

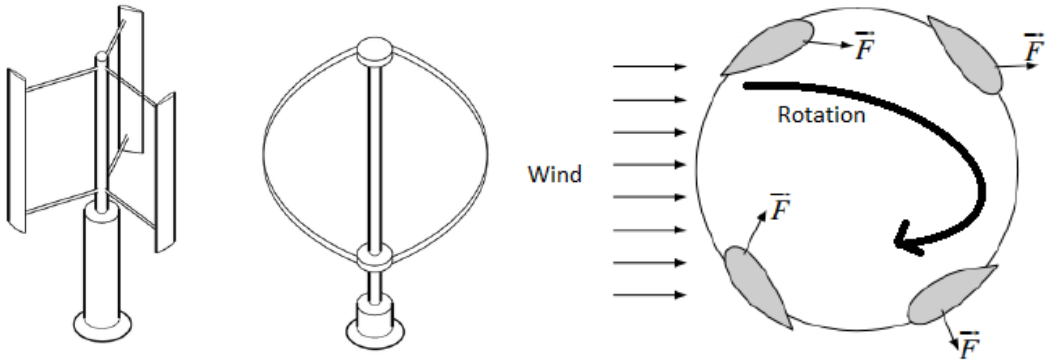
Figure 1.3 - (a) The Savonius type wind turbine. (b) The principle of the Savonius rotor.

The Savonius rotor consists of two blades shaped like half-cylinders, with their cross-section resembling the letter "S." It can also be constructed with multiple stages, each made up of two half-cylinders. When exposed to wind, the blades rotate on their axis, with one blade capturing the wind while the other moves against it [14]. This wind turbine generates energy through drag force and requires a high starting torque. The design is straightforward and can function in any wind direction, although its aerodynamic efficiency is relatively low [15].

1.3.1.2. Darrieus rotor

This type, illustrated in Figure 1.3, was invented and patented by the French engineer George Darrieus in 1926, though it was not developed until the 1970s. The complexity and high manufacturing costs of Darrieus's vertical axis wind turbines (VAWTs) made them less competitive compared to horizontal axis wind turbines (HAWTs) [16].

The Darrieus rotor functions through the aerodynamic forces produced by a rotating profile in a flow, spinning in a plane perpendicular to its axis of rotation. The normal component of the drag force pushes the rotor, while the tangential component causes it to rotate [17].



(a) (b)

Figure 1.4 - (a) Darrieus type wind turbines. (b) Darrieus rotor principle.

1.3.2. Horizontal axis wind turbines

Horizontal axis wind turbines are far more commonly used, despite often needing a blade orientation system and a nacelle that contains the entire conversion mechanism. Their primary advantage is their superior aerodynamic efficiency compared to vertical axis wind turbines. They also have the benefit of being able to start on their own and require less space at ground level. Horizontal axis wind turbines come in different designs, including two-blade, three-blade (the most prevalent, as shown in Figure 1.5), or multi-blade configurations [28], [29], [30].

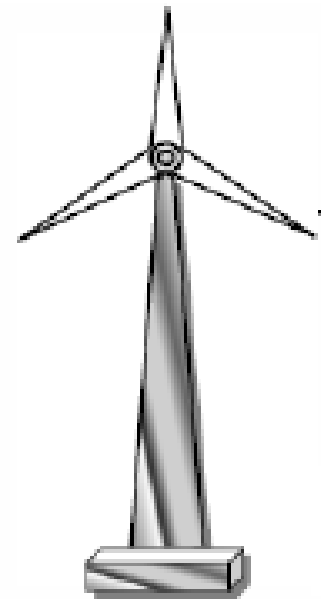


Figure 1.5 - Horizontal axis wind turbine.

There are two categories of horizontal axis wind turbines, as shown in Figure 1.6 [31]:

- **Upwind**: The wind blows onto the front of the blades towards the nacelle. The blades are rigid, and the rotor is oriented according to the wind direction by a mechanism, such as a tail for very small turbines and an active system for larger ones.

- **Downwind**: The wind blows onto the back of the blades away from the nacelle. Although the rotor in this setup is self-orienting, the upwind configuration is more commonly used because it is simpler, provides better efficiency, and offers greater stability for high power outputs. In the downwind position, the wind passes through the nacelle and tower before reaching the blades, causing wind disturbances [32].

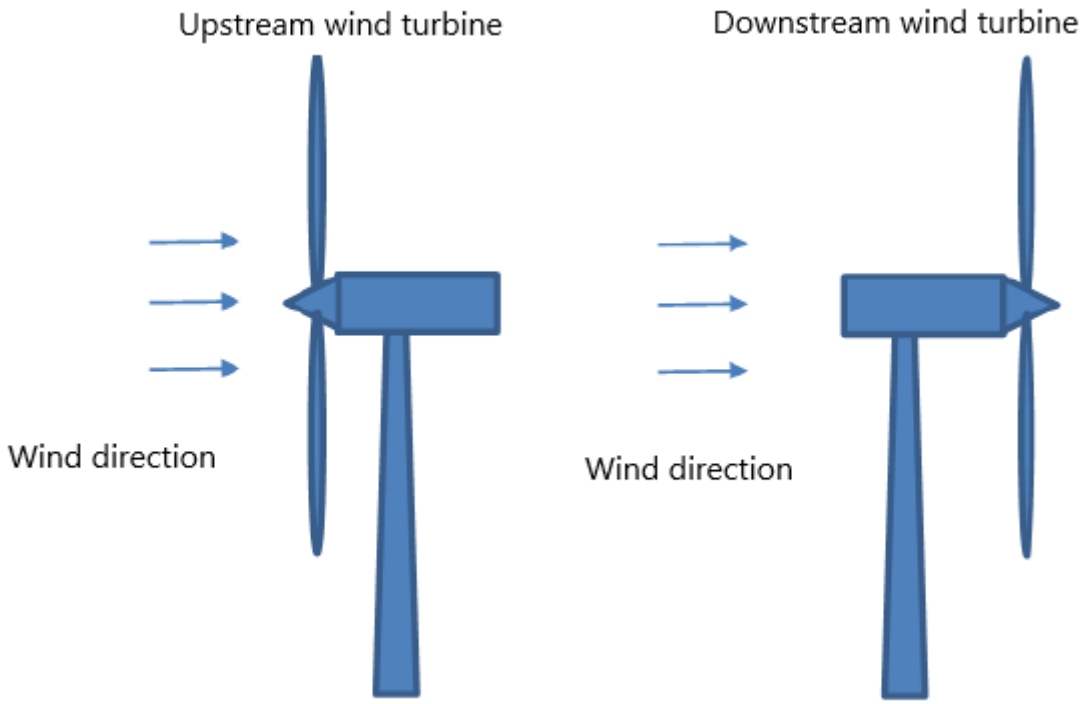


Figure 1.6 - Types of Horizontal Axis Wind Turbines.

Wind turbines are divided into three categories according to their power output and rotor diameter. Table 1.1 illustrates this classification [33].

Table 1.1 - Classification of Wind Turbines

Scale	**Rotor diameter**	**Delivered Power**
Small	Less than 12 m	Less than 40kW
Medium	12 m to 45 m	40kW to 1MW
Large	46 m and more	1MW and more

1.4. Components of a horizontal axis wind turbine

A HAWT (Horizontal Axis Wind Turbine) consists of a tower and a nacelle mounted on top of the tower. The nacelle contains several components, each contributing a specific function in the process of converting wind energy into electrical energy. Figure 1.6 [20] shows the main components of a HAWT, including the turbine rotor, the gearbox, the generator, the control system, the transformer, and finally the connection to the grid [34].

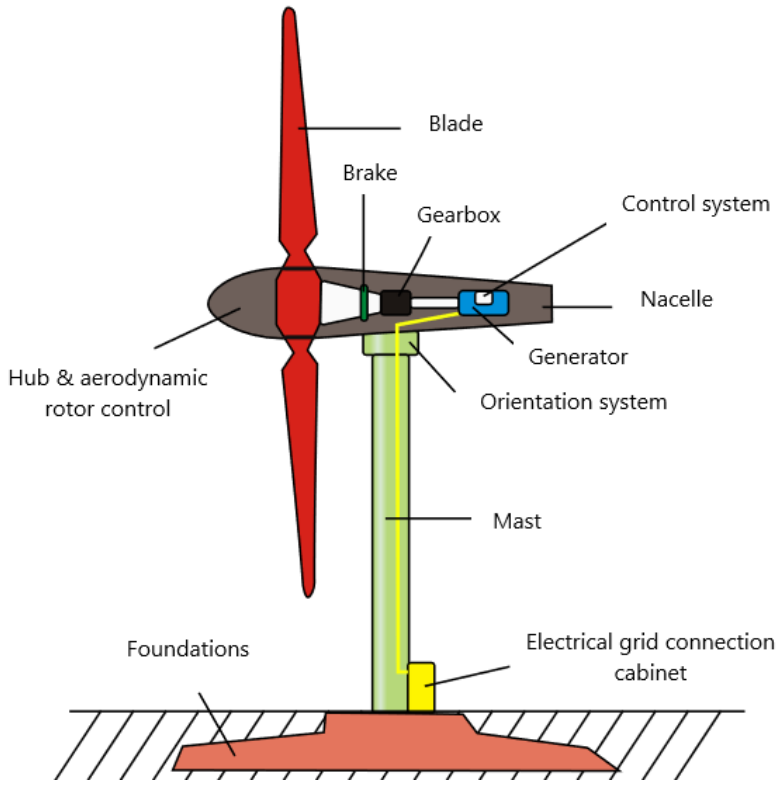


Figure 1.7 - Components of a horizontal axis wind turbine

(https://commons.wikimedia.org/wiki/File:Schema_eolienne.svg?uselang=fr)

1.4.1. The rotor

The aerodynamic rotor of a wind turbine captures wind power and converts it into mechanical kinetic power. It is primarily composed of the blades assembled onto the hub [35].

- **The blades**

  The blades rotate under the effect of the wind. They capture the wind's energy and transfer it to the rotor hub.

- **The hub**

  The hub connects the machine's low-speed shaft to the blades. It is the component that holds the blades and its orientation system is called the hub. It must be capable of withstanding strong vibrations and shocks, particularly during the start-up of the wind turbine or when the wind speed changes suddenly [36].

1.4.2. The nacelle

The nacelle contains the essential components of a wind turbine, including the gearbox, generator, anemometer, and wind vane. Positioned at the front of the nacelle is the turbine rotor, which consists of the blades and the hub [37].

- **The gearbox**

  The gearbox links the slow-speed shaft to the high-speed shaft, converting the low rotational speed from the blades into a higher speed.

- **The generator**

  The generator is an electromechanical device that transforms mechanical power into electrical power. It typically includes a stator and a rotor. The stator is a fixed part with a three-phase winding, while the rotor, which rotates, creates the magnetic field.

  In wind energy conversion systems, whether they are fixed or variable speed, three types of electrical generators are most commonly used [38]. These machines are:

  - Squirrel-cage asynchronous generators.
  - Doubly-fed asynchronous generators (DFIG).
  - Synchronous generators.

  Early wind turbines used squirrel-cage asynchronous machines with either a fixed or variable ratio gearbox. However, the need to increase power and size of wind turbines to reduce electricity costs has led to the use of power electronics converters, which are significantly more expensive than the generator itself. These constraints have driven manufacturers to adopt doubly-fed asynchronous generators, which use a low-power converter (30% of the nominal power) connected between the grid and the rotor of the generator. The DFIG is currently the most widely used solution in onshore wind turbines [39, 40].

  As for synchronous generators, they are recommended for offshore wind turbines because the permanent magnet version eliminates the need for a gearbox, thus reducing maintenance costs as well as the weight and size of the nacelle [40].

- **The anemometer**

  The anemometer measures the wind speed continuously and informs the control system when to initiate or halt turbine operation. Typically, a wind turbine starts operating at wind speeds of 3 to 4 m/s and stops at around 25 m/s (a process known as "feathering") [41].

1.4.3. The tower

The tower, or mast, is made from steel or concrete and supports the entire turbine structure. It allows access to the nacelle and contains the connection cabinet that links the turbine to the electrical grid. As wind speed rises with altitude, taller towers enable turbines to harness more wind energy and produce greater amounts of electricity. Over the past few decades, the height of turbine towers has grown considerably, with some now exceeding 150 meters [21].

1.5. Kinetic Wind Energy - Conversion to Electrical Energy and the Betz Law

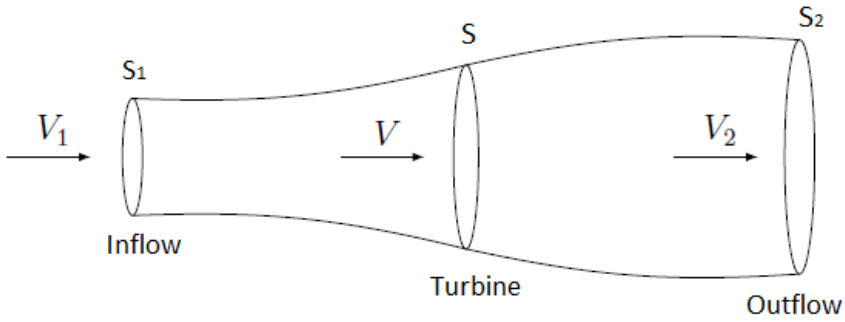


Figure 1.8 - Streamtube around a wind turbine

Let's examine the horizontal-axis wind system shown in Figure 1.8, where the wind speed V_1 is indicated upstream of the wind turbine, and the speed $V_2$is shown downstream [42]. Assuming that the wind speed passing through the rotor equals the average of the upstream wind speed V_1 and the downstream wind speed V_2. We have:

$$V_{moy} = \frac{(V_1+V_2)}{2} \quad (1.1)$$

Given that air is incompressible, the mass flow rate, representing the mass of air with density ρ crossing the surface S in one second, is described as follows [22]:

$$m = \frac{\rho S(V_1+V_2)}{2} \quad (1.2)$$

Where ρ is the air density and S is the area swept by the rotor. The power P_m from upstream to downstream, expressed as the rate of change of kinetic energy (Newton's second law), is given by [®43]:

$$P_m = \frac{m(V_1^2+V_2^2)}{2} \quad (1.3)$$

By substituting mmm with its expression given in equation 1.2 [44]:

$$P_m = \frac{\rho S(V_1^2-V_2^2)(V_1+V_2)}{4} \quad (1.4)$$

The corresponding power P_{mt} of a theoretically undisturbed wind, passing through the same surface S without a decrease in speed, i.e., at speed V_1, is given by [45]:

$$P_{mt} = \frac{\rho S V_1^3}{2} \quad (1.5)$$

The ratio between the power extracted from the wind and the total power theoretically available is then [46]:

$$\frac{P_m}{P_{mt}} = \frac{(1+\frac{V_2}{V_1})(1-(\frac{V_2}{V_1})^2)}{2} \quad (1.6)$$

This ratio, given by Equation (1.6) and illustrated in Figure 1.9, defines the power coefficient, commonly denoted by C_p. This coefficient was introduced by the German engineer Albert Betz in 1919 and was published in his book "*Wind Energie und ihre Ausnutzung durch Windmühlen*" [22,23]. According to Betz, this coefficient has a maximum value of 0.59. However, in practice, C_p values never reach this maximum due to inefficiencies and losses associated with various configurations. Each wind turbine is characterized by its own power coefficient, which is expressed as a function of the specific speed ratio λ and the blade pitch angle [22].

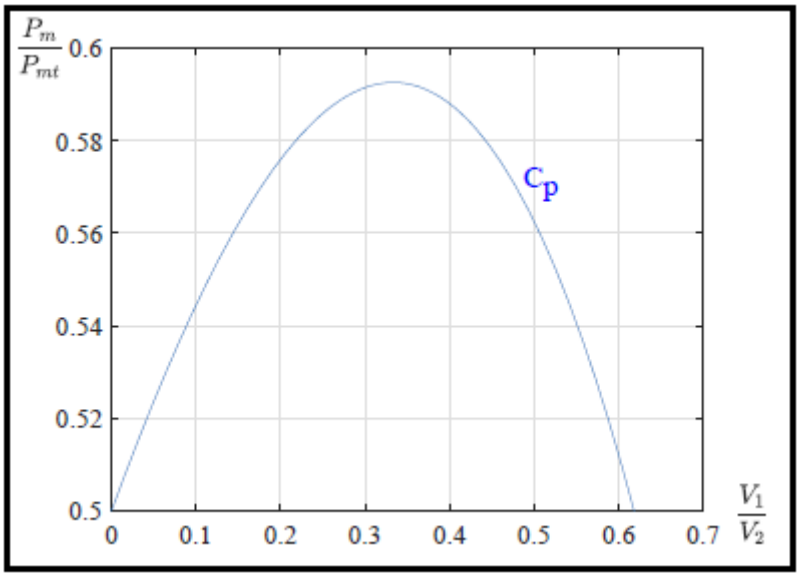


Figure 1.9. $\frac{P_m}{P_{mt}}$ as functions of $\frac{V_2}{V_1}$

1.6. Aerodynamic power Control

The power output of wind turbines is dependent on wind speed. At higher wind speeds, it becomes necessary to regulate the aerodynamic power of the turbine to prevent damage. Wind

turbines are designed to operate within a specific wind speed range, which is bounded by the cut-in speed (V_{cut-in}) and the cut-out speed ($V_{cut-out}$). If the wind speed exceeds these limits, the turbine must be shut down to safeguard both the generator and the turbine itself. Control strategies for aerodynamic power vary depending on the operating conditions of the turbine. Figure 1.10 illustrates the four distinct operating zones of the wind turbine [47].

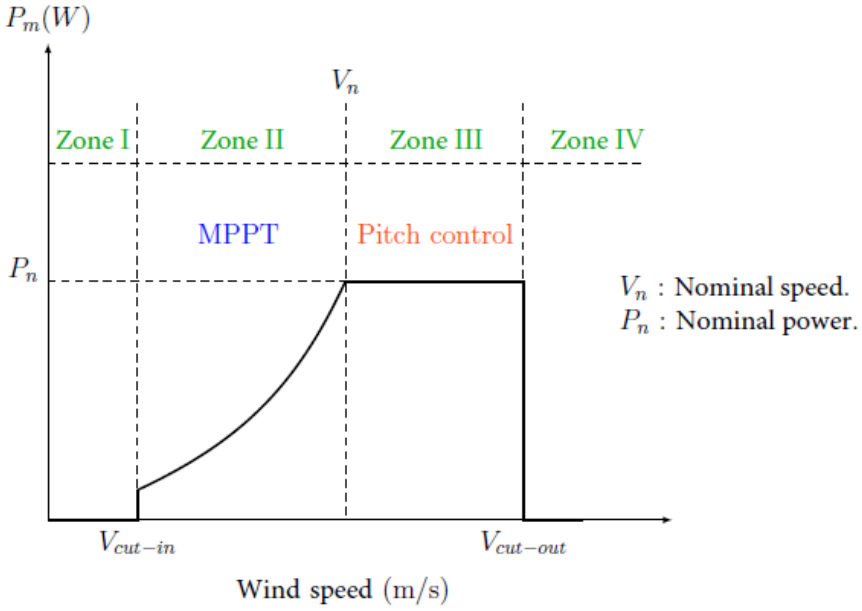


Figure 1.10 - Power characteristic as a function of wind speed

- **Zone I**: The wind speed is low and insufficient to start the wind turbine.
- **Zone II**: The wind turbine operates at partial load. The wind speed reaches a minimum level required to start the turbine. As the wind speed increases, the turbine's rotational speed also rises until it reaches its maximum. The turbine will operate to extract the maximum amount of power through Maximum Power Point Tracking (MPPT). MPPT control adjusts the turbine's mechanical torque to match the wind speed while keeping the pitch angle constant (often zero). MPPT can be achieved through various methods, with the following being the most commonly used in the literature [24, 25]:
  - ✓ Control of the Tip Speed Ratio (TSR): The optimal TSR for a given wind turbine remains constant regardless of wind speed. By keeping the TSR at its optimal value, the turbine can maximize the extracted energy. This approach is known in the literature as MPPT with speed regulation.
    - Control of Optimal Torque: This method involves adjusting the torque based on a reference torque corresponding to the maximum power output of the wind turbine at

a given wind speed. This approach is referred to in the literature as MPPT without speed regulation.

- Power Signal Feedback (PSF) Control: This method requires knowledge of the wind turbine's maximum power curve, which can be obtained through simulations or experimental tests. The optimal power is generated either using a pre-determined power-speed curve or by applying the turbine's power output formula, where wind speed or turbine speed serves as the input. A controller, typically a Proportional-Integral (PI) controller, is used to minimize the error between the optimal power and the actual power. Subsequently, data points for the maximum power output and the corresponding turbine speed must be recorded in a lookup table [48].

✓ The Perturb and Observe (P&O) Method: This approach involves making small adjustments to a control variable and observing the resulting changes in the target function until the slope of the function reaches zero.

✓ The "Hill Climbing Search" Method: This approach does not require prior knowledge of the wind turbine or generator. The method involves online measurement of the turbine's power output and observation of the rate of change in power with respect to speed, specifically $\frac{dp}{d\omega}$ to identify the maximum power. MPPT is achieved when $\frac{dp}{d\omega} = 0$, by adjusting the rotor speed or the duty cycle of the converter [26, 27].

❖ **Zone III**: In this zone, the turbine operates at a constant rotational speed, and the power output is capped at 15% of the turbine's rated power. This speed is regulated by adjusting the blade pitch angle. Recently, wind turbines with pitch control mechanisms have become the most widely used type. This control method is prevalent for managing aerodynamic power. When the wind speed is below the rated speed, the pitch control system maintains the blades at a zero angle to maximize the power coefficient. In gusty conditions, the controller adjusts the pitch angle β to limit the turbine's power output to its rated value. Literature suggests that the pitch control, which aims to set the reference pitch angle β_{ref}, can be implemented through three primary methods [49]:

- From the Pitch Angle Curve as a Function of Wind Speed: This control strategy is straightforward to implement if the wind speed can be measured directly.
- From the Generator Speed: By inputting the difference between the measured speed and its reference value into a PI controller, you can obtain the reference value for the pitch angle β_{ref}.

- From the Generator Power: By inputting the difference between the generator's power output and its rated power into a PI controller, you can derive the reference pitch angle β_{ref}.

1.7. Configurations of wind energy conversion systems

The configurations of wind energy conversion systems generally depend on the type of generator used and the structure of the power converter that enables the control of the energy produced by the generator. There are two main families of configurations, [43], [44]:

- The fixed-speed generator configuration (not the turbine).
- The variable-speed generator configuration.

Up until the mid-1990s, most wind turbines installed were fixed-speed models with a capacity of 1.5 MW or less, utilizing squirrel-cage induction machines directly connected to the grid. These turbines operated consistently at a constant speed. Nowadays, the majority of wind turbines are designed for variable-speed operation. Based on the type of generator, power electronics, and the control over both power and speed, wind energy conversion systems (WECS) are typically grouped into four main categories.

Up until the mid-1990s, most wind turbines installed were fixed-speed models with a capacity of 1.5 MW or less, utilizing squirrel-cage induction machines directly connected to the grid. These turbines operated consistently at a constant speed. Nowadays, the majority of wind turbines are designed for variable-speed operation. Based on the type of generator, power electronics, and the control over both power and speed, wind energy conversion systems (WECS) are typically grouped into four main categories [50].

1.7.1 Fixed-speed wind turbine

Fixed-speed wind turbines were the first type to be developed. In this system, the squirrel-cage induction generator (SCIG) is directly connected to the electrical grid through a transformer. The generator's speed is determined by the grid's frequency and the number of pole pairs. A gearbox is typically needed to adjust the speed difference between the turbine and the generator, allowing the generator to produce its rated power at the designed wind speed [51].

These induction machines draw reactive power from the grid, necessitating capacitive compensation (using capacitor banks) at the grid connection point. However, the reactive power is not controlled, and the speed is not optimized for aerodynamic efficiency. This causes significant fluctuations in the generated electrical power during wind gusts [52].

Additional drawbacks of this type of wind turbine include high mechanical stress, large machine size, noise, low efficiency, and reliability challenges. The general structure of this type of WECS is illustrated in Figure 1.11.

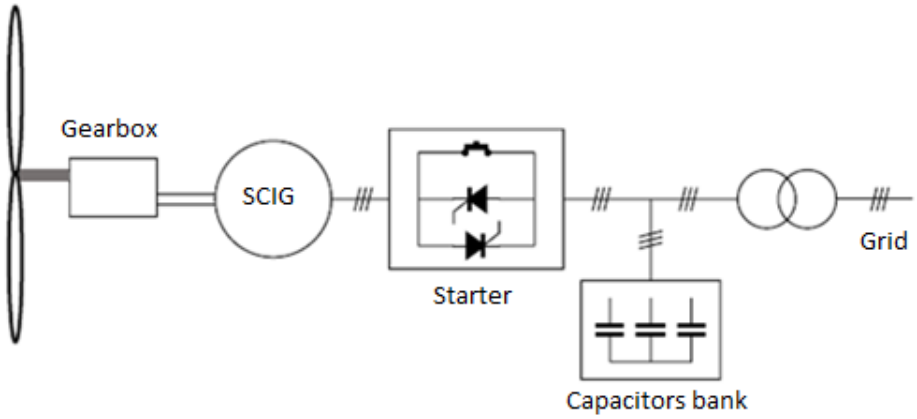


Figure 1.11 – SCIG based Wind Energy Conversion System.

1.7.2 Variable-speed wind turbines based on an asynchronous generator

This design employs a wound rotor induction generator (WRIG), which is directly connected to the grid. It also requires a soft starter to ensure a smoother connection to the grid and a reactive power compensator (capacitor bank) to supply the reactive power needed for the generator's magnetization. A distinctive feature of this system is its adjustable rotor resistance, which can be varied to manage slip and thereby control the system's output power [53].

The control system typically encompasses both the adjustment of the variable resistance and the management of the pitch angle. The overall structure of this type of Wind Energy Conversion System (WECS) is illustrated in Figure 1.12.

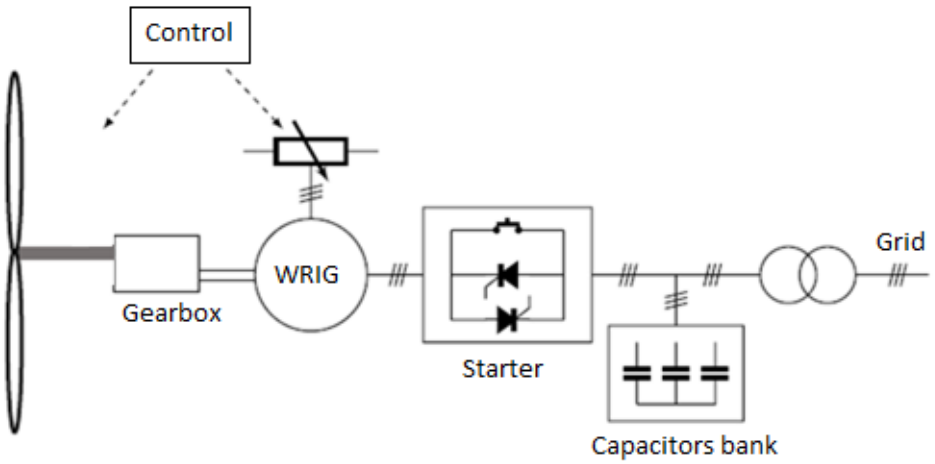


Figure 1.12 – WRIG based Wind Energy Conversion System

1.7.3 Variable-speed wind turbines based on a Doubly Fed Induction Generator (DFIG)

This configuration describes Wind Energy Conversion Systems (WECS) utilizing a Doubly Fed Induction Generator (DFIG). In this arrangement, the generator is linked to the grid through power converters—typically sized at approximately 25% to 30% of the generator's rated power—connected to the rotor circuit. The DFIG operates with variable-frequency converters, usually comprising two AC/DC and DC/AC converters connected by a DC bus [54].

In this system, the DFIG delivers power to the grid through the stator, while the rotor can either supply or absorb power depending on the generator's speed. If the generator exceeds synchronous speed, the rotor feeds power into the grid through the converters. Conversely, if it operates below synchronous speed, the rotor draws power from the grid via the converters. These frequency converters manage reactive power and ensure a smoother grid integration. Speed control is typically constrained to around 30% of synchronous speed, allowing for effective management of both active and reactive power, which enhances system performance. Additionally, the power electronic converters enable the wind turbine to function as a more dynamic energy source for the grid [55]. The general structure of this type of WECS is depicted in Figure 1.13.

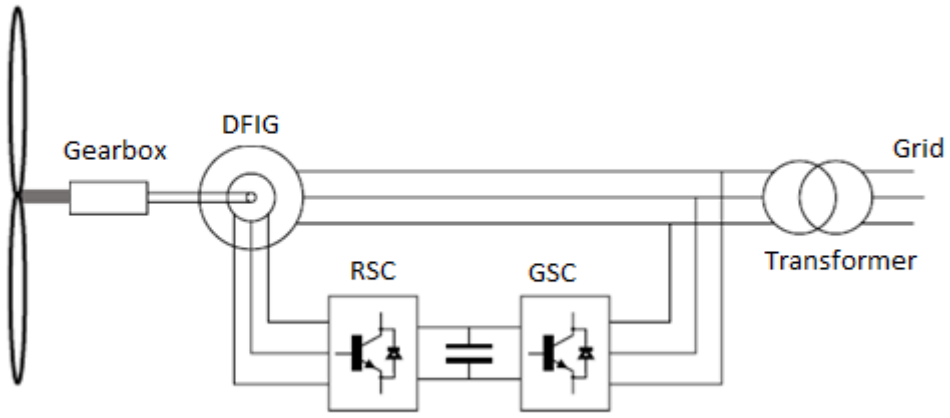


Figure 1.13 – DFIG based Wind Energy Conversion System.

1.7.4 Variable-speed wind turbines based on a permanent magnet synchronous generator (PMSG)

This setup involves variable-speed wind turbines using a Permanent Magnet Synchronous Generator (PMSG). In this arrangement, the generator connects to the grid through high-capacity frequency converters linked by a DC bus. These converters enable rapid control of both active and reactive power [56].

This kind of generators has become more popular recently but have entered the market gradually. Compared to Double Fed Induction Generators (DFIGs), PMSG based WECS offer a wider range of speed control and can be connected directly to the wind turbine without a gearbox. This eliminates issues like noise, maintenance, and installation costs. However, the requirement for converters to handle the full power exchange between the generator and the grid results in higher expenses [57].

As illustrated in Figure 1.14, this type of WECS includes a synchronous generator connected to a diode bridge rectifier, a boost converter, and a pulse-width modulation (PWM) inverter.

This technology enables the extraction of maximum energy from the wind at low wind speeds by optimizing the turbine's speed, while also reducing mechanical stress on the turbine during wind gusts [58].

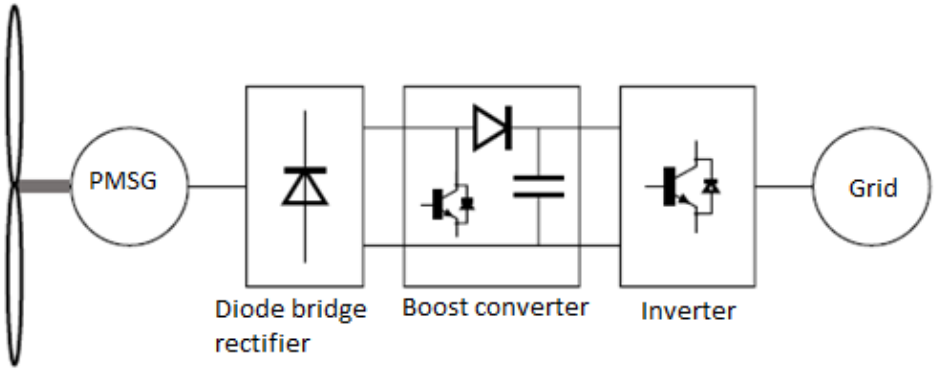


Figure 1.14 – PMSG based wind energy conversion system.

1.7.5 Comparison between the two types of configurations (Fixed-speed and variale-speed)

A comparison of the two modes of electricity generation, fixed speed and variable speed, is provided in Table 1.2 [29].

Criteria	Fixed speed	Variable speed
Speed Stability	Constant, dependent on grid frequency	Adjustable based on wind conditions
Efficiency	Less efficient, especially at low loads	More efficient, adjusting speed to conditions
Complexity	Simple system	Requires controllers and converters
Cost	Lower installation cost	Higher cost due to additional components

Response to Load Variations	Limited flexibility	High flexibility to maximize production
Maintenance	Less maintenance required	More complex maintenance due to additional controls

Table 1.2 - Comparison between the two operation modes

1.8. Principles and operating modes of the doubly fed induction machine (DFIM)

1.8.1 Operating principle

The Doubly Fed Induction Machine (DFIM) is similar to conventional induction machines but includes additional functionalities that allow it to operate at speeds slightly above or below its natural synchronous speed [33]. The stator windings of the DFIM are connected to a three-phase power supply, which dictates the frequency of the stator current f The stator currents generate a rotating magnetic field in the air gap. The rotational speed of this field relative to the stator is given by [59]:

$$\Omega_s = \frac{\omega_s}{p} \tag{1.7}$$

Where:

p: the number of pole pairs of the machine.

ω_s: the stator angular frequency (rad/s).

ω_s being proportional to **f**: $\omega_s = 2\pi f$ (1.8)

The rotor rotates relative to the stator at the speed ω_r. The relationship between the stator angular frequency **ωs** and the rotor angular frequencyω_r is given by [60]:

$$\omega_r = \omega_s - \omega_m \tag{1.9}$$

ω_m: the electrical angular frequency of the machine (rad/s).

$$\omega_m = p_m \Omega_m \tag{1.10}$$

Ω_m: mechanical rotational speed of the rotor (rad/s).

The slip g, which defines the relative speed of the rotor compared to that of the stator, is given by [61]:

$$g = \frac{\omega_s - \omega_m}{\omega_s} \tag{1.11}$$

Based on the sign of the slip, four distinct operating modes of the machine can be identified.

1.8.2 Operation in sub-synchronous motor mode.

In this mode of operation, the grid supplies power to the stator. A portion of this power is converted into mechanical energy, while the remaining portion, referred to as slip power, is fed back into the grid via the rotor's slip rings. In this scenario, the machine operates as a motor below its synchronous speed. This operating mode is commonly known as slip energy recovery in the literature [34, 35] and is depicted in Figure 1.15 [35].

Disregarding losses, the mathematical conditions describing this operation are:

$$g > 0, P_s > 0, P_{mec} > 0, P_r = g.P_s > 0$$

g : the slip.

P_s : the stator active power (W).

P_{mec} : the mechanical power (W).

P_r : the rotor active power (W).

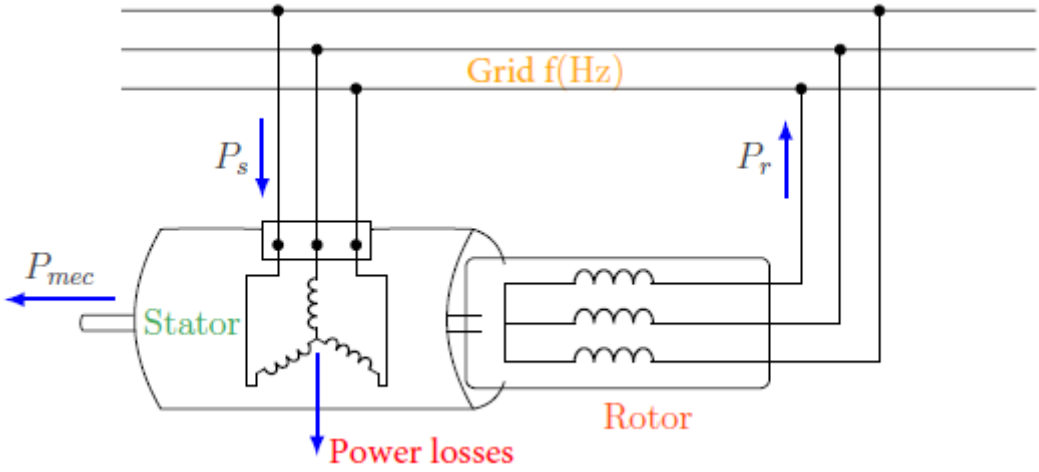


Figure 1.15 – Operation in sub-synchronous motor mode.

1.8.3 Operation in super-synchronous motor mode

In this mode of operation, part of the power drawn from the grid is transferred to the rotor and converted into mechanical power. Consequently, both the stator and rotor contribute to the power supplied to the machine. As a result, the machine operates in motor mode at speeds above synchronous speed. In this condition, the rotating magnetic field produced by the rotor windings is shifted by 180 degrees relative to that of the stator. This operational mode is depicted in Figure 1.16. The mathematical conditions describing this operation are as follows [62]:

$$g < 0, P_s > 0, P_{mec} > 0, P_r = g.P_s < 0$$

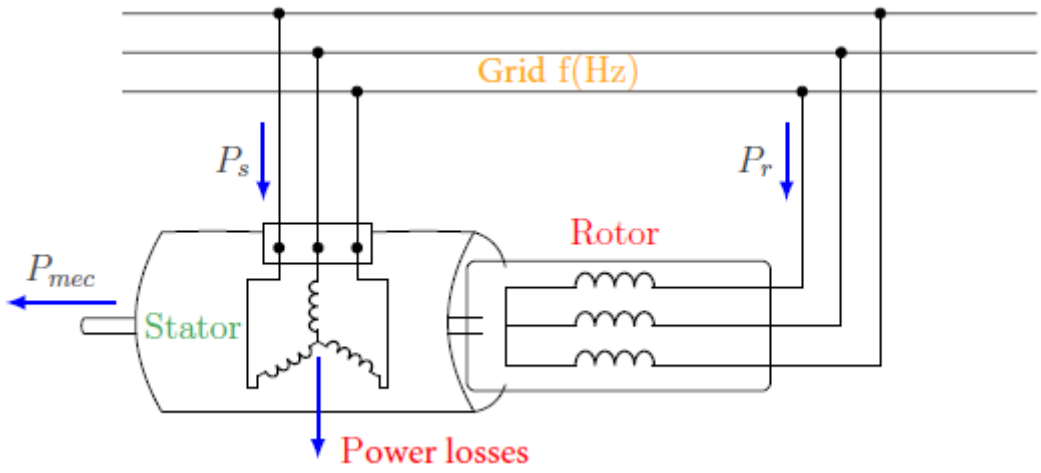


Figure 1.16 – Operation in super-synchronous motor mode

1.8.4 Operation in sub-synchronous generator mode

In this operating mode, the turbine provides mechanical power to the machine. The power is supplied to the grid through the stator, and a portion of this power passing through it is reabsorbed by the rotor via the converters. In this case, the static converters can supply up to 30% of the nominal power of the machine [63].

This describes generator operation at speeds below synchronous speed. Figure 1.17 illustrates this mode of operation. The mathematical conditions governing this behavior are as follows:

$$g > 0, P_s < 0, P_{mec} < 0, P_r = g.P_s < 0$$

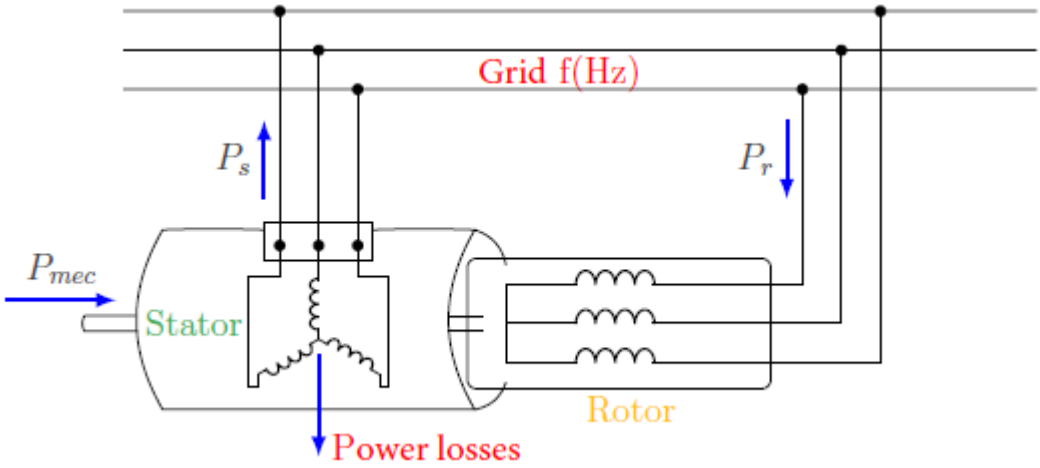


Figure 1.17 – Operation in sub-synchronous generator mode

1.8.5 Operation in super-synchronous generator mode

The machine is continuously driven by the turbine, and almost all of the mechanical power provided to the machine is transferred to the grid via the stator and the rotor windings, with

some losses. A portion of this power, corresponding to g.P_s , is transmitted through the rotor. Thus, the machine operates as a generator at speeds above synchronous speed. This operating mode is illustrated in Figure 1.18. The mathematical conditions that describe this operation are as follows [64]:

$$g < 0, P_s < 0, P_{mec} < 0, P_r = g.P_s > 0$$

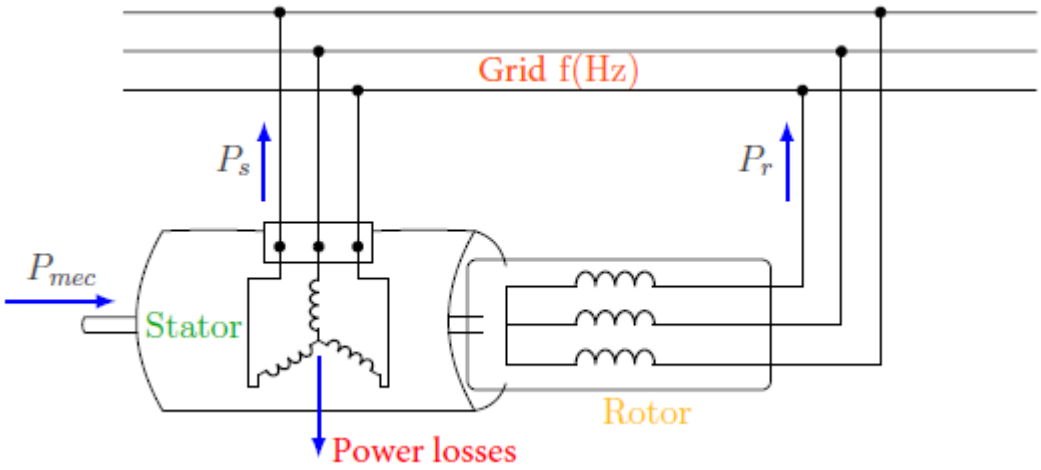


Figure 1.18 – Operation in super-synchronous generator mode.

However, in the last two modes, the machine's speed remains close to synchronous speed. This means that the converters are designed to manage only the slip power, which is at most 30% of the machine's nominal power. As a result, the nominal rotor power exchanged amounts to 30% of the nominal stator power [65].

1.9. Configurations of Converters Related to the DFIG

The key feature of the DFIG is its operation of the converters within a slip power range, which constitutes a portion of the total power. Different configurations of the DFIG have been described in the literature [66].

1.9.1 Kramer Structure: Diode Bridge and Thyristor Bridge

This structure consists of a diode rectifier connected to the machine side and a thyristor inverter connected to the grid side. This configuration is illustrated in Figure 1.19. The smoothing inductance between the two converters serves to absorb instantaneous differences between the rectifier and inverter voltages and limits the ripple in the DC bus current. The main advantage of this setup is its low cost due to the use of thyristors. However, this configuration only allows power generation in super-synchronous mode, thus supplying energy to the grid through both the stator and rotor [67].

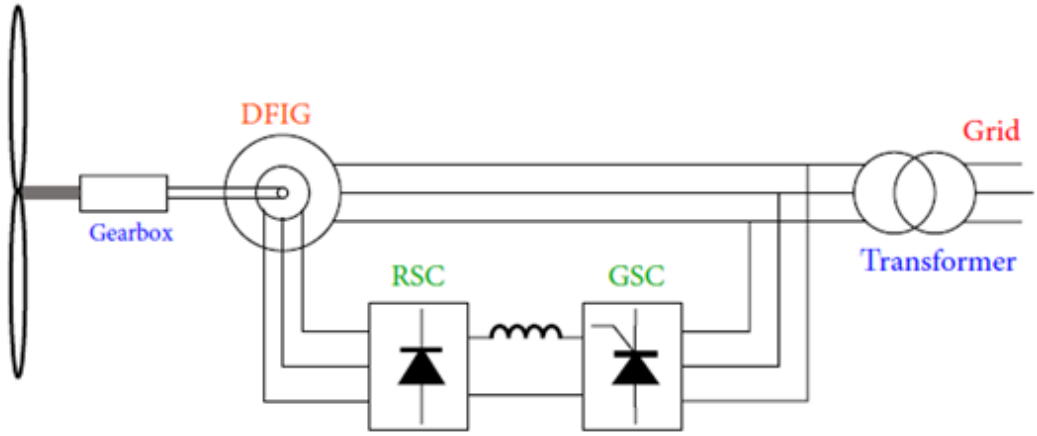


Figure 1.19 – Kramer Structure.

1.9.2 Structure of diode bridge and transistor bridge

This configuration, shown in Figure 1.20, involves replacing the thyristor-based inverter (from the previous structure) with a transistor-based inverter using Pulse Width Modulation (PWM). In this setup, the stator frequency is kept close to its nominal value. As a result, no low-frequency harmonic currents are injected by the inverter. This structure allows for reactive power control but does not permit speed control of the generator due to the use of the diode bridge [68].

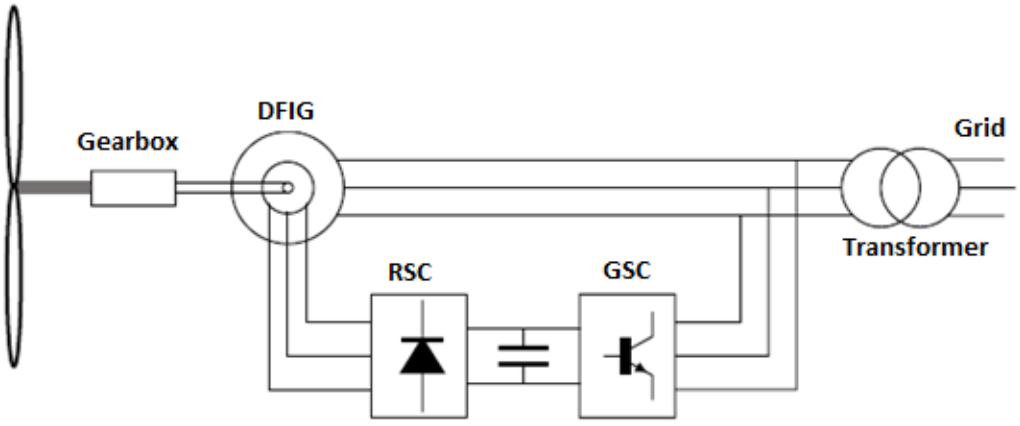


Figure 1.20 - DFIG powered by a diode bridge and a PWM-based inverter.

1.9.3 Scherbius Structure: Cycloconverters

The basic principle of the cycloconverter was developed by Louis A. Hazeltine in 1923 and patented in 1929. A cycloconverter is a direct AC-AC converter that uses a network of power semiconductor switches to connect the power supply directly to the machine without any

intermediate DC link capacitors. It enables the conversion of a constant amplitude and frequency three-phase AC voltage into a variable amplitude and frequency three-phase AC voltage [69].

The cycloconverter facilitates bidirectional energy flow between the rotor and the grid. Additionally, it offers a speed variation range that is twice as wide as that provided by the Kramer structure. This configuration is illustrated in Figure 1.21.

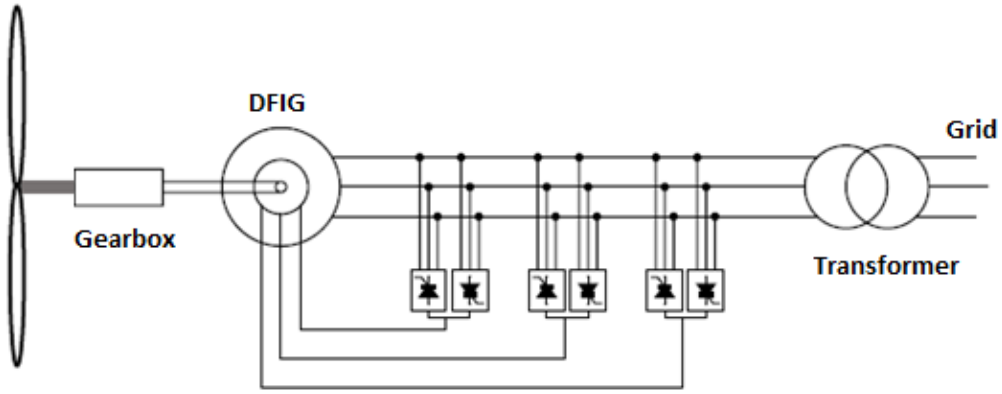


Figure 1.21 - Scherbius structure with cycloconverter.

1.9.4 Scherbius Structure with PWM Converters

This structure uses two identical converters connected by a DC bus (capacitor), based on IGBT or MOSFET transistors. One converter is connected to the rotor side, and the other is connected to the grid side. This configuration is illustrated in Figure 1.22. Many studies have been presented with this type of converter. Although the converters used in this configuration are very similar, there are significant differences in control strategies and the complexity of each [70].

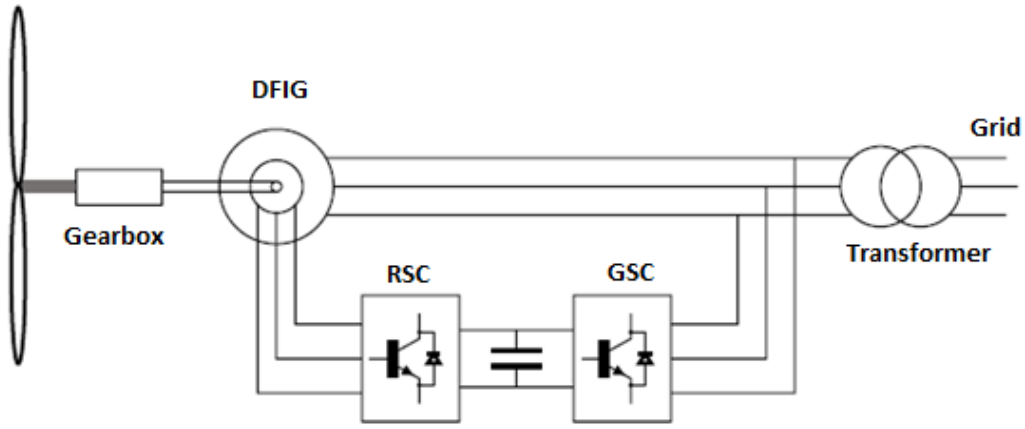


Figure 1.22 - Scherbius Structure with PWM Converters.

1.10. Methods to Improve Wind Turbines Using DFIG (Doubly-Fed Induction Generator)

The wind turbine equipped with a DFIG (Doubly-Fed Induction Generator) is currently the most widely adopted solution worldwide, particularly in onshore wind farms. This status as the favored and dominant candidate of the DFIG justifies the impressive number of research studies and articles published over the past decades on DFIG-based wind turbines. The objective of this research is to improve the performance of wind turbines by ensuring [71]:

- A maximum power extraction from a wide range of wind speed variations.
- A precise control of the active and reactive power injected into the electrical grid by the wind turbine.
- The reduction of torque oscillations and harmonics in the generated currents and electrical power.
- Control the operation of the wind turbine in case of disturbances in the electrical grid to contribute to grid stability efforts [44].

Traditional control methods typically rely on stator flux orientation using proportional-integral (PI) controllers [53], [54]. While these methods offer average performance, their main drawback is their limited robustness to disturbances and variations in the generator's parameters [72].

Many control strategies have been proposed to address the drawbacks of traditional methods, including neural networks (NN) [55], sliding mode control (SMC) [43], [56], fuzzy logic techniques (FLT) [57], direct torque control (DTC), and direct power control (DPC) [44], [58], [59]. Both DPC and DTC can effectively reduce the total harmonic distortion (THD) of the stator current compared to traditional field-oriented control (FOC). However, the use of traditional hysteresis comparators in DTC and DPC strategies leads to torque and rotor flux ripples in DFIG-based wind turbines [11].

However, the traditional sliding mode controller (SMC), known for being one of the simpler nonlinear controllers to implement, can produce oscillations known as the "chattering" phenomenon [60]. This occurs due to the discontinuous nature of the control law and can disrupt system operation and stability, causing mechanical vibrations and oscillations in currents and power [61], [62]. In recent years, various solutions have been proposed to improve traditional SMCs for wind systems based on DFIGs by reducing chattering while maintaining or enhancing controller robustness. These improvement techniques include using artificial intelligence methods [19], [20], [21], combining traditional SMC with a disturbance observer [24], [63],

synergistic controls [64], and terminal synergistic controls [65]. These approaches aim to address the limitations of traditional SMC techniques and mitigate chattering issues. However, higher-order sliding mode control (HOSMC) is an ideal alternative for reducing chattering and ensuring robust performance.

Among the promising solutions to enhance the performance and efficiency of traditional control methods, fuzzy logic controllers and artificial neural networks stand out for their ability to handle complex and nonlinear systems. Fuzzy logic controllers [72] are known for their flexibility and adaptability, using intuitive rules to manage complex behaviors. Their ability to handle uncertainties and imprecisions makes them particularly effective in dynamic environments. Similarly, artificial neural networks [73] offer a powerful approach for controlling nonlinear systems. Their ability to learn from data and adapt to new situations provides a significant advantage in improving response times and strengthening the robustness of controlled systems [74], [75].

1.11. Thesis Objectives

The primary goals of this doctoral thesis are designed to address several of the issues outlined earlier. In general, the objectives set forth are as follows:

- Design and simulate a wind energy conversion system linked to the power grid, featuring a Doubly Fed Induction Generator (DFIG) and a back-to-back converter.
- Development of a control method using the super-twisting algorithm to enhance direct power control based on sliding mode controllers and reduce oscillations in power and currents.
- Development of a more effective approach than the super-twisting algorithm, which combines super-twisting method control with fuzzy logic to further enhance direct power control based on sliding mode techniques.
- Development of a more advanced approach than the super-twisting algorithm, which integrates super-twisting method control with neural networks to further enhance direct power control based on sliding mode techniques. This new approach aims to leverage the learning capabilities of neural networks to refine control strategies, optimize performance, and reduce oscillations in power and currents beyond the capabilities of the super-twisting algorithm alone.

- Compare the system's performance using the proposed methods against the traditional DPC method, in terms of tracking accuracy and robustness with respect to the machine's parametric variations.
- carry out Processor-in-the-loop (PIL) tests to validate and optimize the proposed control methods in a real-time simulation environment. The implementation of these controllers on a dSPACE 1104 system will demonstrate their efficiency and robustness, guaranteeing their practical applicability and reliability before deployment in the real world.

The MATLAB/Simulink 2021b software environment and the dSPACE 1104 R&D controller board will be utilized to simulate and implement each model and control technique developed in this thesis.

1.12. Summary

An extensive bibliographic overview of wind energy and wind turbines is given in this chapter. The first section introduces the various kinds of wind turbines and then describes the parts that make up a horizontal-axis wind turbine. The transformation of wind kinetic energy into electrical energy is the next topic covered in the chapter, along with an explanation of the Betz limit and the wind turbine's operational areas. The four types of wind energy conversion systems that are now in use are also discussed, with an emphasis on systems that utilize doubly-fed induction machines and the various combinations that can be achieved with them as well as the objectives of this thesis are discussed at the end of the chapter.

The ideas presented in the following thesis are limited to wind energy conversion systems that utilize a doubly-fed induction motor.

Chapter 2: Modeling a DFIG-based wind energy conversion system

2.1. Introduction

The Doubly Fed Induction Machine (DFIM) has been known since 1899 [42, 43]. Originally researched for high-speed motor applications, it has gained significant attention in the wind energy conversion systems (WECS) sector due to its various advantages over other generator types. These advantages include the ability to operate at variable speeds with reduced mechanical constraints [44], reactive power compensation due to converters designed to handle only a fraction of the nominal power (around 25% to 30%), and minimized power losses in the converters [45–47].

Figure 2.1 illustrates the configuration of a DFIG-based WECS. In this setup, the stator windings of the generator are directly connected to the grid, while the rotor windings are linked to AC-DC-AC power converters through slip rings. The power converters include a machine-side converter (MSC) and a grid-side converter (GSC), which are connected by a capacitor.

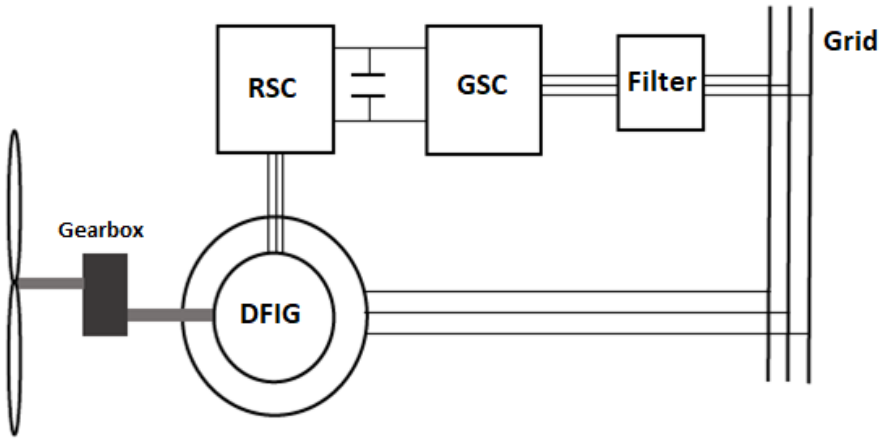


Figure 2.1 - Functional diagram of a wind turbine based on a Doubly Fed Induction Generator (DFIG) connected to the grid.

2.2. Modeling of the wind turbine

2.2.1. Aerodynamic model

Wind Energy Conversion System (WECS) is a system that transforms the kinetic energy of the incoming airflow into electrical energy. This conversion takes place with the help of two main components: the first is the extraction device, which captures the mechanical energy produced by the wind turning the wind turbine rotor, and the second is the generator, which converts the rotational mechanical power into electrical current. The wind, with the speed v, applied to the turbine blades, sets them in motion and generates kinetic power transferred to the turbine P_ω, described by [76]:

$$P_\omega = \frac{1}{2}\rho\pi R^3 v^3 \tag{2.1}$$

With:

ρ: the air density (approximately 1.225 kg/m³ at 15°C).

R: the radius of the blades.

The wind's kinetic energy cannot be entirely harnessed by the wind turbine. Instead, only a portion of this energy is converted into aerodynamic power at the turbine's rotor. This portion is represented by the power coefficient C_p of the wind turbine. The power measured at the turbine hub is thus a fraction of the total kinetic power P_ω, as described by the following equation (2.2):

$$P_t = \frac{1}{2} C_p(\lambda, \beta) \rho \pi R^3 v^3 \tag{2.2}$$

C_p: the power coefficient, is a function of λ and β provided by manufacturers, with a theoretical maximum limit of 0.59 (see section 1.5).

β represents the blade pitch angle, and λ is the tip speed ratio, defined by [77]:

$$\lambda = \frac{\Omega_t R}{v} \tag{2.3}$$

Ω_t: the turbine rotational speed.

In the context of this thesis, we will use an approximate expression for the power coefficient, which is derived from various research studies [78]:

$$C_p(\lambda, \beta) = c_1 \left(\frac{c_2}{\lambda_i} - c_3 \beta - c_4 \right) e^{\frac{c_5}{\lambda_i}} + c_6 \lambda_i \tag{2.4}$$

C_i for i=1,….6 are the constant coefficients of the turbine.

With
$$\frac{1}{\lambda_i} = \frac{1}{\lambda + 0.08\beta} - \frac{0.035}{\beta^3 + 1} \tag{2.5}$$

2.2.2. Modeling of the mechanical components

3.2.2.1. Gearbox model

The gearbox is used to adapt the slow rotation speed of the turbine Ω_t with the generator's faster rotational speed Ω_m, and to convert the aerodynamic torque C_{aer} into mechanical torque C_m using the following mathematical formulas [79]:

$$C_m = \frac{C_{aer}}{G} \tag{2.6}$$

$$\Omega_m = G . \Omega_t \tag{2.7}$$

G : the gear ratio.

3.2.2.2. Dynamic shaft model

The dynamic shaft includes two inertial components: one for the turbine rotor and one for the generator rotor. The total inertia J is the sum of the generator's inertia J_m and the turbine's inertia J_t adjusted to the generator's rotor. The generator's inertia is driven by the high-speed shaft, with the shaft torque C_m being opposed by the generator's electromagnetic torque C_{em}.

The dynamic behavior of this system is described by [80]:

$$\left(\frac{J_t}{G^2} + J_m\right)\frac{d\Omega_m}{dt} + f_v\Omega_m = C_m - C_{em} \tag{2.8}$$

Where:

J_t : the moment of inertia of the turbine (kg.m²).

J_m : the moment of inertia of the DFIG (kg·m²).

f_v :the viscous friction coefficient of the DFIG (N.m.s.rad⁻¹).

C_m : the mechanical torque applied to the DFIG shaft (N.m).

C_{em} : the electromagnetic torque of the DFIG (N.m).

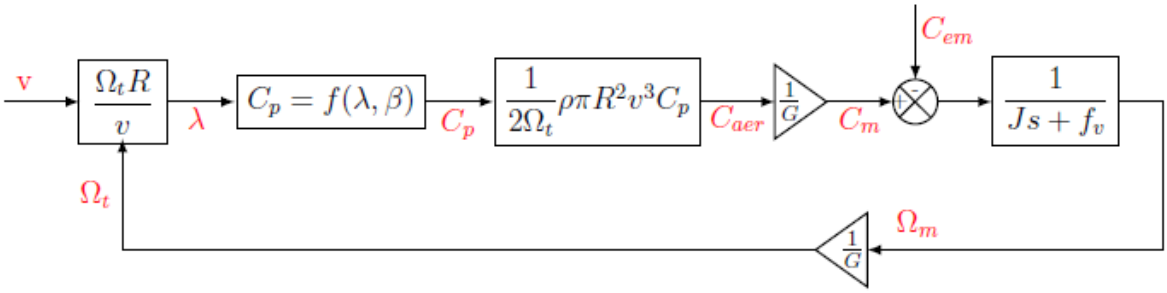


Figure 2.2 – Block diagram of a wind turbine.

2.3. DFIG modeling

2.3.1. Three-phase model of the DFIG

The DFIG model can be represented by three stator windings and three rotor windings, as shown in the following Figure 2.3:

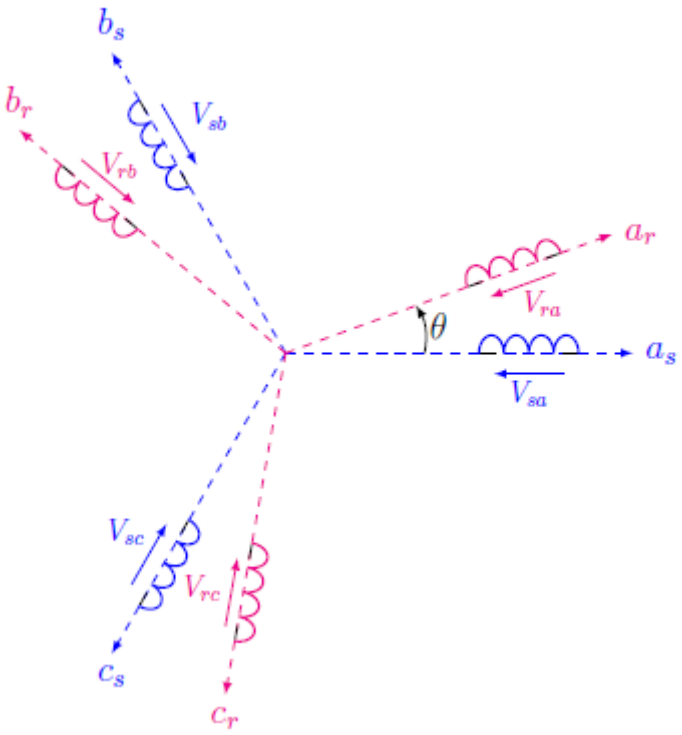


Figure 2.3 – The three-phase stator and rotor windings of the DFIG.

The simplified equivalent circuit of a DFIG is illustrated in the following Figure 2.4:

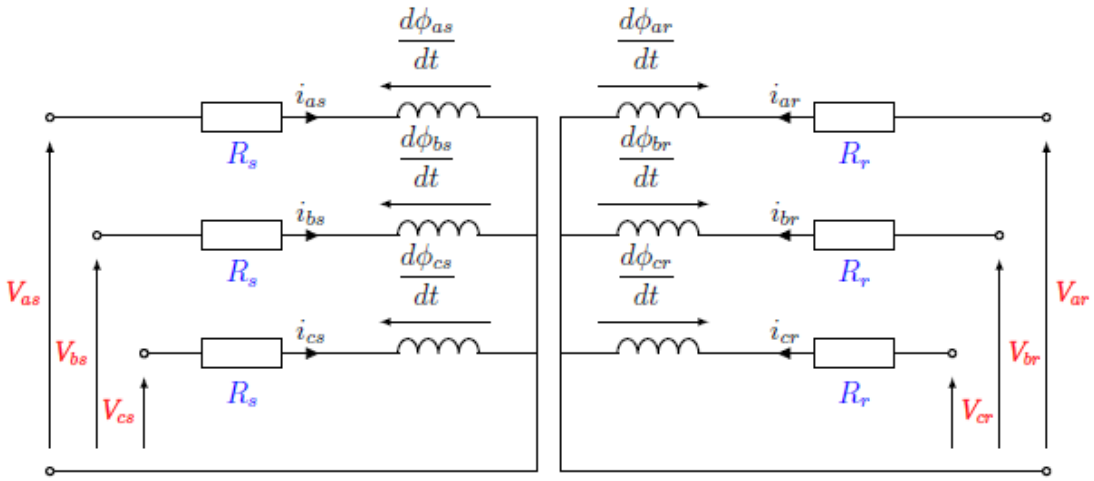


Figure 2.4 – Equivalent electrical circuit of the DFIG.

3.3.1.1. Electrical equations in the (abc) reference frame

The following electrical equations describe the instantaneous voltages, currents, and fluxes of the machine. They are expressed in the following matrix form [81]:

- **For the stator windings:**

$$[V_s] = [R_s].[I_s] + \frac{d}{dt}[\phi_s] \quad (2.9)$$

Where

$$[V_s] = \begin{bmatrix} V_{sa} \\ V_{sb} \\ V_{sc} \end{bmatrix} ; \ [R_s] = \begin{bmatrix} R_s & 0 & 0 \\ 0 & R_s & 0 \\ 0 & 0 & R_s \end{bmatrix} ; \ [I_s] = \begin{bmatrix} i_{sa} \\ i_{sb} \\ i_{sc} \end{bmatrix} ; \ [\phi_s] = \begin{bmatrix} \phi_{sa} \\ \phi_{sb} \\ \phi_{sc} \end{bmatrix}$$

V_{sa} , V_{sb} and V_{sc} : Stator phase voltages for phases a, b, and c, respectively (V).

R_s : Resistance of a stator phase (Ω).

i_{sa} , i_{sb} and i_{sc} : Stator phase currents for phases a, b, and c, respectively (A).

ϕ_{sa} , ϕ_{sb} and ϕ_{sc} : Stator phase fluxes for phases a, b, and c, respectively (Wb).

- **For the rotor windings:**

$$[V_r] = [R_r].[I_r] + \frac{d}{dt}[\phi_r] \quad (2.10)$$

Where

$$[V_r] = \begin{bmatrix} V_{ra} \\ V_{rb} \\ V_{rc} \end{bmatrix} ; \ [R_r] = \begin{bmatrix} R_r & 0 & 0 \\ 0 & R_r & 0 \\ 0 & 0 & R_r \end{bmatrix} ; \ [I_r] = \begin{bmatrix} i_{ra} \\ i_{rb} \\ i_{rc} \end{bmatrix} ; \ [\phi_r] = \begin{bmatrix} \phi_{ra} \\ \phi_{rb} \\ \phi_{rc} \end{bmatrix}$$

V_{ra} , V_{rb} and V_{rc} : Stator phase voltages for phases a, b, and c, respectively (V).

R_r : Resistance of a stator phase (Ω).

i_{ra} , i_{rb} and i_{rc} : Stator phase currents for phases a, b, and c, respectively (A).

ϕ_{ra} , ϕ_{rb} and ϕ_{rc} : Stator phase fluxes for phases a, b, and c, respectively (Wb).

3.3.1.2. Magnetic equations

The magnetic equations of the DFIG describe the stator and rotor fluxes as functions of the stator and rotor currents, as well as the various inductances. They are given by [82]:

- **At the stator level :**

$$[\phi_s] = L_s.[I_s] + M.[I_r] \quad (2.11)$$

- **At the rotor level** :

$$[\phi_r] = L_r.[I_r] + M.[I_s] \quad (2.12)$$

L_s, L_r : the stator and rotor cyclic inductances respectively (H).

M : the cyclic mutual inductance between the stator and rotor (H).

2.3.2. Two-Phase modeling of the DFIG

3.3.2.1. Model of the DFIG in the αβ Reference Frame

The model of the DFIG (Doubly Fed Induction Generator) in the stationary αβ reference frame is based on the Clarke transformation, a mathematical transformation used to simplify the analysis of three-phase circuits. Following this step, these stationary vectors are converted into a rotating dq reference frame, as explained in the next section. To perform this transformation, the direct Clarke matrix (2.13) and inverse Clarke matrix (2.14) are used [83].

$$C_{abc} = \frac{2}{3}\begin{bmatrix} 1 & \frac{-1}{2} & \frac{-1}{2} \\ 0 & \frac{\sqrt{3}}{2} & \frac{-\sqrt{3}}{2} \end{bmatrix} \tag{2.13}$$

$$C_{\alpha\beta} = \begin{bmatrix} 1 & 0 \\ \frac{-1}{2} & \frac{\sqrt{3}}{2} \\ \frac{-1}{2} & \frac{-\sqrt{3}}{2} \end{bmatrix} \tag{2.14}$$

The (abc) quantities of the DFIG projected in the αβ reference frame are given using the direct Clarke matrix as follows [84]:

$$\begin{bmatrix} \omega_\alpha \\ \omega_\beta \end{bmatrix} = C_{abc}\begin{bmatrix} \omega_a \\ \omega_b \\ \omega_c \end{bmatrix} \tag{2.15}$$

ω can represent voltage, current, or stator or rotor flux.

$$\begin{bmatrix} \omega_a \\ \omega_b \\ \omega_c \end{bmatrix} = C_{\alpha\beta}\begin{bmatrix} \omega_\alpha \\ \omega_\beta \end{bmatrix} \tag{2.16}$$

The equations of the DFIG in the stationary reference frame (αβ) are given by [85]:

- **Electrical equations:**

$$V_{s\alpha} = R_s . i_{s\alpha} + \frac{d\phi_{s\alpha}}{dt} \tag{2.17}$$

$$V_{s\beta} = R_s . i_{s\beta} + \frac{d\phi_{s\beta}}{dt} \tag{2.18}$$

$$V_{r\alpha} = R_r.i_{r\alpha} + \frac{d\phi_{r\alpha}}{dt} \tag{2.19}$$

$$V_{r\beta} = R_r.i_{r\beta} + \frac{d\phi_{r\beta}}{dt} \tag{2.20}$$

- **Magnetic equations:**

$$\phi_{s\alpha} = L_s.i_{s\alpha} + M.i_{r\alpha} \tag{2.21}$$

$$\phi_{s\beta} = L_s.i_{s\beta} + M.i_{r\beta} \tag{2.22}$$

$$\phi_{r\alpha} = L_r.i_{r\alpha} + M.i_{s\alpha} \tag{2.23}$$

$$\phi_{r\beta} = L_r.i_{r\beta} + M.i_{s\beta} \tag{2.24}$$

The equivalent circuit of the DFIG in the αβ reference frame is shown in Figure 2.5.

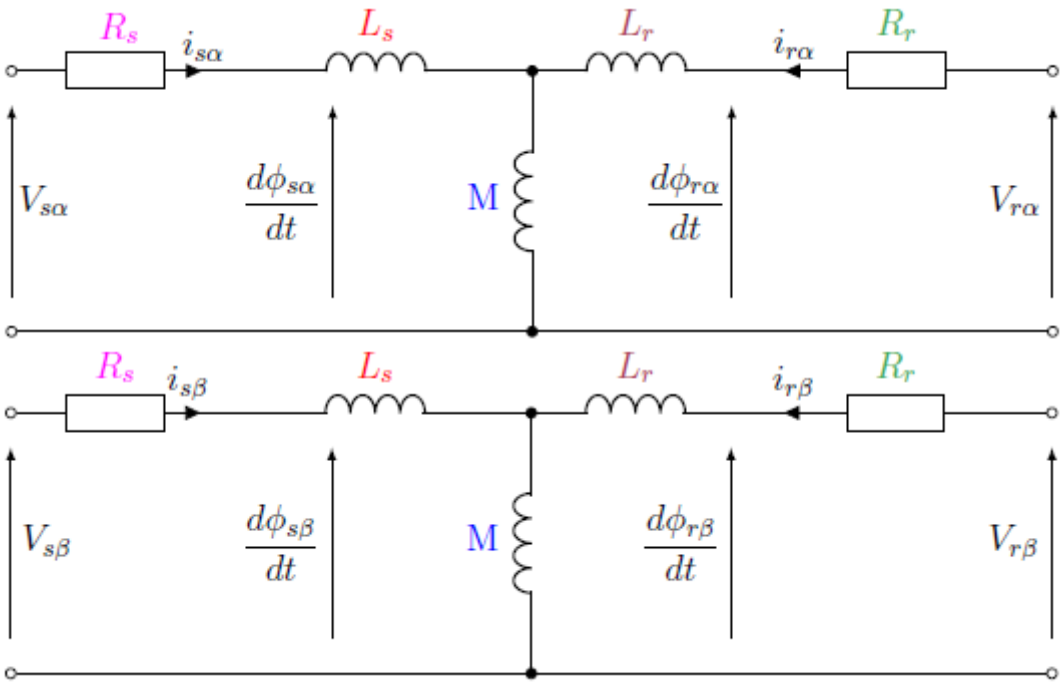


Figure 2.5 - Equivalent circuit of the DFIG in the αβ reference frame.

- **The powers expressions**

The active and reactive stator and rotor powers of the DFIG are given by [86]:

$$P_s = \frac{3}{2}(V_{s\alpha}.i_{s\alpha} + V_{s\beta}.i_{s\beta}) \tag{2.25}$$

$$Q_s = \frac{3}{2}(V_{s\beta}.i_{s\alpha} - V_{s\alpha}.i_{s\beta}) \tag{2.26}$$

$$P_r = \frac{3}{2}(V_{r\alpha}.i_{r\alpha} + V_{r\beta}.i_{r\beta}) \tag{2.27}$$

$$Q_r = \frac{3}{2}(V_{r\beta}.i_{r\alpha} - V_{r\alpha}.i_{r\beta}) \tag{2.28}$$

- **Electromagnetic torque expression**

Magnetic energy is produced by the reciprocal flux between the rotor and stator, and this electromagnetic torque is represented by [89]:

$$C_{em} = \frac{3}{2} p \frac{M}{L_s}(\phi_{s\alpha}.i_{r\beta} - \phi_{s\beta}.i_{r\alpha}) \tag{2.29}$$

3.3.2.2. DFIG model in the Park reference frame

The generator is represented by its Park model, which transforms the three-phase (a, b, c) equations into the rotating two-phase dq reference frame through the Clarke transformation. This approach simplifies the model, making it easier to model and analyze the DFIG [90]. The transformation is performed using the direct Park matrix (2.30) and the inverse Park matrix (2.31).

$$P(\theta) = \frac{2}{3}\begin{bmatrix} \cos(\theta) & \cos(\theta - \frac{2\pi}{3}) & \cos(\theta + \frac{2\pi}{3}) \\ -\sin(\theta) & -\sin(\theta - \frac{2\pi}{3}) & -\sin(\theta + \frac{2\pi}{3}) \\ \frac{1}{2} & \frac{1}{2} & \frac{1}{2} \end{bmatrix} \tag{2.30}$$

Where θ is the angle between the winding axis and the Park reference frame axis [48, 49].
The inverse Park matrix is given by:

$$P(\theta)^{-1} = \begin{bmatrix} & -\sin(\theta) \\ \cos(\theta) & \\ \cos(\theta - \frac{2\pi}{3}) & -\sin(\theta - \frac{2\pi}{3}) \\ \cos(\theta + \frac{2\pi}{3}) & \\ & -sin(\theta + \frac{2\pi}{3}) \end{bmatrix} \tag{2.31}$$

The stator and rotor quantities are then expressed in the dq reference frame, as shown in Figure 2.6.

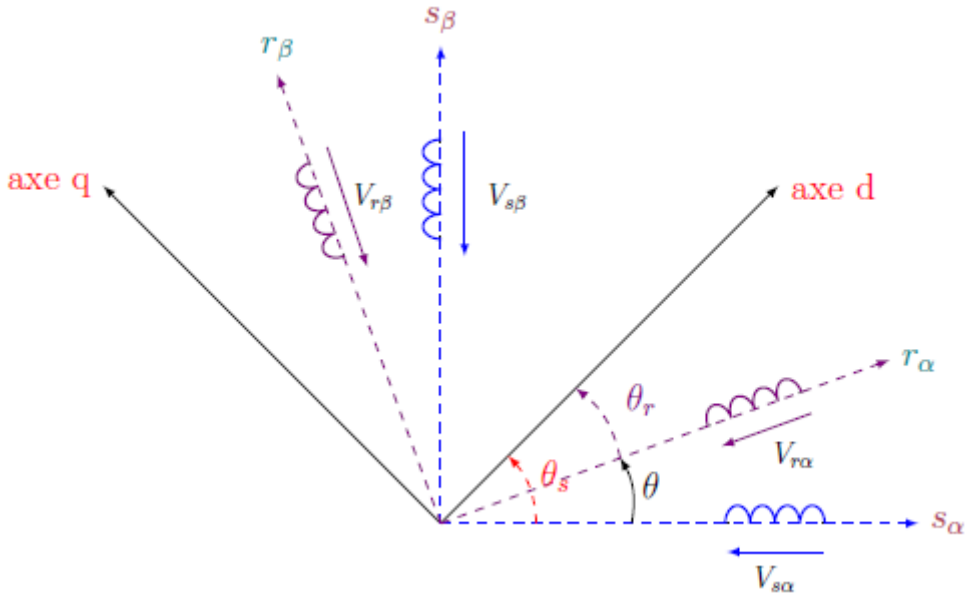


Figure 2.6 - Two-phase model of the DFIG.

s : for stator quantities.
r : for rotor quantities.
The angles θ, θ_s, and θ_r are related by the following equation:

$$\theta = \theta_s - \theta_r \tag{2.32}$$

The stator and rotor quantities are given using the Park matrix as follows:

$$\begin{bmatrix} \omega_d \\ \omega_q \end{bmatrix} = P(\theta) \begin{bmatrix} \omega_a \\ \omega_b \\ \omega_c \end{bmatrix} \tag{2.33}$$

Conversely:

$$\begin{bmatrix} \omega_a \\ \omega_b \\ \omega_c \end{bmatrix} = P(\theta)^{-1} \begin{bmatrix} \omega_d \\ \omega_q \end{bmatrix} \tag{2.34}$$

The equations for the DFIG in a rotating reference frame at the electrical speed ω_s, with the rotor rotating at the electrical speed ω_r, are as follows [90]:

- **Electrical equations:**

$$V_{sd} = R_s.i_{sd} + \frac{d\phi_{sd}}{dt} - \omega_s.\phi_{sq} \tag{2.35}$$

$$V_{sq} = R_s.i_{sq} + \frac{d\phi_{sq}}{dt} + \omega_s.\phi_{sd} \tag{2.36}$$

$$V_{rd} = R_r.i_{rd} + \frac{d\phi_{rd}}{dt} - \omega_r.\phi_{rq} \quad (2.37)$$

$$V_{rq} = R_r.i_{rq} + \frac{d\phi_{rq}}{dt} - \omega_r.\phi_{rd} \quad (2.38)$$

- **Magnetic equations:**

$$\phi_{sd} = L_s.i_{sd} + M.i_{rd} \quad (2.39)$$

$$\phi_{sq} = L_s.i_{sq} + M.i_{rq} \quad (2.40)$$

$$\phi_{rd} = L_r.i_{rd} + M.i_{sd} \quad (2.41)$$

$$\phi_{rq} = L_r.i_{rq} + M.i_{sq} \quad (2.42)$$

- **The power expressions**

The power and torque expressions in the dq reference frame are equivalent to the equations in the αβ reference frame. The stator and rotor active and reactive powers of the DFIG are given respectively by [81]:

$$P_s = \frac{3}{2}(V_{sd}.i_{sd} + V_{sq}.i_{sq}) \quad (2.43)$$

$$Q_s = \frac{3}{2}(V_{sq}.i_{sd} - V_{sd}.i_{sq}) \quad (2.44)$$

$$P_r = \frac{3}{2}(V_{rd}.i_{rd} + V_{rq}.i_{rq}) \quad (2.45)$$

$$Q_r = \frac{3}{2}(V_{rq}.i_{rd} - V_{rd}.i_{rq}) \quad (2.46)$$

- **Electromagnetic torque expression**
-

The mutual flux between the rotor and the stator generates magnetic energy, which produces an electromagnetic torque expressed by [91]:

$$C_{em} = \frac{3}{2} p \frac{M}{L_s}(\phi_{sd}.i_{rd} - \phi_{sq}.i_{rd}) \quad (2.47)$$

The equivalent circuit of the DFIG in the dq reference frame is illustrated in Figure 2.7 [44, 50, 51].

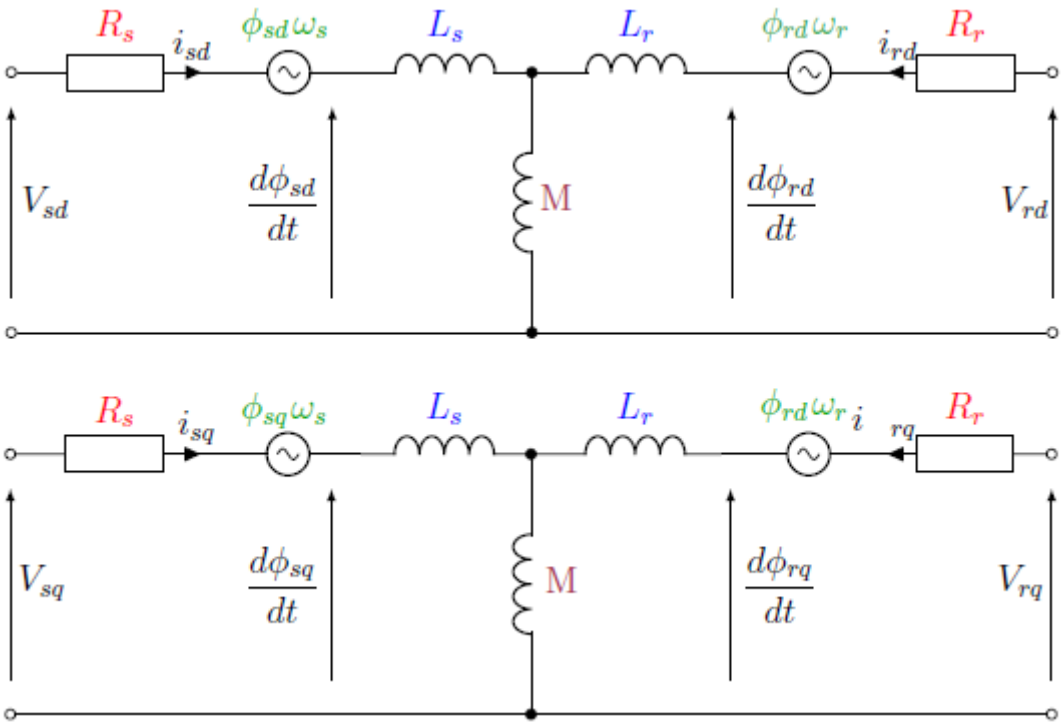


Figure 2.7 - Equivalent circuit of the DFIG in the dq reference frame.

Notes :

- In steady-state conditions with a sinusoidal voltage supply, the dq components of voltages, currents, and fluxes remain constant, whereas the αβ components vary sinusoidally.
- The machine model follows the motor convention. Therefore, for a generator, the output power is associated with ($-C_{em}$).

2.4. Combining DFIG with power converter

Traditionally, the power electronics converter used to connect the rotor voltages to the grid consists of two three-phase inverters placed back-to-back. A capacitor is inserted between the two converters to filter the DC bus voltage (see Figure 2.8). However, the stator of the DFIG is directly connected to the electrical grid [11], [44], [67], [72].

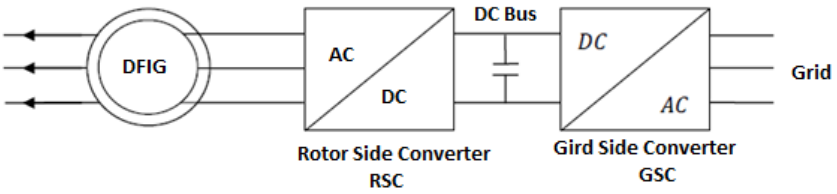


Figure 2.8 - Components of the DFIG Power System

This section outlines the critical aspects of power converters used in WECS systems with a DFIG, focusing on the rotor-side converter (RSC) and the grid-side converter (GSC). The RSC operates at varying frequencies depending on wind speed and can regulate both active power (or torque) and reactive power (or rotor flux) delivered to the grid through its output voltages. This functionality allows it to manage the power factor at the stator terminals [52]. On the other hand, the primary role of the GSC is to maintain a stable DC bus voltage. Additionally, it adjusts or absorbs reactive power based on the voltage requirements. The control of the GSC is not covered in this thesis. The connection between the RSC and GSC is facilitated by the DC bus capacitor, which acts as an energy storage component. A transformer may be used to connect the GSC or stator to the grid. Both converters are described in detail, with models developed assuming ideal switches [92, 93, 94].

2.4.1. Rotor-side converter (RSC)

The RSC is a two-level converter that converts AC voltages and currents to DC. It is modeled using ideal switching cells. The switching control is achieved through the signals S_a, S_b, and S_c. The schematic of the three-phase two-level RSC controlling the rotor of the DFIG is illustrated in Figure 2.9.

This converter can operate in two modes [11], [44], [67], [72]:

- **Rectifier Mode**: to send rotor energy to the grid when operating in super-synchronous mode (rotor speed higher than the synchronous speed dictated by the grid frequency).
- **Inverter Mode**: supplies energy to the rotor during sub-synchronous operation (rotor speed lower than the synchronous speed). In this case, energy is transferred from the grid to the rotor of the DFIG.

This converter consists of three separate arms, each containing two switches that operate in a complementary manner. However, these two switches must never be closed simultaneously to avoid short-circuiting the source.

The structure of this converter (inverter) that supplies power to the rotor of the DFIG is depicted in Figure 2.9. The switches are implemented using a combination of an IGBT with a reverse diode [44], [67].

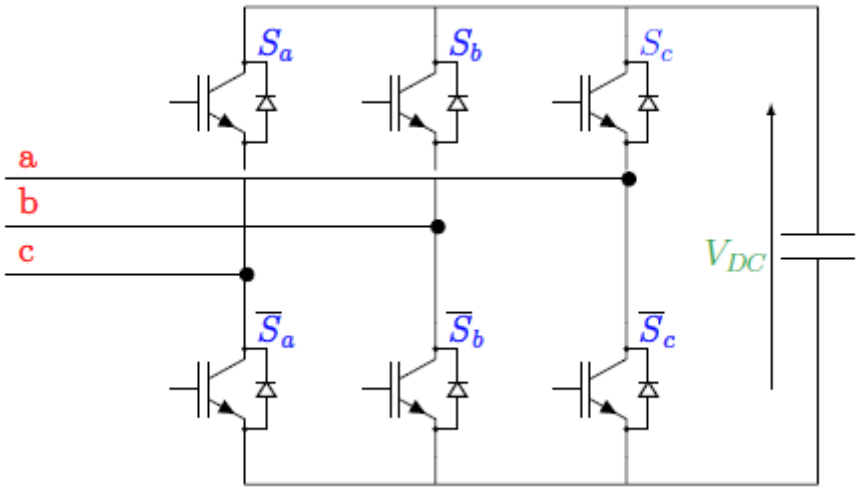


Figure 2.9 – Rotor side converter (RSC).

The switches on the same arm must be controlled in a complementary manner to ensure the continuity of the alternating currents in the load, while also preventing short-circuiting of the source. The states of the switches, assumed to be ideal, can be defined by three Boolean control variables *Sj* , (*j*=*a*, *b*, *c*).

- $S_j = 0$: the case where the upper switch is open and the lower switch is closed.
- $S_j = 1$: the case where the upper switch is closed and the lower switch is open.

The output voltages of the converter with respect to the neutral point of the three-phase system are given by [95]:

$$V_{jn} = V_{jo} - V_{no} \;;\; j = a,b,c \tag{2.48}$$

The voltage between the neutral (n) and the negative potential of the DC bus voltage (o) is necessary, so assuming the load is balanced, the result is [96]:

$$V_{an} + V_{bn} + V_{cn} = 0 \tag{2.49}$$

Substituting equation (2.48) into the last equation gives [97]:

$$V_{no} = \frac{1}{3}(V_{ao} + V_{bo} + V_{co}) \tag{2.50}$$

Substituting the latter expression into equation (2.48) gives [98]:

$$V_{an} = \frac{2}{3}V_{ao} - \frac{1}{3}(V_{bo} + V_{co}) \tag{2.51}$$

$$V_{bn} = \frac{2}{3}V_{bo} - \frac{1}{3}(V_{ao} + V_{co}) \tag{2.52}$$

$$V_{cn} = \frac{2}{3}V_{co} - \frac{1}{3}(V_{ao} + V_{bo}) \tag{2.53}$$

Or directly from a command order:

$$V_{an} = \frac{V_{DC}}{3}(2S_a - S_b - S_c) \tag{2.54}$$

$$V_{bn} = \frac{V_{DC}}{3}(2S_b - S_a - S_c) \tag{2.55}$$

$$V_{cn} = \frac{V_{DC}}{3}(2S_c - S_a - S_b) \tag{2.56}$$

Equations (2.54), (2.55) and (2.56) can be expressed as follows [99]:

$$\begin{bmatrix} V_{an} \\ V_{bn} \\ V_{cn} \end{bmatrix} = \frac{V_{DC}}{3}\begin{bmatrix} 2 & -1 & -1 \\ -1 & 2 & -1 \\ -1 & -1 & 2 \end{bmatrix}\begin{bmatrix} S_a \\ S_b \\ S_c \end{bmatrix} \tag{2.57}$$

Using the logic variables representing the state of the switches, the rotor voltage vector can be written as [100]:

$$\overrightarrow{V_r} = V_{r\alpha} + jV_{r\beta} = \sqrt{\frac{2}{3}}V_{DC}(S_a + S_b e^{j\frac{2\pi}{3}} + S_c e^{j\frac{4\pi}{3}}) \tag{2.58}$$

Depending on the eight permissible switching states of S_a, S_b and S_c, eight different combinations are available.

Table 2.1 shows all possible combinations.

Vector	S_a	S_b	S_c	V_{ao}	V_{bo}	V_{co}	V_{an}	V_{bn}	V_{cv}
V_0	0	0	0	0	0	0	0	0	0
V_5	0	0	1	0	0	V_{DC}	$\frac{-V_{DC}}{3}$	$\frac{-V_{DC}}{3}$	$\frac{2V_{DC}}{3}$
V_3	0	1	0	0	V_{DC}	0	$\frac{-V_{DC}}{3}$	$\frac{2V_{DC}}{3}$	$\frac{-V_{DC}}{3}$
V_4	0	1	1	0	V_{DC}	V_{DC}	$\frac{-2V_{DC}}{3}$	$\frac{V_{DC}}{3}$	$\frac{V_{DC}}{3}$
V_1	1	0	0	V_{DC}	0	0	$\frac{2V_{DC}}{3}$	$\frac{-V_{DC}}{3}$	$\frac{-V_{DC}}{3}$
V_6	1	0	1	V_{DC}	0	V_{DC}	$\frac{V_{DC}}{3}$	$\frac{-2V_{DC}}{3}$	$\frac{V_{DC}}{3}$
V_2	1	1	0	V_{DC}	V_{DC}	0	$\frac{V_{DC}}{3}$	$\frac{V_{DC}}{3}$	$\frac{-2V_{DC}}{3}$
V_7	1	1	1	V_{DC}	V_{DC}	V_{DC}	0	0	0

Table 2.1 - The components of the rotor voltage in the abc reference frame

By applying the Clarke transformation, it is possible to express the three-phase voltages V_{an}, V_{bn}, and V_{cn} in the αβ reference frame. The components $V_{r\alpha}$ and $V_{r\beta}$ of the rotor voltage are given by [100]:

$$\begin{bmatrix} V_{r\alpha} \\ V_{r\beta} \end{bmatrix} = \frac{2}{3} \begin{bmatrix} 1 & \frac{-1}{2} & \frac{-1}{2} \\ 0 & \frac{\sqrt{3}}{2} & \frac{\sqrt{3}}{2} \end{bmatrix} \begin{bmatrix} V_{an} \\ V_{bn} \\ V_{cn} \end{bmatrix} \tag{2.59}$$

By substituting equation (2.57) into equation (2.59), the components $V_{r\alpha}$ and $V_{r\beta}$ of the rotor voltage can be expressed in terms of S_a, S_b, and S_c:

$$\begin{bmatrix} V_{r\alpha} \\ V_{r\beta} \end{bmatrix} = \frac{2V_{DC}}{3} \begin{bmatrix} 1 & \frac{-1}{2} & \frac{-1}{2} \\ 0 & \frac{\sqrt{3}}{2} & \frac{\sqrt{3}}{2} \end{bmatrix} \begin{bmatrix} S_a \\ S_b \\ S_c \end{bmatrix} \tag{2.60}$$

Table 2.2 shows the eight different voltages in the αβ reference frame.

Vector	S_a	S_b	S_c	V_α	V_β
V_0	0	0	0	0	0
V_5	0	0	1	$\frac{-V_{DC}}{3}$	$\frac{-V_{DC}}{\sqrt{3}}$
V_3	0	1	0	$\frac{-V_{DC}}{3}$	$\frac{V_{DC}}{\sqrt{3}}$
V_4	0	1	1	$\frac{-2V_{DC}}{3}$	0
V_1	1	0	0	$\frac{-2V_{DC}}{3}$	0
V_6	1	0	1	$\frac{V_{DC}}{3}$	$\frac{-V_{DC}}{\sqrt{3}}$
V_2	1	1	0	$\frac{V_{DC}}{3}$	$\frac{V_{DC}}{\sqrt{3}}$
V_7	1	1	1	0	0

Table 2.2 - The components of the rotor voltage in the αβ reference frame.

2.4.2. DC bus Modeling

The DC bus serves as the connection between the grid-side converter and the rotor-side converter, facilitating power balance between the two converters and striving to maintain a constant voltage across its terminals. Figure 2.9 illustrates a simplified model of the DC bus.

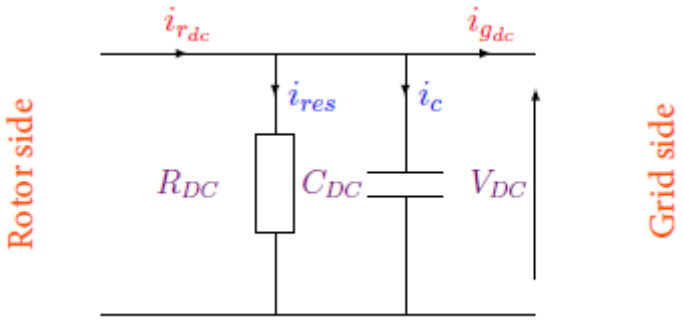


Figure 2.10 - Model of the DC bus

The temporal evolution of the DC bus voltage is obtained by integrating the capacitive current.

$$V_{DC} = \frac{1}{C_{DC}} \int i_c dt \tag{2.61}$$

or

$$\frac{dV_{DC}}{dt} = \frac{i_c}{C_{DC}} \tag{2.62}$$

The current through the capacitor is given by [90]:

$$i_c = i_{r_{dc}} - i_{g_{dc}} - i_{res} \tag{2.63}$$

$i_{r_{dc}}$: the current from the rotor to the DC bus (A).

$i_{g_{dc}}$: the current from the DC bus to the grid (A).

i_{res} : the current through the resistance (A).

On the other hand, these currents can be calculated from the AC currents of the converters [90]:

$$i_{r_{dc}} = -S_a.i_{ar} - S_b.i_{br} - S_c.i_{cr} \tag{2.64}$$

$$i_{g_{dc}} = -S_{a_g}.i_{ag} - S_{b_g}.i_{bg} - S_{c_g}.i_{cg} \tag{2.65}$$

i_{ag} , i_{bg} and i_{cg} : the currents flowing through the output of the grid-side converter (A).

S_{a_g} , S_{b_g} and S_{c_g} : the control signals of the grid-side converter.

2.4.3. Grid Side Converter (GSC)

The grid-side part includes the grid side converter, the grid-side filter, and the grid voltage. The converter and the filter interact with the grid to transfer the active power that the converter either extracts from or injects into the rotor. Figure 2.11 depicts a simplified model of the grid-side system [90].

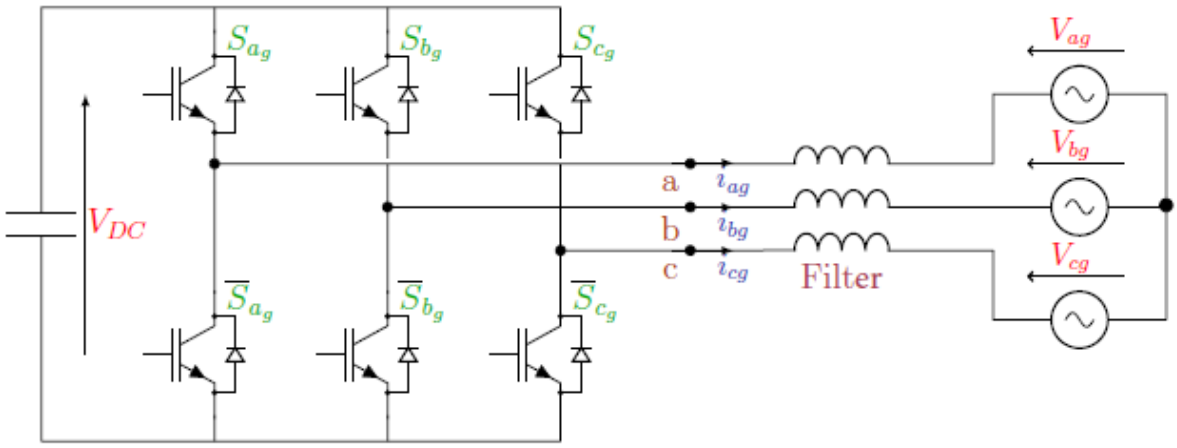


Figure 2.11 – Grid Side Converter (RSC)

The Grid Side Converter (GSC) is modeled using ideal switching cells. It converts voltages and currents from DC to AC. The switches are controlled by the signals S_{a_g}, S_{b_g} and S_{c_g}.

Different combinations of S_{a_g}, S_{b_g} and S_{c_g} create eight distinct output voltages. Two of these voltage combinations, V_0 and V_7, are referred to as null vectors because they produce zero voltage at each phase output. The remaining voltages are phase-shifted by 60 degrees. The GSC is modeled in the same way as the RSC presented in section 2.4.1.

2.4.4. Modeling of the filter

The grid-side filter is shown in Figure 2.12. It connects each output phase of the converter to the grid and serves to attenuate current harmonics. The filter consists of an inductance L_f and a resistance R_f [30, 53].

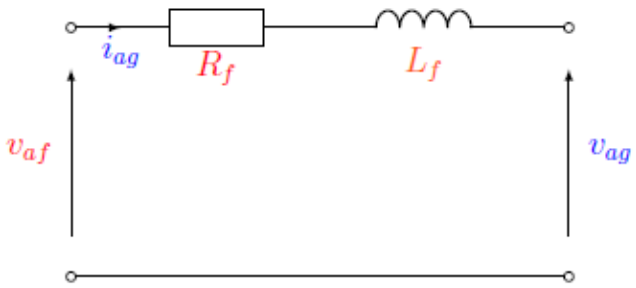


Figure 2.12: Model of the phase (a) filter

The electrical equations of the filter system representing this connection can be easily derived:

$$v_{af} = R_f.i_{ag} + L_f.\frac{di_{ag}}{dt} + v_{ag} \tag{2.66}$$

$$v_{bf} = R_f.i_{bg} + L_f.\frac{di_{bg}}{dt} + v_{bg} \tag{2.67}$$

$$v_{cf} = R_f.i_{cg} + L_f.\frac{di_{cg}}{dt} + v_{cg} \tag{2.68}$$

v_{ag}, v_{bg}, and v_{cg}: the voltages supplied by the grid (V).

v_{af}, v_{bf}, and v_{cf}: the output voltages of the converter relative to the neutral point (V).

2.4.5. Modeling of the grid

The grid voltage is typically supplied by a transformer. This voltage is represented as a three-phase AC voltage source, assumed to be balanced and sinusoidal under normal operating conditions [30]. The three-phase voltages of the symmetric system are defined as follows [20]:

$$V_{ag} = V_m.\cos(\omega_s.t) \tag{2.69}$$

$$V_{bg} = V_m.\cos(\omega_s.t - \frac{2\pi}{3}) \tag{2.70}$$

$$V_{cg} = V_m.\cos(\omega_s.t - \frac{4\pi}{3}) \tag{2.71}$$

V_m: amplitude of maximum phase voltage.

2.4.6. Pulse Width Modulation (PWM) control

Control commands for managing the states of switches in two-level converters can be generated using various modulation techniques. Pulse Width Modulation (PWM) is one of the

most commonly used methods in many communication systems. Its main purpose is to control the power delivered to different electrical devices [30].

PWM works by shaping each half-cycle of the converter's output voltage. This is achieved by comparing a triangular carrier signal with a reference signal, which represents the desired output voltage. The resulting output voltage is defined according to the following principle

$$S_i = 1 \quad \text{if} \quad v_i^* \succ v_{trg} \ , \quad i = a,b,c \tag{2.72}$$

v_i^* : The reference voltages for each phase.

v_{trg} : The triangular signal.

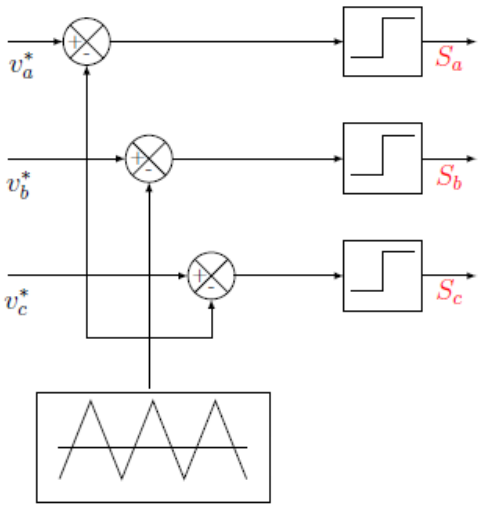


Figure 2.13 - Principle of PWM control.

✓ **The modulation index**

This index expresses the relationship between the carrier frequency (the frequency of the triangular signal) and the reference signal (the frequency of the modulating signal):

$$m_f = \frac{f_p}{f_{ref}} \tag{2.73}$$

In order to generate a high-quality output voltage, the carrier frequency should not be set too high, as this could lead to significant switching losses in the semiconductors. Therefore, when determining an appropriate value for m_f, it's important to strike a balance between the quality of the output voltage and the power losses within the converter [101].

✓ **Amplitude index :**

This index defines the relationship between the amplitude of the reference signal and that of the triangular carrier signal:

$$m_m = \frac{v_{ref}}{v_p} \tag{2.74}$$

Figure 2.14 shows an example of a pulse-width modulated signal.

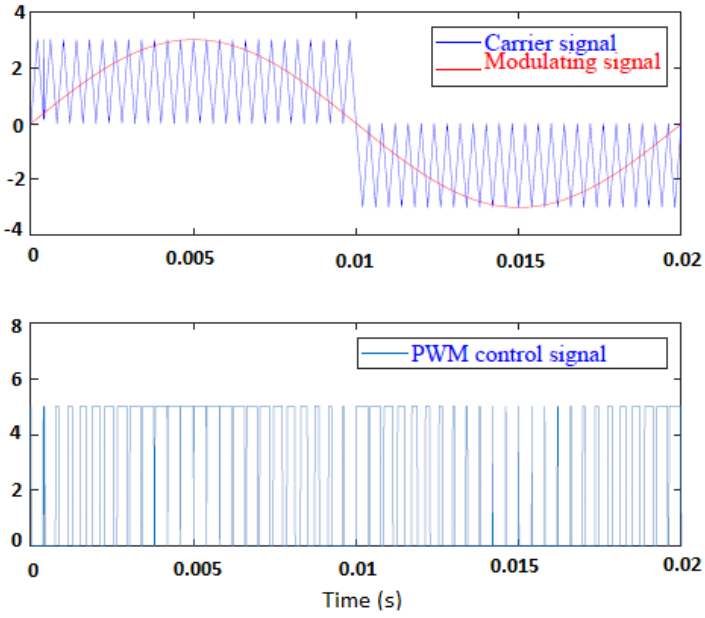


Figure 2.14 - Example of signal generation using PWM.

The three-phase converter shown in Figure 2.9, which has three arms, requires three modulation indices: m_a, m_b, and m_c. The voltages between the midpoint of each phase arm and the 0 V node of the connection with the DC bus are given by [102, 103, 104]:

$$v_{ao} = m_a.V_{DC} \tag{2.75}$$

$$v_{bo} = m_b.V_{DC} \tag{2.76}$$

$$v_{co} = m_c.V_{DC} \tag{2.77}$$

The modulation indices vary sinusoidally and are given by [54]:

$$m_a = \frac{1}{2} + m.\sin(\omega t) \tag{2.78}$$

$$m_b = \frac{1}{2} + m.\sin(\omega t - \frac{2\pi}{3}) \tag{2.79}$$

$$m_c = \frac{1}{2} + m.\sin(\omega t + \frac{2\pi}{3}) \tag{2.80}$$

The resulting output voltages are expressed as follows:

$$V_{ab} = \sqrt{3}V_{DC}m_a \sin(\omega t - \frac{\pi}{6}) \tag{2.81}$$

$$V_{bc} = \sqrt{3} V_{DC} m_b \sin(\omega t - \frac{5\pi}{6}) \quad (2.82)$$

$$V_{ca} = \sqrt{3} V_{DC} m_c \sin(\omega t + \frac{\pi}{2}) \quad (2.83)$$

2.5. Summary

In this chapter, we have covered the comprehensive modeling of the entire wind energy conversion system. This includes:

- The Wind Turbine: An overview of how the wind turbine is integrated into the system.
- The Doubly-Fed Induction Generator (DFIG): We detailed its model in various reference frames:
  - ✓ abc Reference Frame: The traditional three-phase reference frame.
  - ✓ αβ Reference Frame: The stationary reference frame used for simplifying calculations.
  - ✓ Park Reference Frame: The rotating reference frame used to analyze and control the generator dynamics more effectively.
- The Rotor-Side Converter: This component's role and its interaction with the induction generator.
- The DC Bus: Its function in connecting the machine-side converter to the grid-side converter and maintaining power balance.
- The Grid-Side Converter: We examined its connection to an RL filter and its role in interfacing with the grid.
- The Grid: The final component of the system, highlighting its integration and interaction with the rest of the components.

Lastly, we provided an overview of the Pulse Width Modulation (PWM) technique, which is employed to control the power converters within the system. This technique involves modulating the width of the pulses to control the output voltage and current of the converters, ensuring efficient and effective operation of the entire wind energy conversion system.

Chapter 3: Direct Power Control (DPC) of Doubly-Fed Induction Generator

3.1. Introduction

The significant similarity between an electric machine powered by a three-phase voltage inverter and a three-phase PWM rectifier connected to the grid has led to the development of a control technique similar to DTC, known as Direct Power Control (DPC). The first implementation of this control method was introduced by T. Neghouchi in 1998 [30], aimed at the direct control of instantaneous active and reactive power in a three-phase PWM rectifier without requiring grid voltage sensors. Since then, this approach has been further developed, and several configurations have been proposed by [15]. The common goal of this control method is to ensure the extraction of sinusoidal currents while maintaining a unity power factor, with decoupled control of active and reactive power. The various DPC configurations mentioned in the literature can be classified into two main categories:

- **DPC using the voltage vector (V-DPC)**: The configurations of DPC presented in references [31], [XU06], and [32] are based on the position of the voltage vector within the stationary α-β reference frame.
- **DPC using virtual flux**: In references [33], [MAL04], and [34], the proposed configurations rely on the calculation of a virtual flux for control.

These control strategies offer greater simplicity and robustness compared to vector control, primarily due to their reduced dependence on machine parameters. In this chapter, we introduce the DPC technique for regulating the stator's active and reactive power. The approach involves selecting an optimal voltage vector to minimize the discrepancies between the measured and reference values, keeping them within predefined hysteresis bands [35], [36], [37], [38], [39]. This method ensures efficient power management while maintaining system stability and precise control over power output.

This control approach treats the Rotor Side Converter "RSC" as a unified system, where the control vector consists of switching states. Its main advantages include a fast dynamic torque response and low dependency on machine parameters [40], [41], [42]. However, the primary drawback of this control strategy is the presence of power oscillations and current harmonics generated by the DFIG, due to the variable switching frequency [21], [23].

To address the significant computational time constraints and mitigate the limitations of conventional DPC control, we have developed a technique that reduces power level oscillations by enforcing a constant switching frequency [11], [12], [21], [25], [30]. In this approach, the switching table is replaced with pulse-width modulation (PWM), and the two hysteresis

comparators are substituted with Super-Twisting Sliding Mode controllers, resulting in enhanced performance and smoother operation [45], [47].

Before moving on to Direct Power Control (DPC), which focuses more on regulating the active and reactive power at the generator level, it is important to understand how MPPT control optimizes wind energy extraction upstream in the energy conversion process.

Finally, the simulation results for the MPPT control are presented first. Following that, simulation results are provided to highlight the performance improvements brought by the two proposed control techniques: classical DPC (DPC-C) and STSMC-DPC-PWM, in controlling the wind energy conversion system.

3.2. Maximum power extraction technique

3.2.1. MPPT control with speed feedback

The wind turbines used for electricity generation must maximize power output by efficiently harnessing the available wind energy. This is why numerous control systems for wind turbines are developed, acting either on the mechanical part through the blade pitch angle or on the electrical part by controlling the electric machine via power electronics, in order to maximize energy conversion [10].

The optimal point for maximizing power extraction from a wind turbine is determined by the prevailing aerodynamic conditions. To achieve the highest possible power capture, the performance coefficient Cp, which reflects the turbine’s aerodynamic efficiency, must be optimized. This coefficient is influenced by the generator's speed, or more specifically, the tip-speed ratio (TSR). As a result, it is crucial to develop control strategies that optimize power generation and, consequently, the electromagnetic torque by adjusting the turbine's speed to a desired reference, despite fluctuations in wind speed [25].

One of the most effective approaches for maximizing wind energy utilization is Maximum Power Point Tracking (MPPT). This technique involves continuously identifying the optimal operating point for extracting the maximum available power. Various MPPT techniques are employed, with one of the most common being based on the Tip-Speed Ratio (TSR). The operating principle of TSR-based MPPT is depicted in Figure 3.1.

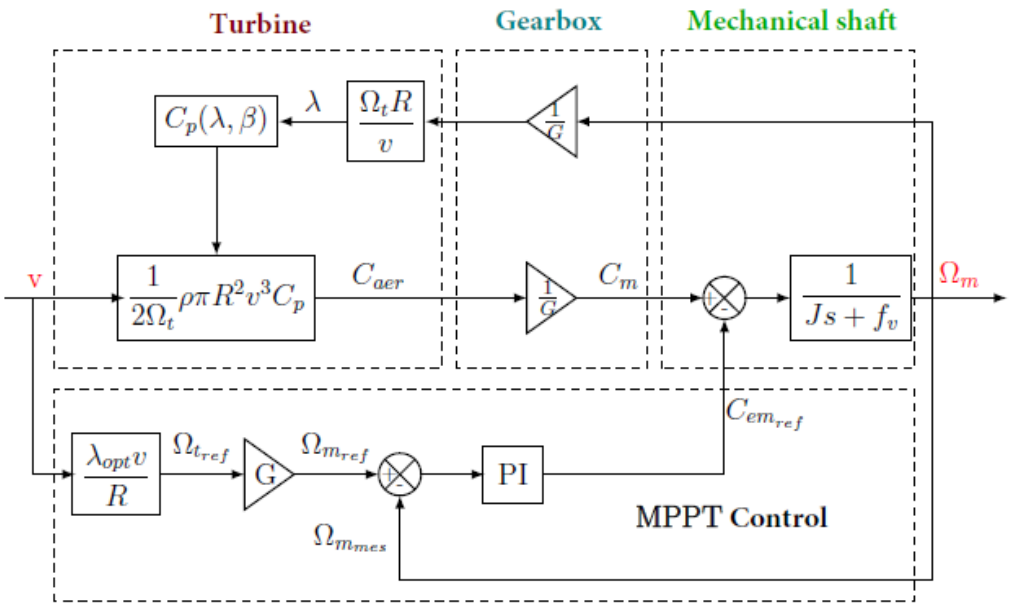


Figure 3.1 - MPPT control with speed feedback.

This method consists of maintaining the specific speed at its optimal value λ_{opt} by adjusting the electromagnetic torque to fix the mechanical rotational speed at a reference value ω_{ref}, which allows for maximum power extraction. Thus, the rotational speed control of the DFIG must be performed. The optimal value λ_{opt} corresponds to the maximum power coefficient, enabling the capture of maximum power for each different wind speed. Therefore, according to equation (2.3), the reference rotational speed is given by [12]:

$$\Omega_{t_{ref}} = \frac{\lambda_{opt}.v}{R} \tag{3.1}$$

The reference electromagnetic torque, which ensures that the rotational speed matches its reference value, is obtained from the output of a Proportional-Integral (PI) speed controller. This controller allows for the regulation of the rotational speed. The controller is illustrated in the following Figure 3.2.

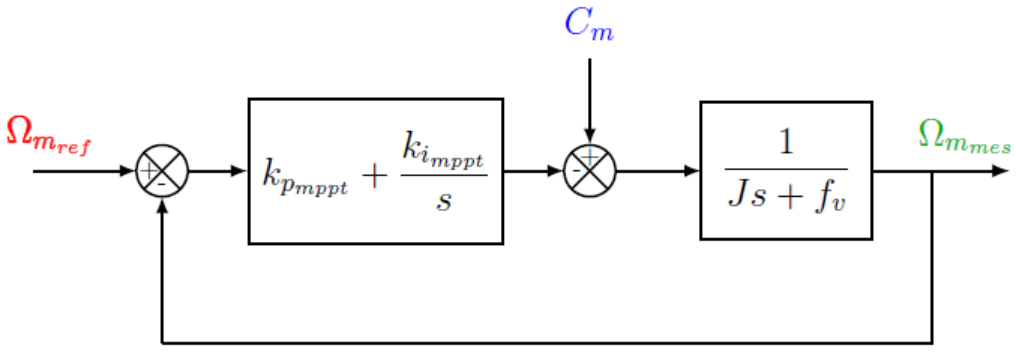


Figure 3.2 - Speed controller used for MPPT.

The closed-loop transfer function of this controller is given by [50]:

$$F(s)=\frac{(K_{p_{MPPT}}+\frac{K_{i_{MPPT}}}{s}).\frac{1}{J_s+f_v}}{1+(K_{p_{MPPT}}+\frac{K_{i_{MPPT}}}{s}).\frac{1}{J_s+f_v}} \tag{3.2}$$

$$F(s)=\frac{K_{p_{MPPT}}.s+K_{i_{MPPT}}}{J.s^2+(f_v+K_{p_{MPPT}})s+K_{i_{MPPT}}} \tag{3.3}$$

F(s) is a second-order transfer function. The proportional gain K_{pMPPT} and integral gain K_{iMPPT} of the PI controller are determined by matching the canonical form of a second-order transfer function [50]:

$$\frac{K_{p_{MPPT}}.s+K_{i_{MPPT}}}{\frac{s^2}{\omega_{n_{MPPT}}^2}+\frac{2\xi_{MPPT}}{\omega_{n_{MPPT}}}s+1} \tag{3.4}$$

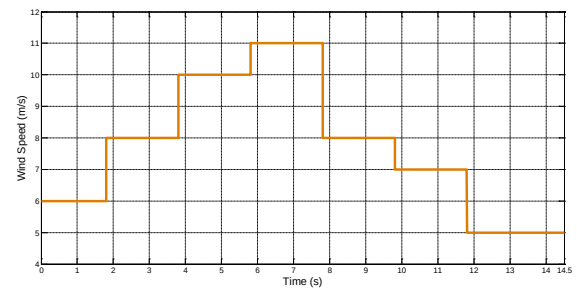
$\omega_{n_{MPPT}}$: The natural frequency.

ξ_{MPPT} : The damping.

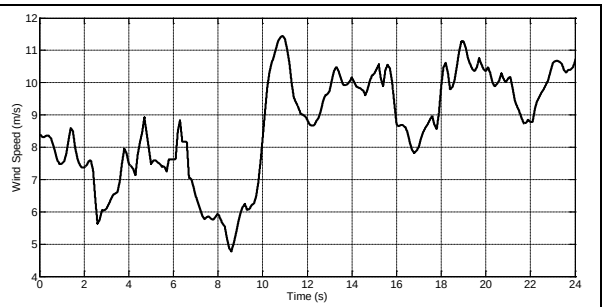
3.2.2. Matlab/Simulink Simulation results

The MPPT control of the wind energy system is simulated in MATLAB/SIMULINK 2021b for two different scenarios. The first test was performed using a step wind profile (figure 3.3a, and the second test was conducted with a variable wind profile (figure 3.3b). The results are shown in the following figures.

The parameters of the studied DFIG-based wind energy conversion system are presented in Appendix A.



a) Step wind profile



b) Variable wind profile

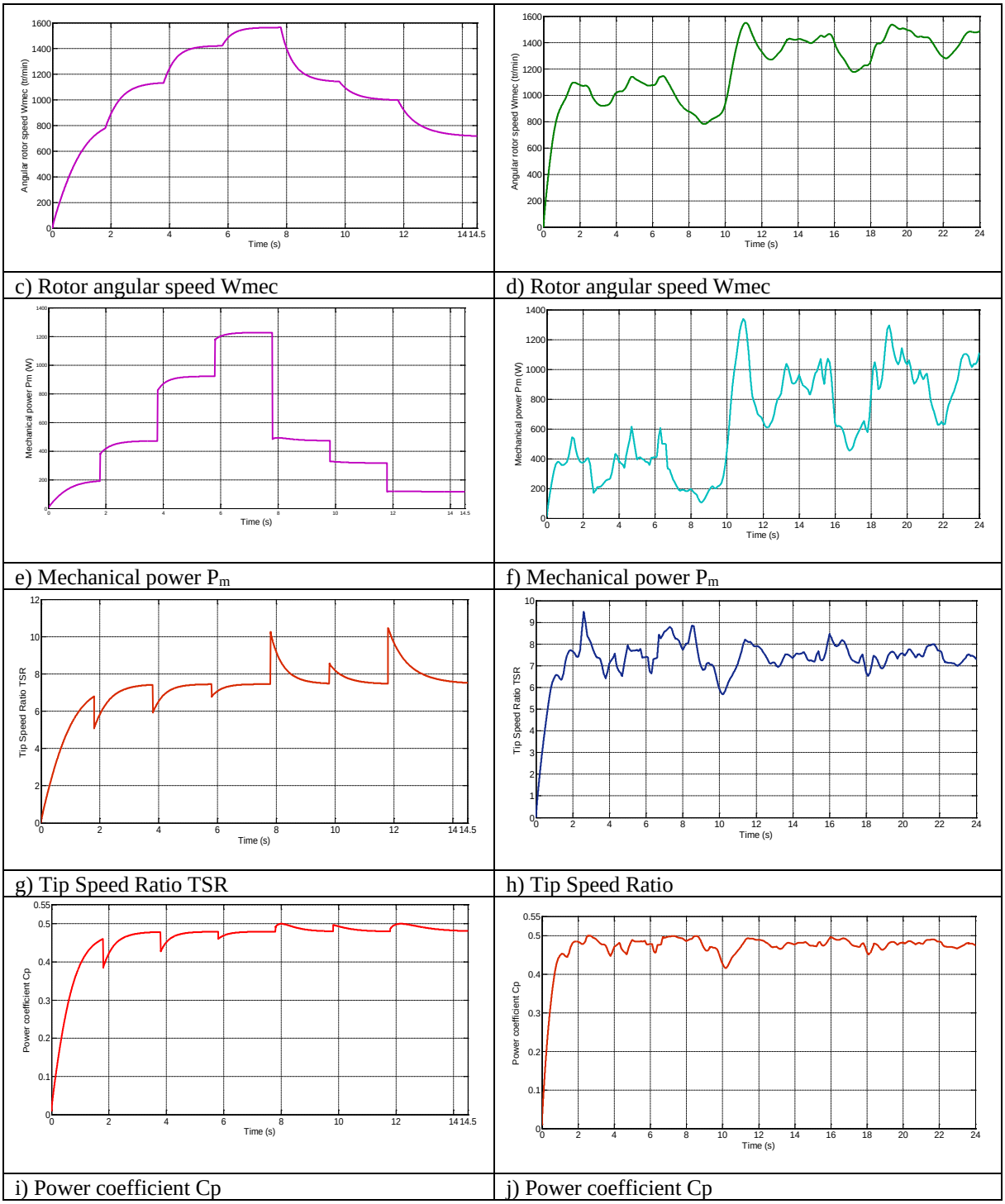


Figure 3.3 – MPPT simulations results

The figures 3.3c and 3.3d represent the rotor angular speed under different wind profiles. Figure 3.3c corresponds to the step wind profile, while Figure 3.3d corresponds to the variable wind profile. In both cases, the rotor speed adjusts according to the wind changes, with the MPPT algorithm likely trying to maintain the optimal rotor speed for maximum power extraction.

In Figure 3.3c, the angular speed follows the step changes in the wind, adjusting smoothly to maintain efficiency.

Figure 3.3d shows a more fluctuating response due to the variable wind conditions, but the rotor speed appears to track the wind changes effectively.

The figures 3.3e and 3.3f present the mechanical power follows the wind profile, but the output is smoother in Figure 3.3e due to the step nature of the wind. In contrast, Figure 3.3f shows more fluctuations, consistent with the variable wind profile. Both plots suggest that the MPPT is successfully extracting maximum power by adjusting the turbine's mechanical output according to the wind speed.

The figures 3.3g and 3.3h display the Tip Speed Ratio (TSR), which is crucial for optimal turbine performance. The TSR reflects the relationship between the rotational speed of the turbine and the wind speed. Figure 3.3g shows the TSR for the step wind profile, where the ratio adjusts smoothly to match the changing wind conditions. Figure 3.3h shows the TSR for the variable wind profile, where it fluctuates more but still stays within the expected range, indicating that the MPPT algorithm is maintaining the turbine near its optimal operating point. Figure 3.3i shows that Under the step wind profile, the power coefficient Cp quickly stabilizes at its optimal value (~0.48) within 2 seconds and remains steady, indicating the MPPT controller's rapid response and ability to maintain maximum power extraction despite abrupt wind changes.

Figure 3.3j indicates that with the variable wind profile Cp shows minor fluctuations but stays near the optimal value over 24 seconds, highlighting the MPPT controller's robustness and effectiveness in adapting to continuous, random wind variations.

In both cases, the MPPT control successfully maximizes the power output from the wind turbine.

3.3. Direct Power Control

3.3.1. A review of various direct power controls

Several control techniques have been employed to modify the output behavior of industrial systems, particularly in the renewable energy sector. These techniques vary in complexity, implementation ease, and operational principles. Among them, Direct Power Control (DPC) stands out as one of the most prominent linear techniques, especially in controlling Doubly Fed Induction Generators (DFIG) used in wind energy systems. DPC operates by estimating active (Ps) and reactive (Qs) powers, using these estimates to generate power errors. These errors are then applied to a switching table (ST), with two-level hysteresis controllers (HCs) regulating

the power output. DPC offers simplicity, ease of implementation, and a fast dynamic response, which makes it widely used in industrial applications.

However, DPC has limitations. One of its major drawbacks is high total harmonic distortion (THD) and fluctuations in both power and current, especially when system parameters like the machine's resistance (Rs) vary. This sensitivity to parameter changes is especially problematic in renewable energy systems where conditions, such as wind speed, fluctuate frequently. These limitations, including increased power ripples and reduced current quality, make DPC unsuitable for applications requiring high-quality power output. The reliance on power estimation further compounds these issues, leading to decreased performance when system parameters change or when malfunctions occur. For instance, in a system with a 1.5 MW DFIG, simulations showed that DPC performed poorly under variable wind speed conditions due to parameter sensitivity.

To address these drawbacks, researchers have proposed several intelligent control strategies. These include genetic algorithms (GAs), neural networks (NNs), and fuzzy logic (FL). In these strategies, the conventional HCs in DPC are often replaced by proportional-integral (PI) regulators or eliminated entirely in favor of intelligent controls. The advantage of these approaches is their ability to improve system robustness and reduce power fluctuations, thereby enhancing the overall current quality and reducing THD. For example, GA can optimize PI controller parameters, while NN and FL-based controllers can offer adaptive control solutions to deal with dynamic system changes.

In addition to intelligent controls, several nonlinear control strategies have been developed to improve the robustness and performance of DPC. These strategies include sliding mode control (SMC), synergetic control (SC), super-twisting control (STC), and fractional-order control. These techniques aim to overcome DPC's limitations by reducing power fluctuations and improving current quality, especially under varying DFIG parameters. Nonlinear controllers, like STC, offer advantages such as robustness and simplicity, making them suitable for complex systems like wind energy generation. However, some of these nonlinear methods increase the complexity of the system, which can lead to higher costs and greater difficulty in maintenance and implementation.

In efforts to further refine DPC, pulse width modulation (PWM) and space vector modulation (SVM) have been integrated into control schemes to generate switching pulses for the inverter. While these techniques can enhance power quality, they also introduce added complexity and cost. For example, using neural PWM for controlling DFIG systems has been shown to significantly improve power dynamics and reduce THD, as verified through simulations

conducted using MATLAB. However, reliance on power estimation remains a recurring problem in DPC systems, as estimation errors can cause performance degradation, especially in systems with fluctuating parameters.

Researchers have also explored the use of fractional-order controllers, which can offer enhanced robustness and current quality in systems with changing parameters. These controllers, such as fractional-order STC, improve energy system performance by reducing ripples and THD while maintaining system stability under various operating conditions.

Another promising development is the integration of multiple control strategies. For example, combining SMC with SC or NNs has shown improvements in system robustness and performance. These hybrid strategies allow for better control over the DFIG's output by compensating for the drawbacks of traditional DPC, such as high THD and power fluctuations. However, hybrid control strategies often face challenges related to system complexity and the need for parameter tuning, which can complicate their practical implementation.

Despite these improvements, intelligent and nonlinear control methods also have their limitations. For instance, the absence of a clear mathematical framework for tuning parameters in intelligent controllers like NNs and FL can make it difficult to achieve optimal performance. Moreover, reliance on power estimation remains a key challenge, as estimation errors can lead to fluctuations and reduced efficiency, particularly when system malfunctions occur.

In conclusion, while Direct Power Control (DPC) is widely used due to its simplicity and fast dynamic response, it faces significant limitations related to power quality, sensitivity to parameter changes, and reliance on power estimation. To address these issues, various intelligent and nonlinear control strategies have been proposed, including genetic algorithms (GAs), neural networks (NNs), fuzzy logic (FL), sliding mode control (SMC), and super-twisting control (STC). These strategies offer improved robustness, reduced THD, and better current quality, but often at the cost of increased system complexity and implementation challenges. The ongoing research aims to strike a balance between simplicity, robustness, and performance, making these advanced control techniques viable solutions for improving the performance of DFIG-based renewable energy systems.

3.3.2. Principle of Classical Direct Power Control (C-DPC)

The study of literature is sometimes surprising. Generally, systems evolve from very simple foundations, which become more complex over time. The transition from vector control to direct torque and flux control (DTC) is marked by a major simplification of the control

algorithm. However, one might genuinely wonder why the development of Direct Power Control (DPC) for active and reactive power did not precede the development of DTC [20]. Indeed, while the simplification of the control algorithm was significant in the first case, it is equally so when we consider the transition from DPC to DTC. The development of this new control technique (compared to DTC) is based exactly on the same vector relations that govern DTC. However, instead of focusing on controlling components estimated from machine parameters, DPC focuses solely on the exchange of active and reactive power between the machine and its power source. Additionally, since instantaneous power can be calculated without requiring rotational reference frame transformations, the angle of rotor phase position is no longer necessary. Furthermore, because power is directly calculated from currents and voltage, knowledge of machine parameters is no longer required, which is as astonishing as the performance it delivers—enough to make any electric drive manufacturer envious [41].

To better understand the operating principle, we can refer back to the vector diagrams of direct torque and flux control but instead discuss active and reactive power. It is understood that an increase in torque (angle δ) at constant speed implies an increase in the power consumed by the machine. It is worth noting that positive power is absorbed by the machine in motor mode, while it is negative in generator mode. This relationship also holds in generator mode, where an increase in torque reduces the power generated by the machine (increases positive power). Essentially, one simply needs to replace the term torque with active power and flux with reactive power in DTC to obtain a drive with direct active and reactive power control. Unfortunately, a major difficulty remains in calculating the rotor flux angle. In this regard, Direct Power Control provides a robust way to determine the current sector of the rotor flux [45].

The overall structure of the DPC-C, using a predefined switching table, applied to the rotor-side three-phase converter “RSC” is shown in figure 3.4.

The principle of DPC involves selecting a switching sequence (S_a, S_b, S_c) for the semiconductors constituting the RSC (Rotor Side Converter) based on a switching table. This selection is made by evaluating the errors εP_s and εQ_s between the reference values of active and reactive power (P_s^* and Q_s^*), and the real values (P_s and Q_s), provided by two hysteresis comparators with digitized outputs H_P and H_Q, respectively. The selection is also influenced by the sector (zone) in which the rotor flux vector is located [51], [52], [53].

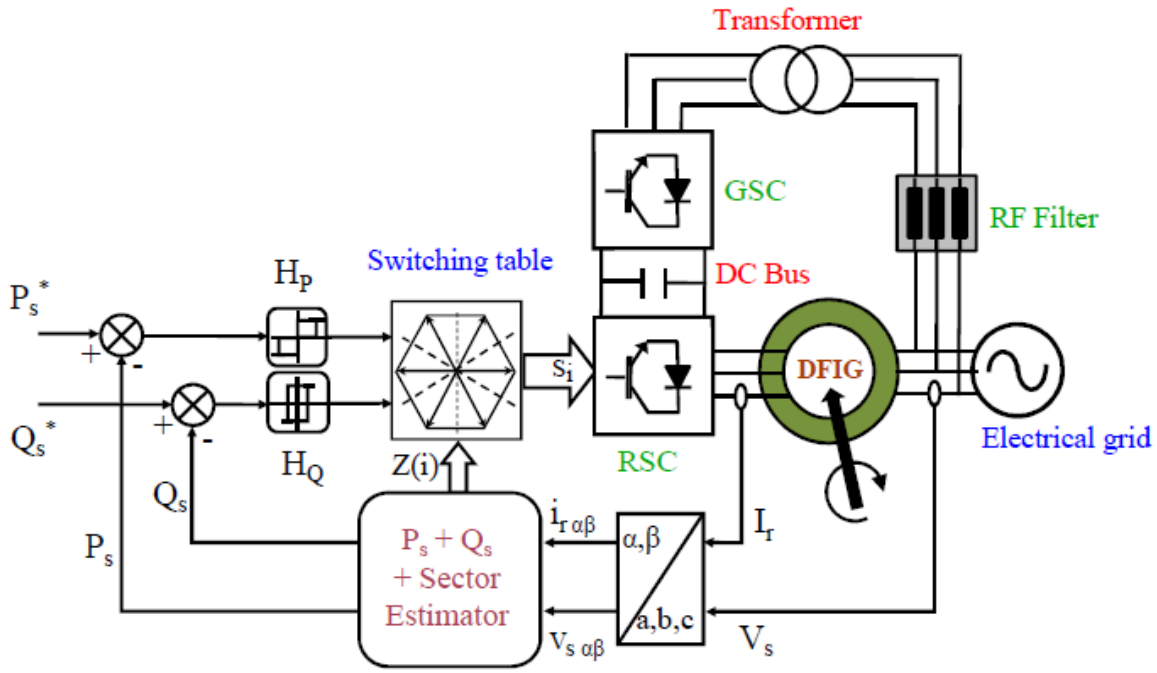


Figure 3.4 - Configuration of the Classical DPC (C-DPC) of the DFIG.

3.3.3. Classical DPC of DFIG

In order to arrive at a switching table that ensures simultaneous control of active and reactive power across all sectors, it is essential to study the variations caused by the application of each control vector on these quantities, during a complete period of rotor voltage. The control vectors selected in this switching table must ensure the reduction of the tracking error for both active and reactive power simultaneously [31].

3.3.3.1. Estimation of active and reactive power

There are three methods to calculate active and reactive power:

- By measuring the currents and voltages;
- By estimating the grid voltages and measuring the currents;
- By estimating the virtual flux and measuring the currents.

Instead of measuring the power on the line, by capturing the rotor currents and estimating P_s and Q_s, this approach provides anticipatory control of power in the stator windings. It is important to note that the DPC control will be based on the simplified model of the DFIG (see Chapter 2), which assumes the stator phase resistance is negligible. We can derive the relationships for P_s and Q_s based on the two components of the rotor flux in the (αr-βr) reference frame. This reference frame rotates along with the rotor of the DFIG [TRE09]. The active and

reactive powers are controlled using two hysteresis comparators, with the measured values of the powers being estimated from the following equations [30]:

$$P_s = -\frac{3}{2}\frac{L_m}{\sigma L_s L_r} V_s \phi_{r\beta} \tag{3.1}$$

$$Q_s = \frac{3}{2}\left(\frac{V_s}{\sigma L_s}\psi_s - \frac{V_s L_m}{\sigma L_s L_r}\phi_{r\alpha} \right) \tag{3.2}$$

Where:

$$\phi_{r\alpha} = \sigma L_r i_{r\alpha} + \frac{L_m}{L_s}\psi_s \;;\; \phi_{r\beta} = \sigma L_r i_{r\beta} \;;\; \left|\overline{\psi_s}\right| = \frac{\left|\overline{V_s}\right|}{\omega_s} \text{ and } \sigma = 1 - \frac{L_m^2}{L_s L_r}$$

by introducing the angle δ, which is between the stator and rotor flux vectors, P_s and Q_s become:

$$P_s = -\frac{3}{2}\frac{L_m}{\sigma L_s L_r}\omega_s |\psi_s||\psi_r| \sin\delta \tag{3.3}$$

$$Q_s = \frac{3}{2}\frac{\omega_s}{\sigma L_s}|\psi_s|\left(\frac{L_m}{L_r}|\psi_r|\cos\delta - |\psi_s| \right) \tag{3.4}$$

The derivative of the two equations in (3.3 and 3.4) gives [50]:

$$\frac{dP_s}{dt} = -\frac{3}{2}\frac{L_m \omega_s}{\sigma L_s L_r}|\psi_s|\frac{d\left(|\psi_r|\sin\delta\right)}{dt} \tag{3.5}$$

$$\frac{dQ_s}{dt} = \frac{3}{2}\frac{L_m \omega_s}{\sigma L_s L_r}|\psi_s|\left(\frac{d\left(|\psi_r|\cos\delta\right)}{dt} \right) \tag{3.6}$$

As seen in the equations (3.5 and 3.6), these last two expressions show that the stator active and reactive powers can be controlled by adjusting the relative angle δ between the stator and rotor flux vectors and their amplitudes (Figure 3.5) [60].

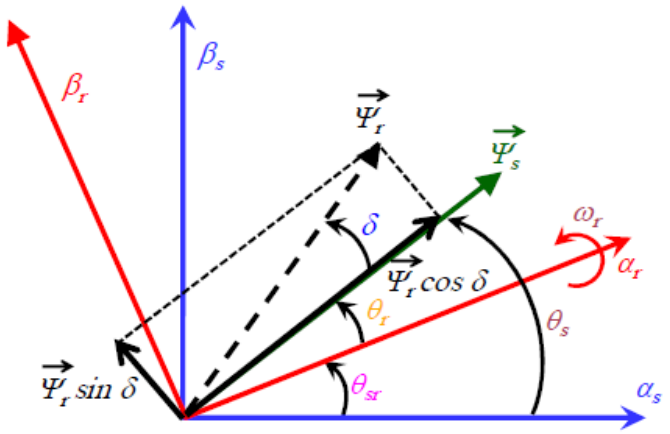
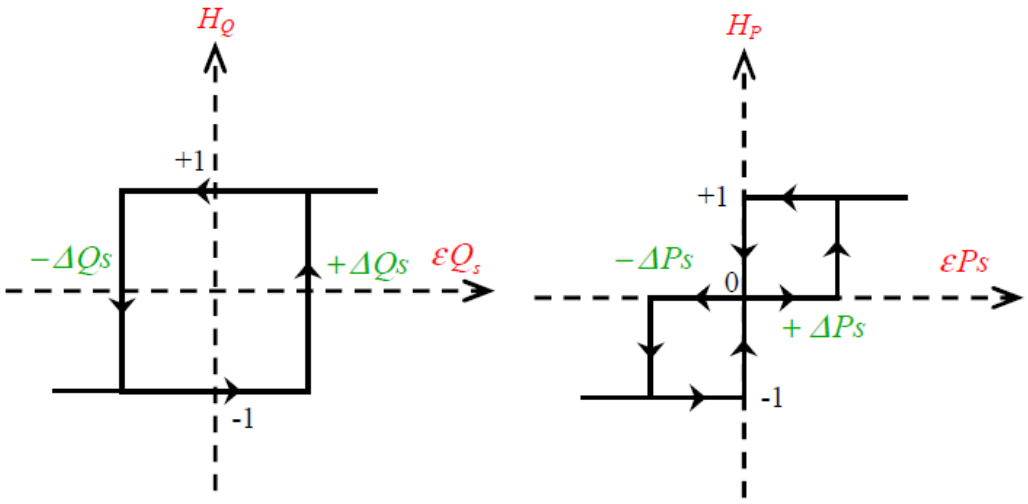


Figure 3.5 - The decomposition of the rotor flux vector in the (α-β) reference.

3.3.3.2. Choice of hysteresis comparators

To achieve optimal dynamic performance, the selection of a two-level hysteresis controller is considered the most straightforward and effective solution for managing active and reactive power. These comparators (Figure 3.6) are designed to control the exchange of active and reactive power between the DFIG and the power grid in both directions, accommodating both sub-synchronous and super-synchronous operating modes of the DFIG [100].

DPC for the DFIG is based on selecting a rotor voltage vector in such a way that the errors between the measured and reference values are minimized and maintained within the boundaries of the hysteresis bands [101].



(a) (b)

Figure 3.6 - Hysteresis Comparators: (a) Reactive Power. (b) Active Power,

These hysteresis comparators, applied to active and reactive power, enable the detection of control zone exceedances and ensure compliance with:

$$\begin{cases} Si & \varepsilon Q_s \geq \Delta Q_s \Rightarrow H_Q = 1 \\ Si & \varepsilon Q_s \leq -\Delta Q_s \Rightarrow H_Q = -1 \\ Si & \varepsilon P_s \geq \Delta P_s \Rightarrow H_P = 1 \\ Si & -\Delta P_s \leq \varepsilon P_s \leq \Delta P_s \Rightarrow H_Q = 1 \\ Si & \varepsilon P_s \leq -\Delta P_s \Rightarrow H_Q = -1 \end{cases} \quad (3.7)$$

Analog comparators have a notable drawback: the sampling frequency is variable. However, this issue can be resolved by using discrete comparators. With this approach, power variations are not kept exactly within the hysteresis band, but instead operate with a fixed sampling time [46].

3.3.3.3. Formulation of the switching table

It is well established in the literature that the treatment of active and reactive power in Direct Power Control (DPC) is analogous to the control of torque and flux in Direct Torque Control (DTC). Accordingly, the contribution of rotor flux helps in correcting the stator power factor, thereby reducing the reactive power consumption of the machine. This relationship holds true regardless of the machine's operating mode. To select the optimal rotor voltage vector, it is essential to determine the relative position of the rotor flux within the six sextants. A three-phase inverter with two voltage levels can generate eight distinct voltage vector combinations, which can be applied to the rotor terminals of the DFIG. Of these, six are active voltage vectors and two are zero vectors. There are six active vectors and two zero vectors [99].

The division of the complex plane into six angular zones Z_i (i=1,...,6) can be determined by the following relation:

$$\frac{-\pi}{6} + (i-1)\frac{\pi}{3} \leq Z(i) < \frac{\pi}{6} + (i-1)\frac{\pi}{3} \quad (3.8)$$

It follows that Table 5.1 of the optimal vectors is derived in the same manner, prioritizing active power control over reactive power control. The signals H_P and HQ, along with the position of the rotor flux vector δ, serve as the inputs to this truth table, while the switching states S_a,S_b,S_c represent its outputs [61].

		Comparator	3 levels			3 levels		
			2 levels			2 levels		
		Reactive Power : H_Q	1			-1		
		Active Power : H_P	1	0	-1	1	0	-1
Sector Z(i) with respect to δ angle	1	(330°, 30°)	V_5	V_7	V_3	V_6	V_0	V_2
	2	(30°, 90°)	V_6	V_0	V_4	V_1	V_7	V_3
	3	(90°, 150°)	V_1	V_7	V_5	V_2	V_0	V_4
	4	(150°, 210°)	V_2	V_0	V_6	V_3	V_7	V_5
	5	(210°, 270°)	V_3	V_7	V_1	V_4	V_0	V_6
	6	(270°, 330°)	V_4	V_0	V_2	V_5	V_7	V_1
V_0=[0,0,0] ; V_1=[1,0,0] ; V_2=[1,1,0] ; V_3=[0,1,0] ; V_4=[0,1,1] ; V_5=[0,0,1] ; V_6=[1,0,1] ; V_7=[1,1,1]								

Table 3.1 – Selection table of optimal vectors (active and reactive power). [50]

Although switching table 3.1 is commonly used in DPC (Direct Power Control), it is by no means the only one. Numerous alternative switching tables have been proposed in the literature [51], [52], [53], [54], [55], [56], and we have tested several of them through simulations. The results obtained from these different tables are nearly identical [96].

However, the core principle behind DPC control lies in the continuous movement of the rotor flux within the machine. When sampled at sufficiently high intervals, the rotor flux appears to move progressively through each sector in sequence. Analyzing Table 5.1 shows that, for instance, if the rotor flux is in sector 2 and vector V3 has just been applied, the resulting change in stator reactive power will inevitably be negative, as vector V3 reduces reactive power. If the observed behavior deviated from this, it would suggest an error in our sector estimation, implying that the flux might actually be in sector 1 or 5. However, since the flux was previously in sector 2, it is highly unlikely for it to have jumped to sector 5, as that would require it to skip over two sectors. This explanation is further supported by the reference tables (Tables 3.2 and 3.3), which are based on the information in Table 5.1 [97].

	V_0	V_1	V_2	V_3	V_4	V_5	V_6	V_7
Sector 1	0	0	-	+	0	+	-	0
Sector 2	0	-	0	-	+	0	+	0
Sector 3	0	+	-	0	-	+	0	0
Sector 4	0	0	+	-	0	-	+	0
Sector 5	0	+	0	+	-	0	-	0
Sector 6	0	-	+	0	+	-	0	0

Table 3.2 - Monitoring of reactive power variation.

The first reference table (Table 3.2) checks the condition for reactive power variation. That is, it verifies whether the variation in reactive power measured at the stator corresponds to the expected variation for the current sector and vector.

In response to the reactive power variation check, if there is an inconsistency between the expected and measured values, Table 3.3 suggests modifying the current sector. For example, let's revisit the previous example where we assume that the flux is in sector 2. Following the application of vector 3, the reactive power variation at the stator is found to be positive, which contradicts the predictions of Table 3.2. In this case, Table 3.3 recommends decrementing (-1) the current sector. Referring again to Table 3.2, for sector 1 and vector 3, the expected reactive power variation now matches the measured value [98].

	V_0	V_1	V_2	V_3	V_4	V_5	V_6	V_7
Sector 1	0	0	-1	+1	0	-1	+1	0
Sector 2	0	+1	0	-1	+1	0	-1	0
Sector 3	0	-1	+1	0	-1	+1	0	0
Sector 4	0	0	-1	+1	0	-1	+1	0
Sector 5	0	+1	0	-1	+1	0	-1	0
Sector 6	0	-1	+1	0	-1	+1	0	0

Table 3.3 - Sector update table

In the case of divergence, the current sector must be updated according to Table 3.3 [53], [54], [55], [56], [56] by shifting its position clockwise (-1), counterclockwise (+1), or simply maintaining its previous position (0). In this scenario, the sampling period of the DPC must be sufficiently short to ensure that the rotor flux never misses transitioning between two adjacent sectors. However, it can be noted that, within any given sector, for instance, in the $i^{ème}$ sector, vectors V_i and V_{i+3} are not applied [65]. Based on these conclusions, Table 3.1 can be reinterpreted in terms of active and reactive power to generate Table 3.4 below.

Variable	**Increasing**	**Decreasing**
Reactive power	V_{i+2} , V_{i-2}	V_{i+1} , V_{i-1}
Active power	V_{i-2} , V_{i-1}	V_{i+1} , V_{i+2}

Table 3.4 - Generalized table of voltage vectors for DPC control

3.3.4. Simulation results

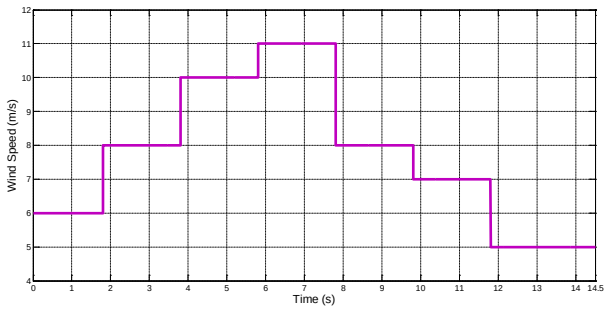
In this section, the classical DPC control of the 1.5 kW DFIG (Appendix A) was tested through simulations in the MATLAB/SIMULINK 2021b environment. The sampling frequency of this simulation is 10 kHz.

Two types of tests were applied to the system, as shown in Figure 3.13, to observe its control behavior:

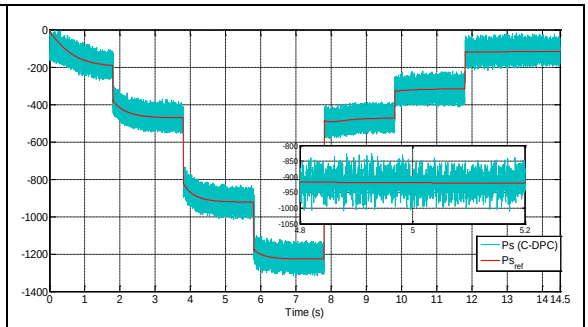
- Test under step wind profile (with MPPT control).
- Test under variable wind speed (with MPPT control).

3.3.4.1. Simulations results under step wind profile of C-DPC strategy

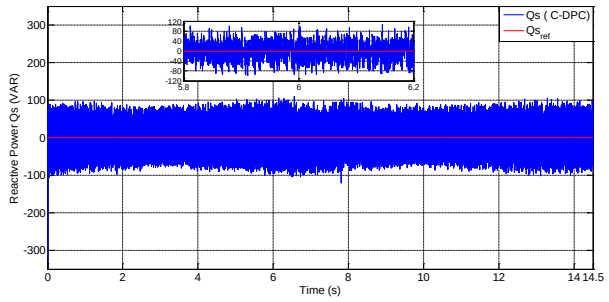
Figure 3.7 shows the simulation results of the DFIG-based WECS controlled by C-DPC strategy.



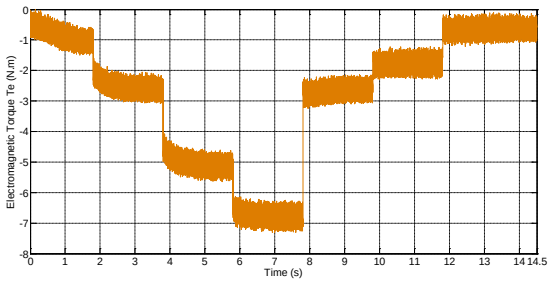
a)Wind speed profile



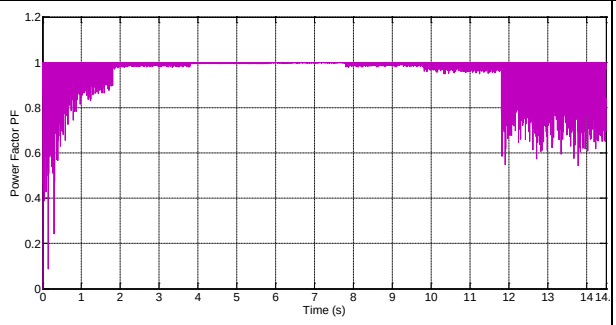
b)Active power Ps (C-DPC)



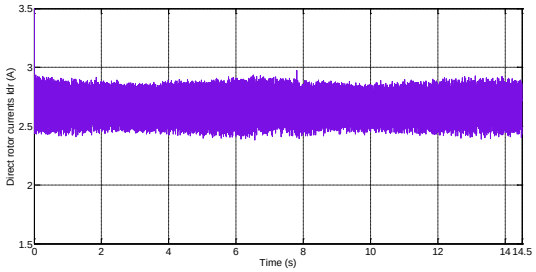
c)Reactive power Qs (C-DPC)



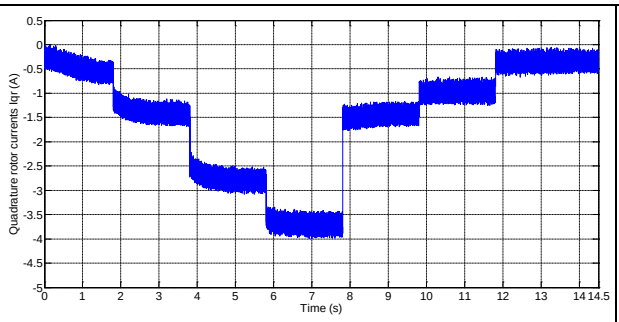
d)Electromagnetic torque Te (C-DPC)



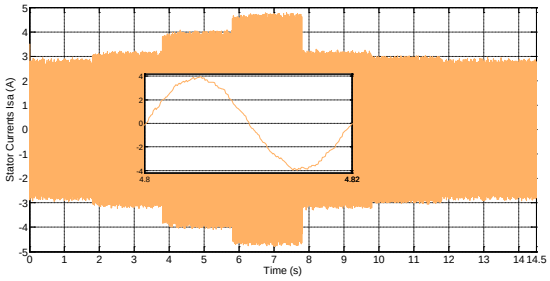
e) Power factor PF (C-DPC)



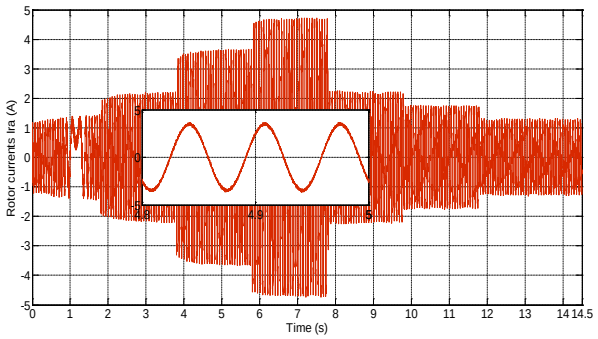
f) Direct rotor current Idr (C-DPC)



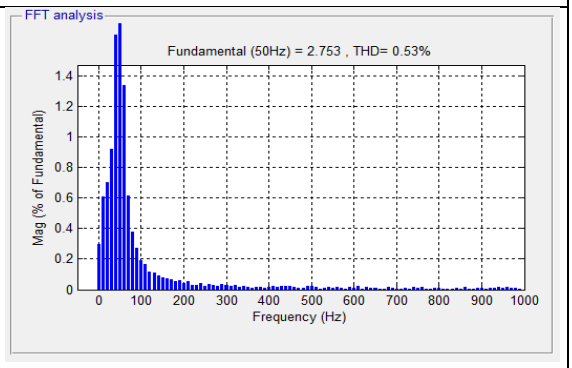
g) Quadrature rotor current Iqr (C-DPC)



h) Stator currents Isa (C-DPC)



i) Rotor current Ira (C-DPC



j) THD of Stator current Isa

Figure 3.7 – Simulation results of C-DPC with step wind profile

In Figure 3.7b, the active power (Ps) shows notable ripples when responding to changes in wind speed. Although the supplied DFIG power effectively follows the step wind profile, these undulations are a clear indication of DPC problems. Such undulations can affect the quality of the power delivered to the grid, potentially leading to issues such as increased harmonics, reduced energy efficiency, and stress on the electrical components. Oscillations in active power can also cause voltage instabilities, especially in large-scale wind farms, where smooth power delivery is crucial for maintaining electrical grid stability.

Similarly, in Figure 3.7c, the reactive power Qs displays important oscillations. These ripples can still contribute to energy quality issues, affecting the voltage regulation of the wind energy conversion system. Maintaining steady reactive power is critical for ensuring a stable power factor and minimizing losses in the transmission system. reference reactive power is imposed null to guarantee a power factor always close to 1.

Reactive power ripples can lead to inefficient operation and increased energy losses.

The figure 3.7d of electromagnetic torque Te reveals ripples that emphasize the main limitations of the C-DPC strategy. These undulations lead to mechanical stress on parts such as the drivetrain, which may result in long-term wear. Moreover, the existence of ripples suggests instability in the control system the presence of ripples indicates that the control system is unstable, which negatively impacts power efficiency. These fluctuations also place additional

stress on power electronic components, potentially leading to overheating and failure. Thus, minimizing these torque oscillations is crucial to improving system efficiency and reliability even though C-DPC can track variations in wind speed.

The figure 3.7e shows that the power factor (PF) initially reaches near unity, reflecting efficient power delivery, though a slight drop towards the end indicates potential control imperfections or losses under specific conditions.

In Figures 3.7f and 3.7g, the direct rotor current (Idr) remains relatively stable with minor fluctuations, while the quadrature rotor current (Iqr) shows more marked changes, corresponding to wind speed and torque variations, although it also exhibits oscillations that could be optimized.

In figure 3.7h, a sinusoidal waveform with minor perturbations is displayed by the stator current (Isa), underscoring the need for improved control as it might affect power quality and raise system stress. There are more oscillations in the rotor current (Ira) (see figure 3.7i), which indicates mechanical and electrical stressors that need to be reduced to increase system reliability.

Although the stator current's THD (total harmonic distortion) of 0.53% is within allowable bounds, it may be lowered to enhance power quality and lower harmonic losses. Although C-DPC has good control overall, its oscillations and moderate THD (see figure 3.7j) suggest areas for improvement in terms of stability and performance.

		***Ps* (W)**	***Qs* (VAR)**
C-DPC	**Ripples**	180	200
	Overshoot	95	115
	SSE	100	70
	Response time	3.5 ms	2.9 ms

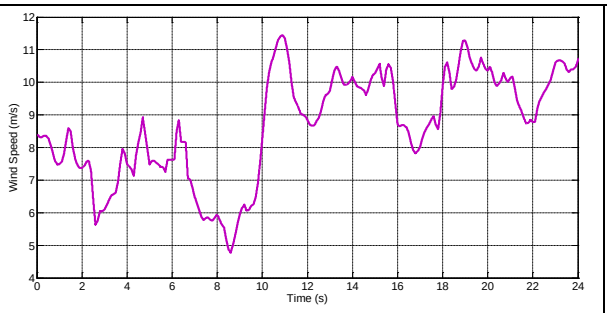
Table 3.5 –Response time, overshoot, and energy ripples in the first test (step wind profile)

Those results presented in Table 3.5 highlight key performance metrics for the C-DPC (Classic Direct Power Control) under a step wind profile. The active power (Ps) and reactive power (Qs) exhibit significant ripples, with values of 180 W and 200 VAR, respectively. These fluctuations indicate substantial instability during power transitions, which could affect overall system efficiency. Furthermore, the overshoot for Ps is 95 W, while for Qs it reaches 115 VAR, reflecting the system’s difficulty in smoothly handling sudden changes in wind conditions. The steady-state error (SSE) is also notable, particularly for Ps, with a value of 100 W, indicating that the system struggles to converge to the desired setpoint during steady-state operation. On the positive side, the response times for both Ps and Qs are quick, at 3.5 ms and 2.9 ms,

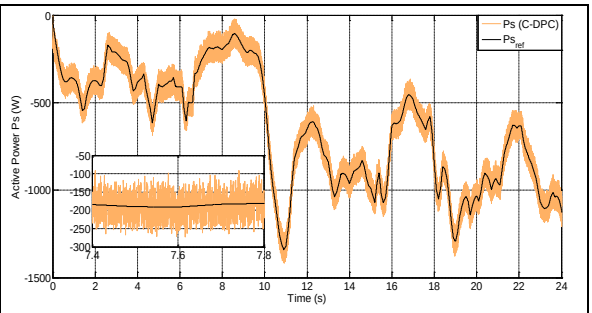
respectively. However, this fast response appears to come at the cost of increased instability, as seen in the high ripples and overshoot.

3.3.4.2. Simulations results under variable wind profile of C-DPC strategy

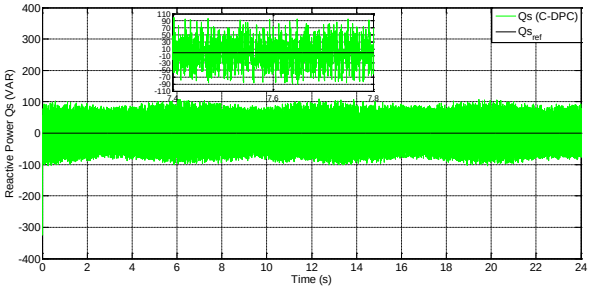
The following figures show the simulation results of the DFIG-based WECS system under a variable real wind profile.



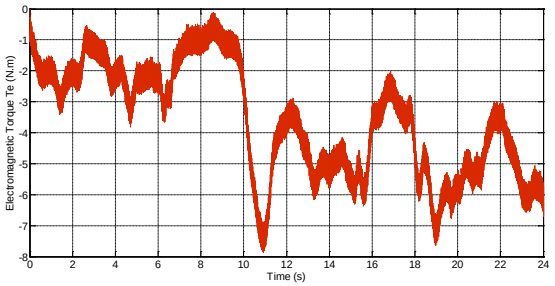
a) Variable wind speed profile



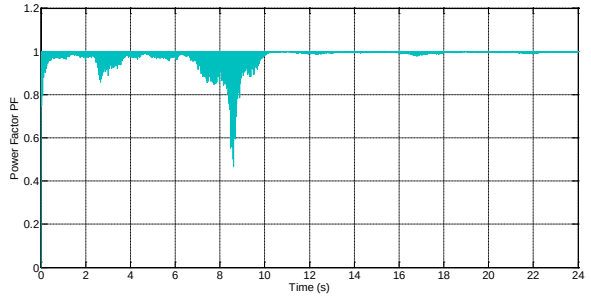
b) Active power Ps (C-DPC)



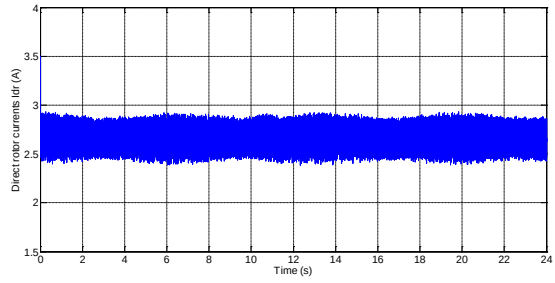
c) Reactive power Qs (C-DPC)



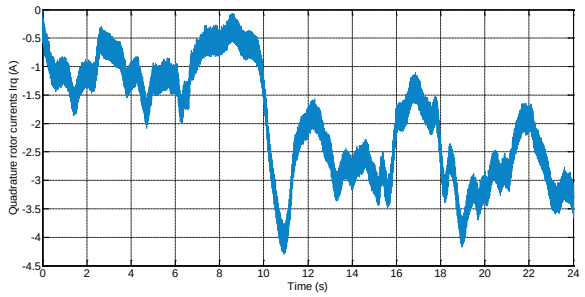
d) Electromagnetic torque Te (C-DPC)



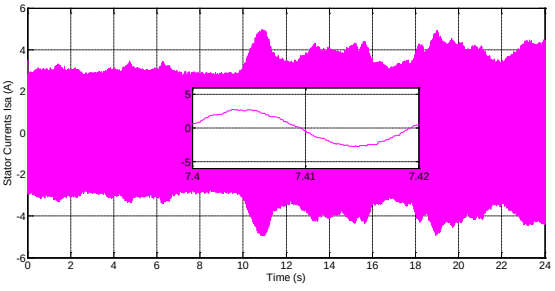
e) Power factor PF (C-DPC)



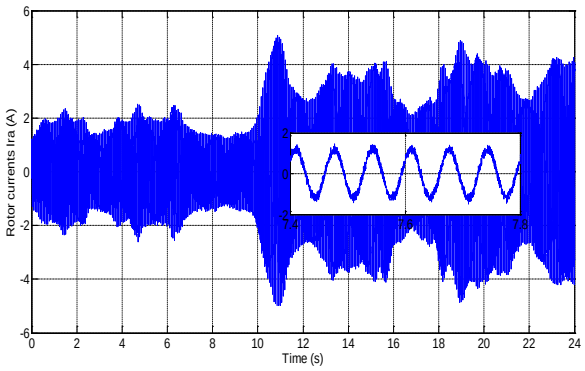
f) Direct rotor current Idr (C-DPC)



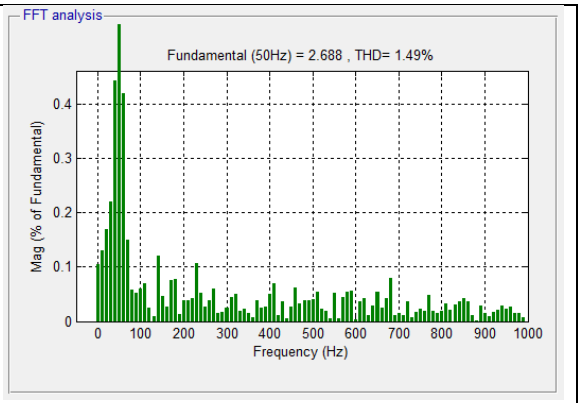
g) Quadrature rotor current Iqr (C-DPC)



h) Stator currents Isa (C-DPC)



i) Rotor current Ira (C-DPC



j) THD of Stator current Isa (C-DPC)

Figure 3.8 – Simulation results of C-DPC with variable wind profile

Figure 3.8a shows variable wind speed profile, simulating real profile in Assila-city, Morocco.

The active power Ps, as depicted in figure 3.8b, exhibits discernible oscillations while tracking the wind speed. The cause of these oscillations is the wind's quick changes in speed, which require the control system to make adjustments all the time, making the power supply unstable and inefficient.

Figure 3.8c shows reactive power Qs, which remains relatively stable despite the variable wind. This stability indicates effective voltage regulation by C-DPC, as reactive power is less affected by wind speed changes. Reference reactive power Qs_{ref} is imposed null to guarantee a power factor always close to 1.

The electromagnetic torque Te is shown in Figure 3.8d, and it exhibits noticeable oscillations. The source of these is the direct correlation between torque and wind speed, which puts mechanical stress on the powertrain as it constantly modifies to fit changing circumstances.

For the most part, the power factor (PF) (see figure 3.8e) stays close to unity, suggesting effective power transfer; but, it momentarily decreases during periods of wind speed variability, indicating transient problems with the quality of the power.

Figure 3.8f illustrates how the direct rotor current (Idr) is stable in spite of varying wind conditions, demonstrating how well C-DPC manages this parameter. In contrast, the quadrature rotor current (Iqr) (see figure 3.8g) shows notable oscillations, reflecting variations in wind speed and demonstrating the system's ongoing, if rather unstable, modifications to retain control. Figure 3.8h, the stator currents (Isa), show a sinusoidal waveform with discernible ripples, indicating current oscillations that may eventually affect power quality and raise thermal stress on electrical components. Overall, the direct rotor current is well controlled;

nevertheless, the real wind profile causes oscillations in the quadrature rotor current and stator currents, which compromise the stability and efficiency of the system.

The rotor current Ira exhibits notable fluctuations, as seen in Figure 3.8i, which are a result of the system's ongoing modifications to the fluctuating wind profile. These oscillations point to rotor current control instability, which can lead to mechanical and electrical stress and eventually lower system reliability.

The stator current Isa's THD, shown in Figure 3.8j, is 1.49%, which is within allowable bounds for power quality. Even though this THD is rather low, more decrease would enhance power quality and lower losses associated with harmonics. Due to wind fluctuation, the rotor current is unstable overall, while the stator current keeps its THD level within an acceptable range, balancing system performance and power quality.

		***Ps* (W)**	***Qs* (VAR)**
C-DPC	**Ripples**	150	210
	Overshoot	80	120
	SSE	60	85
	Response time	3.7 ms	3.05 ms

Table 3.6 – Response time, overshoot, and energy ripples in the second test (variable wind profile)

The results presented in Table 3.6 highlight the performance of the C-DPC system in terms of ripples, overshoot, steady-state error (SSE), and response time under a step wind profile. The system exhibits relatively fast response times for both active power Ps at 3.7 ms and reactive power Qs at 3.05 ms, indicating its ability to fast react to variations in wind conditions. However, this quick response comes at the cost of stability, as seen in the significant ripples and undulations (150 W for Ps and 210 VAR for Qs), suggesting that the control system struggles to maintain a smooth power output during transient conditions. The high overshoot values (80 W for Ps and 120 VAR for Qs) further illustrate the system's difficulty in handling sudden wind changes, as it allows power to spike above the desired setpoints before settling down.

Additionally, the steady-state error (SSE) remains considerable, particularly for reactive power, with an SSE of 85 VAR, indicating that the system fails to fully converge to the target reactive power value, even after reaching a steady state. The active power SSE, while lower at 60 W, still suggests room for improvement in accuracy. The combination of high ripples, overshoot, and SSE indicates that the system prioritizes speed over precision, potentially affecting the overall efficiency and quality of power delivered to the grid.

To address these issues, advanced control strategies such as ANN, fuzzy logic or sliding mode control could be introduced to reduce ripples and provide more stable control. Predictive control methods could also help anticipate wind changes and reduce overshoot, ensuring smoother transitions. Finally, improving the steady-state accuracy through adaptive control techniques would help minimize SSE, ensuring the system consistently reaches the desired power setpoints. Overall, while the C-DPC system demonstrates fast responsiveness, it would benefit from enhancements aimed at improving stability and control precision, particularly under dynamic wind conditions.

3.4. The design of the second-order sliding mode control (STSMC)

As is well known, the sliding mode control method is among the most popular, widespread, and robust nonlinear control methods. However, its main drawback is the presence of oscillations, known as chattering, [41], [50].

Several techniques have been proposed in the literature to minimize the chattering phenomenon. However, second-order sliding mode control (SOSMC) is considered one of the best alternatives to reduce chattering and increase robustness during the convergence phase towards the sliding surface [60]. The second-order sliding mode control variants, such as the "twisting algorithm," "suboptimal algorithm," and "super twisting algorithm" (STSMC), aim to apply a sliding mode involving the sliding surface and its time derivative in finite time [25], [61], [62]. In this chapter, we have chosen the super-twisting algorithm due to its advantages. Unlike the first two methods (the "twisting algorithm" and the "suboptimal algorithm"), the STSMC algorithm only uses the sliding surface and does not require the computation of its derivative.

This control law converges in finite time with a trajectory similar to that of the Twisting algorithm (Figure 3.9). The main advantages of this algorithm are the continuity of the control and the absence of the need for the derivative of SSS. This control is composed of an algebraic (non-dynamic) term and an integral term. Therefore, this algorithm can be considered a nonlinear generalization of a PI controller [63]. The Super-Twisting control law is composed of two parts. The first, U_1, is defined by its derivative with respect to time, while the second, U_2, is continuous and depends on the sliding variable. For a real sliding mode, the control law will be given by [63], [64]:

$$U = U_1(t) + U_2(t) \tag{3.9}$$

$$\overset{*}{U}_1(t) = \begin{cases} -U & if \quad |U| > U_M \\ -\alpha sat(S) & if \quad not \end{cases} \tag{3.10}$$

$$U_2 = \begin{cases} -\zeta |S_0|^{\delta} sat(S) & if \quad |U| > S_0 \\ -\zeta |S|^{\delta} sat(S) & if \quad not \end{cases} \tag{3.11}$$

Where S is the sliding surface.

To ensure the stability of the system, α, ζ , and δ must satisfy the following conditions [65]:

$$\begin{cases} \alpha > \dfrac{C_0}{K_m} & if \quad 0 < \delta < 0.5 \\ \zeta^2 > \dfrac{4C_0K_M(\alpha + C_0)}{K_m^3(\alpha - C_0)} & if \quad \delta = 0.5 \end{cases} \tag{3.12}$$

Where S_0, C_0, K_m, and K_M are positive constants.

If $S_0 = \infty$, a simplified version of the STSMC algorithm will be given by [65]:

$$\begin{cases} U = -\zeta |S|^{\delta} .sat(S) + U_1 \\ \overset{*}{U}_1 = -\alpha .sat(S) \end{cases} \tag{3.13}$$

There are other functions that can replace the sign function, such as the sat function and the smooth function [66], [67].

We take $\delta = 0.5$ in our case, and we set $\alpha_1 = \alpha$ and $\alpha_2 = \zeta$.

The STSMC algorithm then becomes:

$$U = \alpha_1 |S|^{0.5} .sat(S) + \int \alpha_2 .sat(S) \tag{3.14}$$

Equations (3.9) to (3.13) represent the classical STSMC controller, and Figure 3.9 shows the structure of this controller.

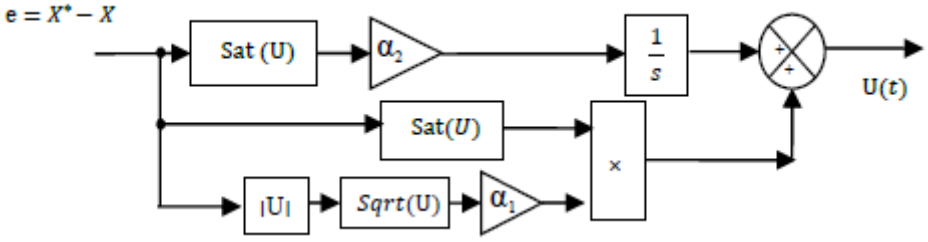


Figure 3.9 – Super-Twisting Sliding Mode controller design

3.4.1. Application of the STSMC control

To address the chattering problem observed in power and current with C-DPC control, we propose a modification to the control strategy. The newly designed control, represented by the STSMC-DPC-PWM technique, aims to reduce power fluctuations, minimize THD, and enhance system robustness. Unlike the conventional DPC technique, this approach utilizes nonlinear control by replacing the two hysteresis comparators with two STSMC techniques to obtain the voltage reference values. Additionally, the PWM technique is used in place of the switching table to regulate the RSC operation of the DFIG. The system operates with a two-level RSC, simplifying both the system and the experimental work. This strategy is applied exclusively to the RSC, while the GSC is considered an uncontrolled inverter to further simplify design and implementation. As a result, this proposed system offers simplicity, ease of embedded application, low cost, and high robustness, making it highly practical [100, 101].

Figure 3.10 represents the command applied to this study to lower energy fluctuations and improve the system's dynamic performance. In addition, this control scheme is to be implemented on a 1.5 kW DFIG. This command strategy is distinguished by robustness because of the use of the STC technique, as this controller is flexible for adjusting and is not a part of the mathematical DFIG model-based wind turbine system [100].

This control has similarities in using the same references (Ps^* and Qs^*) and the same estimation formulas, estimating the *Qs* and *Ps* to calculate the power errors. In this proposed strategy, the MPPT technique is also employed to determine the active power reference for Ps. Thus, the Ps value closely changes with the change in WS, which makes the system provide maximum power. Also, both torque and current eventually take the shape of a change in WS because *Ps* is associated with both current and torque where torque and current can be calculated from *Ps*. On the other hand, the reactive power reference for *Qs* is set at 0 VAR because in the industrial field, to operate devices, *Ps* is used, not *Qs*. Therefore, the proposed system generates *Ps* only, without *Qs*. Also, determining the power error helps to determine the voltage references. These errors are exploited as input signals to the STC controllers used in the control. To estimate the energies, the flux must be calculated according to the following formulas [2, 3]:

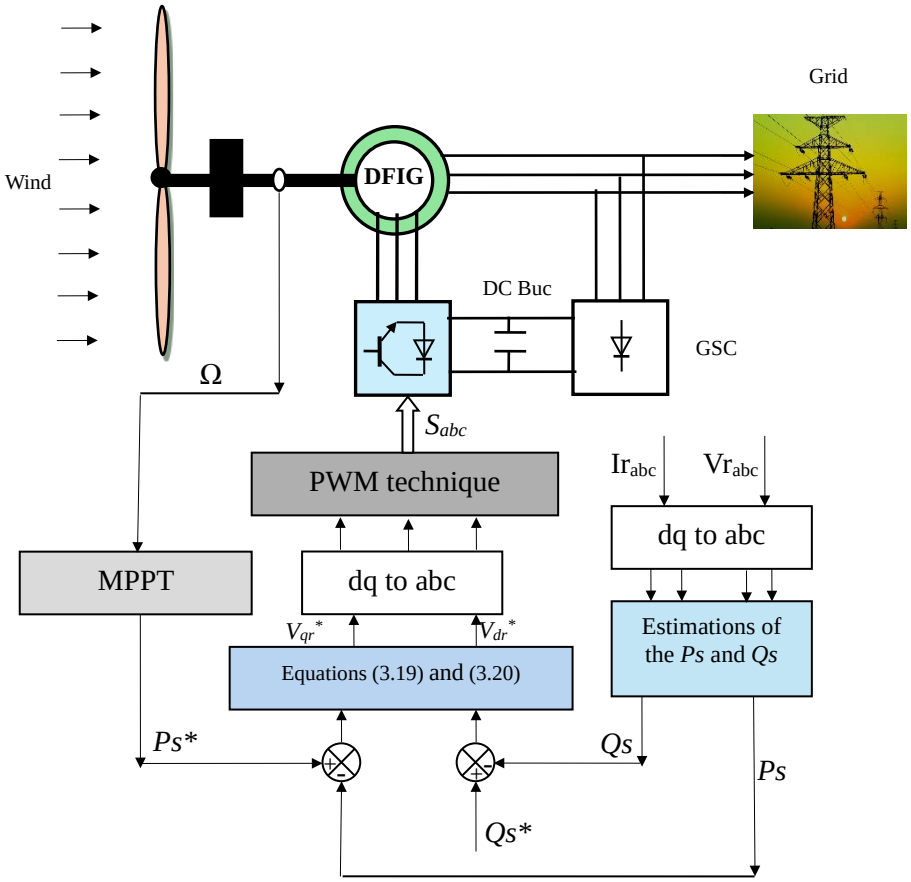


Figure 3.10 – STSMC- DPC-PWM technique of DFIG-WT.

The proposed strategy aims at determining the voltage references using the STC technique depending on the values of the capacity's errors [68].

As it is known, the STC technique or super-twisting algorithm (STSMC) is a non-linear technique distinguished by its simplicity and high potential for enhancing robustness, as this technique were used in several scientific articles [66[,[68]. In [69], the STSMC technique was developed to promote the control features of the DTC technique of DFIG, using a controller for torque and flux control. Also, a the PWM technique generates the pulses for controlling the inverter operation. The performances were compared with the traditional control, which was satisfactory when using the STSMC technique compared to the classical control.

According to work [69], the STC technique can be expressed by Equation (2.17) [97]:

$$u(t) = \alpha_2 \int sat(e(t)) + \alpha_1 \sqrt{|e(t)|}.sat(e(t)) \tag{3.17}$$

where e(t) defines the error (e = X*-X).

Through this equation, STSMC technique is simple and contains two parameters to adjust the response.

To apply STC technique to DFIG, errors must be identified. Two errors are defined: the *Qs*-error and *Ps-e*rror. These errors are described by Equation (2.18) [10].

$$\begin{cases} e_{Qs} = Q_s^* - Q_s \\ e_{Ps} = P_s^* - P_s \end{cases} \tag{3.18}$$

The quadrature rotor voltage reference (V_{qr}^*) is associated with the error of the *Ps*, for the calculation of which Equation (3.19) is used. Thus, the value of this voltage (V_{qr}^*) is related to a change in the WS, as it increases and decreases with the increase and decrease in the WS. The value of the current (I_{qr}^*) corresponding to this voltage also changes based on a change in the WS.

Direct rotor voltage reference (V_{dr}^*) is associated with the *Qs* error and then is calculated according to Equation (3.20). Therefore, the value of this voltage (V_{dr}^*) is almost non-existent because the reference value for the *Qs* is set at 0 VAR, and therefore the corresponding current value (I_{dr}^*) is also set at 0 [87].

$$V_{qr}^* = \alpha_1 \sqrt{\left|e_{Ps}(t)\right|}.sat(e_{Ps}(t)) + \alpha_2 \int sat(e_{Ps}(t)) \tag{3.19}$$

$$V_{dr}^* = \alpha_3 \sqrt{\left|e_{Qs}(t)\right|}.sat(e_{Qs}(t)) + \alpha_4 \int sat(e_{Qs}(t)) \tag{3.20}$$

where, α_1, α_2, α_3, and α_4 are the gains. Using these four gains, the dynamic response of powers can be controlled. Therefore, it is necessary to choose these gains correctly, as the experimentation method can be used to find these gains. Moreover, smart optimization strategies such as genetic algorithms and gray wolf optimization can be used to optimally tune these gains [98].

The Equations (3.19) and (3.20) can be exhibited in Figure 3.11 to clarify and simplify the idea of the suggested work. Remarkable characteristics such as the ease of completion and command of response are highlighted and compared to some commands such as the BC technique [99].

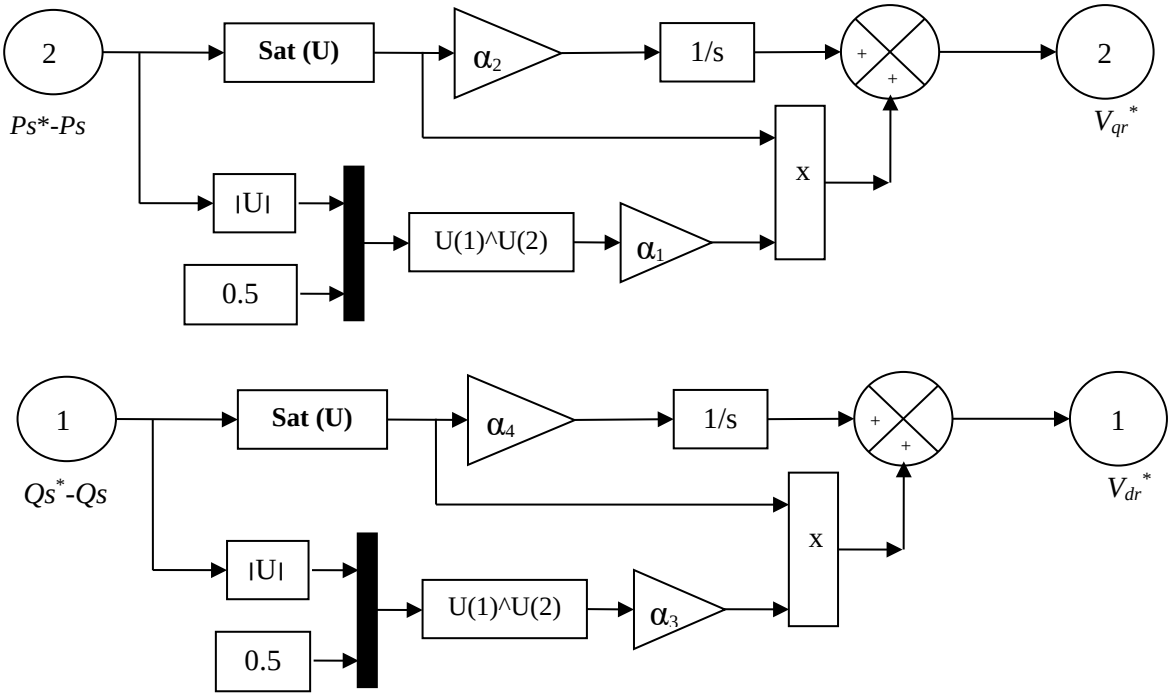


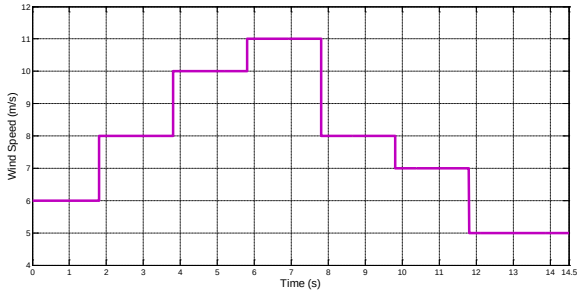
Figure 3.11 – STSMC Controllers of *Ps* and *Qs* powers

3.5. Simulations results

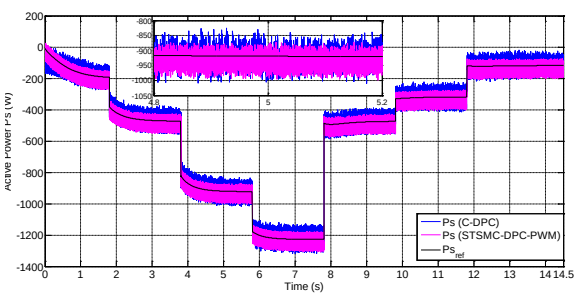
This section studies and analyzes the simulation results between the C-DPC technique and the STSMC-DPC-PWM technique of DFIG. The effectiveness analysis is further investigated with *Ps*, THD of current, torque and *Qs*. The DFIG specifications conducted in this case study are in the appendix A.

3.4.2. First test (Step wind profile)

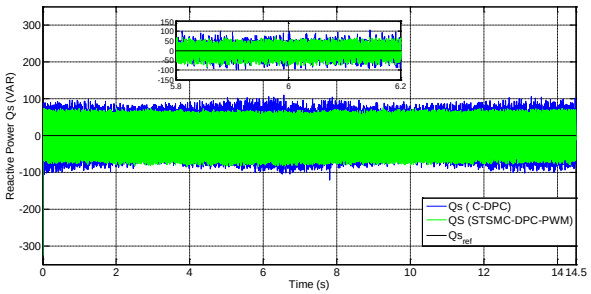
Characteristics of the proposed STSMC-DPC-PWM and traditional DPC strategies are examined in WSs' steps (Figure 3.12a). The graphical results of this test are shown in Figure 3.12. On the other hand, the numerical results of this test are also presented in Table 3.6.



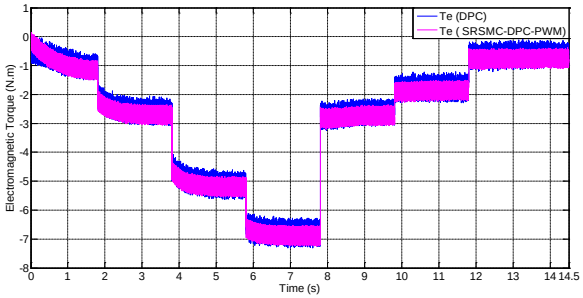
a) Wind speed profile



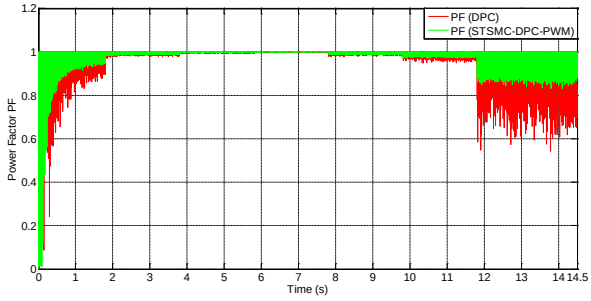
b) Active power Ps



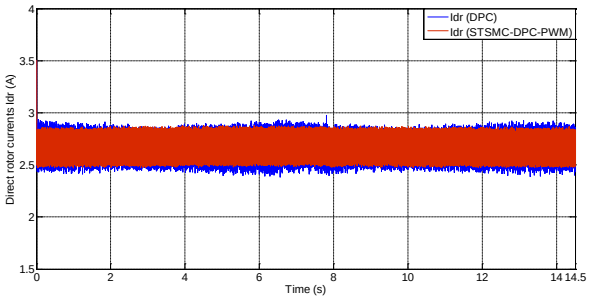
c) Reactive power Qs



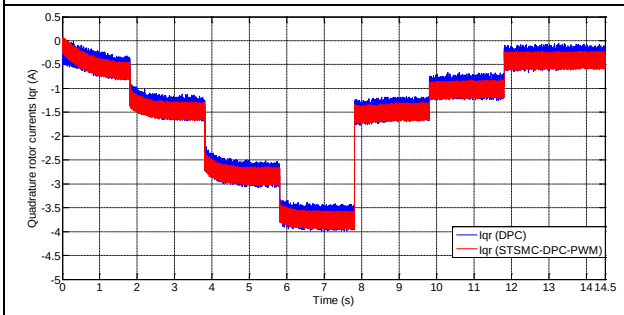
d) Electromagnetic torque Te



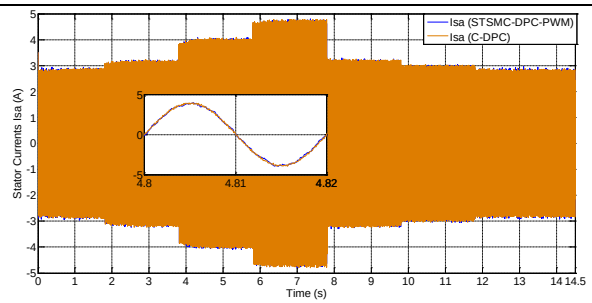
e) Power factor PF



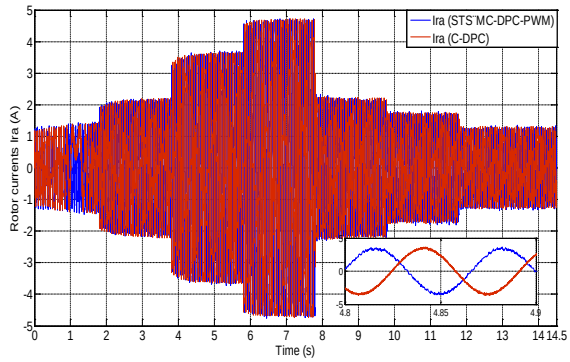
f) Direct rotor current Idr



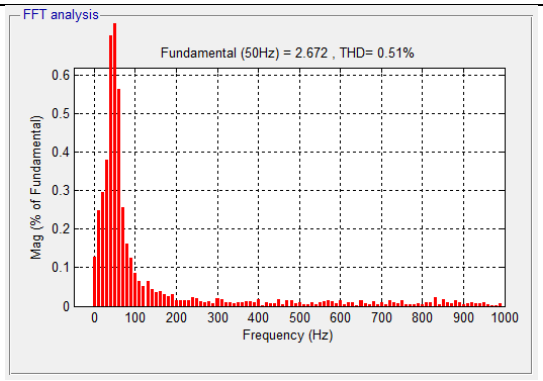
g) Quadrature rotor current Iqr



h) Stator currents Isa



i) Rotor current Ira



j) THD of Stator current Isa (STSMC-DPC-PWM)

Figure 3.12 – Simulations results of C-DPC and STSMC-DPC-PWM

		***Ps* (W)**	***Qs* (VAR)**
DPC	**Ripples**	180	200
	Overshoot	95	115
	SSE	100	70
	Response time	3.5 ms	2.9 ms
STSMC-DPC-PWM	**Ripples**	100	110
	Overshoot	45	50
	SSE	36	30
	Response time	2.65 ms	2.3 ms
Improvement ratios	**Ripples**	44.44%	45%
	Overshoot	52.63%	56.52%
	SSE	64%	57.14%
	Response time	24.29%	20.69%

Table 3.7 – Improvement ratios and SSE, response time, overshoot, and energy ripples in the first test (step wind profile)

The powers are compelled to track the references well, as shown in Figures 3.12b and 3.12c, where the *Ps* has the same change of WS since it rises and lowers with the variations of the WS. Nevertheless, the *Qs* stays unchanged even when the WS changes. Moreover, it has been found that large ripples exist in Ps and *Qs*, and these ripples are more enormous in the classical DPC than the proposed STSMC-DPC-PWM. An important implication of these findings is that new control reduces ripples a little. More specifically, the current and torque vary based on a variation in the *Ps* with ripples in both controls.

The stator currents of the THD with the novel strategy is 0.51%. Therefore, the proposed STSMC-DPC-PWM drastically curtailed the THD value in contrast to the traditional DPC. As this reduction was assessed at 3,77%, it implies that the current quality is much higher in the proposed STSMC-DPC-PWM than the classical DPC. In addition, with fundamental frequency

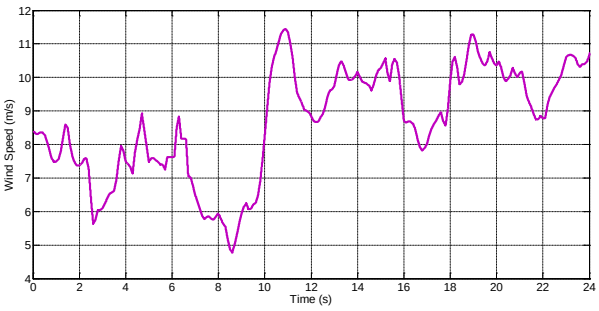
signal (50 Hz), the amplitude of current was 2.735 A and 2.672 A for CDPC and STSMC-DPC-PWM techniques, respectively. Based on these two values, it is noted that the proposed and STSMC-DPC-PWM supplied a good currents quality than the C-DPC. This indicates that the proposed and STSMC-DPC-PWM strategy outperformed the traditional DPC in enhancing the characteristics of the studied energy system.

Table 3.6 shows the numerical results of the third test, and it shows the performance characteristics such as response time, ripples, SSE and overshoot of DFIG performance. From this table, observably, the utilization of the proposed STSMC-DPC-PWM strategy resulted in satisfactory ripples, SSE and overshoot of DFIG performance in contrast to the traditional DPC and the calculated reduction ratios ensures this. For example, unlike the traditional DPC strategy, with STSMC-DPC-PWM, the ripples of *Ps* and *Qs* were lowered by about 44.44 % and 45 %, respectively. The overshoot also was assessed by about 52.63 % and 56.52 % for *Ps* and *Qs*, respectively, in contrast to the traditional DPC. Furthermore, the SSE of power was reduced by about 64 % and 57.14 % for *Ps* and *Qs*, respectively, in contrast to the traditional DPC. However, the STSMC-DPC-PWM led to a longer response time than the traditional DPC. In the other hand, the latter considerably reduced the response time for power by around 24.29% and 57.14% for Ps and Qs, respectively, unlike STSMC-DPC-PWM. This strong point gives our system remarkable rapidity and helps us to take better advantage of wind speeds.

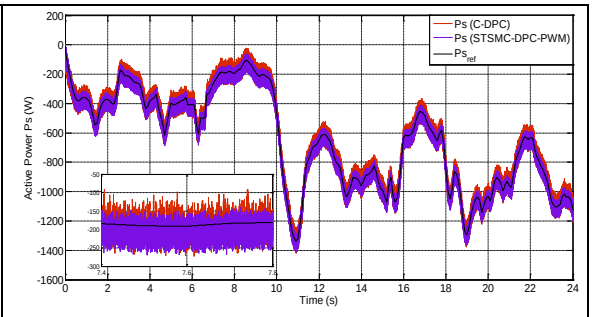
3.4.3. Second test (Variable wind profile)

In this test, the STSMC-DPC-PWM technique is examined in variable WS, using the wind shape in Figure 3.13a. Then, the results are clearly illustrated in Figure 3.13. Powers are compelled to track the references well even in the presence of ripples (Figures 3.13b and 3.13c). Also, *Ps* varies according to a change in WS, while *Qs* remain unchanged with WS. The *Qs* become nil over the simulation period. Torque and current are also displayed in Figures 3.13. It is noted that the torque and current vary significantly with respect to variations in the *Ps*, with ripples in both controls. In Table 3.6, the ripples, overshoot, and SSE are recorded. This table proves that the STSMC-DPC-PWM technique achieves much better results than the DPC technique in many specifications such as overshoot value, SSE and ripples, and minimization ratios prove this, where the proposed STSMC-DPC-PWM strategy both *Ps* and *Qs* reduced ripples by about 36.67 % and 33.33%, respectively in contrast to the traditional DPC strategy. Furthermore, the overshoot value of *Ps* and *Qs* was curtailed by about 37.5 % and 41.67 %, respectively, in contrast to the traditional DPC. Additionally, the STSMC-DPC-PWM provided

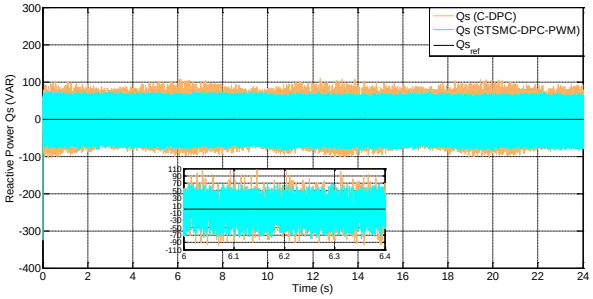
good values for the SSE value of *Ps* and *Qs*, as evidenced by the estimated reduction ratios of 55 % and 35.29 % for *Ps* and *Qs*, respectively, compared to the traditional DPC. The latter ensured satisfactory performance in response time to power compared to the proposed STSMC-DPC-PWM, as the reduction rates for both *Ps* and *Qs* were estimated at 43.38% and 87%, respectively, in contrast to the proposed STSMC-DPC-PWM. Therefore, the response time represent the downside of the proposed STSMC-DPC-PWM, which can be overcome by using other techniques. Notably, the THD is lower when the STSMC-DPC-PWM technique is employed, in contrast to the DPC technique (Figures 313e and 3.13f), where the THD value was 1.24% when using the traditional DPC strategy, while the THD was 0.25% using the proposed STSMC-DPC-PWM technique. Hence, STSMC-DPC-PWM technique minimized the THD value by 79.83% better than the performed DPC technique. Conversely, it is observed from Figures 5e and 5f that the fundamental frequency signal (50 Hz) for a current has the same amplitude value in both controls. This is upside for the proposed STSMC-DPC-PWM technique.



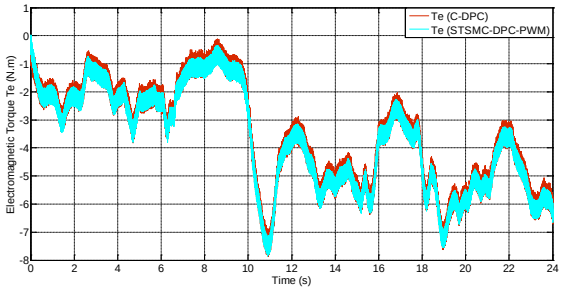
a)Wind speed profile



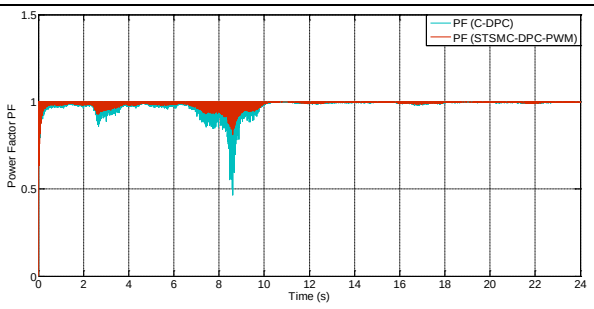
b)Active power Ps

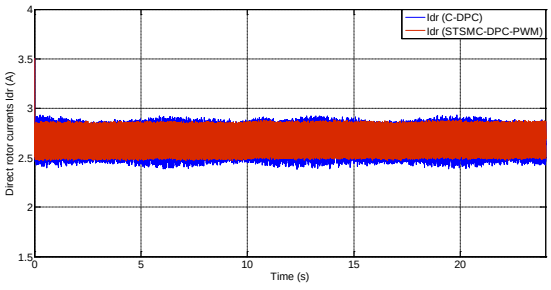


c)Reactive power Qs



d)Electromagnetic torque Te





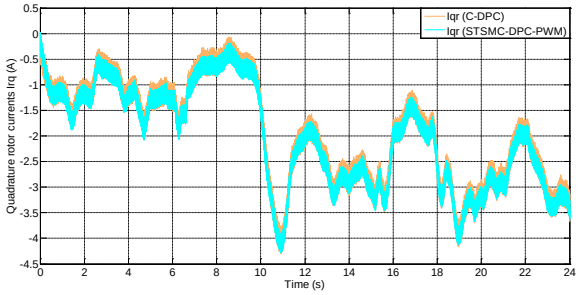
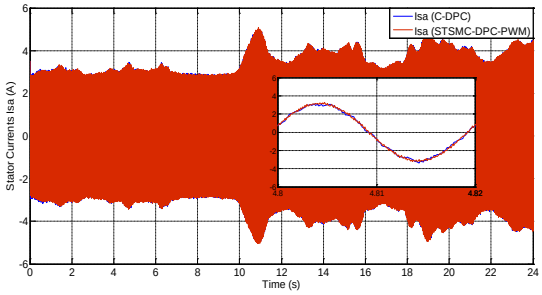
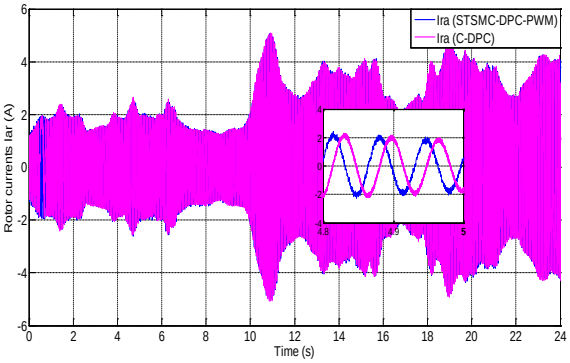
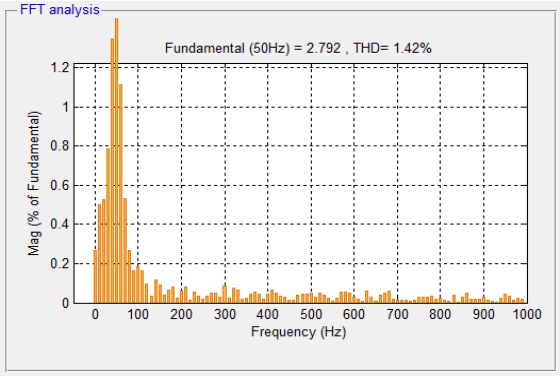
e)Power factor PF	f)Direct rotor current Idr
	
g)Quadrature rotor current Iqr	h)Stator currents Isa
	
i) Rotor current Ira	j) THD of Stator current Isa (STSMC-DPC-PWM)

Figure 3.13 – Simulations results of C-DPC and STSMC-DPC-PWM

		***Ps* (W)**	***Qs* (VAR)**
C-DPC	**Ripples**	150	210
	Overshoot	80	120
	SSE	60	85
	Response time	3.7 ms	3.05 ms
STSMC-DPC-PWM	**Ripples**	95	140
	Overshoot	50	70
	SSE	27	55
	Response time	3.1 ms	2.85 ms
Improvement ratios	**Ripples**	36.67%	33.33%
	Overshoot	37.5%	41.67%
	SSE	55%	35.29%
	Response time	16.22%	6.56%

Table 3.8 – Improvement ratios and SSE, response time, overshoot, and energy ripples in the second test (variable wind profile)

The results in Table 3.8 compare the performance of the C-DPC and STSMC-DPC-PWM control strategies under a variable wind profile (second test) by examining ripples, overshoot, SSE, and response time for both active power (Ps) and reactive power (Qs). The STSMC-DPC-PWM method demonstrates clear improvements across all metrics. Ripples are reduced by 36.67% for Ps and 33.33% for Qs, showing a more stable power output compared to the C-DPC

method. Overshoot sees significant reductions, with 37.5% for Ps and 41.67% for Qs, indicating that the system manages power deviations more effectively. The SSE values are also significantly lower, improving by 55% for Ps and 35.29% for Qs, which highlights better accuracy in reaching the desired power levels. Response times are slightly faster with a 16.22% improvement for Ps and 6.56% for Qs, making the STSMC-DPC-PWM quicker in adapting to wind changes. Overall, the STSMC-DPC-PWM outperforms the traditional C-DPC method in terms of stability, accuracy, and response speed, making it a superior choice for handling variable wind conditions.

3.6. Summary

This chapter describes the classical DPC control and its improvement through the super-twisting sliding mode algorithm to control the RSC of the DFIG. Maximum power extraction is ensured by the MPPT control, which is based on regulating the rotational speed of the turbine. The c-DPC is based on two hysteresis controllers and a switching table to control the rotor-side converter and regulate the active and reactive powers injected into the grid. In contrast, for the STSMC-DPC-PWM technique, we have replaced the switching table with PWM control and the two hysteresis comparators with two STSMC controllers."

The simulation results confirm the good performance of the STSMC-DPC-PWM control in terms of dynamic response and reduction of current and active and reactive power ripples injected into the grid.

The results obtained can be summarized as follows:

- Both control techniques ensure good tracking and dynamic response.
- The STSMC-DPC-PWM control has minimized power and current ripples compared to C-DDPC.

Despite these encouraging results, the chattering phenomenon still persists, and the THD level is somewhat high.

Chapter 4: Fuzzy Super-Twisting Sliding Control-Based Direct Power Control of Doubly Fed Induction Generators.

4.1. Introduction

This chapter proposes a novel method for controlling variable-speed wind turbines based on DFIG in order to minimize the chattering phenomena. The Fuzzy Super-Twisting Sliding Mode Control strategy is used to regulate the power supplied by the DFIG and achieve predetermined control objectives. This technique is characterized by high performance and does not depend on DFIG parameters, making it more efficient than direct power control (DPC) in durability testing [89].

This controller based on the consolidation of the Fuzzy Logic (FL) and the STA is designed to reduce the power ripple and ameliorate the supplied currents and generated power quality of a DFIG controlled by the DPC technique. The FSTSMC is an innovative nonlinear control technique based on the characteristics and advantages of both the FL and the STSMC with robustness and simplicity of control being among the most prominent characteristics of this strategy. The proposed DPC strategy uses two FSTSMC controllers and a PWM to generate control pulses. The results are then benchmarked with the C-DPC method results in the current THD and ripple minimization. Additionally, the response time, overshoot and steady-state error (SSE) of the DFIG power are calculated. The designed technique ensures excellent performance in contrast to the hysteresis comparator-based controller [91].

The objectives achieved are as follows:

- Realization the DPC-FSTA strategy for a DFIG.
- The difficulties of the C-DPC method are overcome.
- The quality of power and current is increased.
- The THD of supplied currents is significantly underestimated.
- The overshoot and SSE of DFIG output is reduced.

The simulation results and control efficiency of the FSTSMC-DPC-PWM confirm the improvement of the system features. In contrast to the C-DPC approach, the FSTSMC-DPC-PWM minimizes the current harmonics by 84.45% and 84.17% for the first (step wind profile) and second tests (variable wind profile), respectively. Additionally, it improved the overshoot of the reactive and active power in the second test by 90.20% and 77.14%, respectively. The experimental results prove and demonstrate the excellent performance and efficiency of the FSTSMC-DPC-PWM.

4.2.Proposed FSTSMC controller

The FSTSMC-DPC-PWM technique combines two different controls, where both STSMC and FL are used to obtain a strategy best featured by its resilient performance. The FL technique is a nonlinear control method which relies heavily on experience and is best featured above all by its robust performance in the face of uncertainties. For this purpose, a suitable solution for the proposed integration process is found. However, STSM is a nonlinear control based on the sliding mode design, as it is unrelated to the system's mathematical structure, making it perform satisfactorily. The drawback of the STSMC technique is that using the sat(u) function leads to chattering, which causes several challenges in the system, such as significant energy fluctuations and poor power quality [90].

Equation (4.1) expresses the mathematical model for the STA technique [95].

$$\begin{cases} u = \lambda_1 |\varepsilon|^r \text{sat}\,(\varepsilon) + u_1 \\ \frac{du_1}{dt} = \lambda_2 \text{sat}\,(\varepsilon) \end{cases} \tag{4.1}$$

where r represents the exponent defined for the STA technique, ε is the linear surface, and λ1 and λ2 are positive values [93].

The FSTSMC is, in short, a variation of the STSMC technique, in which the FL technique is employed to compensate for the sign(u) function to overcome defects and increase performance. Using the FL technique will give the STSMC strategy a new advantage of high durability and outstanding performance, especially if the system parameters change. Equation (4.2) expresses the FSTSMC control proposed in this work [96].

$$u(t) = \lambda_1 (|\varepsilon|)^r \times (\text{Fuzzy}(\varepsilon)) + \lambda_2 \int \big(\text{Fuzzy}(\varepsilon)\big).\, dt \tag{4.2}$$

Equation (4.2) is the mathematical control model for the studied system to overcome the defects of DPC. Equation (4.2) is obtained based on changing Equation (4.1) by adding the FL technique. The resulting control has a high endurance level and can increase system efficacy. In addition, this control is defined by the flexibility of the embedded application and easiness in which it is robust to uncertainties and supporting priority when malfunction in the system exists [100].

This proposed strategy is heavily based on experience to improve the system's properties, as choosing the FL rules requires experience. Therefore, the quantity of rules is chosen to obtain better results and an acceptable dynamic speed. As is well knowledge, in the FL technique, the larger the number of rules is, the superior the results, but there is a negative effect when a more

quantity of rules is used. This negative characteristic represents a slowdown in the system's dynamic response, which is undesirable. Therefore, an appropriate quantity of these rules is precisely chosen to ameliorate the results. Figure 5.1 shows the effectiveness of DFIG DPC based on the proposed control [104].

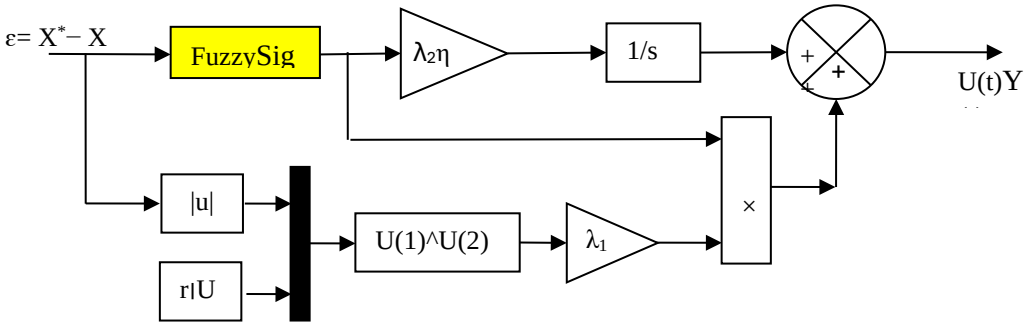
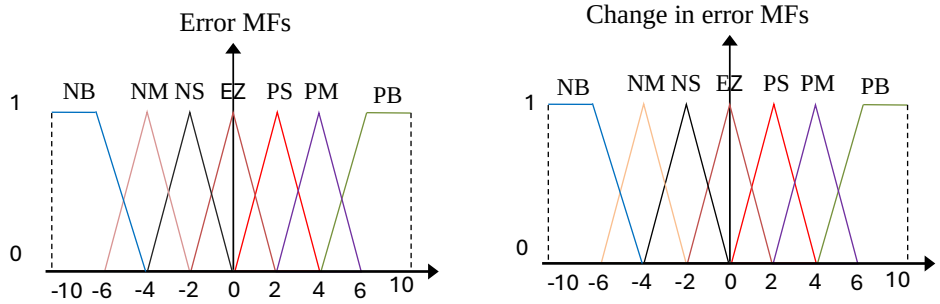


Figure 4.1 - Designed FSTSMC technique.

The Mamdani-type FL technique with 49 rules was chosen, and the membership functions (MFs) shown in Figure 4.2 were used for this purpose. The rules used for this purpose give a good dynamic response, as they do not slow the system, which is very good. The rules used are shown in Table 4.1 [37], where two inputs, ε and Δε, and only one output are used. Therefore, three coefficients are utilized for to adapting and enhancing the FL technique performance [102].

ε / **Δε**	**NB**	**NM**	**NS**	**EZ**	**PS**	**PM**	**PB**
PB	EZ	PS	PM	PB	PB	PB	PB
EZ	NB	NM	NS	EZ	PS	PM	PB
NM	NB	NB	NB	NM	NS	EZ	PS
NB	NB	NB	NB	NB	NM	NS	EZ
PM	NS	EZ	PS	PM	PB	PB	PB
PS	NM	NS	EZ	PS	PM	PB	PB
NS	NB	NB	NM	NS	EZ	PS	PM

Table 4.1. Fuzzy rules



a) Error (ε) **b)** Change in error (Δε)

Figure 4.2 - MFs for inputs.

Figure 5.3 shows the internal structure of the FL technique to overcome the disadvantages of STA, in which three coefficients are engaged to change the response to obtain satisfactory results. The rules are used according to the following relationship [103]:

If (ε is NG) and (Δε is NG), then (output is NG)

If (ε is NM) and (Δε is NP), then (output is NM)

The fuzzy logic implementation has the following characteristics: the OR operator uses the MAX method, the AND operator uses the MIN method, the FIS type is the Mamdani method, the defuzzification operation uses the centroid method, the implication operation uses the MIN method, and the aggregation operation uses the MAX method [78].

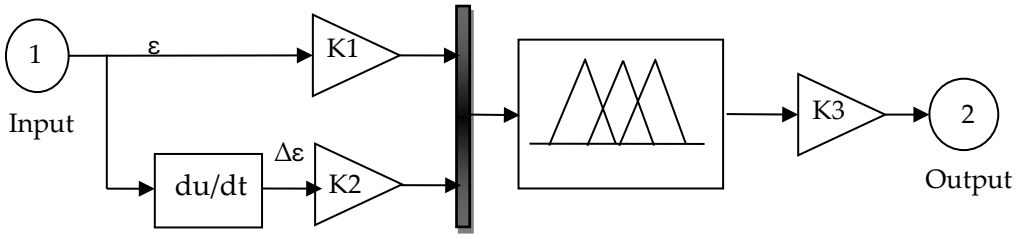


Figure 4.3 - Structure of the FL technique.

Grey wolf optimization (GWO) and genetic algorithms (GA) are two artificial intelligence tactics that are effective in maximizing the benefits of fuzzy logic (FL) control methods. These algorithms find the ideal set of controller parameters that improve system performance by sifting through a large number of possible solutions. Genetic algorithms are able to evolve a collection of solutions through multiple iterations, improving each time based on fitness criteria since they imitate the process of natural selection. Grey wolf optimization is another efficient technique that rapidly approaches optimal solutions. It is modeled after the social hierarchy and hunting habits of grey wolves [99].

Since these techniques may automate the tuning process and produce good results more quickly than manual tuning, they are very helpful in figuring out the proper gains for FL controllers [98].

To fine-tune these control coefficients, comprehensive simulations and experience-based knowledge can be applied in addition to AI-based methodologies. The algorithm can determine which coefficients provide the best overall performance by executing a variety of scenarios with varying operating circumstances and disturbances. These ideal coefficients are those that offer the best control over energy fluctuations, quicker reaction times, and a decrease in total

harmonic distortion (THD), all of which are essential for preserving system stability and power quality [99].

The fuzzy super-twisting sliding mode controller (FSTSMC), a controller constructed with these targeted gains, is described as a potential solution in the next section. This controller greatly improves the system's robustness while simultaneously addressing the problem of energy fluctuations. FSTSMC is a reliable option for enhancing system performance under a range of operating situations since it is particularly good at addressing the non-linearities and inherent uncertainties in power systems. The system can achieve greater stability, fewer ripple effects, and enhanced overall efficiency by combining the flexibility of FSTSMC with the accuracy of AI-optimized gains. This makes the system an appealing option for sophisticated control applications [88, 89, 90, 91].

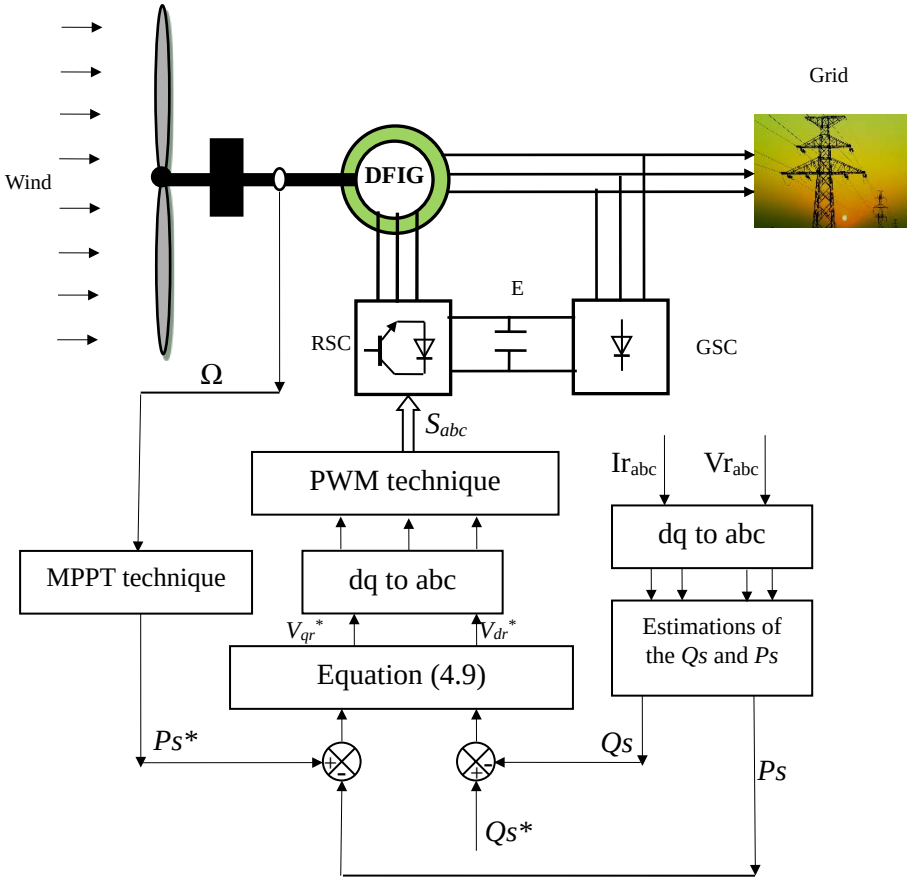


Figure 4.4 - FSTSMC-DPC-PWM technique for a DFIG.

As can be seen from Figure 4.4, this technique has been implemented only to the RSC, whereas a GSC with an uncontrolled inverter was used to facilitate the system complication and demonstrate the efficiency and performance of the FSTSMC-DPC-PWM in enhancing system features such as power fluctuations and THD value.

The FSTSMC-DPC-PWM uses rotor flux estimation, where current and voltage are measured. Equation (4.3) therefore demonstrates the value of the flux components [98, 99].

$$\begin{cases}\Psi_{r\alpha} = \int_0^t (V_r - R_r \times i_{r\alpha})dt \\ \Psi_{r\beta} = \int_0^t (V_r - R_r \times i_{r\beta})dt\end{cases} \tag{4.3}$$

The following Equation (4.4), which utilizes the flux components, is used to determine the absolute value of the rotor flux for this purpose [98].

$$|\Psi_r| = \sqrt{\left(\Psi_{r\beta}^2 + \Psi_{r\alpha}^2\right)} \tag{4.4}$$

The rotor flux can be found using the voltage according to Equation (4.5), where the greater the voltage is, the greater the rotor flux amount [99].

$$\Psi_r = \frac{V_r}{w_r} \tag{4.5}$$

Using Equations (4.6) and (4.7) along with using the former formulas determine DFIG performance. The performance estimation is essential for determining the error in the DFIG power [21, 95].

$$P_s = -\frac{3 \times V_s \times L_m}{2 \times \sigma \times L_s \times L_r} \Psi_{r\beta} \tag{4.6}$$

$$Q_s = \frac{3}{2}\left(-\frac{V_s}{\sigma \times L_s} \Psi_{r\beta} + \frac{V_s \times L_m}{\sigma \times L_s \times L_r} \Psi_{r\alpha}\right) \tag{4.7}$$

From Equations (4.6) and (4.7), the power error is calculated according to Equation (5.8). The latter is necessary to determine the robustness of the command, as the larger the error in the capabilities is, the lower the performance of the control, and vice versa [10].

$$\begin{cases}\varepsilon_{rea} = Q_s^* - Q_s \\ \varepsilon_{act} = P_s^* - P_s\end{cases} \tag{4.8}$$

The voltage references are determined by the FSTA controller based on the power error and these references are computed for the operation of the inverter. The outputs of the FSTSMC-DPC-PWM controllers are the main references for the voltage components, and these components are determined according to Equation (4.9) [98]:

$$\begin{cases}{V_{dr}}^* = \lambda_1 (|\varepsilon_{rea}|)^r \times (\text{Fuzzy}(\varepsilon_{rea})) + \lambda_2 \int \left(\text{Fuzzy}(\varepsilon_{rea})\right).\, dt \\ {V_{qr}}^* = \lambda_1 (|\varepsilon_{act}|)^r \times (\text{Fuzzy}(\varepsilon_{act})) + \lambda_2 \int \left(\text{Fuzzy}(\varepsilon_{act})\right).\, dt\end{cases} \tag{4.9}$$

Figure 4.5 depicts the controllers proposed in Equation (4.9), where the reference values are calculated using the FSTSMC-DPC-PWM controllers. According to this form, one FL-type controller is used for both types of DFIG power. However, the number of parameters in each controller is six; therefore, the total number of parameters is 12. Therefore, the negative impact of this control can be determined by assessing the number of parameters and their adjustment and calculation, as artificial intelligence strategies, such as particle swarm algorithm and genetic algorithms optimization, can facilitate the determination of these values [99].

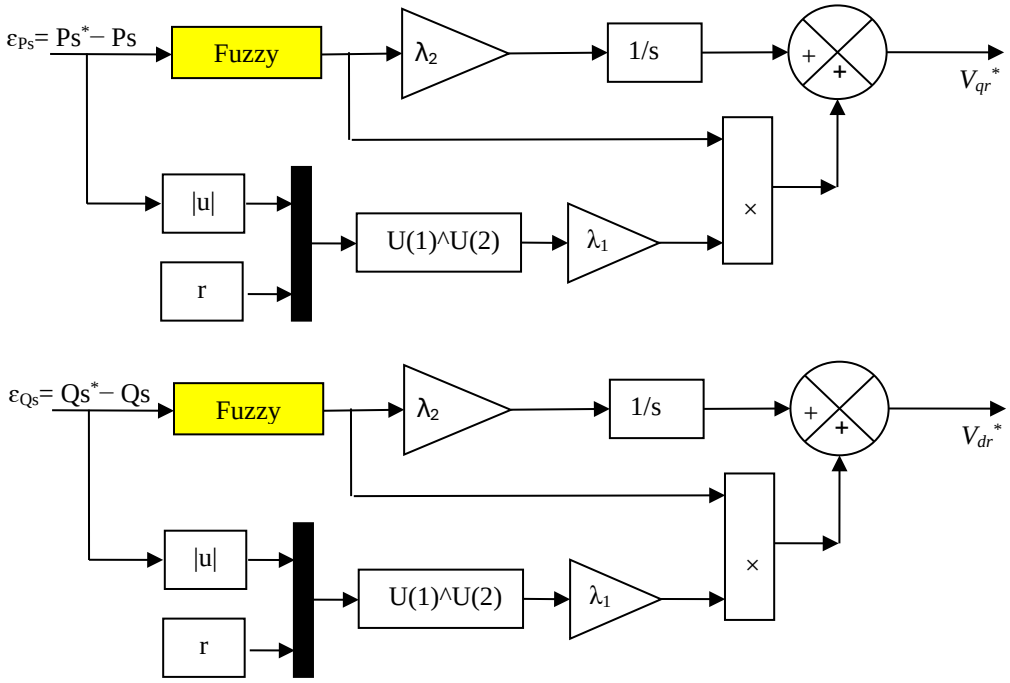


Figure 4.5 - Active and reactive powers FSTSMC-DPC-PWM controllers

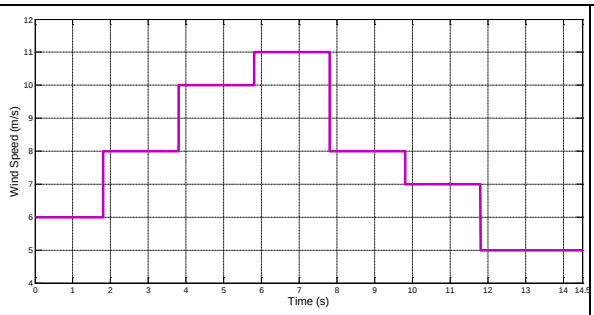
4.3. Simulation Results

In this section, the simulation results attained using Matlab/Simulink 2021b platform are given, and the results of both the C-DPC and the FSTSMC-DPC-PWM techniques are compared. Two tests are proposed that differ in terms of using the wind speed profile change to analyze the performance of the controls used in this work.

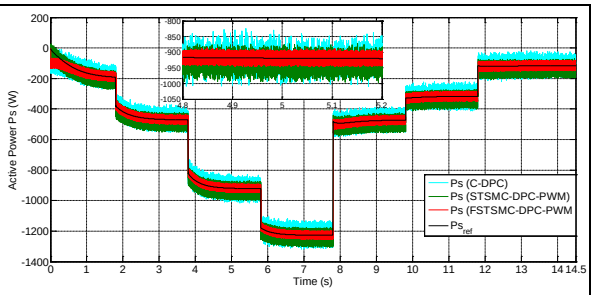
4.3.1. Step wind speed test

In In this first experiment, the wind speed shown in Figure 4.6a is used to assess how well the suggested strategy performs. Figures 4.6 display the graphical results.

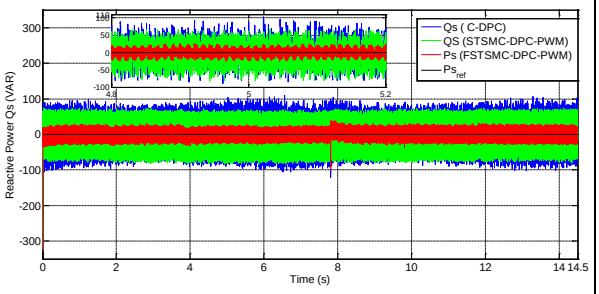
.



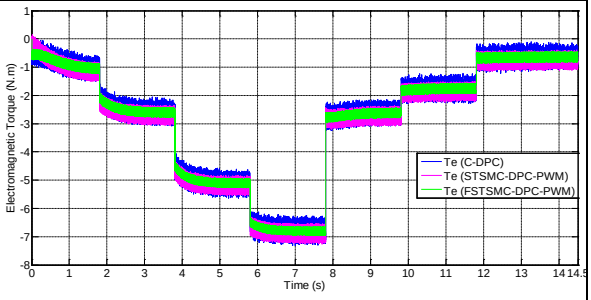
a) Wind speed profile



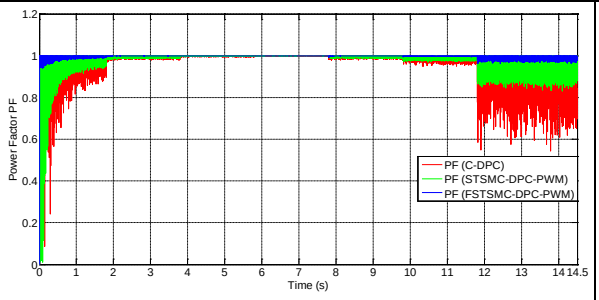
b) Active power Ps



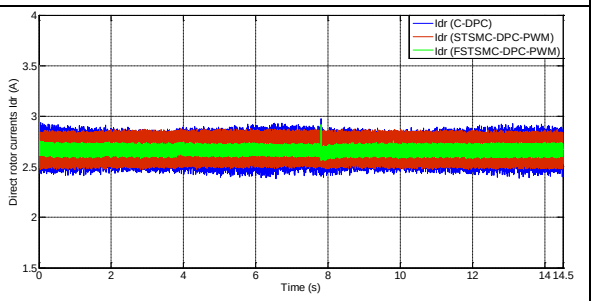
c) Reactive power Qs



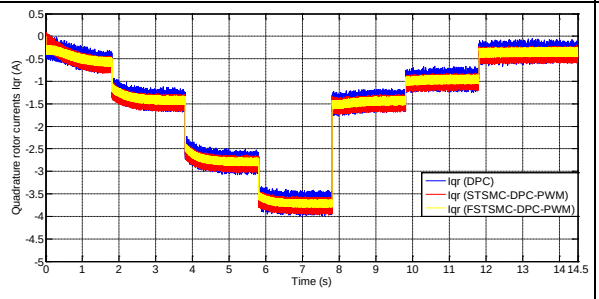
d) Electromagnetic torque Te



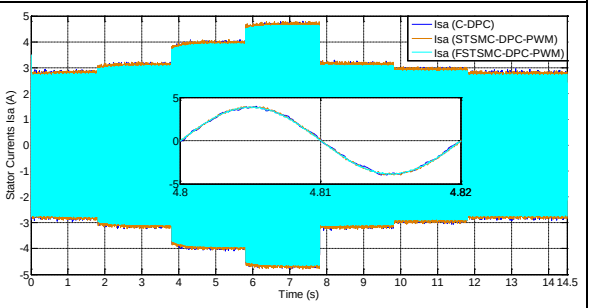
e) Power factor PF



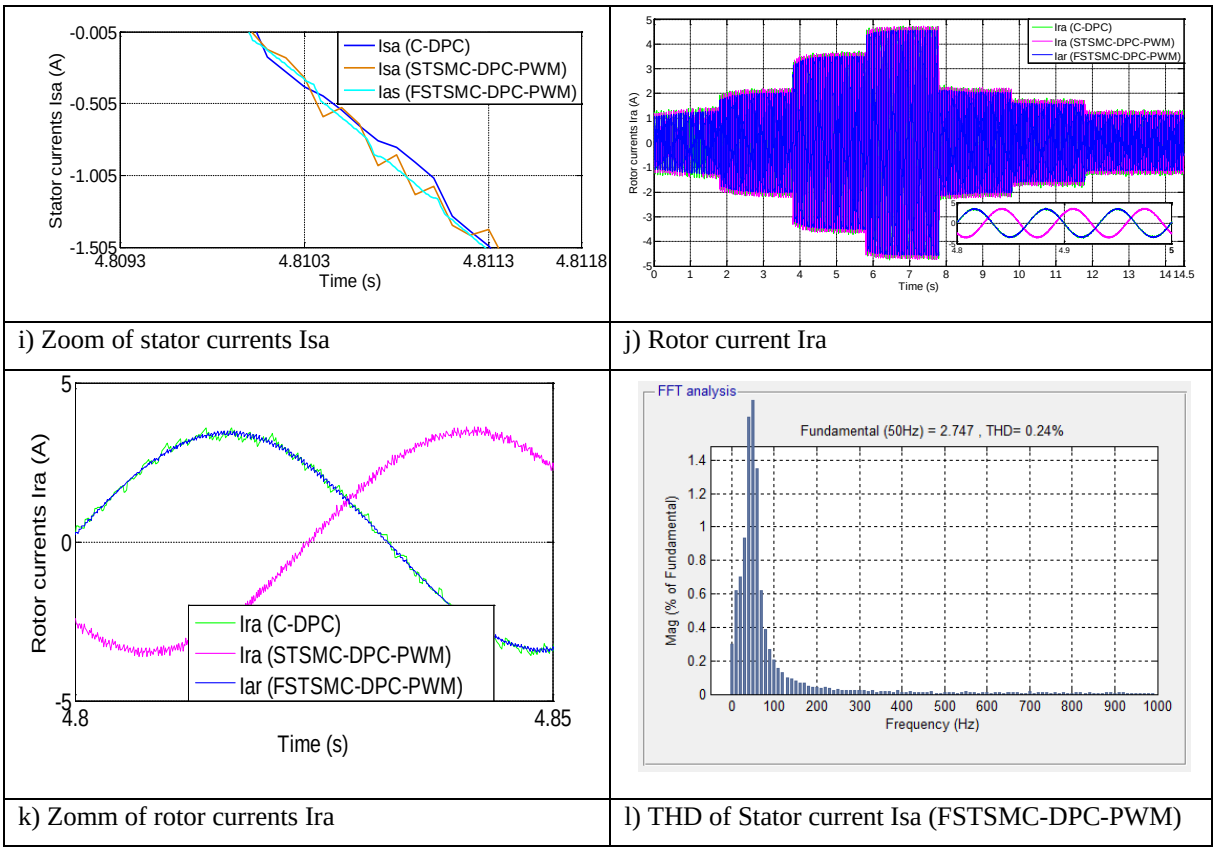
f) Direct rotor current Idr



g) Quadrature rotor current Iqr



h) Stator currents Isa



i) Zoom of stator currents Isa

j) Rotor current Ira

k) Zomm of rotor currents Ira

l) THD of Stator current Isa (FSTSMC-DPC-PWM)

Figure 4.6 – Simulations results of FSTSMC-DPC-PWM under step wind profile

The behavior of the FSTSMC-DPC-PWM in comparison to the C-DPC is shown in Figure 4.6. The numerical results are shown in the table 4.2. Given that the active power varies in response to WS changes, the powers closely follow the references (Figure 4.6b). Nevertheless, because the MPPT is being used, the reactive power has a fixed value of 0 VAR, which keeps it constant despite changes in WS (Figure 4.6c). Additionally, significant ripples are observed in both Ps and Qs, with these ripples being more pronounced in the classical DPC compared to the proposed FSTSMC-DPC-PWM strategy. An important finding is that the new control strategy slightly reduces these ripples. Specifically, the current and torque fluctuate based on variations in Ps, with ripples present in both control methods.

The Total Harmonic Distortion (THD) of the stator currents with the novel strategy is measured at 0.51%. Therefore, the proposed FSTSMC-DPC-PWM significantly reduced the THD value compared to traditional DPC, with a reduction of 54,72%, implying that current quality is much higher under the proposed strategy.

Table 4.2 presents the numerical results from the third test, showing various performance characteristics such as response time, ripple amplitude, steady-state error (SSE), and overshoot of the DFIG. From this table, it is evident that the utilization of the proposed FSTSMC-DPC-

PWM strategy results in significant improvements in ripple reduction, SSE, and overshoot compared to traditional DPC, as the calculated reduction ratios confirm. For instance, the ripples in Ps and Qs were reduced by approximately 72.22% and 80%, respectively, under FSTSMC-DPC-PWM compared to traditional DPC. Additionally, overshoot was reduced by 65.26% for Ps and 79.13% for Qs, while the SSE was lowered by 82% for Ps and 78.57% for Qs, compared to classical DPC. These values indicate that the proposed FSTSMC-DPC-PWM provided better current quality compared to classical DPC, highlighting its superiority in improving the energy system's overall performance

However, it is worth noting that the FSTSMC-DPC-PWM strategy led to a slightly longer response time compared to the traditional DPC. On the other hand, the traditional DPC significantly reduced the power response time by approximately 24.29% and 57.14% for Ps and Qs, respectively, compared to FSTSMC-DPC-PWM. This advantage in response time provides the system with greater rapidity, enabling it to better capitalize on fluctuating wind speeds.

On the other hand, FSTSMC-DPC-PWM significantly increased the power response time by around 22.86% and 41.38% for Ps and Qs, respectively, compared with C-DPC. This is to be expected, as the fuzzy logic algorithm requires a lot of computation time because it processes huge amounts of data.

		***Ps* (W)**	***Qs* (VAR)**
DPC	**Ripples**	180	200
	Overshoot	95	115
	SSE	100	70
	Response time	3.5 ms	2.9 ms
FSTSMC-DPC-PWM	**Ripples**	50	40
	Overshoot	33	24
	SSE	18	15
	Response time	4.3 ms	4.1 ms
Improvement ratios	**Ripples**	72,22%	80%
	Overshoot	65,26%	79.13%
	SSE	82%	78.57%
	Response time	-22.86%	-41.38%

. Table 4.2 – Improvement ratios and SSE, response time, overshoot, and energy ripples in the first test (step wind profile)

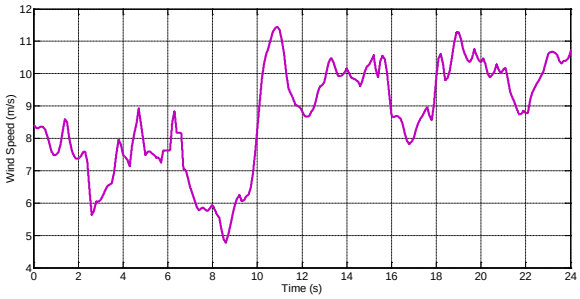
Through these strategic ratios, FSTSMC-DPC-PWM has superior performance compared to DPC. However, despite this high performance, this strategy has a negative effect: it leads to unsatisfactory response time for DFIG performance, as the C-DPC produced better results than the FSTSMC-DPC-PWM.

4.3.2. Test under Variable wind profile of FSTSMC-DPC-PWM

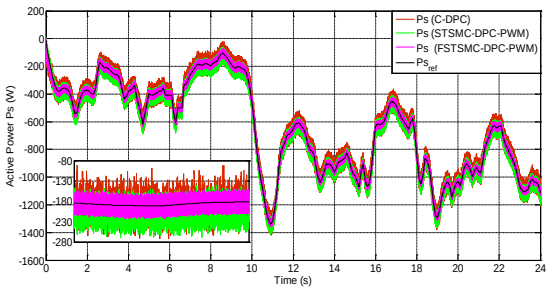
A variable WS is used in this second test, as its shape is different from that of the first test, which provides another advantage for studying the behavior of the FSTSMC-DPC-PWM The overall results of this second experiment are illustrated in Figure 4.7, and the WS profile used is shown in Figure 4.7a. Using a variable WS leads the active power (Figure 4.7b), torque (Figure 4.7d), and stator/rotor current (Figures 4.7e to 4.7k) to vary based on the WS variations, as the value proportionally rises with WS increase. Notably, the ripples in the torque, active power, and current are lower when using the FSTSMC-DPC-PWM, which is good. The reactive power is shown in Figure 4.7c, in which its value unrelated to the variation in WS and fixed, as indicated by the presence of ripples. The latter is larger when utilizing C-DPC than utilizing FSTSMC-DPC-PWM.

Despite the change in WS, the direct rotor current stays fixed and is unaffected by variation in WS, as shown by the presence of large ripples when C-DPC is used, as shown in Figure 4.7l. However, the quadrature rotor current displayed in Figure 4.7m influenced by varying the WS, as it follows the form of the WS variation. It proportionally rises with WS increase. Furthermore, ripples are more common in the DPC than in the FSTSMC-DPC-PWM.

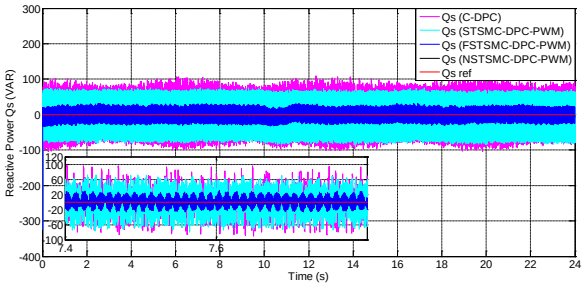
Figure 4.7n illustrates the power factor, which takes a constant value in the existence of fluctuations, as these fluctuations are higher when DPC is used. The THD values of the current in this framework are displayed in Figures 4.7p and 4.7q for using the two controllers. The THD value indicates the current quality, and can be engaged to determine the strategy's performance in enhancing the system features. The THD was 0.22% for DPC and 1.39% for the FSTSMC-DPC-PWM. Therefore, the DPC-FSTA provided highly better THD value than C-DPC, indicating that the current quality is high when the DPC-FSTA is used. Accordingly, by an estimated rate of 84.17%, the FSTSMC-DPC-PWM abated the THD value of the current in contrast to the DPC. The latter is high, indicating the technique's great efficacy and capability for enhancing the system features.



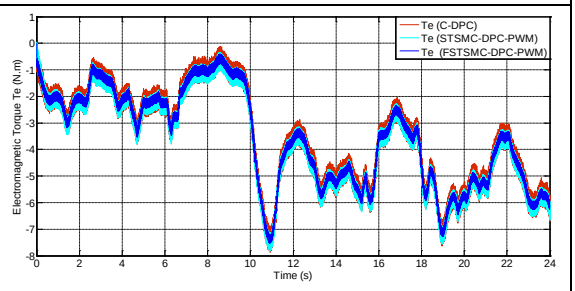
a) Variable wind speed profile



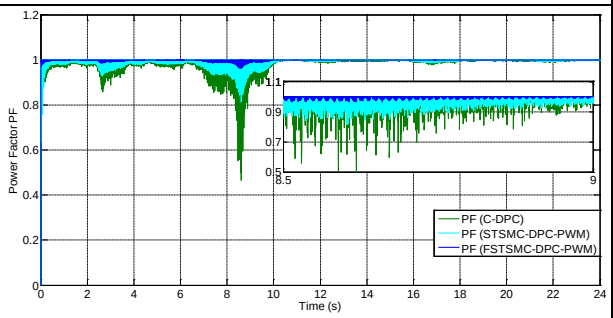
b) Active power Ps



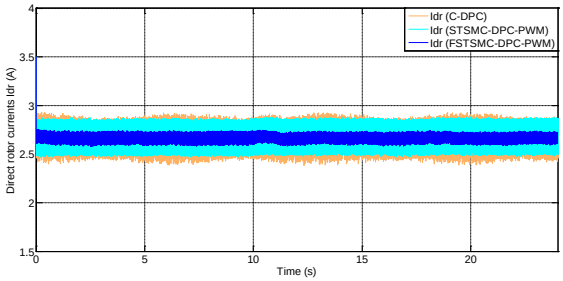
c) Reactive power Qs



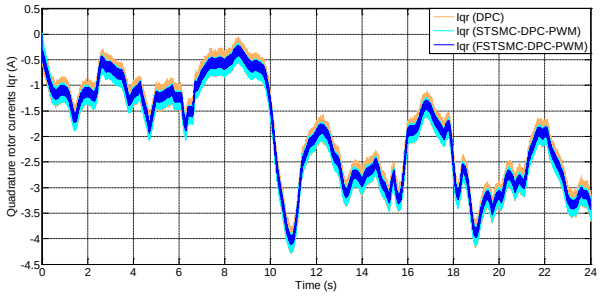
d) Electromagnetic torque Te



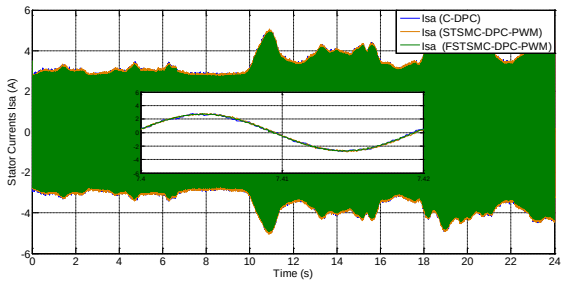
e) Power factor PF



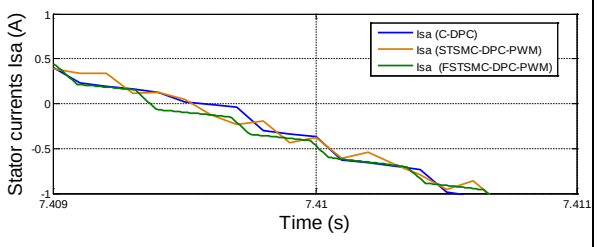
f) Direct rotor current Idr



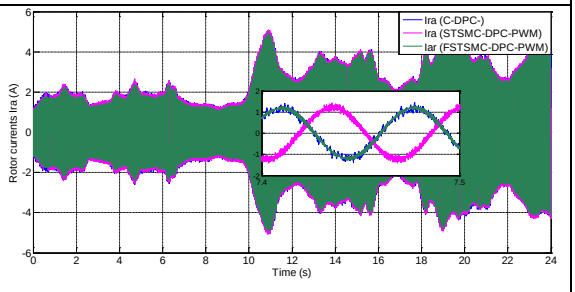
g) Quadrature rotor current Iqr



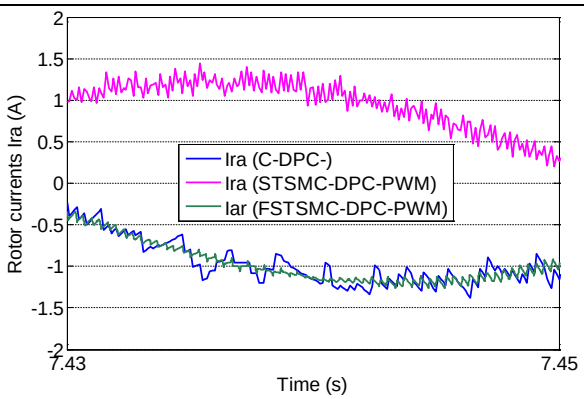
h) Stator currents Isa



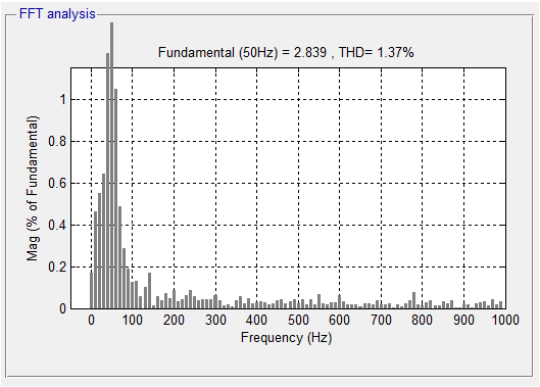
i) Zoom of stator currents Isa



j) Rotor current Ira



k) Zoom of rotor currents Ira



l) THD of Stator current Isa (FSTSMC-DPC-PWM)

Figure 4.7 – Simulations results of FSTSMC-DPC-PWM under variable wind profile

		***Ps* (W)**	***Qs* (VAR)**
C-DPC	**Ripples**	150	210
	Overshoot	80	120
	SSE	60	85
	Response time	3.7 ms	3.05 ms
FSTSMC-DPC-PWM	**Ripples**	60	45
	Overshoot	36	30
	SSE	22	18
	Response time	4.5 ms	4.4 ms
Improvement ratios	**Ripples**	60%	78.57%
	Overshoot	55%	75%
	SSE	40%	64.71%
	Response time	-21.62%	-44.26%

Table 4.3 – Improvement ratios and SSE, response time, overshoot, and energy ripples in the second test (variable wind profile)

Table 4.3 presents the numerical results related to the response time, ripple, SSE, and overshoot for active and reactive power when using both the C-DPC and FSTSMC-DPC-PWM. In addition to the percentages demonstrating performance of the strategies, the DPC-FSTA, unlike the C-DPC, provided very satisfactory values in many aspects such as ripples, SSE and overshoot for both types of DFIG performances. Accordingly, the reduction rates were approximately at 60%, 55%, and 40% for the ripple, SSE and overshoot of active power, respectively. Moreover, for the reactive power, the reduction rates were approximately 78.57%, 75%, and 64.71% for the ripple, SSE, and overshoot, respectively.

The disadvantage of this designed technique lies in the unsatisfactory response time provided, as the C-DPC, unlike the FSTSMC-DPC-PWM, provided a good time for DFIG power with relatively high reduction rates. This percentage reduction was 89.55% and 58.85% for both reactive and active power, respectively. This negative impact is referred to the values

of the FSTSMC-DPC-PWM strategy parameters; however, this consequence can be resolved by using neural networks to enhance performance and the robustness of the system. Neural networks can significantly improve the dynamic response, making them the most appropriate and reliable solution for overcoming the drawbacks of the FSTSMC-DPC-PWM.

4.4. Summary

This chapter proposed a DPC based on integrating fuzzy logic and STSMC to regulate the stator power of a DFIG-based wind turbine. It has been proven that the integration of the two techniques leads to a performance enhancement, especially when changing the wind speed profile. The advantage of the designed strategy is that it is unrelated to the mathematical system model. Simplicity, robustness, and ease of implementation are among the most prominent features of this proposed control. A 49-base fuzzy logic has been used to increase performance and provide a fast dynamic response, as using 49 rules decreases the memory requirements for control application. Additionally, by minimizing the executing time computation of the command output, the time delay presented by the controller is reduced.

The proposed DPC strategy also achieved greater efficiency and effectiveness than did traditional control, as shown by the reduction ratio, where the FSTSMC-DPC-PWM strategy reduced active power overshoot, SSE and ripples by 74.73%, 77.14%, and 73.25%, respectively at arbitrary wind speed. In terms of the stepwise wind speed, the FSTSMC-DPC-PWM strategy, unlike the DPC, yielded good results, as indicated by the reduction percentages of the SSE, overshoot, and ripples of the reactive power, which were 90.32%, 98.13%, and 86.31%, respectively. Additionally, the FSTSMC-DPC-PWM reduces the current THD by 84.17% and 84.45% under variable and step wind speeds, respectively.

Chapter 5: Intelligent Super-Twisting Sliding Mode Control for the DFIG using the Artificial Neural Network

5.1. Introduction

Industrial applications tend to select super-twisting sliding mode controllers (STSMCs) because of their ease of use, low computing complexity, and effectiveness in handling nonlinear systems. In particular, the intelligent STSMC technique has many important benefits, including ease of implementation, high durability, and higher performance even in the face of disruptions and uncertainties in the system. It is also more economical and energy-efficient than conventional controllers because it requires lower gain settings [60].

The energy system outfitted with the intelligent STSMC underwent extensive testing in the MATLAB environment under a range of operational situations, including varying wind speeds, in order to validate the suggested control method. These tests evaluated the system's response to external disturbances and dynamic changes by simulating real-world settings. Next, the intelligent STSMC's performance was contrasted with the traditional STSMC's [102].

The outcomes showed that the intelligent STSMC greatly reduced energy fluctuations, decreased total harmonic distortion (THD), and increased the system's overall robustness and efficiency in addition to improving system stability. This comparison shows how well the intelligent STSMC works to solve the problems caused by erratic wind conditions, which makes it a more dependable option for energy management systems [103].

Furthermore, the intelligent STSMC method was experimentally validated using Processor in-the-Loop Test (PIL) under the dSPACE 1104 Card, confirming the simulation results. The experimental outcomes demonstrated the proposed controller's efficiency and its ability to improve the characteristics of the C-DPC strategy and the overall energy conversion system.

To manage the active and reactive powers (Ps and Qs) of a wind energy generation system based on a doubly-fed induction generator (DFIG-WEG) and to generate the required reference values for operating the rotor side converter (RSC) of the DFIG, the developed control system combines the super-twisting sliding mode controller (STSMC) with neural networks [90, 91].

In addition to its dependability, simplicity, and convenience of use, the neural STSMC (NSTSMC) controller is renowned for its efficient performance in lowering ripples and enhancing current quality. In addition, the pulse width modulation (PWM) technique is used to translate reference values into DFIG via RSC operational pulses [95].

The benefits of the classical direct power control (C-DPC) method, including its simplicity, low parameter dependency, and quick reaction times, are still present in the recently suggested NSTSMC-DPC-PWM technique. The Lyapunov stability method provides complete assurance of the stability of the NSTSMC-DPC-PWM technique [96].

This chapter's major contribution, as demonstrated by both simulation and experimental studies, is the NSTSMC-DPC-PWM approach.

In order to simplify the energy system and show that the suggested method may enhance current and power quality without requiring GSC control, the grid side converter (GSC) is employed in conjunction with an uncontrolled inverter [97, 98].

First, by contrasting its performance with the C-DPC method under various working situations, the suggested strategy was validated in the MATLAB environment. In comparison to the C-DPC method, the numerical and graphical results showed how well the suggested strategy performed and improved the features of the energy system. The second step was using the dSPACE 1104 card to carry out the PIL test in order to validate it, and see if it could improve the energy system's performance in the face of varying wind speeds [99].

The NSTSMC-DPC-PWM strategy's outcomes were contrasted with the experimental findings achieved. As a result, a significant contribution of this study in this chapter is the PIL test of this suggested technique.

This novel command successfully achieved the following objectives:

- Reduced power and current ripples compared to the C-DPC approach.
- Enhanced energy system efficiency based on wind speed, outperforming the C-DPC approach.
- Lowered total harmonic distortion (THD) of current, providing an improvement over the C-DPC method.
- Verified the simulation results and conducted experimental tests to validate the proposed approach with the PIL test.
- Addressed the challenges and limitations of the C-DPC method.
- Increased the resilience and durability of real wind power and energy generation systems.

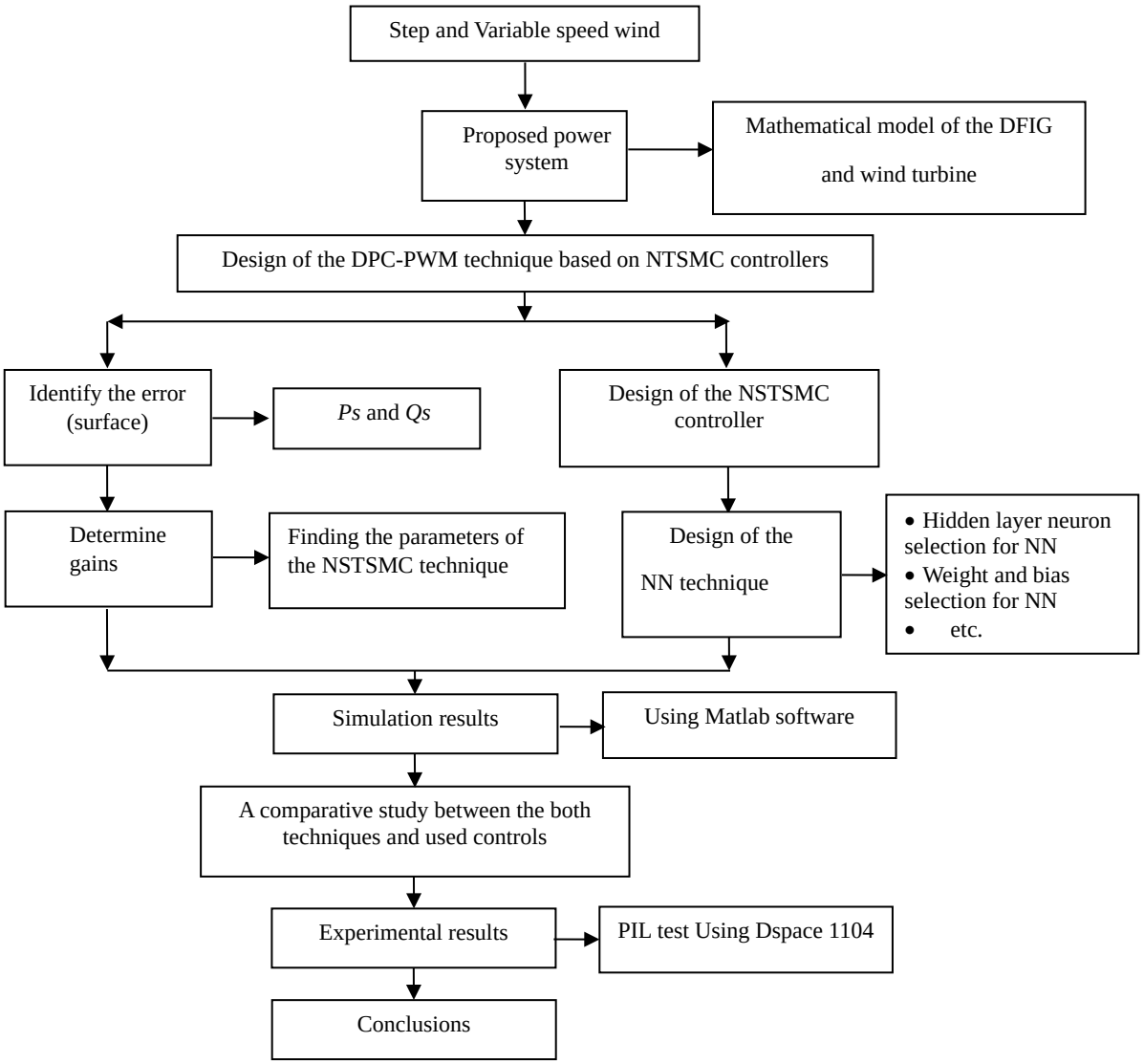


Figure 5.1 - Diagram of research steps.

5.2. Designed NSTSMC-DPC-PWM control technique

One linear control approach that is well-known for its simplicity and convenience of use is the DPC technique. It performs better than a number of other controls, including radial control, since it provides a quick dynamic reaction and doesn't need understanding of the mathematical model of the machine [85]. This method does away with internal loops by creating trigger pulses in the DFIG RSC using a state table. Two HCs are used in this method to regulate and control the DFIG's Ps and Qs [86]. Nevertheless, this strategy's dependence on estimating capabilities, which links it to the machine's parameters—particularly the resistance Rs—is a disadvantage. This resistance varies while the machine runs continually, which has a detrimental impact on the DPC strategy's effectiveness and outcomes. In contrast to FOC, IVC, and DVC approaches, the DPC technique produces less energy ripples [82].

The DPC approach produces greater Ps and Qs ripples and a higher THD value of the currents when compared to predicted and BC procedures. As stated in the introduction, a number of solutions, such as smart, nonlinear, and hybrid approaches, have been developed to solve the drawbacks of the conventional DPC strategy. These methods have produced both positive and bad consequences, thus further study is needed to find the best one in order to get the best outcomes. This section uses hybrid tactics to improve the system's resilience and lessen energy and current ripples, which are the disadvantages of the DPC strategy [83].

Due to their advantageous qualities—such as simplicity and independence from system parameters—this work integrates the STSMC approach with ANN to further boost system robustness, with good results. The benefits of these two tactics over other restrictions led to their selection. As clever techniques, neural networks rely on experience and just need to know the quantity of inputs and outputs—not the mathematical model of the machine or system. Neural networks are the best option for this job to minimize energy ripples and enhance current quality because of their excellent performance and resilience against both internal and external variables. Another significant benefit of using neural networks is their accuracy, which significantly improves system characteristics [84].

The well-known ANN approach is a mathematical model that attempts to mimic human brain skills in terms of machine and control behavior. It draws inspiration from biological neural systems. Many nonlinear processing units, or neurons, are linked together in a neural network via synapses that are assigned numerical values known as weights. Together, these elements successfully surmount the shortcomings of earlier technology. The three levels of a neural network are input, hidden, and output. This model's capacity to adapt to both internal and external information flowing through the network is one of its distinguishing characteristics.

The following equation (5.1) can be used to conceptually model the fundamental structure of a neuron [85]:

$$y_i^{ANN} = f\left(\sum_i^n w_i x_i + b\right) \tag{5.1}$$

The number of neural network inputs, the network outputs vector, the activation function, the neural network input vector, the weight matrix, and the bias are all indicated by the variables n, y_i^{ANN}, f, $x\{x_i, i=1,2,...,n\}$, w_i and b respectively. Usually, the backpropagation approach is used to update the weight matrix, and the bias input (the neuron's threshold or intercept) is either +1 or -1. The flowchart in Figure 2 provides a summary of the stages involved in creating an ANN technique [86].

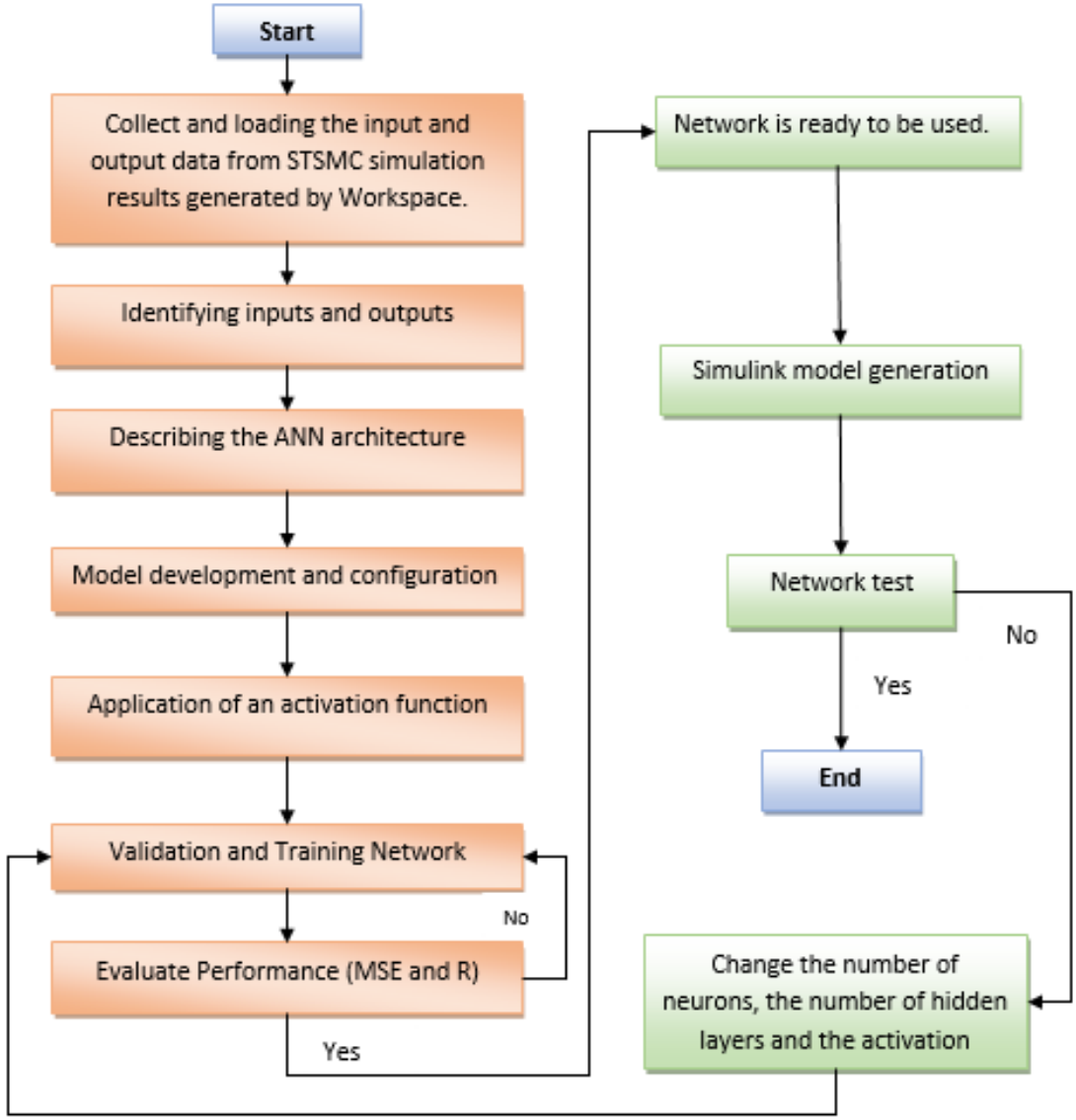


Figure 5.2 - Diagram of the ANN Controller Training Steps.

As shown in Figure 5.2, compiling and importing datasets is the initial stage in building the ANN approach. The simulation results of the STSMC technique, produced with MATLAB (R2021a), Provided the dataset for this new intelligent approach [87].

There are several varieties of neural networks that may be used for this. Furthermore, learning algorithms are linked to neural networks, and the neural controller may be implemented using a variety of techniques [89].

In contrast to the controls discussed before, the technique designed in this chapter introduces a novel NSTSMC controller for controlling the DFIG generated powers. The NSTSMC approach, in contrast to the classical DPC technique, uses one input and one output to the NSTSMC to derive reference voltage values from the power error. The PWM technique is

employed in the interim to provide the pulses required to run the DFIG's RSC. When machine parameters change, the NSTSMC-DPC-PWM strategy seeks to improve present quality, extend the longevity of the energy system, and improve the qualities of the conventional approach. Figure 5.3 shows the new NSTSMC-DPC-PWM method, with one of its main benefits being its resilience [90].

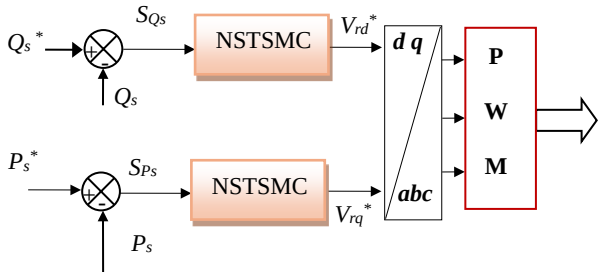


Figure 5.3 - Block diagram of the internal structure of the RSC control.

The suggested approach has several advantages over the IVC technique, including better performance, remarkable resilience, simplicity of use, lack of internal loops, and cost effectiveness.

The proposed NSTSMC-DPC-PWM approach uses the energy error as an input for the NSTSMC approaches, and capacity estimation is used to compute the error. Equation (5.2) shows the capacity estimates employed in this study. The estimation equations are the same as those used in the classic DPC technique, as described in references [45, 46].

$$\begin{cases} Q_s = -\frac{3}{2}\left(\frac{V_s}{\sigma . L_s}\cdot \Psi_{r\beta} - \frac{V_s . L_m}{\sigma . L_s . L_r}\cdot \Psi_{r\alpha}\right) \\ P_s = -\frac{3}{2}\frac{L_m}{\sigma . L_s . L_r}\cdot (V_s . \Psi_{r\beta}) \end{cases} \tag{5.2}$$

STSMC strategy of the *Ps* and *Qs* is conceived to respectively change the q and d-axis voltages as shown in the Equations (5.3) [100, 101]:

$$\begin{cases} V_{dr} = K_1 \left| S_{Q_s} \right|^r \operatorname{sgn}(S_{Q_s}) + \overset{*}{V}_{dr1} \\ \overset{*}{V}_{dr1} = K_2 \operatorname{sgn}(S_{Q_s}) \\ V_{qr} = K_1 \left| S_{P_s} \right|^r \operatorname{sgn}(S_{P_s}) + \overset{*}{V}_{qr1} \\ \overset{*}{V}_{dr1} = K_2 \operatorname{sgn}(S_{P_s}) \end{cases} \tag{5.3}$$

where, $S_{Qs} = Q_{sref} - Q$ is the reactive power error,

$S_{Ps} = P_{sref} - P$ is the active power error.

The MPPT approach is used in this suggested technique to determine the reference value of active power, which makes the value of active power dependent on the pattern of the wind speed change. The condition system stability should be demonstrated by the two constant gains, k1 and k2. The STSMC-Ps and Qs command structure is depicted in Figure 5.4.

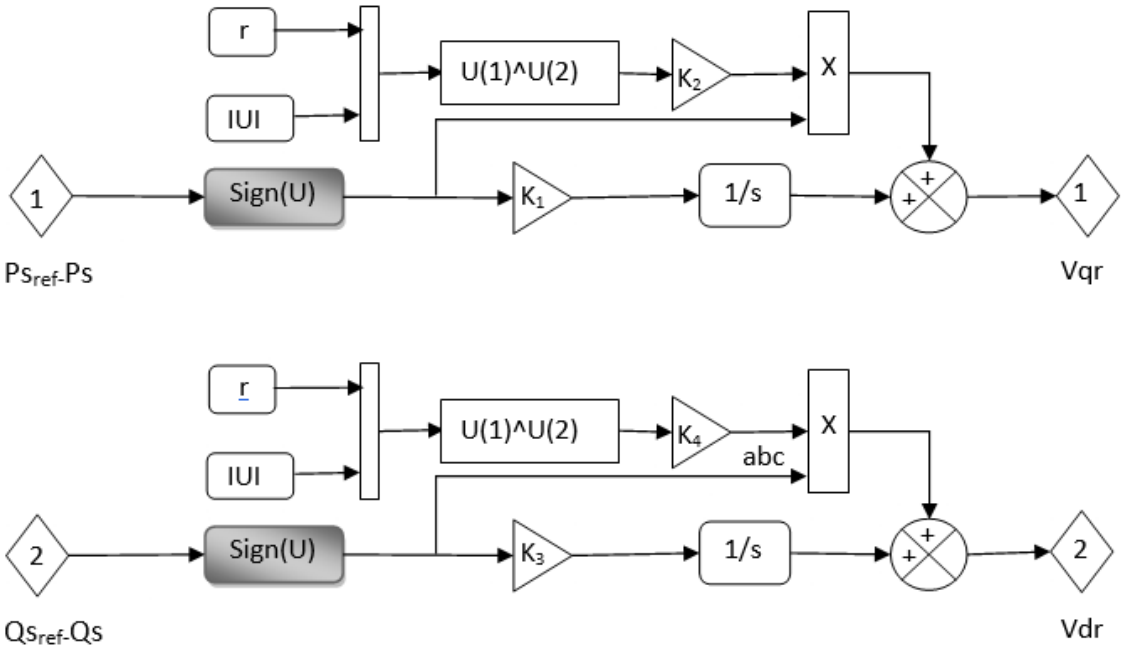


Figure 5.4: The STSMC- Ps and Qs techniques**.**

The following equations (5.4) describe a dynamic system being studied, with the input u, the output y and the state *x* [100, 101]:

$$\begin{cases} \dfrac{dx}{dt} = a(x,t) + b(x,t)u \\ y = c(x,t) \end{cases} \tag{5.4}$$

The challenge with this instruction is to determine, if feasible within limited durations, the input function u = f (y, ẏ) that can guide the system trajectories to the phase plane departure point y = ẏ = 0. The commutation instruction is applied to the time derivative u̇1 of the input variable "u" which is defined as a new state variable [102].

The error (S), where S = y* - y, is connected to the output of the STSMC algorithm. The mathematical model and the method for calculating the parameters are expressed in equations (5.5) and (5.6), respectively [101, 102].

$$\begin{cases} u = |S|^{r} K_1 \, \mathrm{s}at(S) + u_1 \\ \dot{u} = K_2 \, \mathrm{s}at(S) \end{cases} \tag{5.5}$$

$$\begin{cases} K_1 > \dfrac{A_M}{B_m} \\ K_2 \geq \dfrac{4A_M}{B_m^2} \cdot \dfrac{B_M (K_1 + A_M)}{B_m (K_1 - A_M)} \end{cases} \tag{5.6}$$

where, the upper and lower bounds of B and A in the 2nd derivative are represented by $B_M \geq B \geq B_m$ and $A_M \geq |A|$, [100, 102].

$$\frac{d^2y}{dt^2} = A(x,t) + B(x,t)\frac{du}{dt} \tag{5.7}$$

The task at hand involves figuring out the input function u = f (y, ẏ) that may direct the system trajectories to the phase plane departure point y = ẏ = 0, if it is possible to do so in the given time constraints. The time derivative u̇1 of the input variable "u," which is defined as a new state variable [102], is subjected to the commutation instruction. The output of the STSMC method is linked to the error (S), where S = y* - y. Equations (6.5) and (6.6), respectively, represent the mathematical model and the procedure for determining the parameters [101, 102].

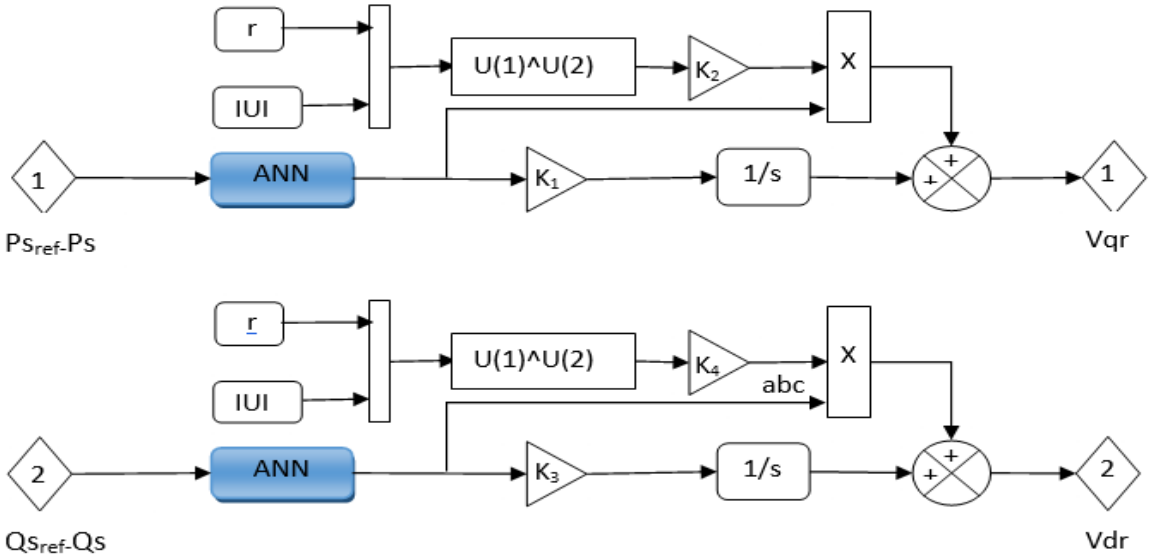


Figure 5.5: The NSTSMC command.

An intelligent control method that is well-known for its simplicity and resilience is the ANN approach [104]. Eight neurons are employed in the hidden layer of the NSTSMC method, whereas one neuron is utilized in each of the input and output layers. The ANN method utilized to boost and increase the STSMC Qs and Ps of the DFIG's performance is shown in Figure 5.7.

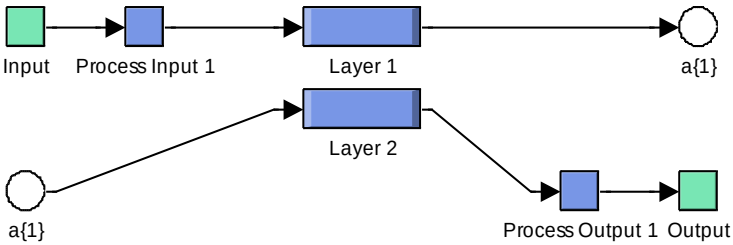


Figure 5.6 - The ANN strategies

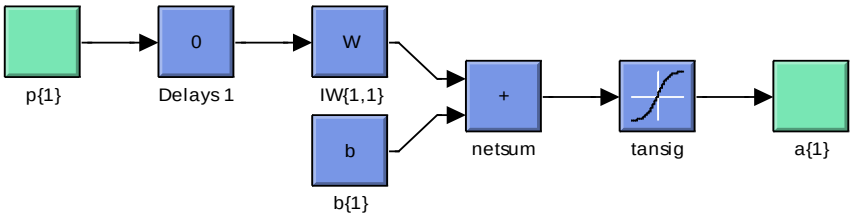


Figure 5.7 - Layer 1.

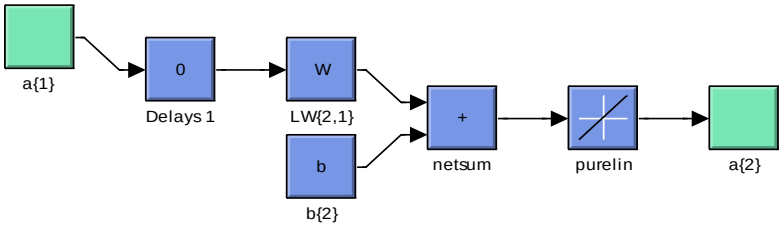


Figure 5.8 - Layer 2.

The Figure 6.8 shows the structure of the hidden layer of the ANN method.

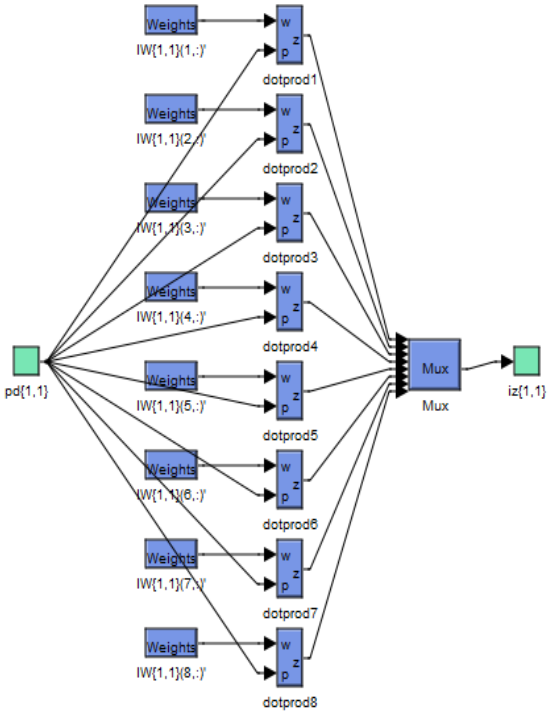


Figure 5. 9 -Hidden layer.

As a result, Table 5.1 displays the properties of the neural network that was utilized to create the two controllers for Ps and Qs control.

Parameters	**Value**
Training	Levenberg-Marquardt algorithm
Coeff of acceleration of convergence(mc)	0.9
net.trainParam.goal	0
Number of neurons in hidden layer 1	8
Performances	Mean Squard Error (mse)
TrainParam.Lr	0.005
TrainParam.mu	0.9
Number of neurons in layer 1	1
TrainParam.goal	0
TrainParam.show	50
TrainParam.epochs	300
Number of neurons in layer 2	1

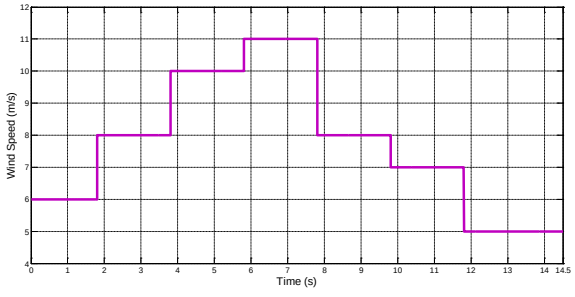
Table 5.1 - Characteristics of the neural algorithms

5.3. Simulations results of NSTSMC-DPC-PWM control technique applied to DFIG

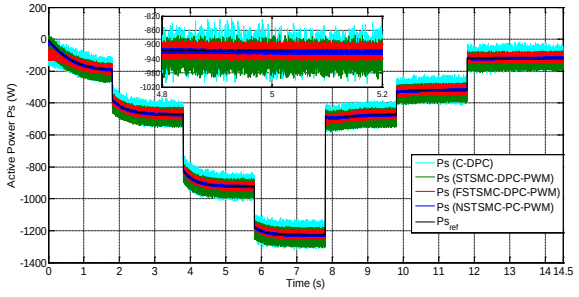
A simulation with Matlab/Simulink 2021b was conducted for two different tests, similar to the other tests performed in this thesis, to facilitate the comparison of the different control strategies presented. The first test used a step wind profile, while the second used a profile with variable wind speed.

5.3.1. Simulation test under step wind profile

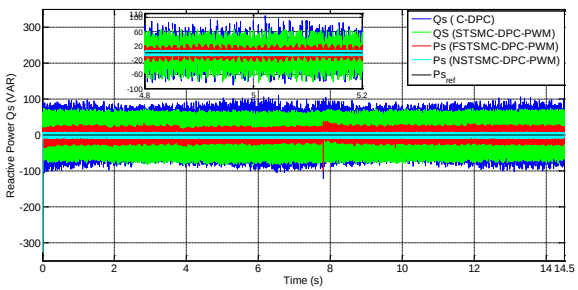
The features of the proposed NSTSMC-DPC-PWM and conventional DPC strategies are analyzed through the WSs' steps (Figure 5.10a). The visual outcomes of this analysis are illustrated in Figure 5.10, while the numerical data from this test is provided in Table 5.2.



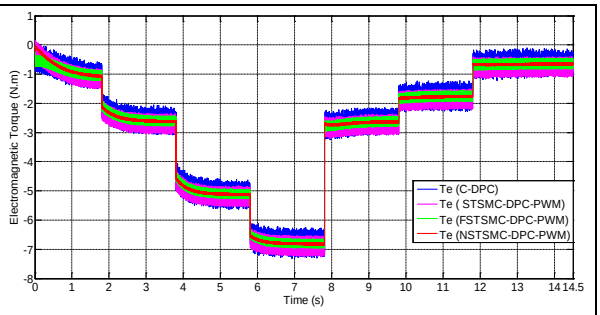
a) Wind speed profile



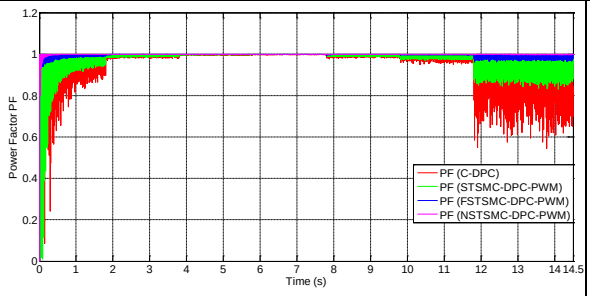
b) Active power Ps



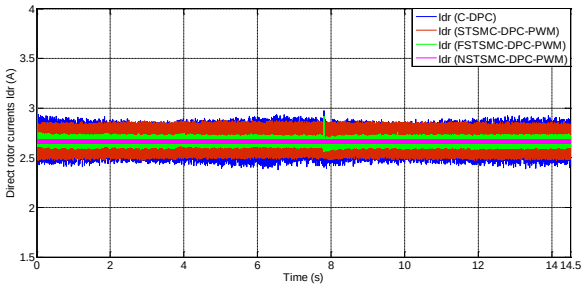
c)Reactive power Qs



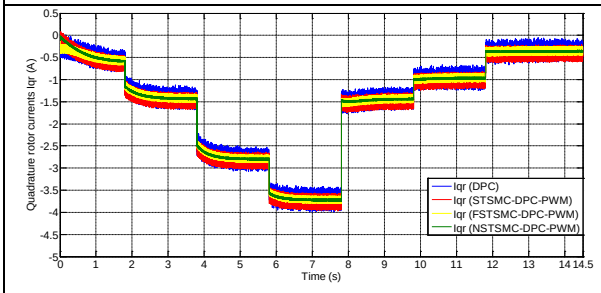
d)Electromagnetic torque Te



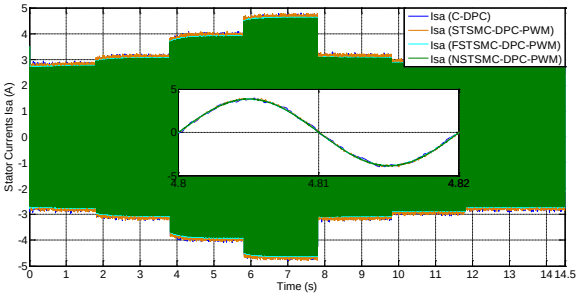
e) Power factor PF



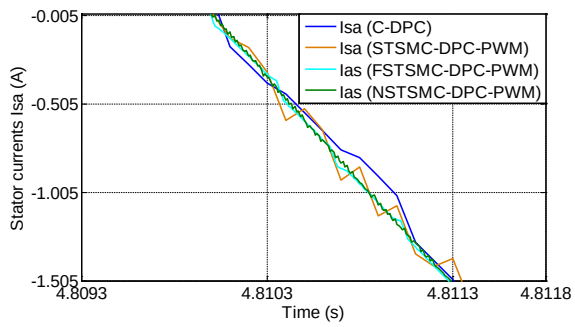
f) Direct rotor current Idr



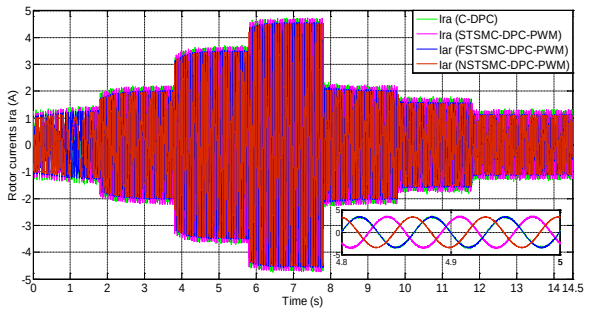
g) Quadrature rotor current Iqr



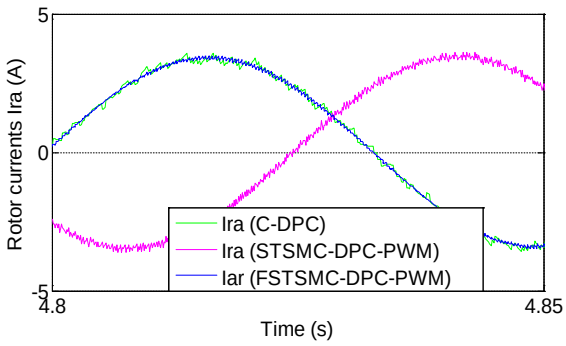
h) Stator currents Isa



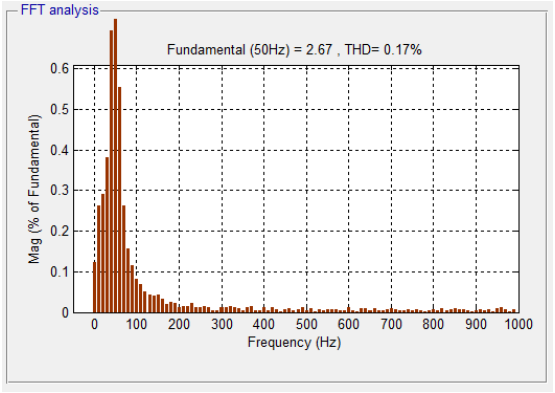
i) Zoom of stator currents Isa



j) Rotor current Ira



k) Zoom of rotor currents Ira



l) THD of Stator current Isa (NSTSMC-DPC-PWM)

Figure 5.10 - Simulation results of NSTSMC-DPC-PWM under step wind test

		***Ps* (W)**	***Qs* (VAR)**
C-DPC	**Ripples**	180	200
	Overshoot	95	115
	SSE	100	70
	Response time	3.5 ms	2.9 ms
NSTSMC-DPC-PWM	**Ripples**	10	12
	Overshoot	6	7.5
	SSE	4	6.5
	Response time	6.5 ms	5.8 ms
Improvement ratios	**Ripples**	94.44%	94%
	Overshoot	93.68%	93.48%
	SSE	96%	90.71%
	Response time	- 85.71%	-100%

Table 5.2 – Improvement ratios and SSE, response time, overshoot, and energy ripples in the first test (step wind profile)

The proposed NSTSMC-DPC-PWM strategy ensures precise tracking of the reference power (Ps and Qs) values, as shown in Figures 5.10b and 5.10c. The DFIG supplied active power Ps adjusts according to step wind speed profile variations, increasing and decreasing with changing in WS, while the reactive power Qs remains unaffected and remains null by following the reference imposed null to guarantee a power factor close to 1. Importantly, few ripples were observed in both powers Ps and Qs, but the classical DPC exhibited more important ripples compared to the NSTSMC-DPC-PWM. This demonstrates that the NSTSMC-DPC-PWM strategy effectively minimizes the undulations with a very remarkable rate, leading to higher performance. Moreover, fluctuations and ripples in current and torque correspond with

changes in Ps, and both control strategies showed ripple effects, though the proposed method performed better. But the new intelligent control system has considerably reduced these ripples.

The total harmonic distortion (THD) in the stator currents using the NSTSMC-DPC-PWM strategy was measured at 0.17%, marking a substantial improvement compared to the traditional DPC, where the THD reduction reached only 67.92% (see Figure 5.10l). This outcome underscores the enhanced current quality provided by the NSTSMC-DPC-PWM approach, confirming its superiority in delivering significantly better overall current performance.

Table 5.2 presents the numerical results of the third test, which compare key performance parameters such as response time, ripple size, steady-state error (SSE), and overshoot. It is clear from the data that NSTSMC-DPC-PWM significantly outperforms the classical DPC by reducing ripples, SSE, and overshoot. Specifically, ripples in Ps and Qs were reduced by about 94.44% and 94%, respectively, while overshoot was reduced by 93.68% for the active power Ps and 56.52% for the reactive power Qs. SSE was also significantly lowered, by 96% for the active Ps and 90.71% for the reactive Qs, when compared to the classical C-DPC. However, the response time for NSTSMC-DPC-PWM was slightly longer than that of the classical DPC.

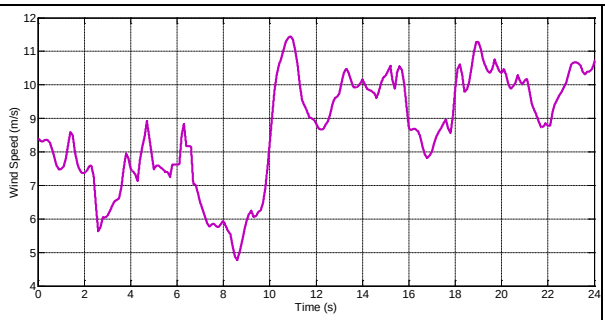
While the NSTSMC-DPC-PWM strategy increased the response time by 85.71% for the generated DFIG active power Ps and 100% for reactive power Qs, it still surpasses the Classical C-DPC in overall performances. Despite the extended response time, NSTSMC-DPC-PWM excels in providing superior power quality and significantly reducing ripples, making it the more effective control strategy. This optimization between ripple minimization and enhanced power quality enables the system to capture energy more efficiently, even in fluctuating wind conditions.

This novel designed NSTSMC-DPC-PWM offers the best performance, particularly in minimizing ripples, while maintaining high power quality.

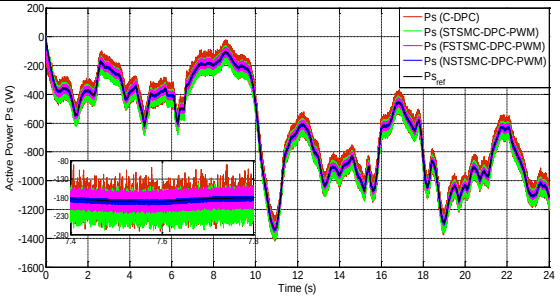
The neural network-based NSTSMC-DPC-PWM approach necessitates a longer response time because of the intricacy of its processing. Neural networks take longer to learn and adjust to changing conditions than simpler control methods because they require many layers and intense computations. Neural networks are also better at handling non-linear systems, although this increases the computing load and slows down response times. This approach reduces ripples and boosts power quality, which increases precision; however, the trade-off is a longer response time since accurate control requires more computational work.

5.3.2. Simulation results under variable wind speed.

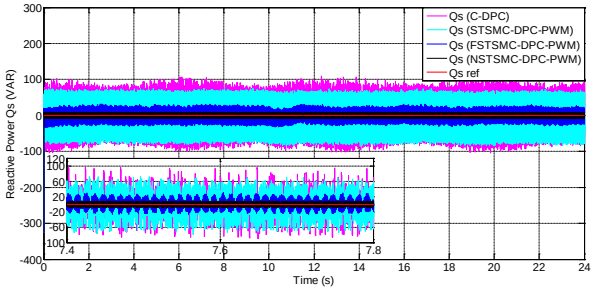
The perfotmances of the proposed NSTSMC-DPC-PWM and C-DPC strategies are examined under the real variable wind speed profile (Figure 5.11a). The simulations results of this analysis are presented in Figure 5.11, while the corresponding numerical data can be found in Table 5.2



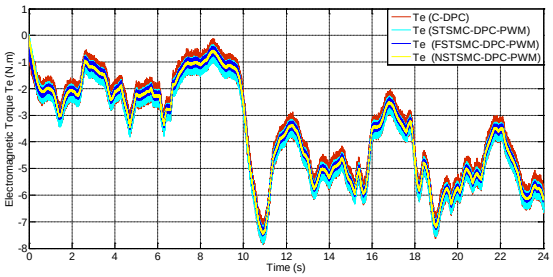
a) Variable wind speed profile



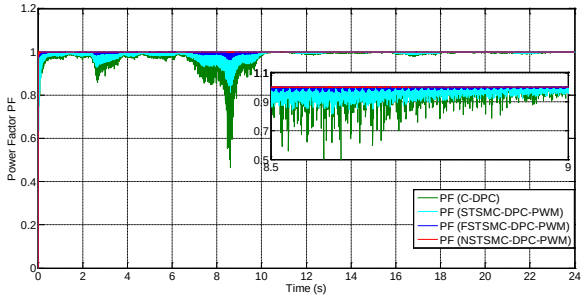
b) Active power Ps



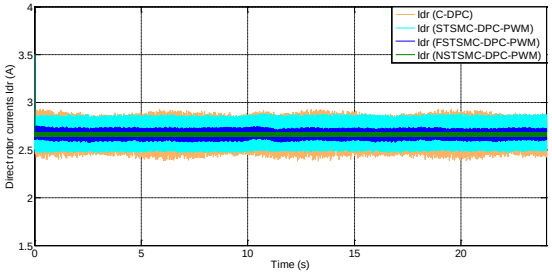
c) Reactive power Qs



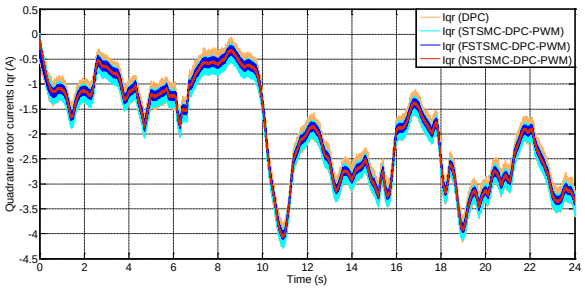
d) Electromagnetic torque Te



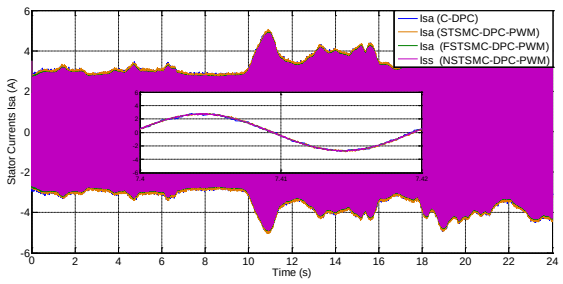
e) Power factor PF



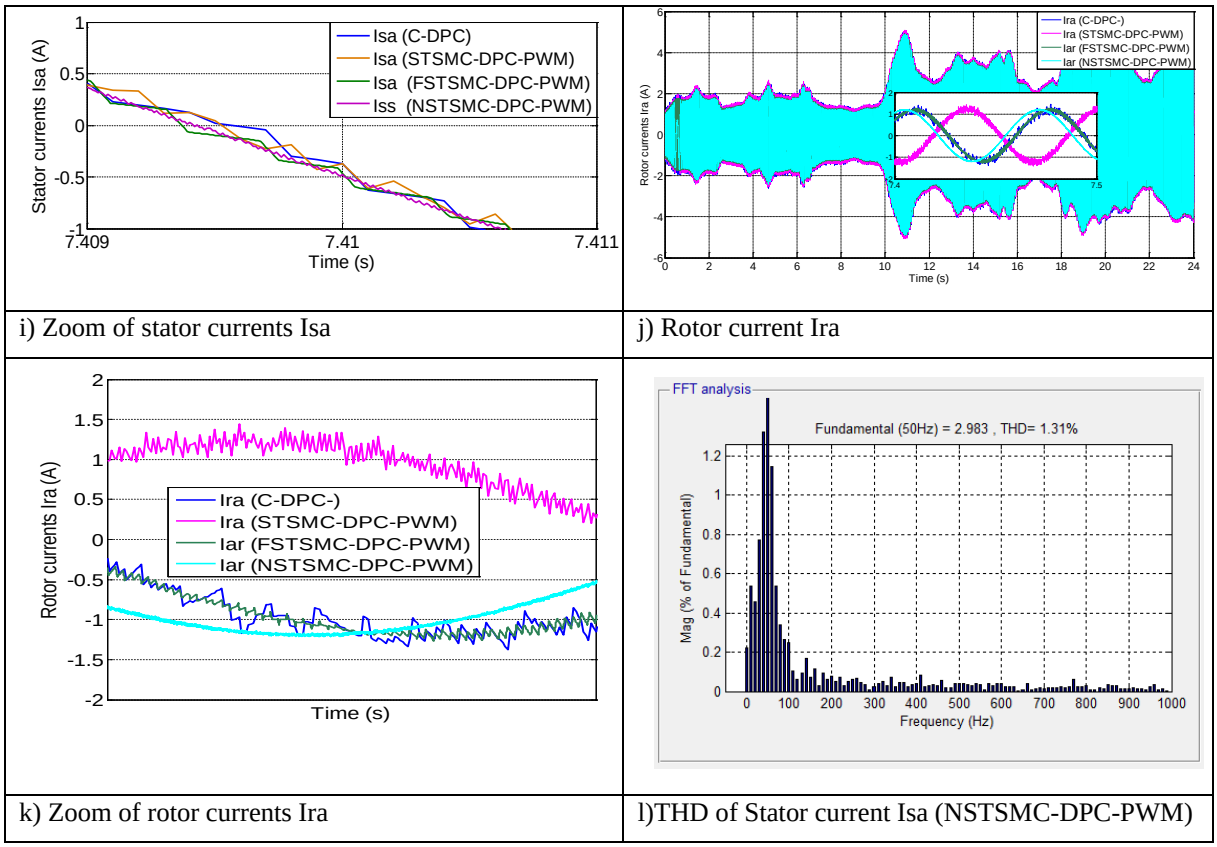
f) Direct rotor current Idr



g) Quadrature rotor current Iqr



h) Stator currents Isa



i) Zoom of stator currents Isa | j) Rotor current Ira

k) Zoom of rotor currents Ira | l)THD of Stator current Isa (NSTSMC-DPC-PWM)

Figure 5.11 - Simulation results of NSTSMC-DPC-PWM under step wind test

		***Ps* (W)**	***Qs* (VAR)**
C-DPC	**Ripples**	150	210
	Overshoot	80	120
	SSE	60	85
	Response time	3.7 ms	3.05 ms
NSTSMC-DPC-PWM	**Ripples**	12	13
	Overshoot	7.5	8
	SSE	6	7.5
	Response time	6.7 ms	6.8 ms
Improvement ratios	**Ripples**	92%	93.81%
	Overshoot	90.63%	93.33%
	SSE	90%	91.18%
	Response time	- 81.08%	- 122.95%

Table 5.3 – Improvement ratios and SSE, response time, overshoot, and energy ripples in the second test (variable wind profile)

The proposed NSTSMC-DPC-PWM strategy ensures accurate tracking of the reference power values Ps and Qs, as demonstrated in Figures 5.11b and 5.11c. Under a variable wind speed profile, the active power Ps supplied by the DFIG adjusts accordingly, increasing and decreasing with modifications in wind speed, while the reactive power Qs remains stable and follows the reference value of zero, maintaining a near-unity power factor. Notably, fewer

ripples were observed in both Ps and Qs compared to the traditional C-DPC, where larger fluctuations occurred. This highlights the superior ability of the NSTSMC-DPC-PWM to significantly reduce ripples, resulting in improved overall performance. Furthermore, while both control strategies showed ripple effects in stator and rotors currents (Isa and Ira) and electromagnetic torque that correspond to changes in the active power Ps, the proposed method performed far better in minimizing these undulations.

The total harmonic distortion (THD) in stator currents with the NSTSMC-DPC-PWM was measured at 1.31%, a remarkable improvement over the traditional C-DPC (THD = 1.49%), where the THD reduction only reached 12.08% (see Figure 5.11l). This significant difference underscores the enhanced current quality provided by the NSTSMC-DPC-PWM, affirming its superiority in delivering overall better current performance.

Table 5.3 displays the numerical results from the third test, comparing key metrics such as response time, ripple magnitude, steady-state error (SSE), and overshoot. The results clearly show that NSTSMC-DPC-PWM outperforms classical DPC in every category. Specifically, ripples in Ps and Qs were reduced by approximately 92% and 93.81%, respectively, while overshoot decreased by 90.63% for the active power Ps and 93.33%for the reactive power Qs. SSE was also significantly reduced, by 90% for te DFIG active power Ps and 91.18 % for DFIG reactive power Qs, in comparison to the classical C-DPC. Despite these improvements, the NSTSMC-DPC-PWM had a slightly longer response time than the classical C-DPC.

Overall, the NSTSMC-DPC-PWM method outperforms the traditional DPC, despite reaction times increasing by 81.08% for the supplied DFIG active power Ps and by 122.95% for the DFIG reactive power Qs. The most efficient control method is the NSTSMC-DPC-PWM since it produces better power quality and significantly lessens ripples despite the longer response times. Even in the presence of varying wind conditions, the system is able to harness energy more efficiently because to this balance between improved power quality and reduced ripple.

In summary, the newly designed NSTSMC-DPC-PWM offers the best performance, particularly in minimizing ripples, while maintaining excellent power quality.

5.3.3. Comparison in term of THD between the developed control strategies in this thesis

Table following table 5.4 presents a comparison of the THD values for the Isa current between the developed control strategies under two different test scenarios: step wind profile (Test 1) and variable wind (Test 2)

	THD value of Isa current	
	Test_1 (step wind profile)	**Test_2 (variable wind)**
C-DPC	0.53%	1.49%
STSMC-DPC-PWM	0.51%	1.42%
FSTSMC-DPC-PWM	0.24%	1.37%
NSTSMC-DPC-PWM	0.17%	1.31%

Table 5.4 – Comparison of THD value

When more sophisticated control schemes are used, the results in the table show a noticeable improvement in lowering the total harmonic distortion (THD) of the Isa current. In all test scenarios, the conventional DPC (C-DPC) exhibits the highest THD values, especially in Test 2 under changeable wind conditions (1.49%), underscoring its shortcomings in terms of handling dynamic wind profiles. On the other hand, the Neural STSMC-DPC-PWM approach performs the best, demonstrating its superiority in reducing current distortion and improving power quality with the lowest THD values in both tests (0.17% in Test 1 and 1.31% in Test 2).

Additionally, the FSTSMC-DPC-PWM approach works noticeably better than C-DPC; in Test 1, for example, it reduces THD by over half (0.17% vs. 0.53%).

These results highlight how neural and fuzzy Super-Twisting sliding mode control methods can be used to increase the durability and efficiency of wind energy systems, particularly when the wind speed varies.

5.3.4. Comparison in term of THD between the NSTSMC-DPC-PWM and other recent works

Table 5.5 provides a comparison of the THD values between the proposed control strategy and various advanced techniques from the literature, highlighting the effectiveness of our approach."

Techniques	**THD (%)**	**References**
DPC-HOSMC	1.66	[85]
Virtual flux DPC	4.88	[86]
DPC with neuro-fuzzy algorithm	2.72	[87]
Intelligent DTC	4.80	[35]
SOSMC	3.13	[73]
FOC	3.70	[3]
ISMC	0.88	[88]
Multi-resonant-based SMC	3.2	[89]
Predictive DTC	2.15	[90]
Test_1	0.17	Proposed DPC-NSTSMC-PWM
Test_2	1.31	

Table 5.5 - Comparison in terms of THD value with other works

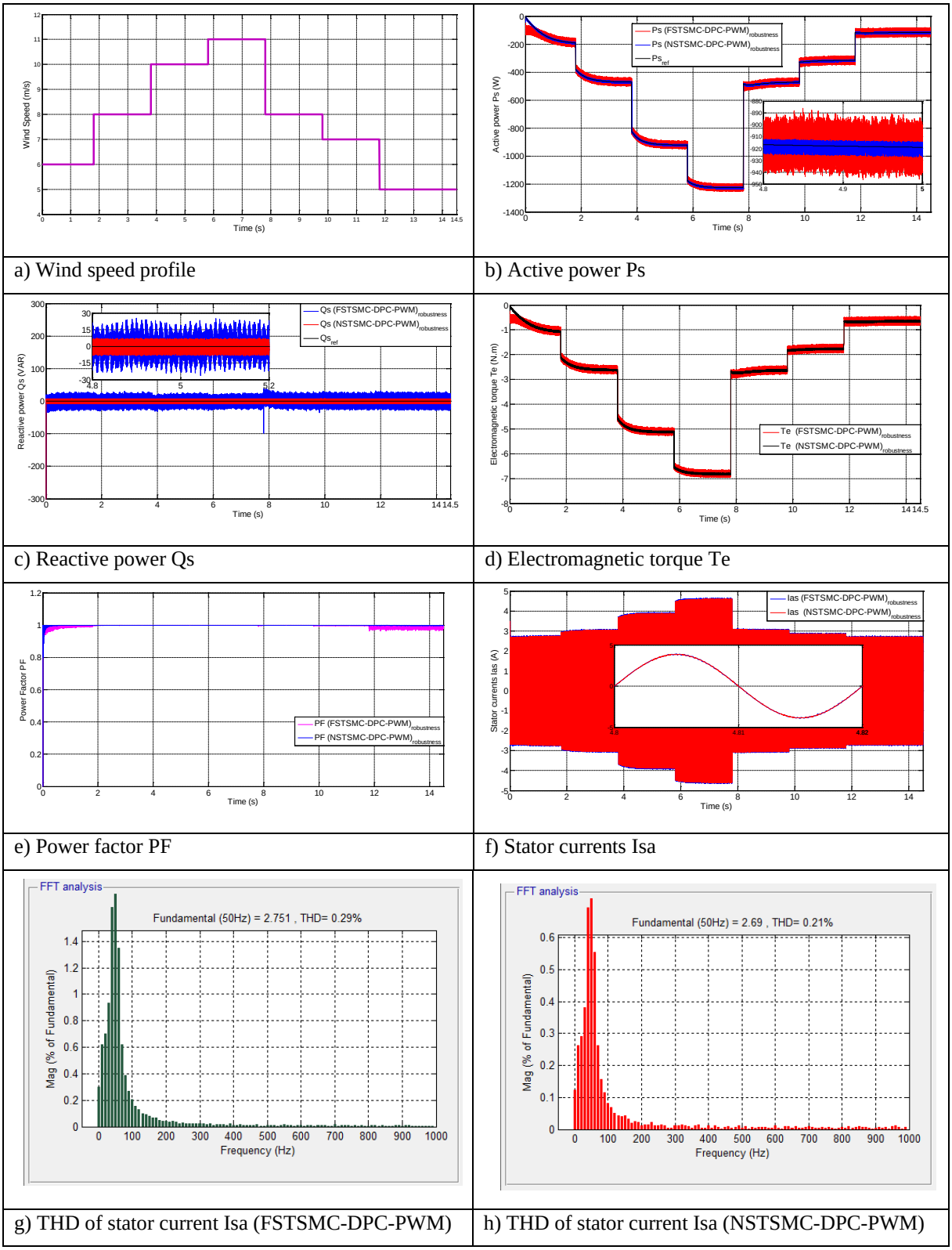
The comparison presented in Table 5.5 highlights the significant improvements achieved by the proposed DPC-NSTSMC-PWM control strategy in terms of reducing THD (Total Harmonic Distortion) values compared to other advanced techniques in the literature. The proposed method achieves a remarkably low THD of 0.17% in Test 1 and 1.31% in Test 2, outperforming all other methods listed in the table. For instance, DPC-HOSMC exhibits a THD of 1.66%, and the widely adopted predictive DTC has a THD of 2.15%, both considerably higher than the proposed technique. Even the intelligent DTC and neuro-fuzzy-based DPC strategies, known for their robustness, show higher THD values of 4.80% and 2.72%, respectively. This demonstrates the superior performance of the proposed DPC-NSTSMC-PWM approach, particularly in reducing current distortions and enhancing the overall power quality, making it a highly efficient and competitive solution for renewable energy systems.

5.4. Robustness test

The parametric identification of the machine does not provide exact and definitive values. Moreover, these values (machine parameters) are often linked to the operating conditions of the machine (heating, load variation, magnetic circuit saturation, air-gap shape, skin effect, flux-weakening regime, etc.). Therefore, we considered it more appropriate to test the influence of potential parameter errors on the performance of the vector control. The robustness test involves varying the parameters of the used DFIG model. Indeed, the calculations of the controllers are based on transfer functions whose parameters are assumed to be fixed. The identification of these parameters is subject to inaccuracies due to the method employed and the measuring instruments. The robustness of the two control methods following changes in the DFIG parameters is tested under the following conditions:

- Resistors Rr, Rs are multiplied by 2 (heating case).
- Inductances Ls, Lr and M are divided by 2 (saturation case).

Figures 5.13 and 5.14 show the simulation results of robustness test for the two proposed strategies FSTSMC-DPC-PWM and NSTSCM-DPC-PWM in this thesis.



a) Wind speed profile

b) Active power Ps

c) Reactive power Qs

d) Electromagnetic torque Te

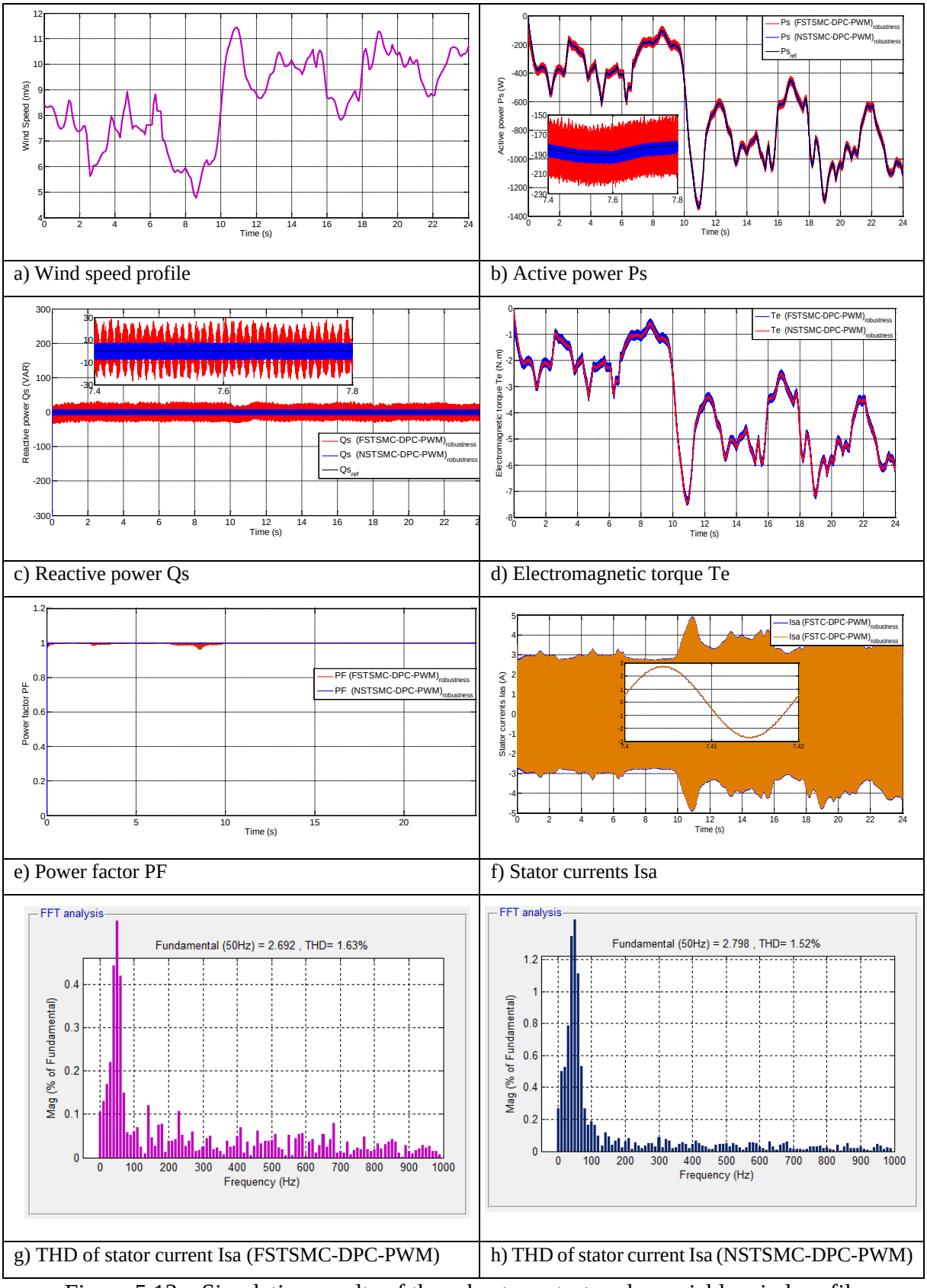
e) Power factor PF

f) Stator currents Isa

g) THD of stator current Isa (FSTSMC-DPC-PWM)

h) THD of stator current Isa (NSTSMC-DPC-PWM)

Figure 5.12 - Simulation results of the robustness test under step wind profile.



a) Wind speed profile

b) Active power Ps

c) Reactive power Qs

d) Electromagnetic torque Te

e) Power factor PF

f) Stator currents Isa

g) THD of stator current Isa (FSTSMC-DPC-PWM)

h) THD of stator current Isa (NSTSMC-DPC-PWM)

Figure 5.13 – Simulation results of the robustness test under variable wind profile

These results (Figures 5.12 and 5.13) show that the active and reactive power curves of the two control methods—FSTSMC-DPC-PWM and NSTSMC-DPC-PWM—have been significantly impacted by the excessive parametric variation applied to the DFIG model. Both the DFIG's transient and steady-state working modes showed these impacts. The power curves' response times increased slightly for both approaches in the transient regimes. Disturbances in the results were noted, nevertheless, and they were more noticeable in the responses of the FSTSMC-DPC-PWM control than the NSTSMC-DPC-PWM control in steady-state regimes.

The FSTSMC-DPC-PWM, which is based on fuzzy logic, has the benefit of dynamically modifying the control parameters to better adapt the system to changes while handling nonlinearities and uncertainties in the system. By mitigating the chattering impact that sliding mode control frequently causes, fuzzy logic helps to improve overall performance in terms of lowering oscillations, boosting stability, and boosting robustness.

Conversely, the artificial neural network (ANN)-based NSTSMC-DPC-PWM gains from its capacity to pick up on and adjust to intricate patterns in the behavior of the system. By effectively adjusting parameters in real time, the ANN strengthens the control system's resilience, particularly when dealing with nonlinearities and changes in parameters. The system's resilience is increased by this extra layer of intelligence, which enables NSTSMC-DPC-PWM to handle disturbances better as seen by its improved steady-state performance.

As can be seen from the accompanying figures, both approaches exhibit a great degree of robustness. However, the neural network-based technique in NSTSMC-DPC-PWM clearly has an edge in preserving stability and flexibility under a variety of operating situations. Using a changeable wind profile, this test aims to demonstrate the tracking effectiveness and control of the suggested command. Mainly, these real-time experimental results confirm the inferences made from the numerical simulation. The experimental and numerical experiments behaved nearly identically.

5.5. Processor-in-the-Loop (PIL) test

The Processor-in-the-Loop (PIL) test was conducted to validate the real-time performance of the developed control strategies, namely FSTSMC-DPC-PWM and NSTSMC-DPC-PWM, for the Doubly Fed Induction Generator (DFIG). The PIL testing methodology integrates the control algorithms directly onto a target processor, allowing for the evaluation of computational efficiency, response time, and overall system behavior under realistic operating conditions. This

is crucial for confirming that the control strategies can be successfully deployed in real-world applications without significant performance degradation [100].

The FSTSMC-DPC-PWM strategy, leveraging fuzzy logic for improved adaptability and robustness, demonstrated its ability to handle nonlinearities and uncertainties effectively. Similarly, the NSTSMC-DPC-PWM, based on artificial neural networks, showcased its learning capabilities by dynamically optimizing control parameters in real time. Both strategies were tested under various scenarios, simulating different wind profiles and grid conditions. The results of the PIL tests showed that both control methods maintained excellent stability, minimized harmonic distortion, and enhanced power quality, with NSTSMC-DPC-PWM exhibiting superior robustness and faster adaptation to parameter changes. These PIL tests confirm the feasibility and efficiency of the developed control strategies for DFIGs in practical applications, proving their readiness for real-time implementation [101].

5.4.1. PIL test with dSPACE 1104

- **dSPACE 1104 controller board**

The dSPACE DS1104 R&D Controller Board is a high-performance tool designed for real-time control applications, particularly useful in research and development. With its seamless integration into MATLAB/Simulink, it enables rapid prototyping and efficient testing of control algorithms for real-world applications. This board is well-suited for a range of systems, including power electronics, electrical drives, renewable energy, and robotics, due to its significant computational power, real-time processing capabilities, and extensive input/output (I/O) options [102].

- **Specifications**

Processor: The DS1104 is equipped with a Motorola PowerPC 603e processor running at 250 MHz, optimized for executing real-time control tasks efficiently. It facilitates fast control loop processing, crucial for high-speed applications [103].

- **Input/Output Ports:**

- Analog Inputs: 8 differential 16-bit analog inputs with a sampling rate of up to 200 kHz for precise sensor data acquisition (e.g., current, voltage) [104].
- Analog Outputs: 8 analog outputs, each 16-bit, used to send control signals to actuators like inverters or motor controllers.
- Digital I/O: 20 digital I/O lines allow for interaction with various digital devices, such as encoders or switches.
- PWM Outputs: 4 PWM channels generate control signals for switching devices like IGBTs or MOSFETs, essential for applications such as motor control.

- Encoder Inputs: 2 incremental encoder interfaces provide accurate feedback for position and speed control, often needed for motors or wind turbines.
- Timers/Counters: The board offers multiple timers and counters for critical real-time tasks, such as precise PWM signal generation and event scheduling [100].

➢ **Communication Interfaces:**

RS232 serial communication enables easy interfacing with external systems or logging data. CAN Bus support allows for real-time communication with automotive and industrial devices, ideal for controlling and monitoring systems like motor drives or grid-connected converters.

➢ **Real-Time Control Features**:

- Fast ADC/DAC converters handle real-time data acquisition and output, ensuring that analog signals are processed quickly and accurately.
- High-priority interrupts ensure time-sensitive tasks are executed immediately, critical for fast control loops.
- The Real-Time Operating System (RTOS) guarantees deterministic execution of control algorithms, enabling precise task scheduling.

➢ Development Environment:

The DS1104's compatibility with MATLAB/Simulink and the dSPACE Real-Time Interface (RTI) offers a graphical environment for designing, simulating, and deploying control systems in real-time. This approach accelerates the development cycle and simplifies testing, making it ideal for complex system designs [98].

➢ **Advantages:**

- Rapid Prototyping: The model-based design in Simulink allows for quick prototyping without manual coding, making the board ideal for applications like wind energy systems, motor control, and power electronics.
- High Accuracy: The 16-bit resolution for both analog inputs and outputs provides exceptional accuracy, essential for applications like motor control and power converters.
- Real-Time Performance: The 250 MHz processor ensures that control loops are processed with minimal latency, making the DS1104 ideal for high-speed real-time applications.
- Versatile I/O: With extensive analog, digital, PWM, and encoder I/O options, the DS1104 can interface with a wide variety of sensors, actuators, and communication systems common in industrial and research applications [99].

- **Comparison with Other Platforms :**

- FPGA: Although FPGAs offer faster processing and higher parallelism, they require specialized hardware programming knowledge and are less integrated with Simulink. The DS1104 offers a more user-friendly, flexible solution for real-time control applications.
- STM32/Raspberry Pi: These low-cost alternatives lack the computational power and real-time control precision of the DS1104, making them better suited for simpler applications. The DS1104 excels in tasks requiring high accuracy, speed, and stability.

- **Application Areas:**

The DS1104 is ideal for research and development in fields such as:

- Power Electronics: Precision control of inverters and converters using real-time modulation techniques.
- Electric Drives: Advanced motor control strategies like Field-Oriented Control (FOC), Direct Torque Control (DTC), and sliding mode control.
- Renewable Energy Systems: Control of wind turbines, photovoltaic systems, and energy storage systems with minimal harmonic distortion and high efficiency [100].

Robotics: Real-time control of robotic systems requiring precise movement and feedback control.

The Processor-in-the-Loop (PIL) test was conducted to validate the real-time performance of the developed control strategies, namely FSTSMC-DPC-PWM and NSTSMC-DPC-PWM, for the Doubly Fed Induction Generator (DFIG). The PIL testing methodology integrates the control algorithms directly onto a target processor, allowing for the evaluation of computational efficiency, response time, and overall system behavior under realistic operating conditions. This is crucial for confirming that the control strategies can be successfully deployed in real-world applications without significant performance degradation [102].

The FSTSMC-DPC-PWM strategy, leveraging fuzzy logic for improved adaptability and robustness, demonstrated its ability to handle nonlinearities and uncertainties effectively. Similarly, the NSTSMC-DPC-PWM, based on artificial neural networks, showcased its learning capabilities by dynamically optimizing control parameters in real time. Both strategies were tested under various scenarios, simulating different wind profiles and grid conditions. The results of the PIL tests showed that both control methods maintained excellent stability, minimized harmonic distortion, and enhanced power quality, with NSTSMC-DPC-PWM exhibiting superior robustness and faster adaptation to parameter changes. These PIL tests

confirm the feasibility and efficiency of the developed control strategies for DFIGs in practical applications, proving their readiness for real-time implementation [103].

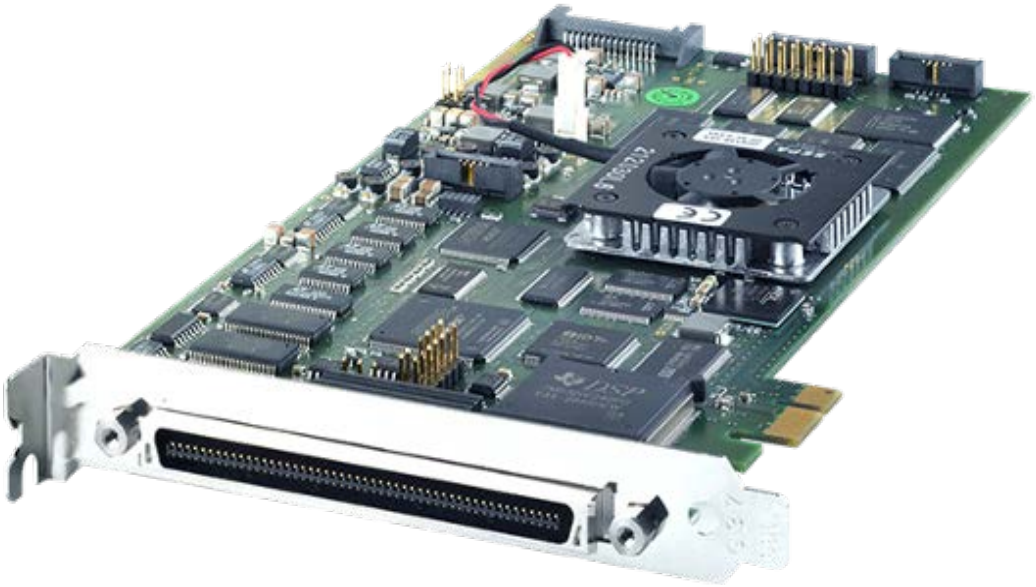


Figure 5.14 - dSPACE DS1104 R&D controller board.

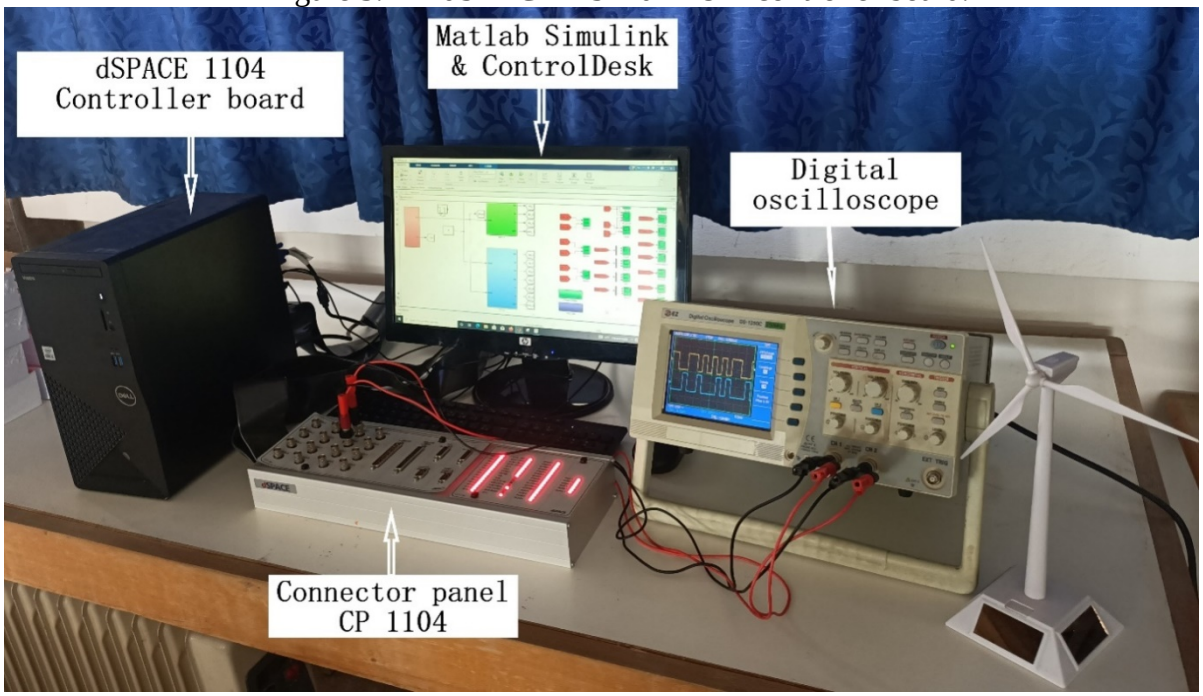
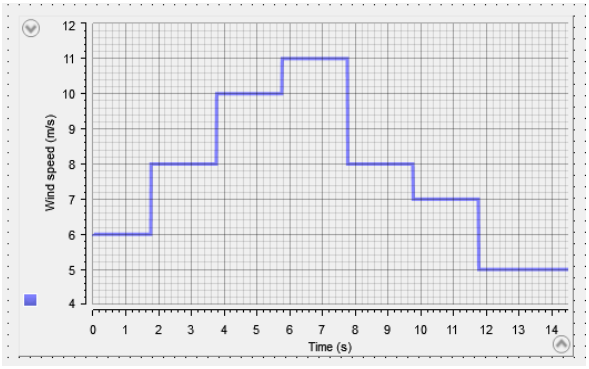


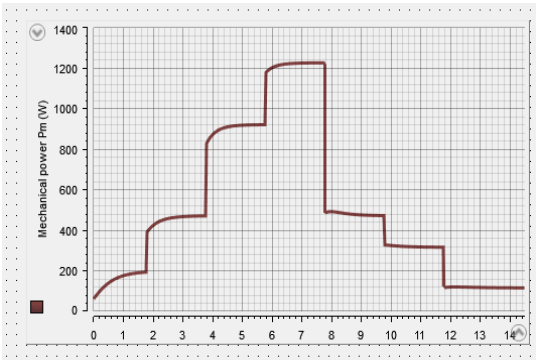
Figure 5-15 - PIL test setups of innovative proposed control strategies.

❖ **PIL test results**

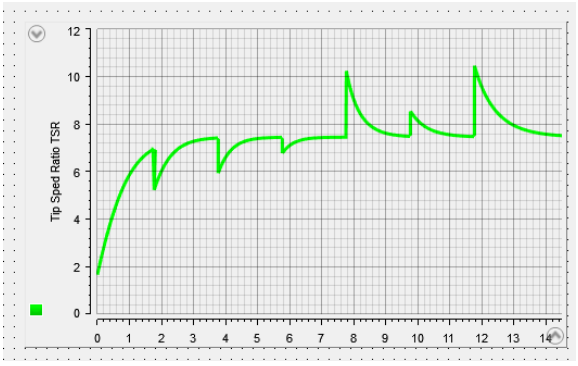
The following figures present the results of the Processor-in-the-Loop (PIL) test (Figure 5.16 and figure 5.17).



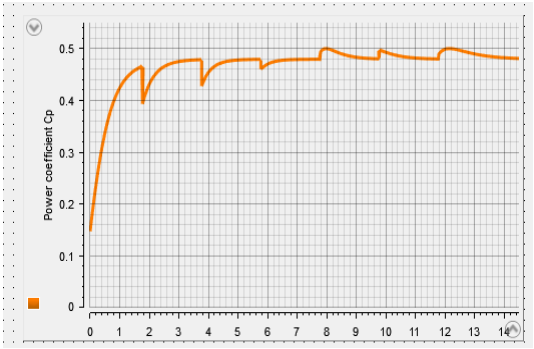
a) Wind speed profile



b) Mechanical power Pm



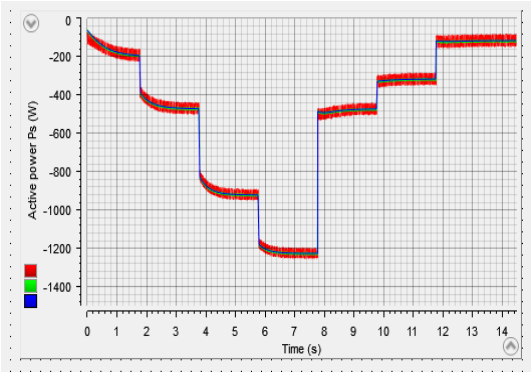
c) Tip Speed Ratio



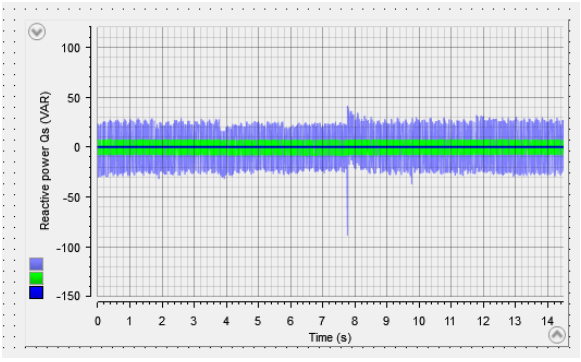
d) Power coefficient Cp



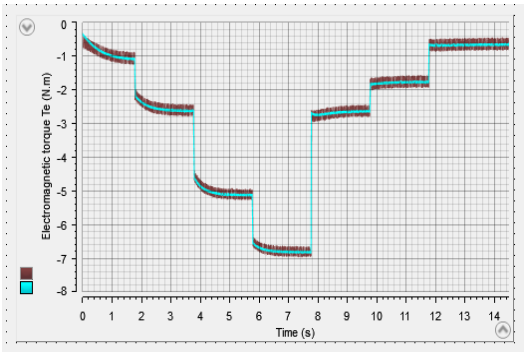
e) Power factor PF



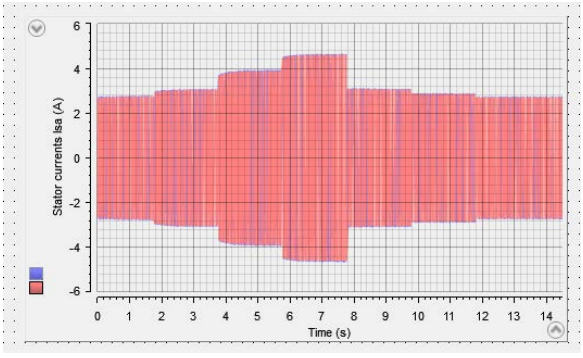
f) Active power Ps



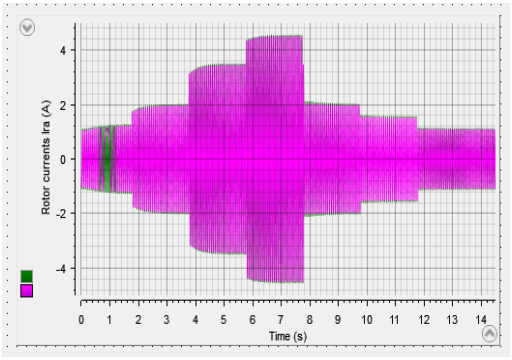
g) Reactive power Qs



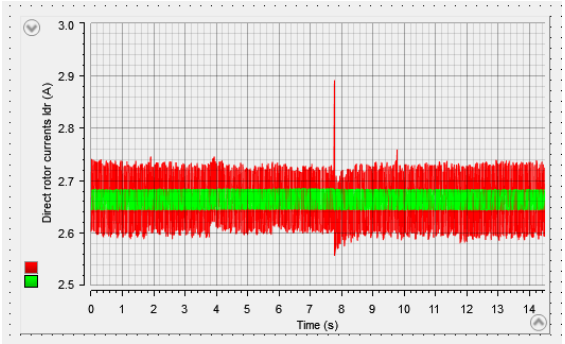
h) Electromagnetic torque Te



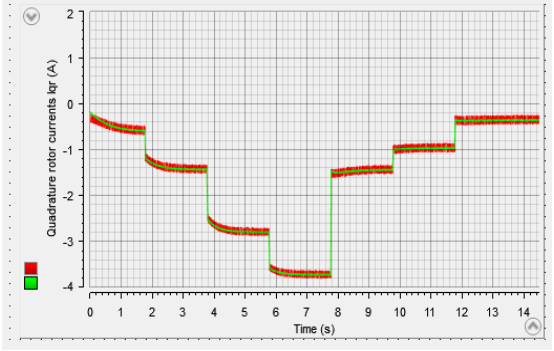
i) Stator currents Isa



j) Rotor currents Ira

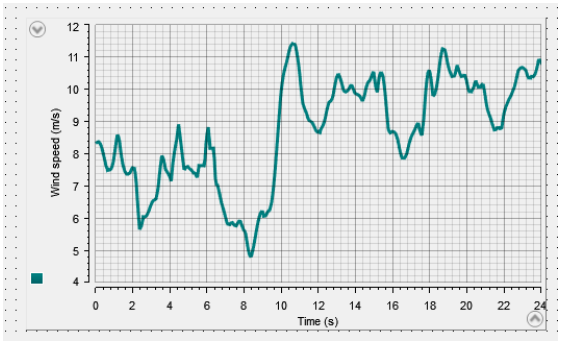


k) Direct rotor currents Idr



l) Quadrature rotor currents Iqr

Figure 5.16 - Results of PIL test under step wind profile



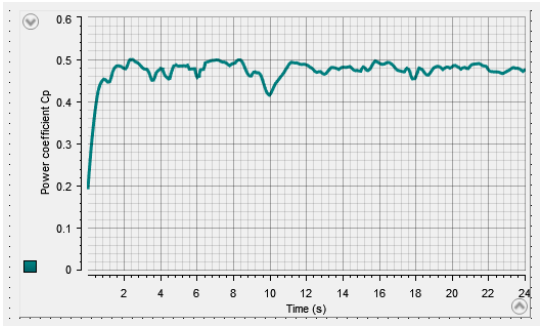
a) Variable wind speed profile



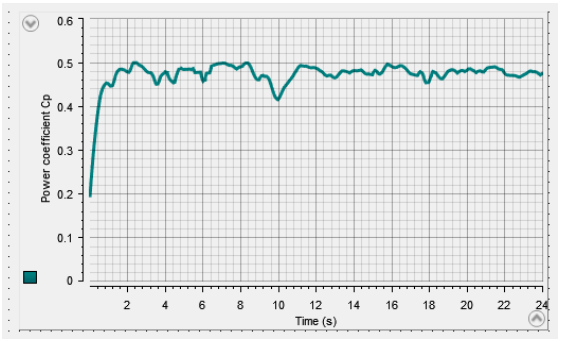
b) Mechanical power Pm



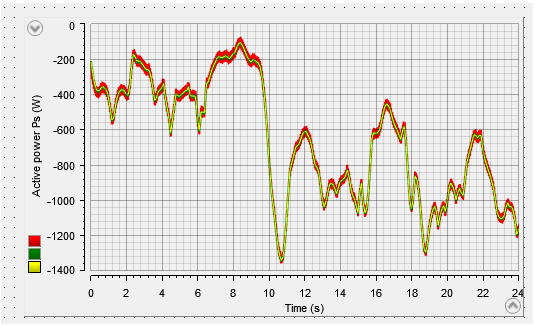
c) Tip Speed Ratio TSR



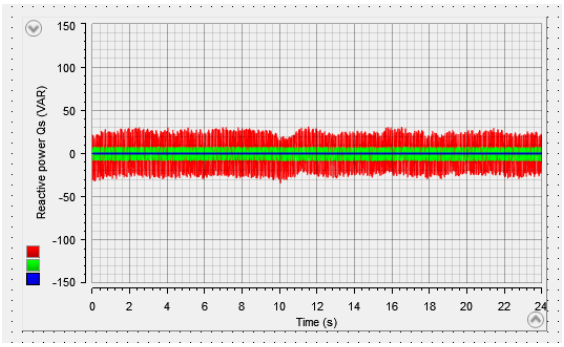
d) Power coefficient Cp



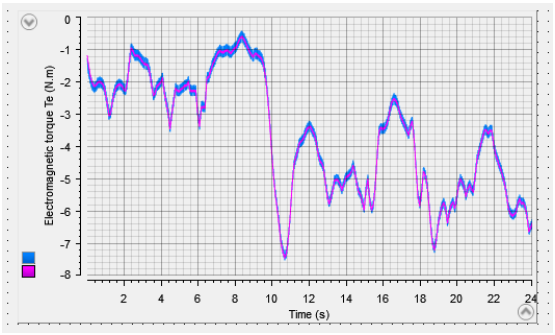
e) Power factor PF



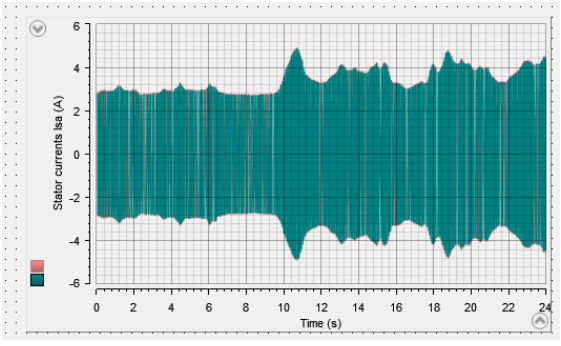
f) Active power Ps



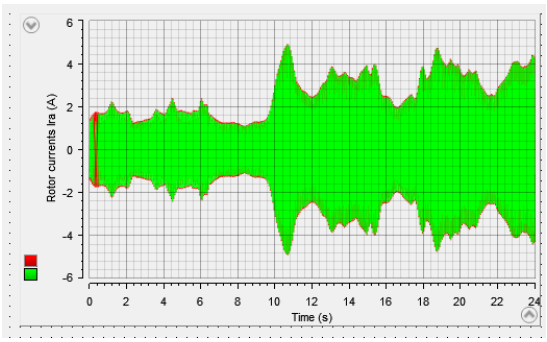
g) Reactive power Qs



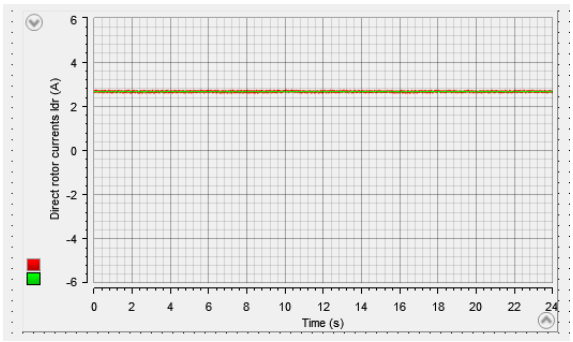
h) Electromagnetic torque Te



i) Stator currents Isa



j) Rotor currents Ira



k) Direct rotor currents Idr



l) Quadrature rotor currents Iqr

Figure 5.17 - Results of PIL test under variable wind profile

The purpose of the Processor-In-the-Loop (PIL) test is to verify how well control algorithms work on real hardware, like a Dspace 1104 This approach replicates the operational environment using simulation tools, but it also models situations close to reality. Prior to a system's complete implementation, the primary objective is to evaluate the control techniques' response time, computational efficiency, and real-time performance. It is feasible to assess how well the FSTSMC-DPC-PWM and NSTSMC-DPC-PWM control strategies function in terms of stability, ripple minimization, and overall system efficiency while taking the processing constraints and response capabilities of the actual hardware into account by putting them through the PIL test.

The results of the Processor-In-the-Loop (PIL) test using the dSPACE 1104 controller board were found to be highly consistent and matched those of MATLAB Simulink simulations for every significant performance parameter. More precisely, there was no difference in the mechanical power P_m—a crucial component in figuring out the energy conversion efficiency—between the simulated and real-time results. Similarly, the Tip Speed Ratio (TSR), an important parameter for determining the aerodynamic efficiency of the wind turbine, shows how precise the control algorithms utilized on the dSPACE 1104 board are. TSR was the same in both tests.

Furthermore, there were no differences in trends or values between the simulation and PIL tests for the power coefficient Cp, a measure of how well the system converts wind energy into mechanical power. As expected by the MATLAB/Simulink simulations, the dSPACE 1104 system maintained the intended value near unity in the power factor (PF), demonstrating this consistency. Reliability of the applied control techniques was confirmed by the matching values of the active power Ps and reactive power Qs, which are essential for assessing the electrical performance of the system in both simulated and real-time settings.

Furthermore, there was no discernible difference in the electromagnetic torque Te, which directly influences the dynamics of the system, between the PIL and the simulated findings, confirming the effectiveness of the control logic in real-time operation. The two test conditions showed identical levels of accuracy for the stator currents Isa and rotor currents Ira, as well as for the individual direct and quadrature rotor current components Idr and Iqr.

These findings verify that the NSTSMC-DPC-PWM and FSTSMC-DPC-PWM strategies, which were used on the dSPACE 1104 controller board, offer dependable real-time control performance that is consistent with the simulation-predicted results. The suggested control strategies' resilience is validated by the congruence of results across several parameters, such as mechanical, electrical, and electromagnetic properties. The seamless and efficient transfer from simulation to real-world application is made possible by this degree of consistency, which guarantees that the system can operate as intended under a variety of circumstances without sacrificing important performance indicators.

Given that wind turbines and other systems that depend on high-precision performance, the high degree of correlation found between the PIL test and the MATLAB Simulink simulations indicates that the control techniques are well-optimized for real-time deployment. The two sets of findings line flawlessly, confirming that the dSPACE 1104 board can handle complicated control tasks. This means that the system can perform as well in simulations as it does in real life when it comes to power output, stability, and response times.

5.6. Summary

This chapter presents the design of the Neural Super-Twisting Sliding Mode Control with PWM (NSTSMC-DPC-PWM) and compares it to the Fuzzy Super-Twisting Sliding Mode Control with PWM (FSTSMC-DPC-PWM). The comparison focuses on various performance metrics, particularly the Total Harmonic Distortion (THD), evaluated for four control strategies developed in this thesis. The analysis demonstrates the superior performance of NSTSMC-DPC-PWM, especially in terms of reducing THD and improving overall power quality compared to the FSTSMC-DPC-PWM.

A robustness test is conducted for both FSTSMC-DPC-PWM and NSTSMC-DPC-PWM to assess their resilience to parameter variations and external disturbances. The results indicate that both control strategies exhibit strong robustness, but the NSTSMC-DPC-PWM shows greater adaptability due to its neural network-based learning capabilities.

Additionally, the chapter discusses the Processor-in-the-Loop (PIL) tests performed on both FSTSMC-DPC-PWM and NSTSMC-DPC-PWM. These tests validate the real-time

implementation of the developed control strategies and confirm their effectiveness in managing dynamic wind conditions and ensuring reliable performance in real-world applications.

General conclusion and perspectives

Wind energy stands as an eco-friendly and sustainable alternative that could potentially become the leading source of renewable energy in the coming decades. To achieve this, it is essential to advance technologies for wind energy conversion and ensure high-quality electricity production.

Wind energy conversion systems based on Doubly-Fed Induction Generators (DFIG) are characterized by complex dynamics and nonlinear behaviors, with parameters that can vary unpredictably over time. Therefore, it is crucial to develop control strategies that can manage these challenges and maintain stable and efficient performance, despite uncertainties in modeling and parameter variations.

The objective of this thesis is to enhance the performance of a wind energy conversion system based on a Doubly Fed Induction Generator (DFIG) to maximize power extraction and supply energy to the electrical grid with minimal harmonics.

The first chapter provides an overview wind energy conversion system.

To begin designing control strategies, it was essential first to model and study the wind energy conversion chain. This includes modeling the wind turbine, the Doubly-Fed Induction Generator (DFIG), and the power electronic converters, as detailed in Chapter 2.

In chapter 3, the direct power control method was examined. This strategy utilizes two hysteresis comparators and a switching table. Simulation results revealed that this method lacks robustness in the face of variations in the parameters of the doubly-fed induction generator (DFIG). Specifically, the generated power exhibits significant fluctuations, and the stator currents show a high level of harmonic distortion.

To enhance the performance of the wind energy conversion system controlled by Direct Power Control (DPC), a nonlinear sliding mode controller was introduced in Chapter 3 to replace the hysteresis comparators in the DPC. However, to mitigate the chattering effect— a primary drawback of sliding mode control— and thus reduce power and current oscillations, a second-order super-twisting sliding mode control (STSMC) was presented and implemented for power regulation. This method involves replacing traditional sliding mode regulators with STSMC regulators. Simulation comparisons between DPC and STSMC-DPC control show that the latter significantly reduces power fluctuations and lowers the total harmonic distortion (THD) in the stator currents.

In Chapter 4, an enhancement of the proposed technique (STSMC-DPC) was introduced by replacing the Sign function of the Super-Twisting algorithm with a fuzzy logic block.

Simulation results show that the STSMC-DPC technique improved with fuzzy logic offers significant performance benefits. These improvements are reflected in reduced fluctuations in active and reactive power, decreased harmonic distortion rates of stator currents, as well as a reduction in steady-state error (SSE) and overshoot.

The remarkable improvements achieved through the use of fuzzy logic encouraged us to explore another artificial intelligence technique, namely artificial neural networks. Thus, in Chapter 5, we replaced the sign function of the STSMC-DPC controller with an artificial neural network block. The Neural-STSMC-DPC controller provides the lowest levels of power oscillations, overshoot, steady-state error (SSE), and current harmonics, while ensuring excellent precision and robustness. Additionally, this precise power control improves the efficiency of the conversion chain, which is a crucial criterion for high-power wind turbines.

For all the work carried out in this thesis, several interesting perspectives are envisaged:

- Explore the use of other control techniques, such as third-order sliding mode control and control the GSC.
- Apply the proposed control methods to enhance the performance of DFIGs in the presence of faults.
- Integrate multi-objective optimization techniques to simultaneously optimize multiple criteria, thereby obtaining various Pareto-optimal solutions that can be selected based on specific requirements.
- Extend the application of the proposed controller to other conversion systems based on Permanent Magnet Synchronous Machines (PMSG).
- Test the proposed controls for double rotor wind systems (counter rotating wind turbines).

References

1. YW. Qiao, Integrated Control of Wind Farms , Facts Devices and the Power Network Using Neural Networks and Adaptive Critic Designs. PhD thesis, Georgia Institute of Technology,2008.

2. P. Tchakoua, R. Wamkeue, M. Ouhrouche, F. Slaoui-hasnaoui, T. A. Tameghe, and G. Ekemb, \Wind Turbine Condition Monitoring : State-of-the-Art Review, New Trends, and Future Challenges," Energies, pp. 2595{2630, 2014.

3. GWEC, \Global Wind Report. Annual Market Update 2017," tech. rep., Global Wind Energy Council, 2018.

4. H. Benbouhenni, N. Bizon, I. Colak, M. I. Mosaad, M. Yessef, “Direct active and reactive powers control of double-powered asynchronous generators in multi-rotor wind power systems using modified synergetic control,” Energy Reports, Vol. 10, pp. 4286-4301, 2023. https://doi.org/10.1016/j.egyr.2023.10.085.

5. Ayrir, W. (2019). Amélioration de la commande directe du couple d'une éolienne à base d'une génératrice asynchrone doublement alimentée par la logique floue (Doctoral dissertation, Abdelmalek Essaadi University, Faculty of Sciences, Tetouan).

6. GASMI, H. (2023). Contribution à l'amélioration de la commande des chaînes de conversion éoliennes (Doctoral dissertation, Université 8 Mai 1945, Guelma).

7. YAHDOU, A. (2017). Commande Hybride par Mode Glissant d’Ordre 2 d’un Système Éolien à Double Rotor (Doctoral dissertation, École Nationale Polytechnique El Harrach, Algiers, Algeria).

8. R. M. Prasad and M. A. Mulla, "Rotor Position-Sensorless Algorithms for Direct Power Control of Rotor-Tied DFIG," in IEEE Transactions on Power Electronics, vol. 36, no. 6, pp. 6213-6217, June 2021, doi: 10.1109/TPEL.2020.3040705.

9. J. Mohammadi, S. Vaez-Zadeh, S. Afsharnia and E. Daryabeigi, "A Combined Vector and Direct Power Control for DFIG-Based Wind Turbines," in IEEE Transactions on Sustainable Energy, vol. 5, no. 3, pp. 767-775, July 2014, doi: 10.1109/TSTE.2014.2301675.

10. S. Ahmad et al., "Direct Power Control Based on Point of Common Coupling Voltage Modulation for Grid-Tied AC Microgrid PV Inverter," in IEEE Access, vol. 10, pp. 109187-109202, 2022, doi: 10.1109/ACCESS.2022.3213939.

11. H. Chojaa, A. Derouich, S.E. Chehaidia, O. Zamzoum, M. Taoussi, H. Benbouhenni, S. Mahfoud, “Enhancement of Direct Power Control by Using Artificial Neural Network for a Doubly Fed Induction Generator-Based WECS: An Experimental Validation,” Electronics, Vol. 11, 4106, 2022. https://doi.org/10.3390/electronics1124410.
12. A. Yousefi-Talouki, S. Zalzar, E. Pouresmaeil, “Direct Power Control of Matrix Converter-Fed DFIG with Fixed Switching Frequency,” Sustainability, Vol. 11, 2604, 2019. https://doi.org/10.3390/su11092604.

13. B. Habib, “Application of DPC and DPC-GA to the dual-rotor wind turbine system with DFIG,” International Journal of Robotics and Automation, Vol.10, No.3, pp. 224-234, 2021. Doi: 10.11591/ijra.v10i3.pp224-234.

14. H. Benbouhenni, Z. Boudjema, A. Belaidi, “Power Control of DFIG in WECS Using DPC and NDPC-NPWM Methods,” Mathematical Modelling of Engineering Problems, Vol. 7, No. 2, pp. 223-236, 2020.

15. S. Khateri-abri, S. Tohidi and N. Rostami, “Improved Direct Power Control of DFIG Wind Turbine by using a Fuzzy Logic Controller,” 2019 10th International Power Electronics, Drive Systems and Technologies Conference (PEDSTC), Shiraz, Iran, 2019, pp. 458-463, doi: 10.1109/PEDSTC.2019.8697581.

16. L. Shang and J. Hu, “Sliding-Mode-Based Direct Power Control of Grid-Connected Wind-Turbine-Driven Doubly Fed Induction Generators Under Unbalanced Grid Voltage Conditions,” in IEEE Transactions on Energy Conversion, vol. 27, no. 2, pp. 362-373, June 2012, doi: 10.1109/TEC.2011.2180389.

17. H. Benbouhenni, “Synergetic control theory scheme for asynchronous generator based dual-rotor wind power,” Journal of Electrical Engineering, Electronics, Control and Computer Science, Vol.7, No.4, 2021.

18. P. Xiong and D. Sun, “Backstepping-Based DPC Strategy of a Wind Turbine-Driven DFIG Under Normal and Harmonic Grid Voltage,” in IEEE Transactions on Power Electronics, vol. 31, no. 6, pp. 4216-4225, June 2016, doi: 10.1109/TPEL.2015.2477442.

19. S. Ouchen, M. Benbouzid, F. Blaabjerg, A. Betka and H. Steinhart, “Direct Power Control of Shunt Active Power Filter Using Space Vector Modulation Based on Supertwisting Sliding Mode Control,” in IEEE Journal of Emerging and Selected Topics in Power Electronics, vol. 9, no. 3, pp. 3243-3253, June 2021, doi: 10.1109/JESTPE.2020.3007900.

20. Y. Han, R. Ma, “Adaptive-Gain Second-Order Sliding Mode Direct Power Control for Wind-Turbine-Driven DFIG under Balanced and Unbalanced Grid Voltage,” Energies, 12, 3886, 2019. https://doi.org/10.3390/en12203886.

21. B. Habib, Z. Boudjema, N. Bizon, P. Thounthong, N. Takorabet, “Direct Power Control Based on Modified Sliding Mode Controller for a Variable-Speed Multi-Rotor Wind Turbine System Using PWM Strategy,” Energies, Vol. 15, No. 10, 2022. https://doi.org/10.3390/en15103689.

22. B. Habib, S. Lemdani, “Combining synergetic control and super twisting algorithm to reduce the active power undulations of doubly fed induction generator for dual-rotor wind turbine system,” Electrical Engineering & Electromechanics, 2021, No. 3, pp. 8-17, 2021. doi: https://doi.org/10.20998/2074-272X.2021.3.02.
23. B. Habib, N. Bizon, I. Colak, P. Thounthong, N. Takorabet, “Application of Fractional-Order PI Controllers and Neuro-Fuzzy PWM Technique to Multi-Rotor Wind Turbine Systems,” Electronics 2022, 11, 1340. https://doi.org/10.3390/electronics11091340.

24. B. Habib, “A direct power control of the doubly fed induction generator based on the three-level NSVPWM technique,” International Journal of Smart Grid, Vol. 3, No. 4, 2019.

25. H. Benbouhenni, D. Zellouma, N. Bizon, I. Colak, “A new PI(1 +PI) controller to mitigate power ripples of a variable-speed dual-rotor wind power system using direct power control,” Energy Reports, Vol. 10, pp. 3580-3598, 2023. https://doi.org/10.1016/j.egyr.2023.10.007.

26. H. Benbouhenni, “Twelve sectors DPC control based on neural hysteresis comparators of the DFIG integrated to wind power,” TECNICA ITALIANA-Italian Journal of Engineering Science, Vol. 64, No. 2, pp. 223-236, 2020.

27. M. Yessef, H. Benbouhenni, M. Taoussi, A. Lagrioui, I. Colak, B. Bossoufi and T. A. H. Alghamdi, "Experimental validation of feedback PI controllers for multi-rotor wind energy conversion systems," in IEEE Access, 2024. doi: 10.1109/ACCESS.2024.3351355.

28. H. Benbouhenni, “24-sectors DPC-FNN method of DFIG integrated to dual-rotor wind turbine,” International Journal of Applied Power Engineering (IJAPE), Vol. 10, No. 4, 2021.

29. H. Benbouhenni, E. Bounadja, H. Gasmi, N. Bizon, I. Colak, “A new PD(1+PI) direct power controller for the variable-speed multi-rotor wind power system driven doubly-fed asynchronous generator,” Energy Reports, Vol. 8, pp. 15584-15594, 2022. https://doi.org/10.1016/j.egyr.2022.11.136.

30. H. Benbouhenni, I. Colak, N. Bizon, “Application of genetic algorithm and terminal sliding surface to improve the effectiveness of the proportional–integral controller for the direct power control of the induction generator power system,” Engineering Applications of Artificial Intelligence, Vol. 125, 106681, 2023. https://doi.org/10.1016/j.engappai.2023.106681.

31. H. Benbouhenni, Fayçal Mehedi, Lemdani Soufiane, “New direct power synergetic-SMC technique based PWM for DFIG integrated to a variable speed dual-rotor wind power,” Automatika, Vol. 63, No.4, pp.718-731, 2022. DOI: 10.1080/00051144.2022.2065801.

32. B. Habib, “Direct active and reactive powers command with third-order sliding mode theory for DFIG-based dual-rotor wind power systems,” International Journal of Natural and Engineering Sciences, Vol.15, No.1, pp. 17-34, 2021.

33. H. Benbouhenni et al., “Fractional-order synergetic control of the asynchronous generator-based variable-speed multi-rotor wind power systems,” in IEEE Access, vol. 11, pp. 133490-133508, doi: 10.1109/ACCESS.2023.3335902.
34. H. Benbouhenni, H. Gasmi, I. Colak, N. Bizon & P. Thounthong, “Synergetic-PI controller based on genetic algorithm for DPC-PWM strategy of a multi-rotor wind power system,” Scientific Report, Vol.13, 13570, 2023. https://doi.org/10.1038/s41598-023-40870-7.

35. H. Benbouhenni, N. Bizon, “A new direct power control method of the DFIG-DRWT system using neural PI controllers and four-level neural modified SVM technique,” Journal of Applied Research and Technology, Vol. 21, No. 1, pp. 36-55, 2023.

36. H. Benbouhenni, N. Bizon, P. Thounthong, I. Colak, P. Mungporn, “A new integral-synergetic controller for direct reactive and active powers control of a dual-rotor wind system,” Measurement and Control, 2023. https://doi.org/10.1177/00202940231195117.

37. H. Benbouhenni, “A comparison study between fuzzy PWM and SVM inverter in NSMC control of stator active and reactive power control of a DFIG based wind turbine systems,” International Journal of Applied Power Engineering (IJAPE), Vol. 8, No. 1, pp. 78-92, 2019.

38. H. Benbouhenni, Z. Boudjema, A. Belaidi, “Comparison study between NPWM and NSVPWM strategy in FSMC control of stator reactive and active powers control of a DFIG-based wind turbine system,” International Journal of Applied Power Engineering (IJAPE), Vol. 9, No. 2, pp. 159-172, 2020.

39. H. Benbouhenni, “ANFIS-sliding mode control of a DFIG supplied by a two-level SVPWM technique for wind energy conversion system,” International Journal of Applied Power Engineering (IJAPE), Vol. 9, No. 1, pp. 36-47, 2020.

40. H. Benbouhenni, N. Bizon, I. Colak, “A Brief Review of Space Vector Modulation (SVM) Methods and a New SVM Technique Based on the Minimum and Maximum of the Three-Phase Voltages,” Iranian Journal of Electrical & Electronic Engineering, Vol. 18, No. 3, pp.1-18, 2022. Doi:10.22068/IJEEE.18.3.2358.

41. H. Benbouhenni, “Comparative study between NSVM and FSVM strategy for a DFIG-based wind turbine system controlled by neuro-second order sliding mode,” Majlesi Journal of Mechatronic Systems, Vol. 7, No. 1, pp. 33-43, 2018.

42. F. Echiheb, Y. Ihedrane, B. Bossoufi, et al., “Robust sliding-Backstepping mode control of a wind system based on the DFIG generator,” Sci Rep, vol. 12, 11782, 2022. https://doi.org/10.1038/s41598-022-15960-7.

43. L. Djilali, A. Badillo-Olvera, Y. Yuliana Rios, H. López-Beltrán and L. Saihi, “Neural High Order Sliding Mode Control for Doubly Fed Induction Generator based Wind Turbines,” in IEEE Latin America Transactions, vol. 20, no. 2, pp. 223-232, Feb. 2022, doi: 10.1109/TLA.2022.9661461.

44. H. Benbouhenni, H. Gasmi, N. Bizon, “Direct Reactive and Active Power Regulation of DFIG using an Intelligent Modified Sliding-Mode Control Approach,” International Journal of Smart Grid-ijSmartGrid, Vol. 6, No. 4, pp. 157-172, 2022. https://doi.org/10.20508/ijsmartgrid.v6i4.266.g229.

45. H. Benbouhenni, I. Colak, N. Bizon, E. Abdelkarim, “Fractional-order neural control of a DFIG supplied by a two-level PWM inverter for dual-rotor wind turbine system,” Measurement and Control, In Press, pp. 1-18, 2023.

46. H. Benbouhenni, N. Bizon, M. I. Mosaad, I. Colak, A. B. Djilali, H. Gasmi, “Enhancement of the power quality of DFIG-based dual-rotor wind turbine systems using fractional order fuzzy controller,” Expert Systems with Applications, Vol. 238, No. Part A, 121695, 2024. https://doi.org/10.1016/j.eswa.2023.121695.

47. Y. Kali et al., “Time Delay Estimation Based Discrete-Time Super-Twisting Current Control for a Six-Phase Induction Motor,” in IEEE Transactions on Power Electronics, vol. 35, no. 11, pp. 12570-12580, Nov. 2020, doi: 10.1109/TPEL.2020.2995773.

48. Y. Tang, Y. Zhang, A. Hasankhani and J. Van Zwieten, “Adaptive Super-Twisting Sliding Mode Control for Ocean Current Turbine-Driven Permanent Magnet Synchronous Generator,” 2020 American Control Conference (ACC), Denver, CO, USA, 2020, pp. 211-217, doi: 10.23919/ACC45564.2020.9147480.

49. S. Mao, H. Tao and Z. Zheng, “Sensorless Control of Induction Motors Based on Fractional-Order Linear Super-Twisting Sliding Mode Observer With Flux Linkage Compensation,” in IEEE Access, vol. 8, pp. 172308-172317, 2020, doi: 10.1109/ACCESS.2020.3024626.

50. L. Guo, H. Wang, N. Jin, L. Dai, L. Cao and K. Luo, "A Speed Sensorless Control Method for Permanent Magnet Synchronous Motor Based on Super-Twisting Sliding Mode Observer," 2019 14th IEEE Conference on Industrial Electronics and Applications (ICIEA), Xi'an, China, 2019, pp. 1179-1184, doi: 10.1109/ICIEA.2019.8834074.

51. Y. Kali, J. Rodas, M. Saad, R. Gregor, K. Benjelloun and J. Doval-Gandoy, "Current control based on super-twisting algorithm with time delay estimation for a five-phase induction motor drive," 2017 IEEE International Electric Machines and Drives Conference (IEMDC), Miami, FL, USA, 2017, pp. 1-8, doi: 10.1109/IEMDC.2017.8002122.

52. Y. M. Alharbi, A. A. A. Alahmadi, N. Ullah, H. Abeida, M. S. Soliman and Y. S. H. Khraisat, "Super Twisting Fractional Order Energy Management Control for a Smart University System Integrated DC Micro-Grid," in IEEE Access, vol. 8, pp. 128692-128704, 2020, doi: 10.1109/ACCESS.2020.3008858.

53. M. Yessef, B. Bossoufi, M. Taoussi, H. Benbouhenni, A. Lagrioui, H. Chojaa, “Intelligent Direct Power Control Based on the Neural Super-Twisting Sliding Mode Controller of a DFIG,” In: Motahhir, S., Bossoufi, B. (eds) Digital Technologies and Applications. ICDTA 2023. Lecture Notes in Networks and Systems, vol. 669, 2023. Springer, Cham. https://doi.org/10.1007/978-3-031-29860-8_73.

54. I. Sami, S. Ullah, S. U. Amin, A. Al-Durra, N. Ullah and J. -S. Ro, "Convergence Enhancement of Super-Twisting Sliding Mode Control Using Artificial Neural Network for DFIG-Based Wind Energy Conversion Systems," in IEEE Access, vol. 10, pp. 97625-97641, 2022, doi: 10.1109/ACCESS.2022.3205632.
55. B. Habib, “A Novel Direct Active and Reactive Power Control Method Using Fuzzy Super Twisting Algorithms and Modified Space Vector Modulation Technique for an Asynchronous Generator-based Dual-rotor Wind Powers,” Iranian (Iranica) Journal of Energy and Environment, Vol.12, No.2, pp. 109-117, 2021.

56. B. Habib, Z. Boudjema, A. Belaidi, “Comparison study between neural STSM and ANFIS-STSM method in DPC control scheme of DFIG-based dual-rotor wind turbines,” International Journal of Mathematics and Computers in Simulation, Vol. 14, pp.73-86, 2020.

57. B. Habib, Z. Boudjema, A. Belaidi, “DPC based on ANFIS super-twisting sliding mode algorithm of a doubly-fed induction generator for wind energy system,” Journal Européen des Systèmes Automatisés, Vol. 53, No. 1, pp. 69-80, February, 2020.

58. H. Gasmi, H. Benbouhenni, Sofiane Mendaci, Ilhami Colak, “A new scheme of the fractional-order super twisting algorithm for asynchronous generator-based wind turbine,” Energy Reports, Vol.9, pp. 6311-6327, 2023. https://doi.org/10.1016/j.egyr.2023.05.267.

59. H. Gasmi, S. Mendaci, S. Laifa, Walid Kantas, H. Benbouhenni, “Fractional-order proportional-integral super twisting sliding mode controller for wind energy conversion system equipped with doubly fed induction generator,” J. Power Electron., Vol. 22, pp. 1357–1373, 2022. https://doi.org/10.1007/s43236-022-00430-0.

60. J. Ying, X. Yuan and J. Hu, "Inertia Characteristic of DFIG-Based WT Under Transient Control and its Impact on the First-Swing Stability of SGs," in IEEE Transactions on Energy Conversion, vol. 32, no. 4, pp. 1502-1511, 2017, doi: 10.1109/TEC.2017.2698521.

61. C. Wu, P. Cheng, H. Nian and F. Blaabjerg, "Rotor Current Oriented Control Method of DFIG-DC System Without Stator Side Sensors," in IEEE Transactions on Industrial Electronics, vol. 67, no. 11, pp. 9958-9962, 2020, doi: 10.1109/TIE.2019.2956415.

62. K. -J. Du, X. -P. Ma, Z. -X. Zheng, C. -S. Li, W. -X. Hu and K. -S. Dong, "LVRT Capability Improvement of DFIG-Based Wind Turbines With a Modified Bridge-Resistive-Type SFCL," in IEEE Transactions on Applied Superconductivity, vol. 31, no. 8, pp. 1-5, Nov. 2021, Art no. 5603005, doi: 10.1109/TASC.2021.3091114.

63. Z. Xie, X. Gao, S. Yang and X. Zhang, "Improved Fractional-order Damping Method for Voltage-controlled DFIG System Under Weak Grid," in Journal of Modern Power Systems and Clean Energy, vol. 10, no. 6, pp. 1531-1541, November 2022, doi: 10.35833/MPCE.2020.000843.

64. Z. -X. Zheng, C. -J. Huang, R. -H. Yang, X. -Y. Xiao and C. -S. Li, "A Low Voltage Ride Through Scheme for DFIG-Based Wind Farm With SFCL and RSC Control," in IEEE Transactions on Applied Superconductivity, vol. 29, no. 2, pp. 1-5, March 2019, Art no. 5601005, doi: 10.1109/TASC.2019.2891687.

65. L. Xiong, P. Li, H. Li, J. Wang, “Sliding Mode Control of DFIG Wind Turbines with a Fast Exponential Reaching Law,” Energies, 10, 1788, 2017. https://doi.org/10.3390/en10111788.

66. Z. Yuhan, W. Kun, S. Wei, L. Zhou, Z. Zhongzhong and J. G. Hao, “Back-Stepping Formation Control of Unmanned Surface Vehicles With Input Saturation Based on

Adaptive Super-Twisting Algorithm," in IEEE Access, vol. 10, pp. 114885-114896, 2022, doi: 10.1109/ACCESS.2022.3217237.

67. P. V. N. M. Vidal, E. V. L. Nunes and L. Hsu, "Output-Feedback Multivariable Global Variable Gain Super-Twisting Algorithm," in IEEE Transactions on Automatic Control, vol. 62, no. 6, pp. 2999-3005, June 2017, doi: 10.1109/TAC.2016.2609602.

68. S. Yin and X. Wang, "Super Twisting Control Design for HSPMSG Voltage Stabilization Based on Disturbance Observation Compensation," in IEEE Transactions on Energy Conversion, vol. 38, no. 2, pp. 1387-1395, June 2023, doi: 10.1109/TEC.2022.3215509.

69. H. Benbouhenni, "Stator current and rotor flux ripples reduction of DTC DFIG drive using FSTSMC algorithm," International Journal of Smart Grid, Vol. 3, No. 4, 2019.

70. D. E. Kamel, M. Abdelkader, B. Larbi, P.M. Alex, B. Van Den, "A comprehensive review of LVRT capability and sliding mode control of grid-connected wind-turbine-driven doubly fed induction generator. Automatika, vol. 57, no.4, pp. 922-935, 2016. DOI: 10.7305/automatika.2017.05.1813

71. F. Amrane, A. Chaiba, "A novel direct power control for grid-connected doubly fed induction generator based on hybrid artificial intelligent control with space vector modulation," Rev. Roum. Sci. Techn.-Electrotechn. Et Energ, vol.61, no.3, pp. 263-268, 2016.

72. I. Yaichi, A. Semmah, P. Wira, Y. Djeriri, "Super-twisting sliding mode control of a doubly-fed induction generator based on the SVM strategy. Periodica Polytechnica Electrical Engineering and Computer Science, vol. 63, no.3, pp.178–190, 2019.

73. E. Najib, D. Aziz, E. Abdelaziz, T. Mohammed, E. Youness, M. Khalid, B. Badre, "Direct torque control of doubly fed induction motor using three-level NPC inverter. Protection and Control of Modern Power Systems, vol. 17, no.4, pp. 1-9, 2019. https://doi.org/10.1186/s41601-019-0131-7.

74. B. Habib, N. Bizon, "Third-Order Sliding Mode Applied to the Direct Field-Oriented Control of the Asynchronous Generator for Variable-Speed Contra-Rotating Wind Turbine Generation Systems," Energies, vol.14, no.18, 5877, 2021. doi: 10.3390/en14185877

75. Y. Quan, L. Hang, Y. He, Y. Zhang, "Multi-Resonant-Based Sliding Mode Control of DFIG-Based Wind System under Unbalanced and Harmonic Network Conditions," Appl. Sci., vol. 9, 2019. https://doi.org/10.3390/app9061124.

76. S. Mahfoud, A. Derouich, A. Iqbal, N. El Ouanjli, "Ant-Colony optimization-direct torque control for a doubly fed induction motor: An experimental validation," Energy Reports, vol. 8, pp. 81-98, 2022. https://doi.org/10.1016/j.egyr.2021.11.239.

77. A. B. Moreira, T.A.D.S. Barros, V.S.D.C. Teixeira, R.R.D. Souza, M.V.D. Paula, E.R. Filho, "Control of Powers for Wind Power Generation and Grid Current Harmonics

Filtering From Doubly Fed Induction Generator: Comparison of Two Strategies. in IEEE Access, vol. 7, pp. 32703-32713, 2019. DOI: 10.1109/ACCESS.2019.2899456.

78. W. Ayrira, M. Ourahoua, B. El Hassounia, A. Haddib, “Direct torque control improvement of a variable speed DFIG based on a fuzzy inference system,” Mathematics and Computers in Simulation, vol. 167, pp. 308-324. 2020. https://doi.org/10.1016/j.matcom.2018.05.014.

79. M. Said, A. Derouich, N. El Ouanjli, M. El Mahfoud, “Enhancement of the Direct Torque Control by using Artificial Neuron Network for a Doubly Fed Induction Motor,” Intelligent Systems with Applications, Vol. 13, pp. 1-18, 2022, https://doi.org/10.1016/j.iswa.2022.20 0 060.

80. A. M. Mohamoud, H. Echiekh, I. Atil, “Enhanced control technique for a sensor-less wind driven doubly fed induction generator for energy conversion purpose,” Energy Reports, Vol. 7, pp. 5815-8333, 2021.

81. M. R. Bengourina, M. Rahil, S. Slani, L. Hassaine, “PSO based direct power control for a multifunctional grid connected photovoltaic system,” International Journal of Power Electronics and Drive System, Vol. 9, No. 2, pp. 610-621, 2018.

82. S. Younes, T. Salah, H. Farid, L. B. Sofia, B. Mohit, M. A. Mosleh, S. A. Mohammed, S. M. G. Sherif, “New intelligent direct power control of DFIG-based wind conversion system by using machine learning under variations of all operating and compensation modes,” Energy Reports, Vol. 7, pp. 6394–6412, 2021. https://doi.org/10.1016/j.egyr.2021.09.075.

83. S. Younes, T. Salah, L. B. Sofia, B. Mohit, S. M. G. Sherif, M. Z. Hossam, K. Salah, “Performance improvement of Hybrid System based DFIG-Wind/PV/Batteries connected to DC and AC grid by applying Intelligent Control,” Energy Reports, Vol. 9, pp. 2027-2043, 2023. https://doi.org/10.1016/j.egyr.2023.01.021.

84. B. Habib, H. Gasmi, I. Colak, “Intelligent Control Scheme of Asynchronous Generator-Based Dual-Rotor Wind Power System Under Different Working Conditions,” Majlesi Journal of Energy Management, Vol.11, No. 3, pp. 8-15, 2022. https://em.majlesi.info/index.php/em/article/view/494.

85. H. Ravikiran, M. Tukaram, “Modified Super Twisting algorithm based sliding mode control for LVRT enhancement of DFIG driven wind system,” Energy Reports, Vol. 8, pp. 3600–3613, 2022. https://doi.org/10.1016/j.egyr.2022.02.235.

86. H. Benbouhenni, I. Colak, N. Bizon, A. G. Mazare, P. Thounthong, “Direct Vector Control Using Feedback PI Controllers of a DPAG Supplied by a Two-Level PWM Inverter for a Multi-rotor Wind Turbine System,” Arabian Journal for Science and Engineering, Vol. 48, No. 7, 2023. https://doi.org/10.1007/s13369-023-08035-w.

87. B. Habib, H. Gasmi, I. Colak, “Backstepping control for multi-rotor wind power systems,” Majlesi Journal of Energy Management, Vol. 11, No. 4, pp. 8-15, 2022. https://em.majlesi.info/index.php/em/article/view/493.101.

88. H. Benbouhenni, B. Nicu, C. Ilhami, “Super-twisting hysteresis controller for multi-rotor wind energy systems,” International Journal of Electronics, pp.1-20, 2024. DOI: 10.1080/00207217.2024.2312086.

89. Ch. Hamid, D. Aziz, Ch. Seif Eddine, Z. Othmane, T. Mohammed, E. Hasnae, “Integral sliding mode control for DFIG based WECS with MPPT based on artificial neural network under a real wind profile,” Energy Reports, Vol. 7, pp. 4809-4824, 2021. https://doi.org/10.1016/j.egyr.2021.07.066

90. B. Bossoufi, M. Karim, A. Lagrioui, M. Taoussi, “FPGA-Based Implementation nonlinear backstepping control of a PMSM Drive,” IJPEDS Int. J. Power Electron. Drive Syst., Vol. 4, pp. 12–23, 2014.

91. F. Echiheb, Y. Ihedrane, B. Bossoufi, et al., «Robust sliding-Backstepping mode control of a wind system based on the DFIG generator,” Sci Rep, Vol. 12, 11782, 2022. https://doi.org/10.1038/s41598-022-15960-7.

92. H. E. Alami, B. Bossoufi, S. Motahhir, E. H. Alkhammash, M. Masud, M. Karim, M. Taoussi, M. Bouderbala, M. Lamnadi, M. El Mahfoud, “FPGA in the Loop Implementation for Observer Sliding Mode Control of DFIG-Generators for Wind Turbines,” Electronics, 2022, 11, 116. https://doi.org/10.3390/electronics11010116.

93. Y. Ibrahim, A. Semmah, W. Patrice, “Neuro-Second Order Sliding Mode Control of a DFIG based Wind Turbine System,” Journal of Electrical and Electronics Engineering, Vol. 13, No. 1, pp. 63-68, 2020.

94. H. Benbouhenni, H. Gasmi, “Comparative Study of Synergetic Controller with Super Twisting Algorithm for Rotor Side Inverter of DFIG,” International Journal of Smart Grid-ijSmartGrid, Vol. 6, No. 4, pp. 144-156, 2022. https://doi.org/10.20508/ijsmartgrid.v6i4.265.g228.

95. H. Benbouhenni, N. Bizon, I. Colak, P. Thounthong, N. Takorabet, “Simplified Super Twisting Sliding Mode Approaches of the Double-Powered Induction Generator-Based Multi-Rotor Wind Turbine System,” Sustainability 2022, 14, 5014. https://doi.org/10.3390/su14095014.

96. B. Habib, H. Gesmi, C. Ilhami, “Comparative study of sliding mode control with synergetic control for rotor side inverter of the DFIG for multi-rotor wind power systems,” Majlesi Journal of Mechatronic Systems, vol. 11, 2023. https://ms.majlesi.info/index.php/ms/article/view/532.

97. K. Xiahou, M. S. Li, Y. Liu, Q. H. Wu, “Sensor fault tolerance enhancement of DFIG-WTs via Perturbation Ob-server-Based DPC and Two-Stage Kalman Filters,” in IEEE Transactions on Energy Conversion, vol. 33, 2018. DOI: 10.1109/TEC.2017.2771250.

98. Habib B., Boudjema Z., Belaidi, A. Indirect vector control of a DFIG supplied by a two-level FSVM inverter for wind turbine system. Majlesi Journal of Electrical Engineering, 2019; 13(1): 45-54.

99. Kong H., He J., Liu Y., Cheng P., Ma, J. Improved Direct Power Control of Doubly Fed Induction Generator Without Phase-Locked Loop. 2020 IEEE Sustainable Power and Energy Conference (iSPEC), Chengdu, China, 2020, pp. 199-204, doi: 10.1109/iSPEC50848.2020.9351036.

100. N. Debdouche, L. Zarour, A. Chebabhi, N. Bessous, H. Benbouhenni, I. Colak, “Genetic algorithm-super-twisting technique for grid-connected PV system associate with filter,” Energy Reports, Vol. 10, pp. 4231-4252, 2023. https://doi.org/10.1016/j.egyr.2023.10.074.

101. H. Gasmi, M. Sofiane, H. Benbouhenni, and N. Bizon, “Optimal Operation of Doubly-fed Induction Generator used in a Grid-Connected Wind Power System,” Iranian Journal of Electrical and Electronic Engineering Vol. 19, No. 2, pp. 2431-2431, 2023. https://doi.org/10.22068/IJEEE.19.2.2431.

102. H. Benbouhenni, “Amelioration effectiveness of torque and rotor flux control applied to the asynchronous generator (AG) for dual-rotor wind turbine using neural third-order sliding mode approaches,” International Journal of Engineering, Transactions C: Aspects, Vol. 35, No. 03, pp.517-530, 2022.

103. T. Pham-Dinh, H. Nguyen-Thanh, K. Uchida and T. Nguyen Gia Minh, "Comparison between modifications of SFOC and DPC in control of grid-connected Doubly Fed Induction Generator under Unbalanced Voltage Dip," The SICE Annual Conference 2013, Nagoya, Japan, 2013, pp. 2581-2588.

104. M. Yessef *et al*., "Real-Time Validation of Intelligent Super-Twisting Sliding Mode Control for Variable-Speed DFIG Using dSPACE 1104 Board," in *IEEE Access*, vol. 12, pp. 31892-31915, 2024, doi: 10.1109/ACCESS.2024.3367828.

Appendix A: Parameters of the Components of the Studied Wind System

Table 1 – DFIG parameters

Name	Numerical Value
Nominal stator voltage	220/380 *V*
Nominal rotor voltage	12 *V*
Nominal current	3.64/6.31 *A*
Nominal power	P_n = 1.5 *kW*
Nominal frequency	f_n = 50 *Hz*
Nominal torque	C_n=*10 N.m*
Power factor	0.89
Number of pole pairs	p = 2
Nominal speed	1440 *tr/min*
Stator resistance	R_s = 0.435 *Ω*
Rotor resistance	R_r = 0.816 *Ω*
Stator inductance coefficient	L_s = 0.071 *H*
Rotor inductance coefficient	L_r = 0.070 *H*
Mutual inductance coefficient	M = 0.069 *H*
Friction coefficient	f = 6.73*10^{-3} *kg.m*^{2}
Moment of inertia	J = 0.3125 *N.s/rad*

Table 2 – Turbine parameters

Name	Numerical Value
Nominal power	P_n = 7,8 *kW*
Air density	ρ = 1.225
Pitch angle	β = 2 °
Number of blades	3
Blade radius	R =3 *m*
Gearbox ratio	G=10,38
Conversion efficiency	η =1
Moment of inertia	J = 0.042 *kg.m*^{2}
Viscous friction coefficient	f = 0.024 *N.s/rad*

Table 3 - Converter parameters

Name	Numerical Value
Apparent power	7 *kVA*
DC bus voltage	800 *V*
DC bus capacitance	C = 33 *µF*
Effective output current	23 *A*
Effective output voltage	180 *V*
Power factor	0.89
Ambient temperature	40 °C
Thermal resistance of heatsink	0.042 *W/°C*